# Did ocean warming, acidification or saturation state control coccolithophorids production through time ?

Alessandro Menini

N°d'ordre NNT : 2020LYSE1185

**THESE de DOCTORAT DE L'UNIVERSITE DE LYON**
opérée au sein de
**l'Université Claude Bernard Lyon 1**

**Ecole Doctorale** N° 341
**(N° ED 341 - Évolution, Écosystèmes, Microbiologie, Modélisation (E2M2))**

**Spécialité de doctorat** : Micropaléontologie
**Discipline** : (Sciences de la Terre)

Soutenue publiquement le 23/10/2020, par :
**(Alessandro Menini)**

---

# Did ocean warming, acidification or saturation state control coccolithophorids production through time ?

---

Devant le jury composé de :

| | | | |
|---|---|---|---|
| | | | Président |
| AUBRY, Marie-Pierre, | Professeur des Universités, | Université de Rutgers (USA) | Rapporteur |
| VILLA, Giuliana, | Professeur des Universités, | Université de Parme (Italie) | Rapporteur |
| MARTINEZ, Mathieu, | Maitre des Conférences, | Université de Rennes 1 (France) | Examinateur |
| LECUYER, Cristophe, | Professeur des Universités, | UCBL Lyon 1 (France) | Examinateur |
| MATTIOLI, Emanuela, | Professeur des Universités | UCBL Lyon1 (France) | Directrice de thèse |
| SUAN, Guillaume, | Maitre de conférences | UCBL Lyon1 (France) | Co-directeur de thèse |
| BEAUFORT, Luc, | Directeur de recherche CNRS, | Aix-en-Provence (France) | Invité |
| QUILLEVERE, Frédéric, | Maitre de conférences, | UCBL Lyon 1 (France) | Invité |

# Table des matières

## Université Claude Bernard – LYON 1

| | |
|---|---|
| Président de l'Université | M. Frédéric FLEURY |
| Président du Conseil Académique | M. Hamda BEN HADID |
| Vice-Président du Conseil d'Administration | M. Didier REVEL |
| Vice-Président du Conseil des Etudes et de la Vie Universitaire | M. Philippe CHEVALLIER |
| Vice-Président de la Commission de Recherche | |
| Directeur Général des Services | M. Damien VERHAEGHE |

## COMPOSANTES SANTE

| | |
|---|---|
| Faculté de Médecine Lyon-Est – Claude Bernard | Doyen : M. Gilles RODE |
| Faculté de Médecine et Maïeutique Lyon Sud Charles. Mérieux | Doyenne : Mme Carole BURILLON |
| UFR d'Odontologie | Doyenne : Mme Dominique SEUX |
| Institut des Sciences Pharmaceutiques et Biologiques | Directrice : Mme Christine VINCIGUERRA |
| Institut des Sciences et Techniques de la Réadaptation | Directeur : M. Xavier PERROT |
| Département de Formation et Centre de Recherche en Biologie Humaine | Directrice : Mme Anne-Marie SCHOTT |

## COMPOSANTES & DEPARTEMENTS DE SCIENCES & TECHNOLOGIE

| | |
|---|---|
| UFR Biosciences | Directrice : Mme Kathrin GIESELER |
| Département Génie Electrique et des Procédés (GEP) | Directrice : Mme Rosaria FERRIGNO |
| Département Informatique | Directeur : M. Behzad SHARIAT |
| Département Mécanique | Directeur M. Marc BUFFAT |
| UFR - Faculté des Sciences | Administrateur provisoire : M. Bruno ANDRIOLETTI |
| UFR (STAPS) | Directeur : M. Yannick VANPOULLE |
| Observatoire de Lyon | Directrice : Mme Isabelle DANIEL |
| Ecole Polytechnique Universitaire Lyon 1 | Directeur : Emmanuel PERRIN |
| Ecole Supérieure de Chimie, Physique, Electronique (CPE Lyon) | Directeur : Gérard PIGNAULT |
| Institut Universitaire de Technologie de Lyon 1 | Directeur : M. Christophe VITON |
| Institut de Science Financière et d'Assurances | Directeur : M. Nicolas LEBOISNE |
| ESPE | Administrateur Provisoire : M. Pierre CHAREYRON |

**Le réchauffement, l'acidification ou l'état de saturation des océans ont-ils contrôlé la production de coccolithophores au fil du temps ?**

RESUME

Les émissions de dioxyde de carbone devraient avoir un impact important sur la chimie des océans au cours des prochaines décennies. Les conséquences les plus importantes sont l'augmentation des températures des eaux de surface et l'acidification des océans, c'est-à-dire la diminution du *p*H de l'eau de mer, de la concentration en ions carbonate et de l'état de saturation du carbonate de calcium. En particulier, l'acidification des océans a un impact profond sur les organismes marins, notamment sur les organismes calcifiants (par exemple les coraux, les foraminifères et les coccolithophores) et est considérée comme une menace majeure pour la biominéralisation (Beaufort et al., 2011). Les espèces de coccolithophoridés (algues haptophytes) vivant dans les couches océaniques de surface sont particulièrement sensibles aux conditions chimiques et physiques des eaux peu profondes. Les coccolithophoridés sont les seuls organismes phytoplanctoniques à effectuer à la fois la photosynthèse et la biocalcification, participant aux pompes de carbone organique et inorganique (Rost et Riebesell, 2004). Des travaux récents montrent que la biocalcification pourrait être gravement affectée par l'acidification actuelle des océans, ce qui entraînerait à terme de profonds changements dans les écosystèmes marins (Fabry et al., 2008). Cependant, certaines études soulignent une résilience particulière des coccolithophores aux événements passés d'acidification des océans, et suggèrent que les températures pourraient être le principal facteur environnemental contrôlant la biocalcification (Gibbs, 2016).

Bien que la réponse des coccolithophores aux changements à court terme de température, de la $pCO_2$ ou du *p*H est bien connue par le nombre croissant d'études sur des échantillons d'eau de culture ou de surface, la résilience au niveau spécifique à long terme face aux changements de ces paramètres environnementaux, ainsi que le potentiel séculaire de surmonter les conditions critiques, sont mal connus. La réponse à long terme des coccolithophores aux changements de température, de $pCO_2$ ou de *p*H ne peut être abordée qu'en étudiant le record fossile. La principale question scientifique de mon doctorat concerne le rôle joué par les changements

sévères de $pCO_2$ passés sur la calcification des coccolithophores. Mon hypothèse de travail est que ce paramètre n'a pas agi directement sur le potentiel de biocalcification mais indirectement, en augmentant la température et l'altération des continents qui, à leur tour, ont affecté l'alcalinité des océans. En fait, en période d'altération accrue, des flux accrus de $Ca^{2+}$ et de $HCO_3^-$ se sont produits dans les eaux de surface des océans. Nous avons sélectionné deux événements caractérisés par une perturbation du cycle du carbone probablement associé aux fluctuations du $CO_2$, notamment le Pliensbachien-Toarcien (~183 My ago ; Pl-To event et T-OAE) et le Paléocène-Eocène (~55 My ; PETM). Ils sont également associés au réchauffement de l'océan et de l'atmosphère (hyperthermique), mais ils diffèrent car seulement le premier enregistre des dépôts de matière organique plus importants, appelés *black shales*.

Une première partie importante de mon doctorat a été de développer une biostratigraphie à haute résolution des nanofossiles calcaires pour les deux événements. Pour les deux cas d'études, j'ai représenté les événements à nanofossiles par rapport à la courbe des isotopes stables du carbone afin de corréler des localités éloignées.

Afin d'évaluer l'impact des perturbations du carbone, de l'acidification des océans ou des variations de température sur les coccolithophores, et d'évaluer le retour éventuel aux conditions d'avant l'événement, j'ai analysé les changements dans la composition des assemblages de coccolithes fossiles, les abondances absolues (nanofossiles/gramme de roche) et les flux (ou NAR ; nannofossil accumulation rate ; nanofossiles/mètre carré/an) pour ces deux événements. Pour l'intervalle Pliensbachien-Toarcien, j'ai étudié trois sections d'Espagne (La Almunia), de France (Anse St. Nicolas) et du Royaume-Uni (Mochras). Pour le PETM, je me suis concentré sur l'étude des sites ODP de référence 1209 (Shatsky Rise), situés dans le Pacifique tropical et 1263, dans l'océan Atlantique (Walvis Ridge). De plus, je compare les enregistrements des sites océaniques du PETM à une section proximale en Tunisie (Kharouba) afin de comprendre la réponse des nanofossiles calcaires dans des environnements de dépôt similaires au cours des deux intervalles de temps. Pour les deux événements, je compare ces sections aux données de la littérature afin de fournir une perspective globale des changements paléocéanographiques qui ont affecté ces organismes planctoniques. Pour les deux événements, les assemblages de nanofossiles suggèrent que la stratification des océans induite par le réchauffement et la diminution de la disponibilité des nutriments sont les principaux facteurs déclenchant

la diminution de l'export de carbonate dans l'océan profond. En utilisant une méthodologie récemment développée au Laboratoire de Géologie de Lyon (Brazier et al., 2015), j'ai étudié les changements de la chimie des carbonates océaniques pour le PETM en utilisant la composition isotopique du calcium des coquilles d'une espèce de foraminifères planctoniques, qui s'est avérée suivre les changements de la saturation en carbonate et des concentrations en ions carbonate.
Nos résultats corroborent également les données empiriques et de modélisation suggérant que la stratification des océans induite par le réchauffement anthropique aura un impact important sur la productivité primaire, les bilans carbones et les écosystèmes.

Mots-clés : PETM, T-OAE, Pliensbachien-Toarcien, nanofossiles calcaires, production de carbonate pélagique, cycle du carbone, cycle du calcium

Discipline: Sciences de la Terre, Biostratigraphie, Paleoceanographie

Laboratoire de Géologie de Lyon: Terre, Planètes, Environnement
UMR CNRS 5276 (CNRS, ENS, Université Lyon1)
Université Claude Bernard, Lyon1
Campus de la Doua, bâtiment Géode
2, rue Raphaël Dubois
69622 Villeurbanne Cedex
France

**Did ocean warming, acidification or saturation state control coccolithophorids production through time?**

ABSTRACT

Ongoing carbon dioxide emissions are expected to severely impact ocean chemistry in the next few decades. The most important consequences are rising sea-surface temperatures and ocean acidification, i.e., decreases in sea-water *p*H, carbonate ion concentration and saturation state of calcium carbonate. In particular, ocean acidification deeply impacts marine organisms, especially calcifying biota (e.g. corals, foraminifera and coccolithophorids) and is considered as a major threat for biomineralization (Beaufort et al., 2011). Coccolithophorids (Haptophyte algae) species living in surface oceanic layers are particularly sensitive to chemical and physical conditions in shallow waters. Coccolithophorids are the only phytoplanktonic organisms to perform at the same time photosynthesis and biocalcification, participating to the carbon organic and inorganic pumps (Rost and Riebesell, 2004). Recent works show that biocalcification could be severely hampered under the current ocean acidification eventually leading to profound changes in marine ecosystems (Fabry et al., 2008). Some studies, however, point to a particular resilience of coccolithophorids to past ocean acidification events, and suggest that temperatures could be the main environmental factor controlling biocalcification (Gibbs, 2016).

Although the response of coccolithophorids to short term changes in temperature, *p*CO2 or *p*H is well constrained by the increasing number of studies on cultured or surface-water samples, the long term species-specific resilience to change in these environmental parameters, as well as the secular potential to overcome critical conditions, is poorly known. The long-term response of coccolithophorids to changes in temperature, *p*CO2 or *p*H can be only approached by studying the fossil record. The main scientific question of my PhD regards the role played by past severe *p*CO2 changes on coccolithophore calcification. Our working hypothesis is that this parameter did not act directly on biocalcification potential but indirectly, by enhancing temperature and continental weathering which in turn affected ocean alkalinity. In fact, in times of enhanced weathering, increased fluxes occurred of $Ca^{2+}$ and $HCO_3^-$ to ocean surface waters.

We selected two past global events characterized by perturbation of the carbon

cycle likely associated with fluctuations of $CO_2$, namely the Pliensbachian-Toarcian (~183 My ago; Pl-To event and T-OAE) and the Paleocene-Eocene (~55 My; PETM). They are also associated to warming (hyperthermal), but they differ because only the former records more widespread organic matter deposits, referred to as black shales.

A first important part of my PhD was to develop a high-resolution calcareous nannofossils biostratigraphy for the two events, given that this is the basis for any paleoceanographic study. For both case studies, I plotted the nannofossil events against the $\delta^{13}C$ stable isotopes curve in order to define the precise ranking of the biovevents and correlate remote localities.

In order to assess the impact of carbon perturbations, ocean acidification or temperature variations on coccolithophorids, and to appraise the eventual recovery to pre-event conditions, we analyzed changes in fossil coccoliths assemblage composition, absolute abundances (nannofossils/grams of rock) and fluxes (nannofossils/square meter/year) for these two events. For the Pliensbachian-Toarcian interval I studied three sections from Spain (La Almunia), France (Anse St. Nicolas) and United Kingdom (Mochras). For the PETM I focused on the study of the references ODP Sites 1209 (Shatsky Rise), located in the Tropical Pacific and 1263, in the Atlantic Ocean (Walvis Ridge). Also, I compare PETM deep-sea records to a proximal section in Tunisia (Kharouba) in order to compare the response of calcareous nannofossils in similar depositional environments across the two-time interval. For both events, I compare these sections to literature data in order to provide a global perspective of the paleoceanographic changes that affected these planktonic organisms. For both events, nannofossils assemblages suggest to warming-induced ocean stratification and lowered nutrient availability as main triggers for diminished calcium carbonate export into the ocean. Using a methodology recently developed in the host institute (Brazier et al., 2015), I investigated changes in ocean carbonate chemistry for the PETM through the use of the calcium isotope composition of the shells of one species of planktonic foraminifera, which has been shown to track changes in carbonate saturation and carbonate ions concentrations.

Our findings also corroborate empirical and modeling data suggesting that anthropogenic warming-induced ocean stratification will strongly impact primary productivity, carbon budgets and ecosystems.

Keywords : PETM, T-OAE, Pliensbachian-Toarcian, calcareous nannofossils, pelagic carbonate production, carbon cycle, calcium cycle

Discipline: Earth Sciences, Biostratigraphy, Paleoceanography

## Résumé étendu en français

Les émissions de dioxyde de carbone devraient avoir un impact important sur la chimie des océans au cours des prochaines décennies. Les conséquences les plus importantes sont l'augmentation des températures des eaux de surface et l'acidification des océans, c'est-à-dire la diminution du *p*H de l'eau de mer, de la concentration en ions carbonate et de l'état de saturation du carbonate de calcium. En particulier, l'acidification des océans a un impact profond sur les organismes marins, notamment sur les organismes calcifiants (par exemple les coraux, les foraminifères et les coccolithophores) et est considérée comme une menace majeure pour la biominéralisation (Beaufort et al., 2011). Les espèces de coccolithophoridés (algues haptophytes) vivant dans les couches océaniques de surface sont particulièrement sensibles aux conditions chimiques et physiques des eaux peu profondes. Les coccolithophoridés sont les seuls organismes phytoplanctoniques à effectuer à la fois la photosynthèse et la biocalcification, participant aux pompes de carbone organique et inorganique (Rost et Riebesell, 2004). Des travaux récents montrent que la biocalcification pourrait être gravement affectée par l'acidification actuelle des océans, ce qui entraînerait à terme de profonds changements dans les écosystèmes marins (Fabry et al., 2008). Cependant, certaines études soulignent une résilience particulière des coccolithophores aux événements passés d'acidification des océans, et suggèrent que les températures pourraient être le principal facteur environnemental contrôlant la biocalcification (Gibbs, 2016).

Bien que la réponse des coccolithophores aux changements à court terme de température, de la $pCO_2$ ou du *p*H est bien connue par le nombre croissant d'études sur des échantillons d'eau de culture ou de surface, la résilience au niveau spécifique à long terme face aux changements de ces paramètres environnementaux, ainsi que le potentiel séculaire de surmonter les conditions critiques, sont mal connus. La réponse à long terme des coccolithophores aux changements de température, de $pCO_2$ ou de *p*H ne peut être abordée qu'en étudiant le record fossile, étant donné que les coccolithophores possèdent un enregistrement fossile excellent depuis leur apparition au Trias superieur. La principale question scientifique de mon doctorat concerne le rôle joué par les changements sévères de $pCO_2$ passés sur la calcification des coccolithophores. Mon hypothèse de travail est que ce paramètre n'a pas agi

directement sur le potentiel de biocalcification mais indirectement, en augmentant la température et l'altération des continents qui, à leur tour, ont affecté l'alcalinité des océans. En fait, en période d'altération accrue, des flux accrus de $Ca^{2+}$ et de $HCO_3^-$ se sont produits dans les eaux de surface des océans.

J'ai sélectionné deux événements caractérisés par une perturbation du cycle du carbone probablement associé aux fluctuations du $CO_2$, notamment le Pliensbachien-Toarcien (~183 My ago ; Pl-To event et T-OAE) et le Paléocène-Eocène (~55 My ; PETM). Ils sont également associés au réchauffement (hyperthermique), mais ils diffèrent car seulement le premier enregistre des dépôts de matière organique plus importants, appelés *black shales*. En utilisant une méthodologie récemment développée au Laboratoire de Géologie de Lyon (Brazier et al., 2015), j'ai étudié les changements de la chimie des carbonates océaniques pour le PETM en utilisant la composition isotopique du calcium des coquilles d'une espèce de foraminifères planctoniques, qui s'est avérée suivre les changements de la saturation en carbonate et des concentrations en ions carbonate.

Nos résultats corroborent également les données empiriques et de modélisation suggérant que la stratification des océans induite par le réchauffement anthropique aura un impact important sur la productivité primaire, les bilans carbones et les écosystèmes.

Dans ce résume étendu je synthétise les résultats principaux pour chaque chapitre de la thèse.

Une première partie importante de mon doctorat a été de développer une biostratigraphie à haute résolution des nanofossiles calcaires pour les deux événements, parce que les zonations standards ne fournissent pas une résolution suffisante pour étudier de courts évènements (200-500 kyrs) comme le PETM ou le T-OAE. Pour les deux cas d'études, j'ai représenté les événements à nanofossiles par rapport à la courbe des isotopes stables du carbone afin de trouver les évènements qui permettent de corréler des localités éloignées. Pour l'intervalle Pliensbachien-Toarcien, j'ai étudié une section d'Espagne (La Almunia) et de France (Anse St. Nicolas). Pour le PETM, je me suis concentré sur l'étude des sites ODP de référence 1209 (Shatsky Rise), situés dans le Pacifique tropical et 1263, dans l'océan Atlantique (Walvis Ridge).

**Biostratigraphie pour l'intervalle Pliensbachien-Toarcien** : Plusieurs études ont porté sur la réponse des nanofossiles calcaires à l'événement anoxique de Toarcian (T-OAE), l'un des événements les plus dramatiques des perturbations environnementales de l'ère mésozoïque. Néanmoins, l'impact des perturbations environnementales marquées sur le nannoplancton calcaire pendant la transition Pliensbachien/Toarcien (Pl/To ; ~183 Ma), légèrement avant le T-OAE, reste comparativement moins bien documenté. Je présente une étude biostratigraphique et chimiostratigraphique à haute résolution de deux sections où la limite Pliensbachien/Toarcien est bien représenté. Une section est située dans le centre de l'Espagne (La Almunia) et la seconde dans le nord-ouest de la France (Anse St. Nicolas). Bien que les deux localités aient été paléographiquement proches l'une de l'autre au Jurassique Inferieur, les dissimilitudes dans les assemblages de nanofossiles suggèrent des conditions paléoenvironnementales différentes. Au-dessus de la limite Pl/To, les abondances absolues (nanofossiles/gramme de roches) et les placolites ont augmenté de manière substantielle dans les deux sections. De même, les isotopes du carbone montrent une tendance à la hausse et une excursion négative à la limite. La comparaison de nos nouvelles données avec sept autres sections de la marge nord et sud de Téthys, montre que le Pl/To correspondait à un événement majeur de diversification des coccolithes. La spéciation du Pl/To a provoqué une réorganisation majeure des assemblages, notamment les murolithes dominent au Pliensbachien Supérieur alors que les placolithes deviennent le groupe dominant à partir du Toarcien Inferieur. Quelques différences sont observées d'une section à l'autre, mais plusieurs premières apparitions (FO) d'espèces sont biostratigraphiquement utiles pour la définition de la limite Pl/To, comme la FO de *Biscutum intermedium*, *Zeugrhabdothus erectus* et *Discorhabdus ignotus*. La perturbation du cycle du carbone à la limite Pl/To s'est produite lors d'un épisode de transgression après un refroidissement prononcé et une baisse du niveau marin qui ont déclenché des hiatus dans de nombreuses localités. La spéciation des nanofossiles calcaires au Pl/To est étroitement lié à tous ces phénomènes. Ainsi, cet événement doit être considéré comme le début de profondes perturbations paléoenvironnementales qui ont culminent avec le T-OAE.

**Biostratigraphie pour le PETM :** La limite Paléocène-Eocène est caractérisée par une excursion négative importante des isotopes du carbone qui correspond au

maximum thermique de l'éocène du paléocène (PETM). La forte excursion négative des isotopes stables du carbone a été retenue comme marqueur de la limite Paléocène-Éocène. Bien qu'elles aient été enregistrées dans plusieurs milieux océaniques et terrestres, les phases du PETM définies par Zachos et al., 2005 et Röhl et al., 2007 (*onset*, *core* de l'événement et *recovery*), ne sont pas correctement datées par les nanofossiles calcaires car les biozonations standard disponibles ne nous permettent pas d'obtenir une résolution suffisante. Je présente de nouvelles données biotratigraphiques à haute résolution provenant des sites 1209 (Shatsky Rise, océan Pacifique tropical) et 1263 (Walvis Ridge, océan Atlantique sud-est) afin de reconstruire précisément la succession des événements biostratigraphiques (première et dernière apparitions, changements dans la composition de l'assemblage), et de les ancrer à un proxy indépendant représenté par la courbe des isotopes stables du carbone. Grace à une comparaison soignée de nos données avec des événements nanofossiles provenant de six sections situées à différentes (paléo)latitudes et dans différents contextes géologiques (de l'océan ouvert aux coupes néritiques) j'ai reconnu 26 événements sur un intervalle de 250 kyrs couvrant le PETM, et je présente une biozonation à haute résolution de cet intervalle. Les événements de nanofossiles calcaires représentés par rapport à la courbe de $\delta^{13}C$ disponibles montrent un certain degré de diachronisme, même en tenant compte des marqueurs de zone précédemment établis. De plus, des discontinuités (*unconformities*) se produisent au début du PETM dans la plupart des sites océaniques, mais dans une moindre mesure dans les sections qui affleurent sur les continents. Je propose une nouvelle biozonation, basée sur des événements reproductibles dans différentes localités, afin d'obtenir une subdivision chronostratigraphique à haute résolution pour cet événement hyperthermique. Je définis ainsi quatre nouvelles zones couvrant le Paléocène superieur et l'Éocène inferieur qui permettent de corréler les localités proximales et distales, et deux sous-zones principalement utiles dans les environnements proximaux. Ces nouvelles zones sont corrélées aux principales tendances de la courbe des isotopes stables du carbone ($\delta^{13}C$) et définissent l'intervalle de pré-excursion (PE-1), l'excursion négative du $\delta^{13}C$ définissant la base de l'Eocène (PE0), le *core* de l'événement et la phase de récupération I (*recovery* I ; PE1) et les intervalles de la phase de récupération II (*recovery* II ; PE2)

Un deuxième aspect fondamental de mon travail de thèse a été l'étude de l'impact des perturbations du cycle du carbone, de l'acidification des océans ou des variations de température sur la biocalcification des coccolithophores au cours des temps géologiques, et d'évaluer le retour aux conditions précédentes à ces perturbations. Pour ce faire, j'ai analysé les changements dans la composition des assemblages de coccolithes fossiles, les abondances absolues (nanofossiles/gramme de roche) et les flux ou NAR (*nannofosil accumulation rate* ; nanofossiles/mètre carré/an) pour ces deux événements. Pour l'intervalle Pliensbachien-Toarcien, j'ai étudié trois sections d'Espagne (La Almunia), de France (Anse St. Nicolas) et du Royaume-Uni (Mochras). Pour le PETM, je me suis concentré sur l'étude des sites ODP de référence 1209 (Shatsky Rise), situés dans le Pacifique tropical et 1263, dans l'océan Atlantique (Walvis Ridge). De plus, je compare les enregistrements du PETM en eaux profondes à une section proximale en Tunisie (Kharouba) afin d'examiner la réponse des nanofossiles calcaires dans des environnements de dépôt similaires sur l'intervalle de deux temps. Pour les deux événements, je compare ces sections aux données de la littérature afin de fournir une perspective globale des changements paléocéanographiques qui ont affecté ces organismes planctoniques. Pour les deux événements, les assemblages de nanofossiles suggèrent que la stratification des océans induite par le réchauffement et la diminution de la disponibilité des nutriments sont les principaux facteurs déclenchant la diminution de l'export de carbonate dans l'océan profond.

**Assemblages et paleocenographie pour le Pliensbachien-Toarcien :** Le scénario classique d'interprétation de l'événement anoxique de Toarcien Inférieur (T-OAE ; ~183 Ma) et de l'excursion négative associée est généralement lié à la libération massive de carbone léger ($^{12}C$) dans les réservoirs de surface, en raison de la mise en place des larges provinces magmatiques des Karoo-Ferrar, de la déstabilisation des hydrates de méthane des marges continentales, ou de la libération thermogénique de méthane due à la mise en place des filons-couches au Karoo-Ferrar. Quelle qu'en soit la cause, on pense que cette libération massive de carbone a favorisé les conditions d'effet de serre, l'amélioration du cycle hydrologique et l'altération des continents. Ces conditions ont finalement favorisé l'apport de nutriments aux bassins peu profonds, soutenant la productivité primaire et, en raison de la consommation

d'oxygène par la respiration de la matière organique, le développement de l'anoxie océanique.

Cependant, plusieurs travaux ont montré que les producteurs primaires, comme les nanofossiles calcaires et les dinoflagellés, ont connu une crise grave pendant le T-OAE, qui a culminé avec une panne de phytoplancton. Par ailleurs, les flux de matière organique ne semblent pas exceptionnels. L'analyse de la taille des nanofossiles dans le trou de forage de Mochras (foré par la BGS en Pays de Galle, Royaume Uni) peut nous aider à résoudre cette énigme. La récupération sédimentaire de la carotte est excellente, la section est continue et bien datée et a fait l'objet d'analyses à haute résolution, ce qui en fait un candidat idéal pour analyser l'évolution combinée de la production de carbonate et de la production primaire. Grâce à la combinaison de la biométrie et des abondances absolues (spécimens par g de roche), nous pouvons estimer les flux de carbonates et de matière organique d'origine nanofossile vers les sédiments. Nous pouvons comparer ces résultats au $\delta^{13}C$, qui reflète les perturbations du cycle du carbone au Toarcien inférieur. Cette étude devrait nous permettre de mieux évaluer les mécanismes d'exportation du carbone inorganique et organique des eaux océaniques de surface vers les sédiments lors des changements climatiques et environnementaux majeurs qui se sont produits au Toarcien.

**Assemblages et paléoocéanographie pour le PETM :** Le réchauffement climatique et la perturbation du cycle du carbone autours de la limite Paléocène-Éocène (PETM, environ 56 Ma) ont été liés à une libération massive de carbone dans le système océan-atmosphère. Des études précédentes ont invoqué une augmentation de la productivité du phytoplancton pour provoquer une baisse de la $pCO_2$, un refroidissement et favoriser une récupération du système (*recovery*). Toutefois, les interprétations des données géochimiques et biotiques divergent quant au moment et au lieu où cette productivité accrue s'est produite. Je présente des données en haute résolution sur les assemblages de nanofossiles, y compris les abondances relatives et absolues (nanofossiles/gramme de roche) d'une section proximale située dans la Tethys (Kharouba) et de deux sites océaniques (sites ODP 1209 et 1263, situés respectivement dans les océans Pacifique et Atlantique) afin de suivre les tendances globales et locales des assemblages de nanofossiles. Ces données, combinées aux enregistrements biotiques publiés, indiquent une accentuation transitoire des gradients trophiques entre le *onset* et le *core* du PETM, avec une diminution de la

productivité dans les sites océaniques oligotrophes, parallèlement à une augmentation de la disponibilité des nutriments dans les zones proximales. Les niveaux de productivité se sont rétablis en domaine pélagique au cours du *recovery*, ce qui pourrait avoir joué un rôle important dans la séquestration du carbone et le retrait du $CO_2$ en association avec l'intensification de la météorisation continentale.

**Modulation du cycle du carbone par le phytoplancton pendant le PETM** : Le Maximum thermique à la limite Paléocène/Eocène du Paléocène (PETM, ~56 Ma), est considéré comme l'un des meilleurs analogues pour les émissions anthropiques de $CO_2$. Pourtant, les principales rétroactions négatives qui ont éliminé l'excès de carbone lors de l'arrêt du PETM restent controversées. La saturation et l'enfouissement des $CaCO_3$, dus à une altération accrue des silicates, sont communément acceptés comme les principaux processus moteurs. Par ailleurs, une baisse de la production nette de $CaCO_3$ des algues induites par le $CO_2$ pourrait avoir déclenché l'accumulation d'alcalinité et la sursaturation, mais ce mécanisme n'est toujours pas étayé par des preuves indirectes. Je présente une étude *multiproxy* des enregistrements des eaux profondes tropicales du Pacifique et de l'Atlantique qui démontre que l'enfouissement des carbonates s'est rétabli aux niveaux pré-PETM environ 30 000 ans plus tard que la saturation. Nous attribuons ce découplage à un effondrement spectaculaire (>60 %) et durable (>80 000 ans) de la production nette de $CaCO_3$ en raison de la stratification des océans induite par le réchauffement et de la diminution de la disponibilité des nutriments. Nos enregistrements montrent que l'excès d'alcalinité qui en résulte a été rapidement consommé lorsque la production et l'enfouissement du CaCO3 ont finalement repris, déclenchant un retrait rapide et massif du carbone tant inorganique qu'organique. Nos conclusions en élucident certains des mécanismes biogéochimiques clés qui ont conduit à la récupération du PETM et soulignent l'importance négligée mais cruciale des seuils biologiques dans la régulation des événements passés et actuels du réchauffement de l'effet de serre.

**Conclusion et synthèse :** Le dernier chapitre de la thèse vise à comparer les deux intervalles de temps pour discuter des aspects similaires et des différences. Pour les deux évènements les données biostratigraphiques ont été représentés par rapport à la courbe des isotopes stables du carbone ($\delta^{13}C$). Pour le Pliensbachien-Toarcien, j'ai pu mettre en évidence qu'il y a un épisode majeur d'apparitions autour de la limite

Pliensbachien-Toarcien, contrairement au T-OAE. Ceci est en partie lié à l'augmentation des placolithes, qui domineront les assemblages pour le reste Mésozoïque et Cénozoïque et en partie liés à des condensations dans plusieurs bassins de la Tethys autour de la limite. Pour le PETM, j'ai pu mettre en évidence que le record sédimentaire a une influence majeure sur l'ordre des évènements. Similairement au Pliensbachien-Toarcien, la présence de discontinuités à la limite explique certaines différences d'une localité à l'autre. Cependant, il existe un certain dégrée de diachronisme, affectant également les marques biostratigraphiques utilisées dans les zonations standards. La limite Paléocène-l'Éocène est caractérisés par plusieurs origines et extinctions, et aussi par des changements au sein des communautés de nanofossiles calcaires. Certains de ces événements, jamais ne pris en compte dans les biozonations antérieures, se sont avérés cohérents, avec un degré de diachronisme moindre que les marqueurs biostratigraphiques utilisés précédemment. Finalement j'obtiens un nouveau schéma de biozonation à haute résolution avec une résolution moyenne de 50-100 kyrs par zone. De plus, je corrèle les événements biostratigraphiques et les nouvelles zones aux différentes phases caractérisant l'excursion négative des isotopes du carbone définissant le Paléocène/Éocène.

En terme d' mplications paleoceanographiques, malgré certaines différences, comme par exemple le fait que pour le Jurassique Inferieur nous ne disposons pas d'enregistrement d'océan ouvert, les changements des abondances absolues et des flux durant les deux évènements, suggèrent iperstratification et oligotrophie des eaux de surface. L'oligotrophie était plus marqué pendant le T-OAE, car même les zones plus proximales montrent une tendance à l'oligotrophie. Au PETM, l'oligotrophie était particulièrement accentue dans les sites océaniques, loin des apports des rivières tandis que dans les coupes proximales on enregistre des conditions fluctuantes.

Un aspect fondamental de ce travail de thèse est l'étude *multiproxy* des enregistrements des eaux profondes tropicales du Pacifique et de l'Atlantique ; ces données démontrant que l'enfouissement des carbonates s'est rétabli à des niveaux pré-PETM environ 30 000 ans après la saturation. Ce découplage entre saturation et enfouissement des carbonates est expliqué par un effondrement spectaculaire (>60 %) et durable (>80 000 ans) de la production nette de $CaCO_3$, dû à la stratification des océans induite par le réchauffement et à la diminution de la disponibilité des nutriments. L'excès d'alcalinité qui en résulte a été rapidement consommé lorsque la

production et l'enfouissement du $CaCO_3$ ont finalement repris, déclenchant un retrait rapide et massif du carbone tant inorganique qu'organique. Ces conclusions élucident certains des mécanismes biogéochimiques clés qui ont conduit à la récupération du PETM et soulignent l'importance négligée mais cruciale des seuils biologiques et donc de la biologie dans la régulation des événements passés et actuels du réchauffement de l'effet de serre.

# Chapitre 1. Introduction

# Introduction

## 1. Les perturbations présentes et futures du cycle inorganique du carbone.

Les émissions de dioxyde de carbone devraient avoir un impact important sur la chimie des océans au cours des prochaines décennies. Les conséquences les plus importantes sont l'augmentation des températures des eaux de surface et l'acidification des océans, c'est-à-dire la diminution du *p*H de l'eau de mer, de la concentration en ions carbonate et de l'état de saturation du carbonate de calcium. La valeur du $CO_2$ atmosphérique aujourd'hui est supérieure de 100 ppmv à la valeur préindustrielle (280 ppmv), et le *p*H moyen de la surface de l'océan a baissé de 0,1 unité, ce qui représente une augmentation d'environ 30 % de $[H^+]$. Selon les prévisions du GIEC (Houghton et al., 2001), le *p*H moyen de l'océan de surface pourrait diminuer de 0.3-0.4 unité par rapport aux valeurs préindustrielles à la fin de ce siècle (Caldeira et Wickett, 2005).

En particulier, l'acidification des océans a un impact profond sur les organismes marins, notamment sur les organismes calcifiants (par exemple les coraux, les foraminifères et les coccolithophores) et est considérée comme une menace majeure pour la biominéralisation (Beaufort et al., 2011). Les espèces de coccolithophoridés (algues haptophytes) vivant dans les couches océaniques de surface sont particulièrement sensibles aux conditions chimiques et physiques des eaux peu profondes. Les coccolithophoridés sont les seuls organismes phytoplanctoniques à effectuer à la fois la photosynthèse et la biocalcification, participant aux pompes de carbone organique et inorganique (Rost et Riebesell, 2004). Des travaux récents montrent que la biocalcification pourrait être gravement affectée par l'acidification actuelle des océans, ce qui entraînerait à terme de profonds changements dans les écosystèmes marins (Fabry et al., 2008). Cependant, certaines études soulignent une résilience des coccolithophores aux événements passés d'acidification des océans (Iglésias-Rodriguez et al., 2008), et suggèrent que les températures pourraient être le principal facteur environnemental contrôlant la biocalcification (Gibbs, 2016).

Grace au nombre croissant d'études sur des échantillons d'eau de culture ou de surface, la réponse des coccolithophores aux changements à court terme de température, de la $pCO_2$ ou du *p*H est bien connue mais la résilience au niveau

spécifique à long terme face aux changements de ces paramètres environnementaux, ainsi que le potentiel séculaire de surmonter les conditions critiques, sont difficiles à quantifier. La réponse à long terme des coccolithophores aux changements de température, de $pCO_2$ ou de *p*H ne peut être abordée qu'en étudiant le record fossile.

## 2. Les coccolithophores dans les océans

Les coccolithophores sont des algues unicellulaires de taille micrométrique du domaine Eukaryota, de l'embranchement Haptophyta et de la classe Prymniophyceae (Billard et Inouye, 2004). Ces algues photosynthétiques produisent à l'intérieur de leur cellule à l'aide de l'appareil de Golgi des plaques composées de carbonate de calcium ($CaCO_3$) appelées coccolithes. Ces plaques sont sont ensuite transportées sur la bordure externe de la cellule pour former un teste appelé coccosphère. Les coccolithophores sont des organiques pélagiques exclusivement marins, très diversifiés en nombre d'espèces et extrêmement abondant dans les océans. A la base de la chaine alimentaire dans les océans, ils participent à la fois par la photosynthèse et la biocalcification au cycle organique et inorganique du carbone. Malgré leur petite taille, leur contribution dans le cycle du carbone est extrêmement importante puisqu'ils produisent environ la moitié du carbonate pélagique total, notamment par le biais de *blooms*. Un *bloom* correspond à la multiplication massive d'une espèce pédant une courte période et lorsque les conditions environnementales sont favorables. Ces événements entrainent une production phénoménale de carbonate de calcium. Les coccolithophores ont une position clés dans les environnements marins actuels, de par leur base dans la chaine alimentaire et leur rôle majeur dans le cycle du carbone.

## 3. Une longue histoire évolutive

Les coccolithophores sont très souvent préservées sous forme de coccolithes isolées dans les sédiments et font partie des nanofossiles calcaires. Ce groupe inclut tous les restes minéralisés issus d'organismes pélagiques micrométriques à test calcaire, indifféremment de leur affinité taxinomique. Les plus anciens nanofossiles calcaires sont représentés par des calcisphères du Carnien (Trias supérieur, 228 Ma) ; les plus anciens coccolithes datent du Norien (Trias supérieur, 210 Ma) (Bown, 1987-1998), appartenant au groupe morphologique des murolithes. Les placolithes, la forme la plus répondue dans l'histoire de coccolithes, n'apparaissent qu'au debut du Pliensbachien (Jurassique Inferieur, 190 Ma) et se diversifient très rapidement à la limite

Pleinsbachien-Toarcien (183 Ma). La longue histoire évolutive des nanofossiles calcaires a été affectée par de nombreux épisodes de crise drastique (e.g., la limite Crétacé/Paléocène ; la limite Paléocène/Eocène) et d'épisodes de diversification (e.g., la limite Pliensbachien/Toarcien, Jurassique moyen ; Suchéras-Marx et al., 2019) qui sont associés à des perturbations des principaux cycles biogéochimiques, tels que des changements de la $pCO_2$, de température ou du *p*H. Bien que la réponse des coccolithophores aux changements à court terme de température, de la $pCO_2$ ou du *p*H est bien connue par le nombre croissant d'études sur les coccolithophores actuelles, la résilience au niveau spécifique à long terme face aux changements de ces paramètres environnementaux, ainsi que le potentiel séculaire de surmonter les conditions critiques, sont mal connus. La réponse à long terme des coccolithophores aux changements de température, de $pCO_2$ ou de *p*H ne peut être abordée qu'en étudiant le record fossile. La principale question scientifique de mon doctorat concerne le rôle joué par les changements sévères de $pCO_2$ passés sur la calcification des coccolithophores. Mon hypothèse de travail est que ce paramètre n'a pas agi directement sur le potentiel de biocalcification mais indirectement, en augmentant la température et l'altération des continents qui, à leur tour, ont affecté l'alcalinité des océans. En fait, en période d'altération accrue, des flux accrus de $Ca^{2+}$ et de $HCO_3^-$ se sont produits dans les eaux de surface des océans.

## 4. Cas d'études : le PETM et le Pliensbachien/Toarcien

Pour répondre à la question scientifique de ce projet de recherche, j'ai sélectionné deux cas d'études : le Maximum Thermique à la limite Paléocène-Eocène (PETM ; 56 Ma) et le Pliensbachien-Toarcien (limite Pliensbachien-Toarcien et l'événement anoxique océanique du Toarcien inférieur ou T-OAE; 183 Ma). Des études précédentes ont mis en évidence que les deux évènements présentent de nombreuses caractéristiques communes (Cohen et al., 2007) :

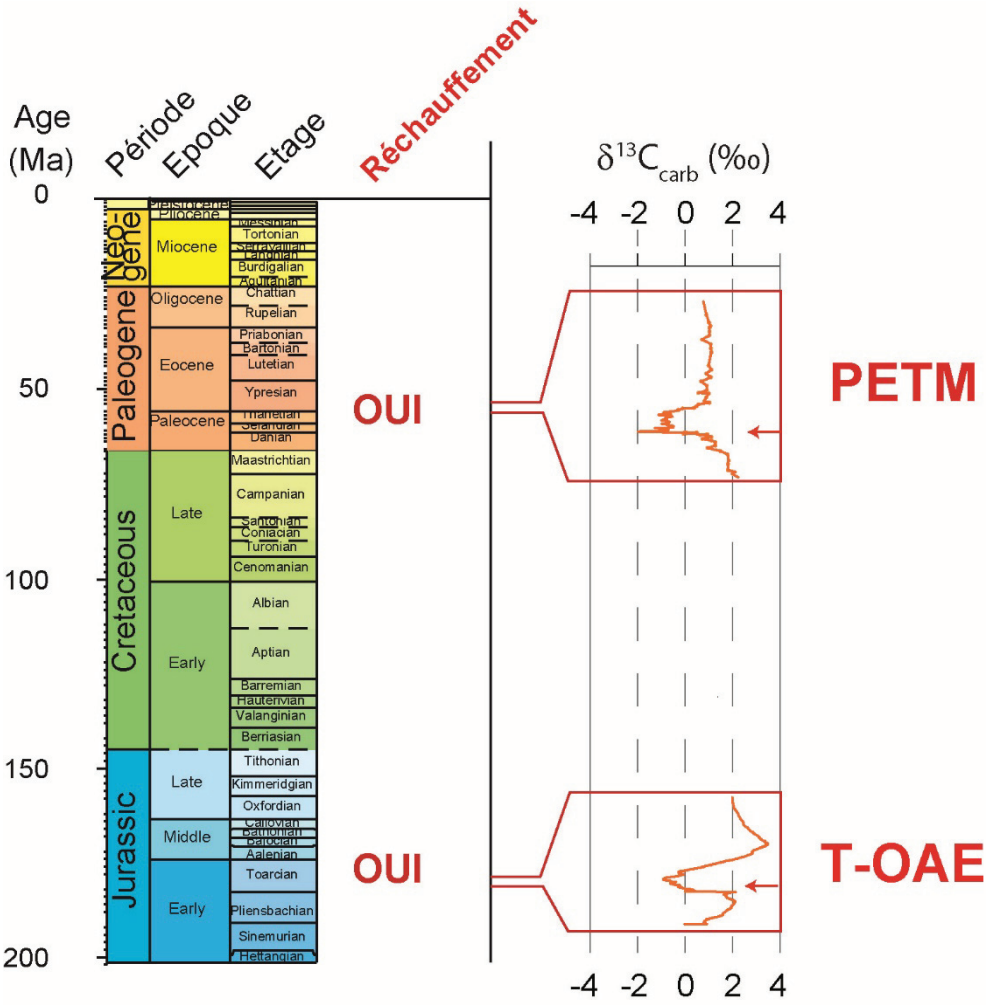


Fig. 1. Représentation des deux cas d'études par rapport à l'échelle des temps géologiques (Gradstein et al., 2012).

- Le grand nombre des enregistrements couvrant le PETM démontre que la perturbation du cycle du carbone a eu une portée mondiale (e.g., Kennet and Stott, 1991 ; Zachos et al., 2003 ; Zachos et al., 2005), et la reconnaissance de l'excursion négative des isotopes du carbone de Toarcien dans les sections de plateformes continentales appartenant à tous les océans, dans des sections épicontinentales et dans des échantillons de bois fossilisé indiquent très probablement un événement mondial (Jenkyns, 1985; Jenkyns et al. 2002).
- Le shift négative du $\delta^{13}C$ qui définit les excursions négatives des isotopes du carbone au PETM et pendant le Toarcien était entre 2 ‰ et 7 ‰ et est observé dans les enregistrements de $\delta^{13}C$ mesuré sur des carbonates $\delta^{13}C_{bulk\ carbonate}$ (e.g., Hesselbo et al., 2007; Bains et al., 1999; Zachos et al., 2005) et sur la

matière organique totale $\delta^{13}C_{TOC}$ qui couvrent les deux intervalles (Pagani et al., 2006; Sluijs et al., 2006; Xu et al., 2018)

- Les deux excursions négatives des isotopes du carbone ont été associées à des accumulations exceptionnellement élevées de carbone organique dans les plateformes continentales et dans les environnements marines épicontinentaux, le COT atteignant environ 15 % à environ 20 % dans certaines sections (Sluijs et al., 2006).
- Les deux excursions négatives des isotopes du carbone ont été associées à des extinctions d'espèces et phytoplancton dans les océans, avec des réorganisations majeures des espèces sur les continents, et avec la preuve d'une soudaine crise mondiale (Bown, 1987 ; Bralower et al., 2002 ; Gibbs et al., 2006b ; Mattioli et al., 2008).
- L'augmentation du lessivage continentale, comme l'indiquent des changements soudains dans la minéralogie des argiles et par une excursion des isotopes de l'osmium au PETM (Ravizza et al., 2001 ; Dickson et al., 2015), et par des excursions abruptes et importantes de isotopes lu strontium, de l'osmium et du calcium (McArthur et al., 2000; Cohen et al., 2004 ; Brazier et al., 2015 ; Percival et al., 2016) pendant le T-OAE.

Bien que plusieurs études se sont focalisées sur la réponse du phytoplancton calcaire aux changements environnementaux durant le PETM et le Pliensbachien-Toarcien, la quantification de la productivité carbonatée versus productivité primaire en réponse aux perturbations du cycle du carbone, de température et de chimie des océans ainsi que l'étude approfondie du rôle du phytoplancton calcaire dans le mécanismes de récupération du système aux conditions précédentes n'a jamais été faite auparavant.

Une première partie importante de mon doctorat a été de développer une biostratigraphie à haute résolution des nanofossiles calcaires pour les deux événements, parce que les zonations standards ne fournissent pas une résolution suffisante pour étudier de courts évènements tels que le PETM ou le T-OAE. Pour les deux cas d'études, j'ai représenté les événements à nanofossiles par rapport à la courbe des isotopes stables du carbone afin de trouver les évènements qui permettent de corréler des localités éloignées. Pour l'intervalle Pliensbachien-Toarcien, j'ai étudié

une section d'Espagne (La Almunia) et de France (Anse St. Nicolas). Pour le PETM, je me suis concentré sur l'étude des sites océaniques ODP (Ocean Drilling Program) 1209 (Shatsky Rise), situés dans le Pacifique tropical et 1263, dans l'océan Atlantique (Walvis Ridge). Ces deux sites enregistrent très finement l'excursion négative des isotopes du carbone et en étant les sites océaniques les moins profonds de l'Atlantique et du Pacifique, sont véritablement les moins affectés par la dissolution generaisée des carbonates due à la remontée de la CCD pendant le PETM (Zachos et al., 2003 ; Zachos et al., 2005 ; Takeda et Kaiho, 2007 ;  Bralower et al., 2014). En étant deux sections de référence pour cette intervalle de temps, de nombreuses études de littérature (e.g., géochimie, micropaléontologie, sédimentologie) existent déjà

Un deuxième aspect fondamental de mon travail de thèse était l'étude de l'impact des perturbations du cycle du carbone, de l'acidification des océans ou des variations de température sur les coccolithophores au cours des temps géologiques, et d'évaluer le retour aux conditions d'avant l'événement. Pour ce faire, j'ai analysé les changements dans la composition des assemblages de coccolithes fossiles, les abondances absolues (nanofossiles/gramme de roche) et les flux (ou NAR, nannofossil accumulation rates ; nanofossiles/mètre carré/an) pour ces deux événements. Pour l'intervalle Pliensbachien-Toarcien, j'ai étudié trois sections d'Espagne (La Almunia), de France (Anse St. Nicolas) et du Royaume-Uni (Mochras). Pour le PETM, je me suis concentré sur l'étude des sites ODP 1209 (Shatsky Rise), situés dans le Pacifique tropical et 1263, dans l'océan Atlantique (Walvis Ridge). De plus, je compare les enregistrements du PETM en eaux profondes à une section proximale en Tunisie (Kharouba) afin d'examiner la réponse des nanofossiles calcaires dans des environnements de dépôt similaires sur l'intervalle de deux temps. Pour les deux événements, je compare ces sections aux données de la littérature afin de fournir une perspective globale des changements paléocéanographiques qui ont affecté ces organismes planctoniques. Pour les deux événements, les assemblages de nanofossiles suggèrent que la stratification des océans induite par le réchauffement et la diminution de la disponibilité des nutriments sont les principaux facteurs déclenchant la diminution de l'export de carbonate dans l'océan profond.

## 5. Biostratigraphie pour l'intervalle Pliensbachien-Toarcien

Dans ce chapitre du manuscrit, je me suis intéressé à la construction d'une biostratigraphie à très haute resolution pour la limite Pliensbachien-Toarcien. Ce chapitre a fait l'objet d'une publication dans la revue internationale *Newsletters on Stratigraphy en 2019*. Plusieurs études ont porté sur la réponse des nanofossiles calcaires à l'événement anoxique de Toarcian (T-OAE), l'un des événements les plus dramatiques des perturbations environnementales de l'ère Mésozoïque. Néanmoins, l'impact des perturbations environnementales marquées sur le nanofossiles calcaire pendant la transition Pliensbachien/Toarcien (Pl/To ; ~183 Ma), légèrement avant le T-OAE, reste comparativement moins bien documenté. Dans ce chapitre, je présente une étude biostratigraphique et chimiostratigraphique à haute résolution de deux sections où le Pl/To est bien représenté. Une section est située dans le centre de l'Espagne (La Almunia) et la seconde dans le nord-ouest de la France (Anse St. Nicolas). Bien que les deux localités aient été proches l'une de l'autre au Jurassique précoce, les dissimilitudes dans les assemblages de nanofossiles suggèrent des conditions paléoenvironnementales différentes. Après la limite Pl/To, les abondances absolues (nanofossiles/gramme de roches) et les placolites (un groupe de coccolithes à structure emboité, Young et al.,1994) augmentent de manière substantielle dans les deux sections. De même, les isotopes du carbone montrent une tendance à la hausse et une excursion négative est constatée à la frontière. La comparaison de nos nouvelles données avec sept autres sections de la marge nord et sud de Téthys, montre que le Pl/To correspondait à un événement majeur de diversification des coccolithes. La spéciation du Pl/To a provoqué un passage prononcé des murolithes aux placolithes. Quelques différences sont observées d'une section à l'autre, mais plusieurs premières apparitions (FO) d'espèces et une réorganisation des assemblages sont documentées dans toutes les localités. Certaines de ces FO sont biostratigraphiquement utiles pour la définition de la limite Pl/To, comme la FO de *Biscutum intermedium*, *Zeugrhabdothus erectus* et *Discorhabdus ignotus*. La perturbation du cycle du carbone à la limite Pl/To s'est produite lors d'un épisode de transgression après un refroidissement prononcé et une baisse du niveau de la mer qui ont déclenché des hiatus dans de nombreuses localités. L'événement à l'origine des nanofossiles calcaires est étroitement lié à tous ces phénomènes. Ainsi, l'événement Pl/To doit être considéré comme le début de profondes perturbations paléoenvironnementales qui ont culminé avec le T-OAE.

## 6. **Biostratigraphie pour le PETM.**

Dans ce chapitre du manuscrit, je me suis intéressé à la construction d'une biostratigraphie à très haute resolution pour la limite Paléocène-Eocène, similairement au chapitre précèdent. Ce chapitre fait l'objet d'une publication qui est actuellement en cours de révision dans la revue internationale *Newsletters on Stratigraphy*. La limite Paléocène-Eocène est caractérisée par une excursion négative importante des isotopes du carbone qui correspond au maximum thermique de l'éocène du paléocène (PETM). La forte excursion négative des isotopes stables du carbone a été retenue comme marqueur de la limite Paléocène-Éocène. Bien qu'elles aient été enregistrées dans plusieurs milieux océaniques et terrestres, les phases du PETM, notamment le *onset*, le *core* de l'événement et la *recovery*, ne sont pas correctement datées par les nanofossiles calcaires car les biozonations standard disponibles ne nous permettent pas d'obtenir une résolution suffisante. Je présente de nouvelles données biotratigraphiques à haute résolution provenant des sites 1209 (Shatsky Rise, océan Pacifique tropical) et 1263 (Walvis Ridge, océan Atlantique sud-est) afin d'évaluer précisément la succession des événements biostratigraphiques (première et dernière apparitions, changements dans la composition de l'assemblage), et de les ancrer à un proxy indépendant représenté par la courbe des isotopes du carbone. Grace à une comparaison soignée de nos données avec des événements nanofossiles provenant de six sections situées à différentes (paléo)latitudes et dans différents contextes géologiques (du large au plateau continental) j'ai reconnu 26 événements à nanofossiles calcaires sur un intervalle de 250 kyrs couvrant le PETM, et je présente une subdivision à haute résolution de cet intervalle. Les événements de nanofossiles calcaires tracés par rapport aux courbes de $\delta^{13}C$ disponibles montrent un certain degré de diachronisme, même en tenant compte des marqueurs zonaux précédemment établis. De plus, des non-conformités se produisent au début du PETM dans la plupart des sites océaniques, mais dans une moindre mesure dans les sections qui affleurent sur les continents. Je propose une nouvelle biozonation, basée sur des événements reproductibles dans différentes localités, afin d'obtenir une subdivision chronostratigraphique à haute résolution pour cet événement hyperthermique. Je définis ainsi quatre nouvelles zones couvrant le Paléocène supérieur et l'Éocène inferieur qui permettent de corréler les localités proximales et distales, et deux sous-zones principalement utiles dans les environnements proximaux. Ces nouvelles zones

sont corrélées aux principales tendances de la courbe des isotopes stables du carbone ($\delta^{13}C$) et définissent l'intervalle de pré-excursion (PE-1), l'excursion négative du $\delta^{13}C$ définissant la base de l'Eocène (PE0), le *core* de l'événement et la phase de récupération I (*recovery* I ; PE1) et les intervalles de la phase de récupération II (*recovery* II ; PE2).

## 7. Assemblages et paléoocéanographie pour le Pliensbachien-Toarcien

Une fois obtenue une biostratigraphie à une résolution suffisante, je me suis intéressé à la réponse des assemblages à nannofossiles calcaires aux perturbations environnementales durant l'évènement à la limite Pliensbachien-Toarcien et l'évènement océanique anoxique du Toarcien Inferieur (183 Ma). Ce chapitre fait l'objet d'un papier qui sera soumis en Octobre au volume spécial intitulé « Carbon Cycle and Ecosystem Response to the Jenkyns Event in the Early Toarcian (Jurassic) » qui sera publié dans le Journal of the Geological Society of Londron.

Le Jurassique Inferieur a été marqué par de multiples périodes de changements climatiques et paléocéanographiques, de changements d'assemblages au sein des écosystèmes benthiques et planctoniques et de perturbations des principaux cycles géochimiques, généralement liés au volcanisme des grandes provinces ignées. Des études antérieures portant sur les nanofossiles calcaires montrent que l'intervalle de temps couvrant le Pliensbachien inférieur et le Toarcien inférieur est caractérisé par une diversification majeure de ce groupe d'algues planctoniques. Au cours des dernières décennies, plusieurs études ont porté sur la réponse des nanofossiles calcaires aux perturbations environnementales du Pliensbachien Supérieur et du Toarcien Inferieur dans le sud de l'océan Téthys. Des études récentes se sont focalisées sur des localités éloignées de la Tethys, tels que le bassin de Néquen, le bassin andin et le Tibet.

Je présente de nouvelles données sur les nanofossiles calcaires provenant du forage Mochras, la section la plus épaisse du Jurassique Inferieur, afin de comprendre les changements de la production primaire et carbonatée en réponse aux changements paléoenvironnementaux dans le Pliensbachien Supérieur et le Toarcien Inferieur. Pour ce faire, j'ai calculé l'abondance absolue et les flux des nanofossiles et je les compare aux données géochimiques et sédimentologiques disponibles. Enfin, en comparant le forage de Mochras avec d'autres sections du même âge, je discute la relation entre les changements paléoenvironnementaux et la production primaire.

8. **Assemblages et paléoocéanographie pour le PETM**

Le réchauffement climatique et la perturbation du cycle du carbone autours de la limite Paléocène-Éocène (PETM, environ 56 Ma) ont été liés à une libération massive de carbone dans le système océan-atmosphère. Des études précédentes ont invoqué une augmentation de la productivité du phytoplancton pour provoquer une baisse de la $pCO_2$, un refroidissement et une récupération environnementale. Toutefois, les interprétations des données géochimiques et biotiques divergent quant au moment et au lieu où cette productivité accrue s'est produite. Je présente des données en haute résolution sur les assemblages de nanofossiles, y compris les abondances relatives et absolues (nanofossiles/gramme de roche) d'une section proximale située dans la Tethys (Kharouba) et de deux sites océaniques (sites ODP 1209 et 1263), situés respectivement dans les océans Pacifique et Atlantique) afin de suivre les tendances globales et locales des assemblages de nanofossiles. Ces données, combinées aux enregistrements biotiques publiés, indiquent une accentuation transitoire des gradients trophiques entre le *onset* et le *core* du PETM, avec une diminution de la productivité dans les sites océaniques oligotrophes, parallèlement à une augmentation de la disponibilité des nutriments dans les zones proximales. Les niveaux de productivité se sont rétablis en domaine pélagique au cours du *recovery*, ce qui pourrait avoir joué un rôle important dans la séquestration du carbone et le retrait du $CO_2$ en association avec l'intensification de la météorisation continentale.

9. **Modulation du cycle du carbone par le phytoplancton pendant le PETM**

Ce chapitre représente un travail fondamental de ce manuscrit, car il vise à clarifier le rôle de la productivité primaire sur le cycle du carbone. De par son interdisciplinarité, ce papier sera prochainement soumis à la revue *Nature* car ces résultats permettent d'expliquer la phase de récupération du PETM, qui reste jusqu'à maintenant objet de profonds débats au sein de la communauté scientifique.

Le Maximum thermique à la limite Paléocène/Eocène du Paléocène (PETM, ~56 Ma), est considéré comme l'un des meilleurs analogues pour les émissions anthropiques de $CO_2$. Pourtant, les principales rétroactions négatives qui ont éliminé l'excès de carbone lors de l'arrêt du PETM restent controversées. La saturation et l'enfouissement des $CaCO_3$, dus à une altération accrue des silicates, sont communément acceptés comme les principaux processus moteurs. Par ailleurs, une

baisse de la production nette de $CaCO_3$ des algues induite par le $CO_2$ pourrait avoir déclenché l'accumulation d'alcalinité et la sursaturation, mais ce mécanisme n'est toujours pas étayé par des preuves indirectes. Je présente une étude *multiproxy* des enregistrements des eaux profondes tropicales du Pacifique et de l'Atlantique qui démontre que l'enfouissement des carbonates s'est rétabli aux niveaux pré-PETM environ 30 000 ans plus tard que la saturation. Ce découplage est expliqué par un effondrement spectaculaire (>60 %) et durable (>80 000 ans) de la production nette de $CaCO_3$ en raison de la stratification des océans induite par le réchauffement et de la diminution de la disponibilité des nutriments. Grace à la mesure des isotopes du calcium ($\delta^{44}/^{40}Ca$) sur des coquilles de l'espèce de foraminifères planctoniques *Morozovella velascoensis*, et à la fragmentation des nannofossiles calcaires ainsi que des foraminifères planctoniques au Sites ODP 1209 (Pacifique tropical) et 1263 (Atlantique tropical), il est possible de tracer les changements d'alcalinité de l'océan pendant le PETM. Ces enregistrements montrent que l'excès d'alcalinité qui en résulte a été rapidement consommé lorsque la production et l'enfouissement du $CaCO_3$ ont finalement repris, déclenchant un retrait rapide et massif du carbone tant inorganique qu'organique. Mes conclusions élucident certains des mécanismes biogéochimiques clés qui ont conduit à la récupération du PETM et soulignent l'importance négligée mais cruciale des seuils biologiques dans la régulation des événements passés et actuels du réchauffement climatique.

## 10. **Conclusion et synthèse**

Le dernier chapitre de la thèse vise à comparer les deux intervalles de temps pour discuter des aspects similaires et des différences. Pour les deux évènements les données biostratigraphiques ont été représentés par rapport à la courbe des isotopes stables du carbone ($\delta^{13}C$). Pour le Pliensbachien-Toarcien, j'ai pu mettre en évidence qu'il y a un épisode majeur d'apparitions autour de la limite Pliensbachien-Toarcien, contrairement au T-OAE. Ceci est en partie lié à l'augmentation des placolithes, qui domineront les assemblages pour le reste Mésozoïque et Cénozoïque et en partie liés à des condensations dans plusieurs bassins de la Tethys autour de la limite. Pour le PETM, j'ai pu mettre en évidence que le record sédimentaire a une influence majeure sur l'ordre des évènements. Similairement au Pliensbachien-Toarcien, la présence de discontinuités à la limite explique certaines différences d'une localité à l'autre. Cependant, il existe un certain dégrée de diachronisme, affectant également les

marques biostratigraphiques utilisés dans les zonations standards. La limite Paléocène-l'Éocène est caractérisée par plusieurs origines et extinctions, et aussi par des changements au sein des communautés de nanofossiles calcaires. Certains de ces événements, jamais ne pris en compte dans les biozonations antérieures, se sont avérés cohérents, avec un degré de diachronisme moindre que les marqueurs biostratigraphiques utilisés précédemment. Finalement j'obtiens un nouveau schéma de biozonation à haute résolution avec une résolution moyenne de 50-100 kyrs par zone. De plus, je corrèle les événements biostratigraphiques et les nouvelles zones aux différentes phases caractérisant l'excursion négative des isotopes du carbone définissant le Paléocène/Éocène.

En terme de implications paleoceanographiques, malgré certaines différences, comme par exemple le fait que pour le Jurassique Inferieur nous ne disposons pas d'enregistrement d'océan ouvert, les changements des abondances absolues et des flux durant les deux évènements, suggèrent iperstratification et oligotrophie des eaux de surface. L'oligotrophie était plus marqué pendant le T-OAE, car même les zones plus proximales montrent une tendance à l'oligotrophie. Au PETM, l'oligotrophie était particulièrement accentuée dans les sites océaniques, loin des apports des rivières tandis que dans les coupes proximales on enregistre des conditions fluctuantes, notamment des phases se stratification alternées à des phases de brassage des eaux.

Un aspect fondamental de ce travail de thèse est l'étude multiproxy des enregistrements des eaux profondes tropicales du Pacifique et de l'Atlantique ; ces données démontrant que l'enfouissement des carbonates s'est rétabli à des niveaux pré-PETM environ 30 000 ans après la saturation. Ce découplage entre saturation et enfouissement des carbonates est expliqué par un effondrement spectaculaire (>60 %) et durable (>80 000 ans) de la production nette de $CaCO_3$, dû à la stratification des océans induite par le réchauffement et à la diminution de la disponibilité des nutriments. L'excès d'alcalinité qui en résulte a été rapidement consommé lorsque la production et l'enfouissement du $CaCO_3$ ont finalement repris, déclenchant un retrait rapide et massif du carbone tant inorganique qu'organique. Ces conclusions élucident certains des mécanismes biogéochimiques clés qui ont conduit à la récupération du PETM et soulignent l'importance de la biologie dans la régulation des événements passés et actuels du réchauffement climatique.

# Chapitre 2.1. New calcareous nannofossil and carbon isotope data for the Pliensbachian/ Toarcian undary (Early Jurassic) in the western Tethys and theirpaleoenvironmental implications.

**Newsletters on Stratigraphy, Vol. 52/2 (2019), 173–196** **Article**
Published online October 4, 2018; published in print March 2019

# New calcareous nannofossil and carbon isotope data for the Pliensbachian/Toarcian boundary (Early Jurassic) in the western Tethys and their paleoenvironmental implications

**Alessandro Menini[1]*, Emanuela Mattioli[1,2], Jorge E. Spangenberg[3], Bernard Pittet[1] and Guillaume Suan[1]**

With 5 figures, 2 plates and 2 tables

**Abstract**. Several studies have focused on the response of calcareous nannofossils to the Toarcian anoxic event (T-OAE), one of the most dramatic events of environmental perturbations of the Mesozoic Era. Nevertheless, the impact of marked environmental perturbations on calcareous nannofossils during the Pliensbachian/Toarcian transition (Pl/To; ~183 Ma), slightly before the T-OAE, remain comparatively less well documented. Here, we present a high-resolution biostratigraphical and chemostratigraphic study of two sections where the Pl/To is well represented. One section is located in Central Spain (La Almunia) and the second one is in North-Western France (Anse St. Nicolas). Although the two localities were paleogeographically close to each-other during the Early Jurassic, dissimilarities in the nannofossil assemblages suggest different paleoenvironmental conditions. Across the Pl/To boundary, absolute abundances (nannofossils/gram of rock) and placolith-coccoliths increased substantially in both sections. Equally, carbon isotopes show a negative excursion at the boundary followed by a trend to more positive values. The comparison of our new data to seven sections located in both Northern and Southern Tethyan margins, shows that the Pl/To corresponded to a major diversification event of coccoliths. The Pl/To speciation caused a pronounced shift from muroliths to placoliths. Some differences are observed from one section to another, but several first occurrences (FO) of species and a reorganization of the nannofossil community are documented in all the localities. Some of these FOs are biostratigraphically useful for the definition of the Pl/To boundary, like the FOs of *Biscutum intermedium*, *Zeugrhabdothus erectus* and *Discorhabdus ignotus*. The carbon cycle perturbation at the Pl/To occurred during a transgressive event after a pronounced cooling event and a sea-level drop that triggered hiatuses in many localities. The origination event of calcareous nannofossils is closely linked to all these phenomena. Thus, the Pl/To event has to be seen as the onset of profound paleoenvironmental perturbations that culminated with the T-OAE.

**Key words.** Pliensbachian, Toarcian, Pl/To event, calcareous nannofossils, biostratigraphy, carbon and oxygen stable isotopes

**Authors' addresses:**
[1] Université de Lyon, UCBL, ENSL, CNRS, LGL-TPE, 69622 Villeurbanne, France. Email: alessandro.menini@univ-lyon1.fr, emanuela.mattioli@univ-lyon1.fr, bernard.pittet@univ-lyon1.fr, guillaume.suan@univ-lyon1.fr
[2] Institut Universitaire de France, Paris, France. Email: emanuela.mattioli@univ-lyon1.fr
[3] Institute of Earth Surface Dynamics (IDYST), University of Lausanne, Building Géopolis, CH-1015 Lausanne, Switzerland. Email: Jorge.Spangenberg@unil.ch
* **Corresponding author**: alessandro.menini@univ-lyon1.fr

 www-borntraeger-cramer.de
DOI: 10.1127/nos/2018/0476 0078-0421/2018/0476 $ 6.00

## 1. Introduction

In the last decade, numerous studies have focused on Lower Jurassic calcareous nannofossil assemblages and biostratigraphy (e. g., Mailliot et al. 2006, Mattioli et al. 2008, 2009, 2013, Reggiani et al. 2010, Fraguas et al. 2010, 2012, Casellato et al. 2015, Peti et al. 2017), with the large majority being dedicated to the Toarcian Anoxic Event (T-OAE; Jenkyns, 1988). Conversely, in spite of recent ratification of the Toarcian GSSP (Rocha et al. 2016), the palaeoenvironmental events occurring across the Pliensbachian/Toarcian boundary (Pl/To) remain poorly investigated. The Pl/To is a prominent event because it precedes the T-OAE by about 800–1000 kyrs (Suan et al. 2008a, Huang and Hesselbo 2014, Martinez et al. 2017) and coincides with a perturbation of the carbon cycle and marked changes in paleotemperature, as respectively reflected by prominent negative carbon isotope excursion (CIE) and a shift toward more negative oxygen isotope values in bulk rock carbonates and brachiopod shells (Hesselbo et al. 2007, Suan et al. 2008a, 2010, Bodin et al. 2010, 2016, Dera et al. 2011 a, Ferreira et al. 2015). Geochemical studies were also perfomed on belemnite rostra calcite (Gomez et al. 2008) but, for the Pl/To, they did not deliver the same negative carbon excursion as brachiopods. Also, sea-level changes have been documented at the Pl/To (Hesselbo 2008, Sabatino et al. 2009, Suan et al. 2010, Pittet et al. 2014), possibly linked to the growth and decay of polar ice caps (Morard et al. 2003, Suan et al. 2010, Korte and Hesselbo 2011). These sea-level changes drove in turn condensation or hiatuses in many epicontinental basins that make the definition of the Pl/To boundary even more complicated (e. g., Blomeier and Reijmer 1999, Léonide et al. 2012, Sandoval et al. 2012, Pittet et al. 2014). Given the recent analysis of sections located outside the western Tethys, which has so far been the most extensively studied region, and due to the recent improvement of our knowledge of remote Toarcian settings, e. g. South America (Nequén Basin in Argentina, Al-Suwaidi et al. 2016, Andean Basin in Chile, Fantasia et al. 2018), North America (Martindale et al. 2017, Them II et al. 2017) and Tibet (Wignall et al. 2006, Fu et al. 2016), there is a growing need for improving the Pl/To stratigraphy in order to perform supraregional correlations. In this study we present data from two successions where the Pl/To boundary is well expressed, namely at Anse St. Nicolas, located in the western margin of France and at La Almunia, in central Spain in the region of Zaragoza. No apparent discontinuities occur in these two sections at the Pl/To transition (Gabilly 1976, Elmi 2007, Gómez et al. 2008).

Besides their continuous Pl/To record, these two sections were located in a key position in the western Tethys, at the crossway between the northern and the southern margins that bring significant differences in terms of floral and faunal assemblages and in terms of environmental conditions (van de Schootbrugge et al. 2005, Mattioli et al. 2008). We present a precise comparison between the new calcareous nannofossils events, assemblages and C isotope data data from these two areas. We then compare our data with ones from other sections from both northern and southern Tethyan domains where ammonite, carbon isotopes and nannofossil data are available (including the recently ratified GSSP at Peniche in Portugal) to provide a comprehensive stratigraphic framework for the Pliensbachian/Toarcian boundary.

## 2. Geological setting

During the Early Jurassic, the western Tethys consisted of shallow epicontinental seas extending between the Laurasian and the African landmasses (Fig. 1A). Several lines of evidence indicate significant paleoclimatic and paleoceanographic differences between the northern subtropical margin (~27–35 °N) and the southern tropical margin (~17–23 °N). Water masses with different properties have been interpreted for the two domains to explain the different ammonite faunas (Cecca and Macchioni 2004 and references herein) and substantial differences in calcareous nannofossil assemblages (Bown 1987, Mattioli et al. 2008). Belemnite oxygen isotope composition, clay mineral and fossil wood assemblages indicate more humid climate conditions in the northern margin, opposed to a more arid climate for the southern part (van de Schootbrugge et al. 2005, Rosales et al. 2006, Dera et al. 2009, Philippe et al. 2017). Consequently, the northern Tethyan margin is characterized by siliciclastic deposits, while the southern margin is dominated by carbonates, likely indicating more arid conditions. Paleogeographic reconstructions show that the southern Tethyan margin featured relatively shallow basins separated by large carbonate platforms (Bassoulet et al. 1993, Thierry and Barrier 2000).

The two sections studied here were located in a key area at the transition between the northern and the southern margins of the Tethys in the Early Jurassic. La

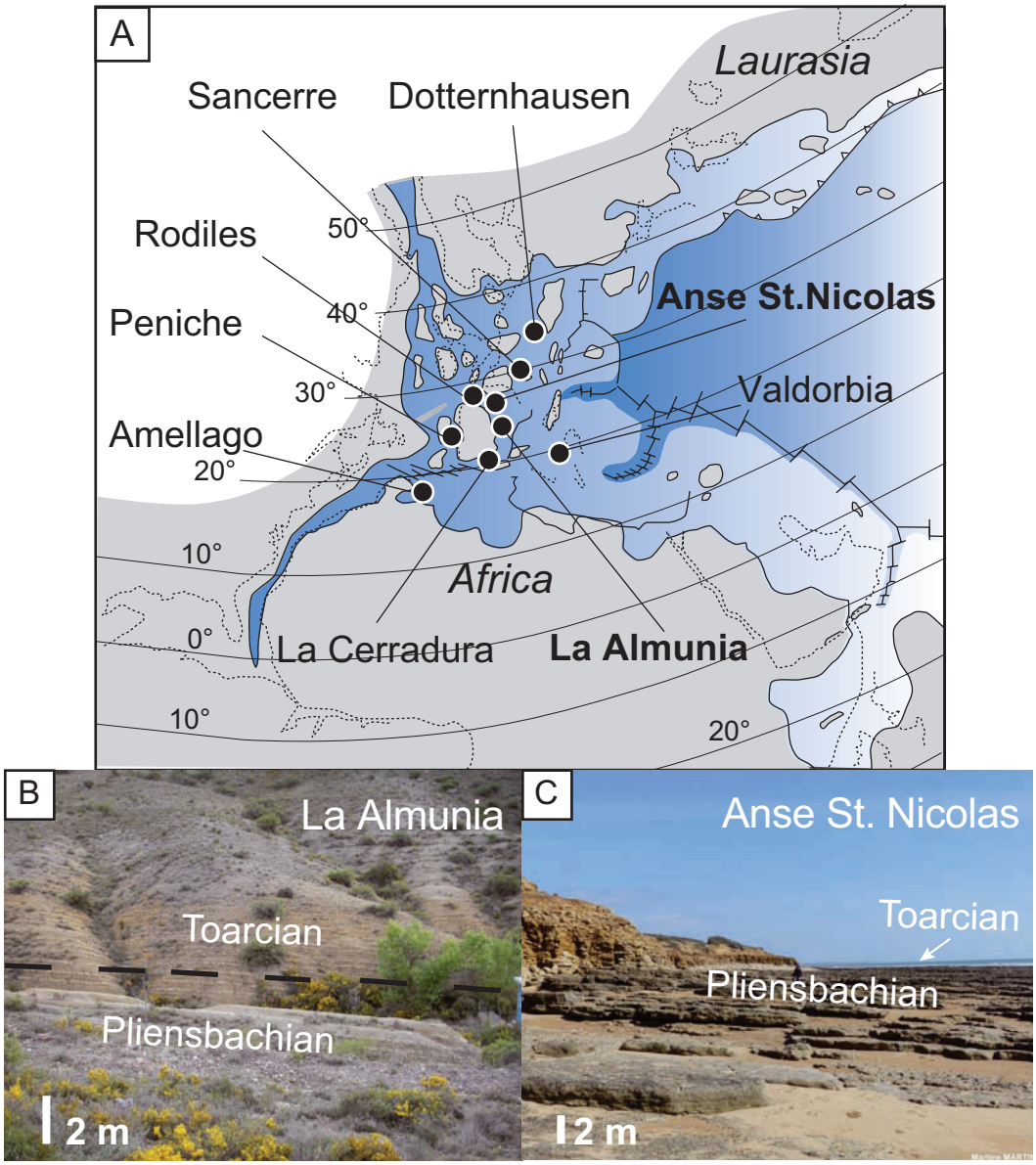


**Fig. 1.** A: Paleogeographic reconstruction of western Tethys at about 183 Ma (after Bassoullet et al. 1993) showing location of the sections studied or used for comparison in this study. La Almunia, La Cerradura, Valdorbia, and Amellago are located in the Southern Tethyan margin. Anse St. Nicolas, Rodiles, Sancerre, and Dotternhausen are located in the Northern Tethyan margin. Peniche was located in the Lusitanian Basin, a N-S elongated corridor in connexion with both Tethyan and NW European regions. B: Field view of La Almunia section, located in central Spain in the region of Zaragoza. The lithology is constituted of marl/limestone alternations. Dashed line represents the Pliensbachian/Toarcian boundary. Scale bar is 2 meter. C: Field view of Anse St. Nicolas section, located in North-West France in the department Vendée. The lithology is constituted of marl/limestone alternations. Pliensbachian beds are well exposed, while Toarcian strata are only accessible during low tides. Scale bar is 2 meters.

Almunia (Fig. 1B) was located in the Iberian Range (Central Spain), while Anse St. Nicolas (Fig. 1B) was located along the north-western epicontinental margin (NW France). Both sections present ammonite assemblages of the Northwestern European Province, although in the La Almunia section taxa both from the NW European and the Mediterranean provinces are recorded (Comas-Rengifo et al. 2010).

La Almunia section is located in central-eastern Spain, at 267.5 km of the National II road Madrid to

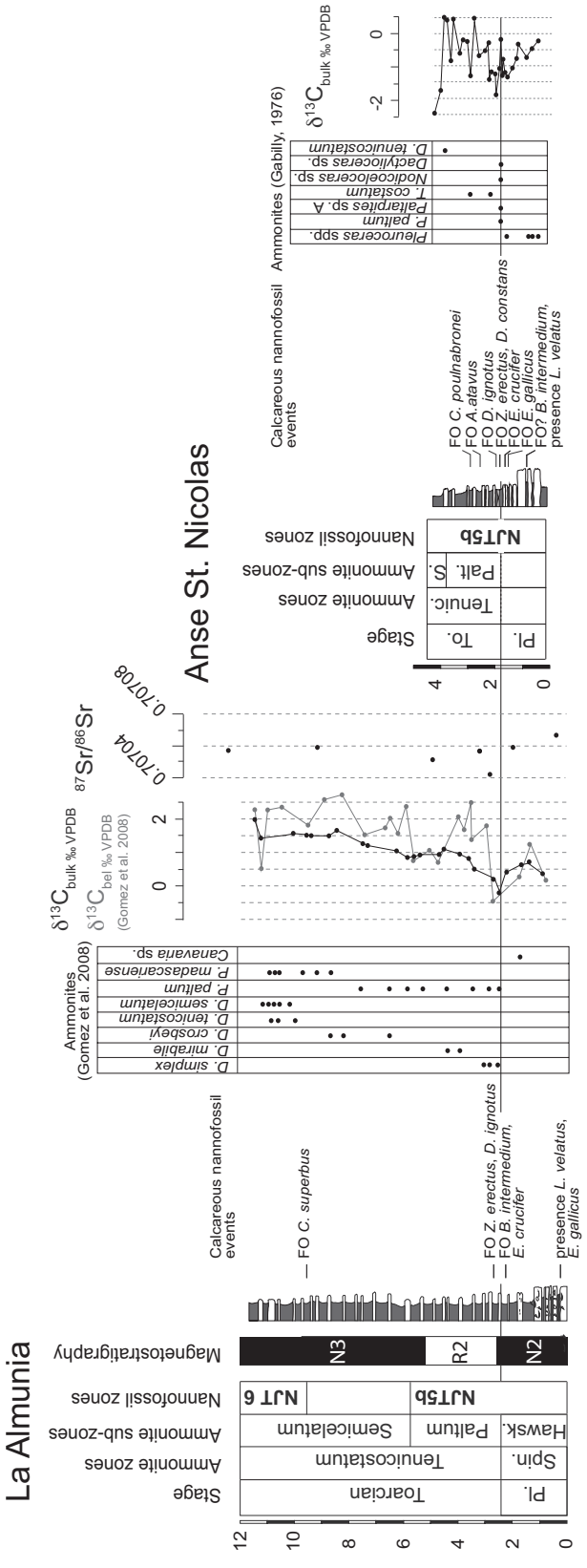


Barcelona, along the "Camino de Las Conchas". Paleogeographically, the section was located to the East of the Iberian Massif. The succession (Fig. 2) consists of marl-limestone alternations and the thickness of the studied interval is 12 m. It records the Hawskerense (upper Pliensbachian), Paltum and Semicelatum (lower Toarcian) sub-zones (Gautier and Mouterde 1964, Goy and Martinez 1990). Ostracod (Arias 1991, 1995) and foraminifer (Herrero 1992) assemblages have also been studied. The ammonite assemblages and stable oxygen and carbon isotope composition of belemnite rostra from this succession have been reported by Gómez et al. (2008).

The Anse St. Nicolas section is located in the western Atlantic margin (NW France), close to Jard in Vendée. Paleogeographically, this area represented the southern, distal margin of the Armorican Massif. In this region, different sections record a relatively complete Pliensbachian/Toarcian transition (Gabilly 1964, 1976, Bécaud 2002, 2005, 2006) based on their ammonite and brachiopod contents. Anse St. Nicolas represents the most complete and expanded section in western France (Gabilly 1976). In particular, this section records a relatively expanded (~10 m) lower Toarcian interval (Gabilly 1976) compared to the nearby historical Toarcian stratotype at Thouars, where the same interval is represented by 0.50 m of sediments

**Fig. 2.** Geochemical and biostratigraphic data for La Almunia and Anse St. Nicolas sections. Ammonite zones and subzones in the two sections are after Elmi et al. (1997). The Pliensbachian/Toarcian boundary corresponds to the passage between Spinatum and Tenuicostatum ammonite zones. Calcareous nannofossil zones are after Mattioli and Erba (1999). The zone NJT5 b is recorded in both sections based on the record of *Lotharingius sigillatus* which is present from the lowest studied samples. Only at La Almunia is recognized the zone NJT6, given the first occurrence of *Carinolithus superbus*. Many first occurrences of calcareous nannofossils are reported. In particular, the first occurrences of *Ethmorhabus crucifer*, *Zeugrhabdotus erectus* and *Discorhabus ignotus* well approximate the Pliensbachian/Toarcian boundary (Pl/To). Carbon isotopes on bulk rock samples are expressed relative to the international standard VPDB. A negative excursion characterizes the Pl/To boundary, followed by a positive recovery phase. Magnetostratigraphy and strontium isotopes of La Almunia are after Comas-Rengifo et al. (2010). The Pl/To boundary lies just below the passage from N2 to R2 magnetozone. Strontium isotope ratios display lower values in correspondence of the Pl/To.

(Courtinat et al. 2007). The succession is represented by marl-limestone alternations characteristic of outer carbonate platform environments (Fig. 2). For the lowermost Toarcian, the ammonite biostratigraphy permits the recognition of the two subzones Paltum and Semicelatum, belonging to the Tenuicostatum zone. At Anse St. Nicolas, the Spinatum zone (uppermost Pliensbachian) is not recognized. The upper Pliensbachian is characterized by the occurrence of ammonites of the *Pleuroceras* genus. These disappear at the Pl/To boundary, when the mass occurrence of *Dactylioceras* is observed (Gabilly 1976). Such an assemblage change attests for the completeness of the boundary, although condensation is not excluded (Rocha et al. 2016). Gabilly (1976) inferred that no discontinuities occur between the last Pliensbachian bed and the first Toarcian level, making the section very suitable for a detailed study of the Pliensbachian/Toarcian event. Such a completeness made of Anse St. Nicolas one of the discussed possible candidates as the stratotype for the Toarcian (Gabilly 1973, 1976, Rocha et al. 2016).

Additional Pliensbachian-Toarcian sections are considered here for comparison of their nannofossil assemblages, namely Dotternhausen (SW Germany), Sancerre (N France), Rodiles (N Spain), the GSSP of the Toarcian at Peniche (Portugal), La Cerradura (S Spain), Valdorbia (Central Italy), and Amellago (Morocco). All these sites benefit from high-resolution carbon isotope data and good nannofossil and ammonite biostratigraphic control (e. g., Mattioli et al. 2008, 2013, Bodin et al. 2010, Fraguas et al. 2012, Reolid et al. 2014, Clemence et al. 2015) and are remarkable for their continuity at the Pl/To boundary. However, in the Sancerre core a discontinuity (D1) was noticed by Pittet et al. (2014; figure 10), and a hiatus was inferred in correspondence of the Pl/To boundary. La Cerradura, Valdorbia and Amellago belong to the southern margin of the Tethys and display ammonites from the Mediterranean Province; Peniche and La Almunia show a mixing of Mediterranean and NW Europe ammonite fauna; Anse St. Nicolas and Dotterhausen belong to the northern margin of Tethys and yield ammonites of the NW Europe Province (see for a synthesis Rocha et al. 2016); the Rodiles section shows a high proportion of common taxa with the UK sections (Gomez et al. 2008).

# 3. Materials and methods

The calcareous nannofossils and bulk rock carbon and oxygen isotopes were analysed for thirty-two samples for the section Anse St. Nicolas, and for twenty-five samples for the section La Almunia, covering the upper Pliensbachian-lower Toarcian transition. Samples were collected every 10 cm for the section Anse St. Nicolas and every 30 cm for the section La Almunia, with a higher sampling density near the boundary (every 5 cm at Anse St. Nicolas; every 10 cm at La Almunia).

## 3.1. Stable isotope analyses

Stable carbon and oxygen isotopes on bulk rock carbonates were analysed at the Institute of Earth Surface Dynamics of the University of Lausanne, Switzerland. Stable carbon ratios ($\delta^{13}C_{carb}$ values) were measured in whole rock samples containing >10 wt.% $CaCO_3$ following the procedure of Spangenberg and Herlec (2006). Samples with clear evidence of diagenetically neoformed or recrystallized carbonates (calcite or dolomite) were not analysed. The analyses were performed in aliquots of powdered whole rock samples (variable weight depending on the $CaCO_3$ content). Sample powders were analysed using a Thermo Fisher Scientific Gas Bench II (Bremen, Germany) carbonate preparation device connected to a Delta Plus XL isotope ratio mass spectrometer that was operated in the continuous helium flow mode (Révész and Landwehr 2002). The $CO_2$ extraction was done by reaction with anhydrous phosphoric acid at 70 °C. Stable carbon isotope ratios are reported in the delta ($\delta$) notation as the per mil (‰) deviation relative to the Vienna Pee Dee belemnite standard (VPDB). The normalization of the measured isotope ratios to the VPDB scale was performed by replicate analyses of an in-house working standard Carrara marble (UNIL-CM, $\delta^{13}C$ = 2.05‰) and international reference materials (RMs) in each run. The $\delta^{13}C$ values of the reference gas and the UNIL-CM were normalized with the RMs NBS-19 limestone with $\delta^{13}C$ = 1.95‰, NBS-18 carbonatite with $\delta^{13}C$ = –5.04‰, and LSVEC lithium carbonate with $\delta^{13}C$ = –46.65‰ (Brand et al. 2014). The repeatability and intermediate precision of the analyses (2$\sigma$), monitored by replicate analyses of the laboratory standard UNIL-CM and the RMs was better than ±0.05‰. The accuracy of the analyses was checked periodically through the analyses of the RMs.

### 3.2. Calcarous nannofossils

Samples for calcareous nannofossils were prepared following the technique described by Beaufort et al. (2014), slightly modified here. A cover slide was weighed before and after a homogeneous suspension of dried rock-powder and water (supersaturated with respect to $CaCO_3$ and with a basic pH) was let to settle on the cover slide for 2 hours in a Petri-dish. After settling of the powder, water was carefully aspired with a water pump relied to a micro-pipette, avoiding any turbulence in the Petri-dish. The residual water on the cover slide was dried, the cover slide was recovered and attached on a microscope slide using Rhodopass resine. This technique allowed the quantification of absolute abundances of nannofossils per gram of rock using the following formula:

$$x = \frac{n * (l * h)}{m * A}$$

where is $x$ is the absolute abundance value, $n$ is the number of counted specimens in a slide, $l$ is the length of the cover slide, $h$ is the height of the cover slide, $m$ is the mass of the weighted sample and $A$ is the studied surface of the sample.

For each sample, 300 specimens of calcareous nannofossils have been counted using a Leica DM750P microscope with a 1000 X magnification. In samples where the richness was extremely low, ~100 nannofossils have been counted. Counting 300 specimens per sample provides us with a limited probability (less than 5 %) not to recover a rare species having a relative abundance of 1 % in the total assemblage (Hay 1972). Each slide was further scanned over two transverses of the slide in order to detect the presence of rare but biostratigraphically significant specimens. For the poorest samples, a threshold of 100 specimens per sample has proven to be significant due to the limited number of species (~50) recorded in the studied interval. Counts of 100 specimens have a satisfactory statistical reliability according to Fatela and Taborda (2002). Also, rarefaction graphs have been constructed in our paper based on the method described by Krebs (1998) and Hammer et al. (2001). These graphs allow the evaluation of theoretical diversity of samples with respect to a reference sample where species richness is higher. It is thus possible to estimate when the sampling size is significant. This is namely when the confidence interval of the tested samples is superimposed to the confidence interval of the reference sample.

The relative abundances of species expressed as percentages were calculated for *Schizosphaerella*, an *incertae sedis* probably corresponding to a dinoflagellate cyst (Bown 1987), with respect to the total nannofossil counts (i. e., coccoliths plus *Schizosphaerella*), while the percentage of coccoliths is calculated with respect to the total coccoliths. Fatela and Taborda (2002) have calculated the confidence interval for species with a proportion of 0.1 (i. e., 1 %) when counting 100 individuals. The confidence interval extends from 0.041 to 0.159 around the value of 1 %. This is the reason why in the rest of the manuscript we only discuss taxa representing more than 5 % in the assemblage.

Nannofossil preservation was evaluated for each sample based on the degree of etching and overgrowth following the classification of Roth et al. (1984). Three classes have been recognized: poor nannofossil assemblages when strong etching is observed along with overgrowth or fragmentation; moderate and good when *Schizosphaerella* fragmentation appears to be limited and delicate coccoliths still present intact structures.

We also calculated the Shannon Index (H), a mathematical expression of species diversity in a community (Shannon and Weaver 1949). It is calculated as follows:

$$H = -\sum_{i=1}^{s} Pi * (\ln(Pi))$$

where $i$ is a species, $s$ is the number of species in the interval (i. e., species richness), $Pi$ is the relative abundance of each species.

The nannofossil biostratigraphic record has been compared to the standard ammonite zones taking into account for the two studied sections.

## 4. Results

### 4.1. Stable carbon isotope results

Stable carbon isotopes values range from –0.5 to 2.0 ‰ VPDB at La Almunia and from –2.0 to 0.5 ‰ VPDB at Anse St. Nicolas (Fig. 2 and supplementary data). The two sections show the same trend, namely a general 1.5‰ increase of the $\delta^{13}C_{carb}$ values from the Pliensbachian to the Toarcian, interrupted by a 0.5 to 1‰ negative excursion at the Pl/To boundary (PT-CIE). The bulk carbonate carbon isotope profile at Almunia shows a very similar trend with that of belemnites from

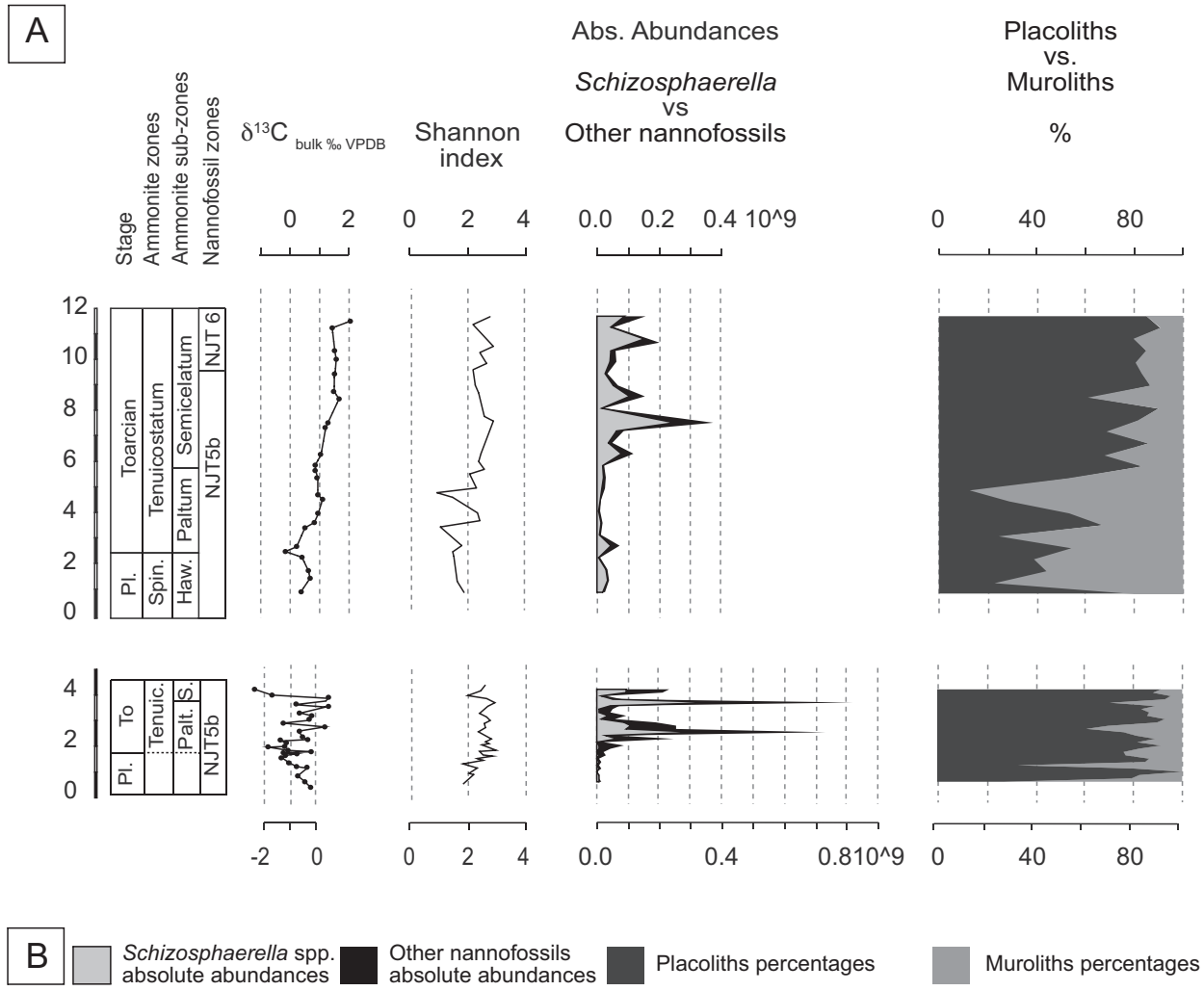


**Fig. 3.** A: La Almunia section. From the Pliensbachian to the Toarcian, an increase in Shannon Index is documented as well as an increase in absolute abundances (nannofossil/gram of rock). Placolith-coccoliths increase in percentage relatively to muroliths and the result is a turnover from murolith- to placolith-dominated assemblages. B: The same trend is observed at Anse St. Nicolas. Two peaks in absolute abundances are seen and these are interpreted as an evidence of sedimentary starvation and nannofossil increased accumulation.

the same section (Gómez et al. 2008). Carbon isotope values show a larger variability at Anse St. Nicolas than at La Almunia (Fig. 2), probably reflecting a lithological control on the signal, with marls displaying lower $\delta^{13}C_{carb}$ than argillaceous limestones. At Anse St. Nicolas the carbon isotope values show a 3‰ negative shift in topmost samples (Fig. 2).

Even though the general trend is very similar in both sections, the $\delta^{13}C_{carb}$ values are overall lower at Anse St. Nicolas compared to La Almunia. This is probably due to the higher organic matter content at Anse St. Nicolas, as organic debris (both wood fragments and algal remains) are commonly observed in nannofossil slides. Given the light isotopic composition of organic matter, a contribution of inorganic carbon produced by oxidative degradation of organic compunds may explain the lower $\delta^{13}C_{carb}$ values as well as the highly fluctuating $\delta^{13}C_{carb}$ trend in Anse St. Nicolas.

## 4.2. Calcareous nannofossils

In both sections, nannofossil preservation is generally moderate to good (see also Plates 1 and 2). In spite of the overall satisfactory preservation of nannofossils, four samples at the base of Anse St. Nicolas (SN 0.05, 0.13, 0.20, 1.12) are barren of nannofossils (see

supplementary data). The Shannon index shows similar values and evolution in the two sections, and the most interesting feature is an increase from values around 2 in the Pliensbachian to values around 3 in the Toarcian (Fig. 3).

The two sections yielded a quite rich and diversified nannofossil assemblage, and even very rare species are sporadically present (e. g., *Diductius constans*). Total relative and absolute abundances are comparable for the two sections with a few differences. A remarkable point is the different contribution of *Schizosphaerella* spp. and coccoliths (Figs. 3 and 4). Indeed, at La Almunia *Schizosphaerella* spp. is the most abundant taxon and constitute between 60 and 90 % of the entire assemblage, with up to 200*10^6 specimens per gram of rock (Figs. 3 and 4). Conversely, at Anse St. Nicolas *Schizosphaerella* spp. is abundant before and after the Pl/To, reaching relative abundances up to 60 % and absolute abundances up to 800*10^6, but its abudance does not exceed 20 % (absolute abundances 50*10^6) in several samples and this taxon is even totally absent in some upper Pliensbachian samples. Other quantitatively significant taxa recorded in both sections are *Lotharingius* spp., *Mitrolithus jansae*, *Crepidolithus crassus*, *Similiscutum cruciulus* group, *Similiscutum finchii*, *Biscutum intermedium*, *Biscutum grande*, *Bussonius prinsii*, *Bussonius leufuensis, Tubirhabdus patulus*, *Parhabdolithus liasicus* (Tables 1 and 2).

The Pl/To boundary records a major turnover in the calcareous nannofossil assemblages. The upper Pliensbachian samples are dominated by muroliths (such as *M. jansae*, *C. crassus*, *T. patulus*, *P. liasicus*), while lower Toarcian samples record an increase in abundance of the placolith-coccoliths. Muroliths are characterised by a simple structure with calcite elements of the distal shield extending vertically, and represent the earliest coccoliths to have appeared in the Late Triassic (Bown 1987, Gardin et al. 2012). The placolith structure is defined by two shields which lie on top of one-another, and are connected by a central tube; the two shields show radial calcite elements (Bown 1987). Taxa such as *Lotharingius* spp., *Similiscutum* spp., *Biscutum* spp. or *Bussonius* spp. became more abundant in the Toarcian. However, this increase of placoliths does not correspond to an effective decrease of muroliths, although their relative abundance decreased. This decrease is a closed-sum effect as muroliths absolute abundances remain more or less constant through the studied interval, while placoliths rapidly increased (Fig. 4).

*Lotharingius* spp. are the most common coccoliths, as recorded in many other lower Jurassic sections. The different species of *Lotharingius* spp. (*L. hauffii*, *L. frodoi*, *L. sigillatus*, *L. crucicentralis*, *L. barozii*, *L. velatus*) account between 30 and 50 % of the assemblage in both sections. *Mitrolithus jansae* is very abundant at La Almunia, where it reaches between 60 and 70 % of total coccoliths, while at Anse St. Nicolas it is present but never exceeds 20 % of coccoliths. *Biscutum* spp. and *Similiscutum* spp., are more abundant at Anse St. Nicolas than at La Almunia: these two genera never exceed 10 %, with the exception of the species *S. finchii*, that reaches peaks of 20 % in both sections. *Bussonius* spp. are more abundant at Anse St. Nicolas; they account for 10–15 % of the assemblage, though at La Almunia they never exceed 10 %. Other taxa are rare and their percentage ranges from 1 % to 5 %.

In both sections, many first occurrences (FO) are recorded around the Pl/To (Fig. 2). *Lotharingius velatus*, which is documented to occur in the uppermost part of the Pliensbachian (Mattioli et al. 2013), is present in the lowermost samples studied both at Anse St. Nicolas and at La Almunia; therefore the FO of this taxon certainly occurs below these samples and cannot be recognized in the studied material. At Anse St. Nicolas, *B. intermedium* is found in the upper Pliensbachian just above the basal barren samples, at the base of the PT-CIE; this horizon may correspond to the FO of the species. At La Almunia, the FO of *B. intermedium* is recorded just below the Pl/To boundary, at the base of the Pl/To negative CIE. The FO of *Ethmorhabdus gallicus* at Anse St. Nicolas is found just below the Pl/To, concomitant with the negative CIE, whereas at La Almunia this species is present from the lowermost sample studied. The FO of *Ethmorhabdus crucifer* is recorded in both sections just below the Pl/To, concomitant with the negative CIE. Two FOs are well documented in both sections at the very base of the Toarcian, Tenuicostatum ammonite Zone (Paltum subzone), namely the FOs of *Zeughrabdothus erectus* and *Discorhabdus ignotus* (Fig. 2). In the Early Toarcian, the FOs of *Axopodorhabdus atavus*, *Diductius constans* and *Carinolithus poulnabronei* are only recorded at Anse St. Nicolas (Paltum subzone). An important event in the early Toarcian is the FO of *Carinolithus superbus*. This event was not found at Anse St. Nicolas, while at La Almunia it is located in the upper part of the section (Semicelatum subzone).

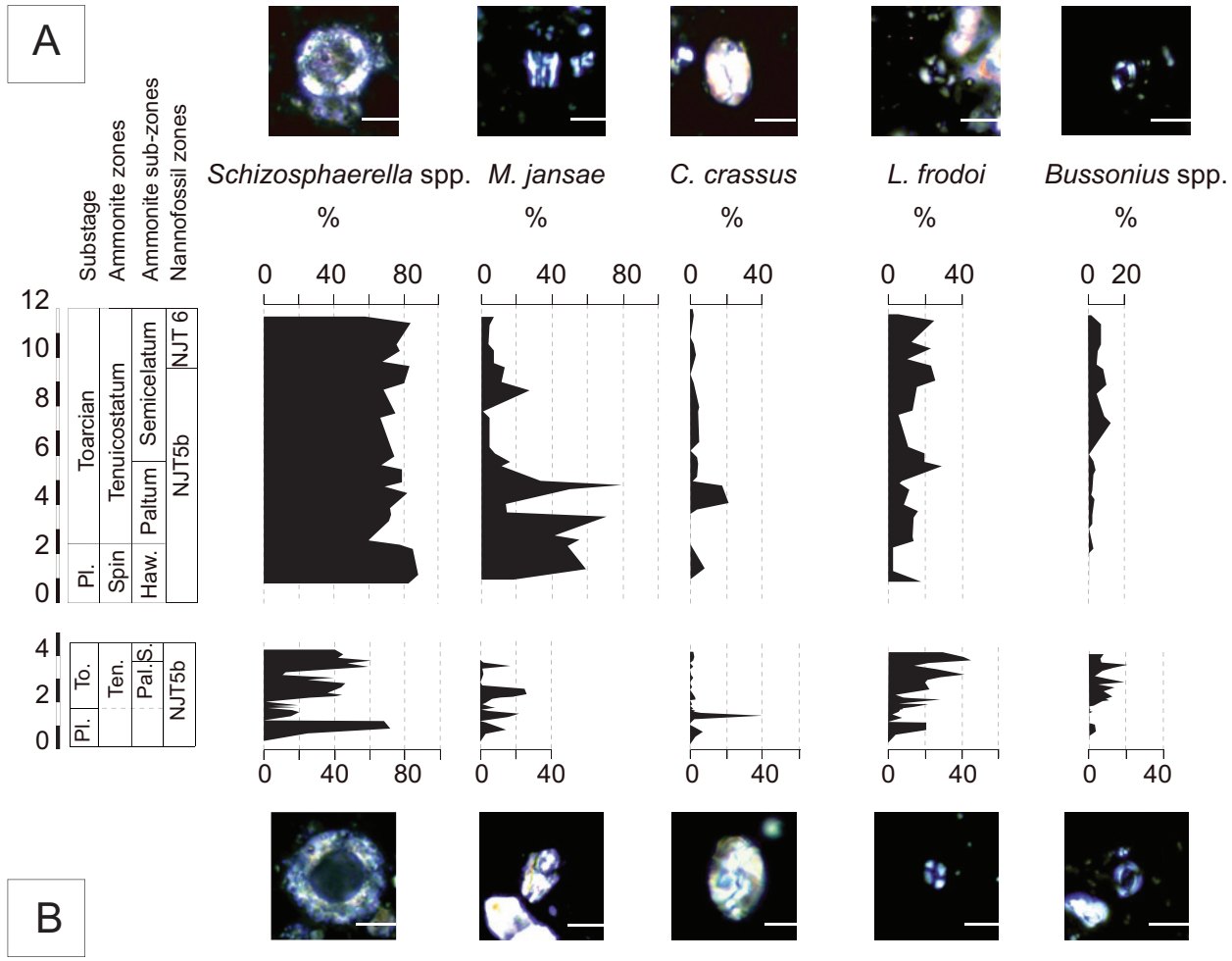


**Fig. 4.** Relative abundances (%) of the most abundant species in the two sections. A: La Almunia section. B: Anse St. Nicolas. *Schizosphaerella* spp. (a probable calcareous dynoflagellate cyst) dominates the assemblages, even if at Anse St. Nicolas it is overall less abundant. The main feature passing from the Pliensbachian to the Toarcian is a general increase in percentage of placoliths, such as *Lotharingius frodoi* or *Bussonius* spp., and a decrease in muroliths, such as *Mitrolithus jansae* or *Crepidolithus crassus*. Scale bar is 5 microns.

## 5. Discussion

### 5.1. Calcareous nannofossil bioevents

Early Jurassic nannofossil biostratigraphy is based on two schemes that are, nowadays, accepted as standard; for the NW European sections the adopted scheme is the one by Bown (1987) modified by Bown and Cooper (1998), and for the south Tethyan settings the reference is Mattioli and Erba (1999). The sections studied here are at the transition between the southern and northern Tethys and, as far as ammonites are concerned, La Almunia displays a mixing of Mediterranean and NW Europe faunas, while Anse St. Nicolas is part of the NW European Province. However, given the nannofossil assemblages and the constant presence or dominance of taxa which are typical of the S-Tethyan margin (i. e., *Schizosphaerella* and *M. jansae*; Bown 1987, Mattioli et al. 2008), the scheme that better applies to our dataset is that of Mattioli and Erba (1999). Based on this work, the base of the Anse St. Nicolas section is dated to the subzone NJT5 b, given the presence of *Lotharingius sigillatus* in the lowermost studied sample and the absence of *C. superbus*. La Almunia encompasses equally the subzone NJT5 b but the upper two meters of the section are attributed to NJT6 zone, given the FO of *C. superbus* in sample LAL 21.

The Pl/To has been considered as a period of elevated evolutionary rates in nannofossils (Bown 1987, Bown and Cooper 1998, Bown et al. 2005) and numerous first occurrences are recorded across the boundary (Bown and Cooper 1998, Mattioli and Erba 1999, Mattioli et al. 2013). Across the Pl/To are successively recorded the FOs of *L. velatus*, *A. atavus*, *B. intermedium*, *Z. erectus*, *D. ignotus, E. gallicus, E. crucifer* and *D. constans*. Most of these coccoliths are placoliths and only two are muroliths, namely *Z. erectus* and *D. constans*. This succession of events is very similar to the record of the Toarcian GSSP of Peniche (Mattioli et al. 2013, Rocha et al. 2016). *Lotharingius velatus* is present from the basal samples in both sections, while the FO of *A. atavus* is only recorded at Anse St. Nicolas. At La Almunia, *E. gallicus* is recorded from the basal sample but at Anse St. Nicolas the first occurrence is in the sample SN1.45, in the upper Pliensbachian. This species was originally described in the Oxfordian (Noël 1965) and subsequent studies extended the range of this species from Bathonian to Kimmeridgian (e. g., Medd 1982). According to Bown (1987), this species first occurred in the Toarcian. Our data show that its range can extend down to the uppermost Pliensbachian.

The FO of *E. crucifer* is recorded at Anse St. Nicolas and La Almunia in the uppermost Pliensbachian, just below the Pl/To boundary. The holotype of this species was defined by Noël (1972) who noticed this species in lower Toarcian sediments. Other authors documented the total range of this species in the lower Toarcian (Bown 1987, Bown and Cooper 1998), and our data precise its FO just below the Pl/To. A very good biohorizon in both sections, as well as in the GSSP section (Mattioli et al. 2013), is the FO of *Z. erectus*. This species first occurs slightly earlier than (Anse St. Nicolas) or in the same sample as (La Almunia) *D. ignotus* in the basal Toarcian, approximating very closely the Pl/To boundary. Bown (1987) already reported a possibile FO of *Z. erectus* in the Pliensbachian. Mattioli et al. (2013) show that, in the GSSP section of Peniche, this last taxon first occurred in the basal Toarcian (basal Polymorphum zone) while in previous works it was noticed in the upper part of Lower Toarcian (Bown 1987, Mattioli and Erba 1999, Mattioli et al. 2004b, 2008). The FO of *D. ignotus* is recorded in the Lower Toarcian in both the studied sections. In the lower Toarcian of the sections studied here, *D. ignotus* is very rare and discontinuous following its FO. Our results are consistent with the data of Mattioli et al (2013). *Discorhabdus ignotus* behaved as a Lazarus species, being absent from the sediments corresponding to the T-OAE in Peniche and other sections (Mattioli et al. 2013). The consistent occurrence of *D. ignotus* is then recorded by the end of the T-OAE (Mattioli et al. 2013).

Finally, the FO of *C. superbus* is recorded in the La Almunia section in the Semicelatum subzone. This event is consistently recorded below the negative CIE characterizing the T-OAE in southern Tethyan sections (Mattioli et al. 2013), but it is documented to occur after the T-OAE negative CIE in England (Bown 1987, Bucefalo Palliani et al. 2002, Boomer et al. 2009).

## 5.2. Calcareous nannofossil diversity and absolute abundance

The Pl/To represents a significant acceleration of evolutionary rates in the history of calcareous nannofossils (Bown et al. 2004). The species richness increased at that time (Bown et al. 2004) but also the Shannon diversity attained significantly higher values in the Lower Toarcian (Fig. 2). The Shannon values recorded at the Pl/To in the two sections studied here are comparable with literature data (Mattioli et al. 2008, Fraguas et al. 2012). Most of the new entries are represented by placolith-coccoliths that also show a remarkable increase in absolute abundances, whilst murolith-coccoliths originations were less numerous and absolute abundances stayed quite steady. Thus, taxa like *Biscutum/Similiscutum* and *Lotharingius* became dominant assemblage components.

Absolute abundances are twice higher passing from the Pliensbachian to the Toarcian in both studied sections (Fig. 3). A similar increase of absolute abundances in the basal Toarcian has already been reported in other sections (Mattioli et al. 2004, 2008), and likely corresponded to a rise in primary productivity (Mattioli et al. 2008). However, at La Almunia the absolute abundance increase is quite steady, while at Anse St. Nicolas two significant peaks are observed (from 200*10^6 to 700–800*10^6; Fig. 3). These two peaks of absolute abundances observed at Anse St. Nicolas are recorded in the same stratigraphic interval as the D1 and D3 discontinuities of Pittet et al. (2014), which have been interpreted as rapid marine transgressions. These two peaks may thus be attributed to condensation intervals due to these rapid transgressive events, as low sedimentary rates may result in a reduced dilution of nannofossils by other sedimentary components, hence causing peaks in abundance (Mattioli and Pittet 2002).

### 5.3. Comparisons of nannofossil bioevents between Tethyan sections across the Pl/To CIE

Anse St. Nicolas and La Almunia sections are here compared to various sections where the Pl/To is recorded continuously, ammonite and calcareous nannofossil biostratigraphy are well established and whole-rock stable carbon isotope are available (Fig. 5). The upper Pliensbachian and the lowest portion of lower Toarcian of all the considered sections can be assigned to the nannofossil zone NJT5 b because of the presence of *L. sigillatus* and the absence of *C. superbus.* We find the FO of *C. superbus* in all the sections but at Anse St. Nicolas because the interval studied is limited to the lowermost Toarcian. This event is recorded in all the sections in the lower Toarcian, during the positive excursion of C isotopes just before the onset of the T-OAE negative CIE as documented in the literature (Mattioli et al. 2013). However, at Rodiles and at Sancerre this event is found at the base of the CIE that characterizes the T-OAE (Fraguas et al. 2012, Clémence et al. 2015). It is possible that this is due to scarcity of *C. superbus* after its first occurrence.

Some other relevant events in the considered sections are the FO of *L. velatus*, *B. intermedium*, *D. ignotus*, *Z. erectus*, *E. gallicus* and *E. crucifer*. The FO of *L. velatus*, which is recorded in the uppermost Pliensbachian at Peniche, Valdorbia and Cerradura, is not detected in the two sections studied here, since *L. velatus* is found in the lowest nannofossil-bearing samples. The FO of *B. intermedium* is found in the uppermost Pliensbachian at La Almunia and potentially at Anse St. Nicolas as well as at Rodiles, Peniche, Valdorbia, Cerradura and Amellago. Both the FO of *L. velatus* and *B. intermedium* are recorded before the Pl/To CIE. The FOs of *D. ignotus* and *Z. erectus* approximate very well the Pl/To boundary as defined by ammonites, and they occur in concomitance of the negative CIE (Fig. 5). At Sancerre only the FO of *Z. erectus* is recorded in a lower interval compared to other sections. At Amellago and Dotternhausen the FO of *Z. erectus* was not found. At Rodiles neither *D. ignotus* nor *Z. erectus* are reported. Recently, Fantasia et al. (2018) studied a section from the Andean Basin which belonged to the Panthalassa Ocean domain. The comparison between ammonite zonation, carbon isotope curve and calcareous nannofossil events shows a succession of bio-horizons, which is very similar to the one we recorded in western Tethys, unless the FO of *C. superbus* that was not found there (Fig. 5). Such a good correlation attests for the valuable potential of nannofossil biostratigraphy for supra-regional correlations in the Lower Jurassic.

After its first record in bulk carbonate and fossil wood at the GSSP of Peniche (Hesselbo et al. 2007), the Pl/To CIE was documented in other Tethyan sections, (e. g., Suan et al. 2008, Littler et al. 2010, Bodin et al. 2016). However, the Pl/To CIE was not recorded in all the localities considered in this paper (e. g., Rodiles and Sancerre; Fig. 5). More puzzlingly, Bodin et al. (2016) have shown that the Pl/To negative CIE recorded by the bulk carbonate fraction in three different successions from the High-Atlas in Morocco is not recorded by organic material from the same samples. They concluded that the Pl/To negative CIE has a strong lithological control, and suggested that the negative CIE might reflect local changes in carbonate-producing sources rather than global carbon cycle perturbations. The negative CIE in the fossil wood profile recorded at the Pl/To in the GSSP at Peniche (Hesselbo et al. 2007) suggests, on the contrary, that the perturbation affected terrestrial environments. It thus remains to be seen whether the Pl/To negative CIE reflects global or local changes in carbon cycling.

The upper Pliensbachian has been interpreted as a cooling period (Morard et al. 2003, Suan et al. 2008, Korte et al. 2011, Gómez et al. 2016), and sea-level experienced a prominent fall followed by a rapid transgression in the earliest Toarcian (e. g., Pittet et al. 2014). The regression-transgression couplet gave rise in turn to hiatuses or condensations in many Tethyan localities and, especially, in those sections which were located in the most proximal settings (Pittet et al. 2014). The occurrence of hiatuses or condensation at the Pliensbachian/Toarcian transition may also account for the differences in terms of ranking of bioevents or of presence/absence of some species in the different sections considered here. Ultimately, the two sections studied here appear amongst the most complete for the Pl/To (e. g., Comas Rengifo et al. 1999, Elmi 2007, Gabilly 1976).

### 5.4. Comparisons with independent proxies

To better constrain the Pl/To nannofossil events recorded in the studied sections, we compared biostratigraphic and carbon isotope data with other additional stratigraphic techniques, namely strontium isotopes ($^{87}Sr/^{86}Sr$) and magnetostratigraphy. We take into

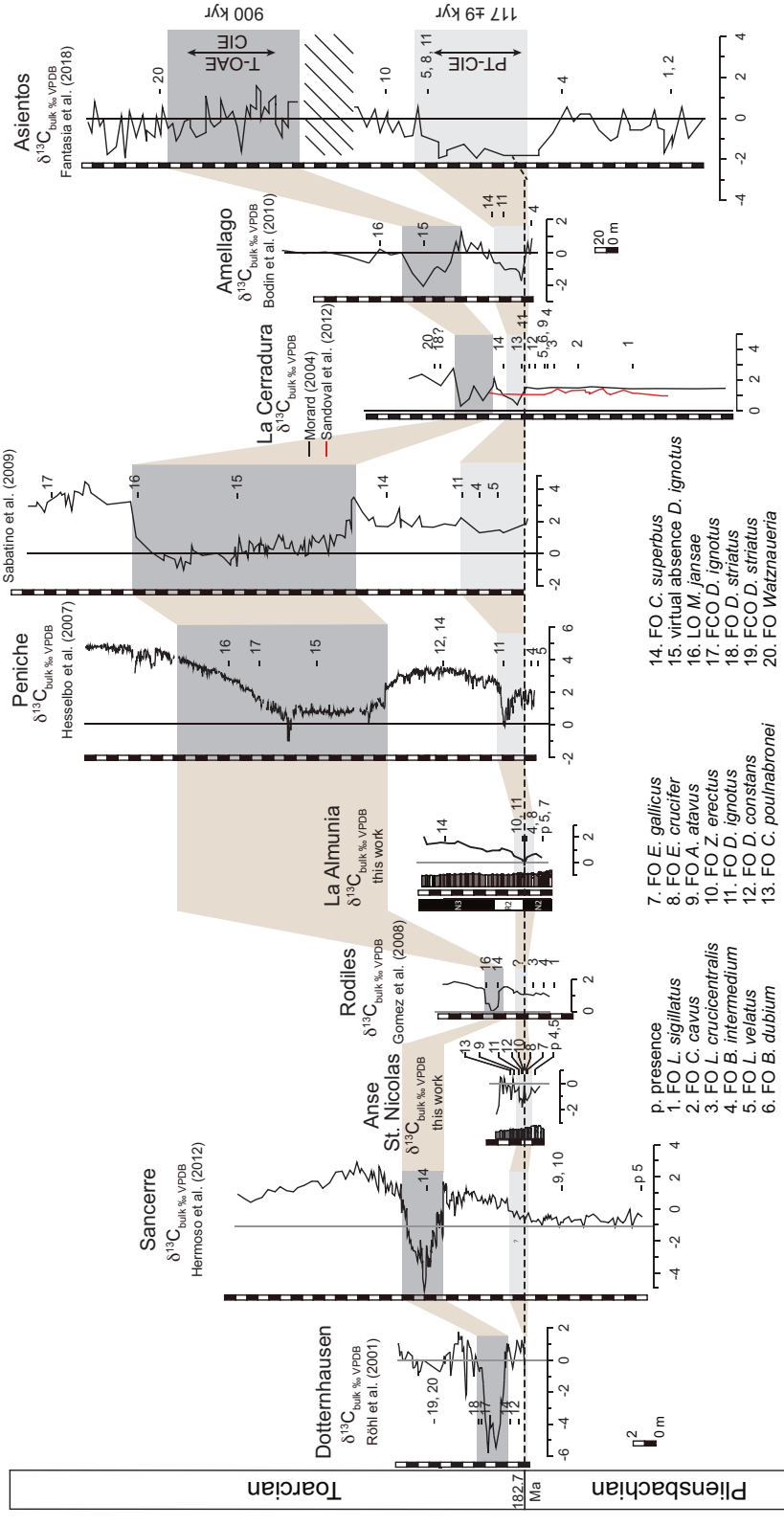


**Fig. 5.** Comparison between La Almunia, Anse St. Nicolas and other Northern and Southern Tethyan sections and proto-Atlantic (Peniche). The recently studied section of Asientos (Fantasia et al. 2018), located in the Andean Basin, is also considered here. Both calcareous nannofossil data and bulk carbonate carbon isotopes are presented. All sections are precisely dated by ammonite biostratigraphy. Nannofossil biostratigraphic data come from the following papers: Mattioli et al. 2008 (Dotternhausen); Clémence et al. 2015 (Sancerre); Fraguas et al. 2012 (Rodiles); Mattioli et al. 2013 (Peniche and Valdorbia); Reolid et al. 2014 (La Cerradura); Bodin et al. 2010 (Amellago). On the right of the figure is reported the duration of the Pl/To CIE (after Martinez et al. 2017). Also the duration of the T-OAE CIE is shown (after Suan et al. 2008). Some of these section are more expanded (e. g., the Peniche GSSP or Amellago in Morocco) while some others are more condensed (e. g. Dotternhausen): this can also be seen in the succession of first occurrence events, which can be either more spaced or more concentrated. Shaded area corresponds to the Pl/To event and the T-OAE (Toarcian Oceanic Anoxic Event). The diversification event of nannofossils takes place across the Pl/To, while during the T-OAE no first occurences are documented. Note that the Pliensbachian/Toarcian negative excursion is not found in all the sections, likely because hiatuses are present at the boundary. The vertical scale is the same for all the sections but Amellago, which is the most expanded section.

account data from Comas Rengifo et al. (2010), who studied the Almunacid de la Cuba section, which is located at ca. 60 km to the SE of la Almunia (35 km South of Zaragoza). Both sections are precisely correlated each-other as well as with the GSSP at Peniche (see Rocha et al. 2016). $^{87}Sr/^{86}Sr$ isotope values of Almunacid de la Cuba section match with previously published data for England (McArthur et al. 2000) and Portugal (Hesselbo et al. 2007), showing a decrease during the Hawskerense ammonite subzone (latest Pliensbachian), reaching a minimum value at around the Pliensbachian/Toarcian boundary and a recovery in the lower Toarcian (Fig. 2). $^{87}Sr/^{86}Sr$ ratio shows distinctive changes across the Pl/To, namely a negative trend that matches with the numerous calcareous nannofossil events recorded across the Pl/To boundary. These combined bio- and chemiostratigraphic events may be used as a reliable proxy to perform global correlations.

From the magnetostratigraphic record available at Almunacid de la Cuba, the Pl/To is very close to the inversion in magnetozone N2/R2 of Comas-Rengifo et al. (2010). This interval also corresponds to minimum values of strontium isotopes and the peak in calcareous nannofossil originations. This magnetic record permits indirect correlation with the Karoo-Ferrar Traps reversed/normal polarity succession, and hence the possible projection of Karoo ages onto the Pl/To. The Pl/To might be correlated to the Karoo basalts from South Africa dated to 182.7±0.8 Ma $^{40}Ar/^{38}Ar$ (Duncan et al. 1997). This is within the error interval but slightly younger than the age measured by Pálfy and Smith (2000), namely 183±1.7/–1–1 Ma, or the 182±1.5 Ma estimated by Ogg (2004).

The Pl/To was a biological key period not only for calcareous nannofossils, but also for many other fossils groups, such as marine invertebrates that experienced stepwise extinction and turnovers (e. g., Little et al. 1995, Morard et al. 2003, Cecca and Macchioni 2004). Nevertheless, for calcareous nannofossils and especially coccolithophorids the Pl/To represents mostly an origination period (high number of FO) and, finally, the key point from which primitive coccolithophorid assemblages (dominated by muroliths) were replaced by the evolutionary successful placolith group still dominating in today oceans. The emergence of the placolith-coccoliths was important because it produced a locked coccosphere, meanwhile the murolith-coccoliths were presumably contiguous, not interlocking at the surface of the cell (Wiggan et al. 2018). Recently, astrochronology has been applied in order to calculate the duration of ammonite and nannofossil zones in expanded sections of Morocco (Martinez et al. 2017). This study has revealed that the interval comprised between the Pl/To and the FO of *C. superbus* lasts between 433±25 and 505±44 kyrs. Such an approach may be applied in the future to our high-resolution dataset in order to better constrain the time lag between single nannofossil events and, finally, calculate real diversification rates.

## 6. Summary and conclusions

The two sections studied here for calcareous nannofossil biostratigraphy and chemostratigraphy at Anse St. Nicolas in W France and La Almunia in central Spain offer the opportunity to perform a high-resolution study across the Pl/To interval. The sections are well dated with ammonites and represent amongst the most continuous records for this time interval, given that often hiatuses and condensations occur in many Tethyan locations. The analysis of carbon stable isotopes reveal a negative excursion that corresponds to the Pl/To event, as already documented in literature for other areas. Although the general trend in diversity and absolute abundance of calcareous nannofossils is very similar in the two section studied here, some differences are observed in assemblage composition (e. g., higher proportions of *Schizosphaerella* in La Almunia), but also in the morphology of the observed species. The two sections being located in different sedimentary basins but not very remote the one with respect to the other, the observed differences may indicate a certain extent of geographical segregation within western Tethys basins.

Calcareous nannofossils experienced at the Pl/To a dramatic origination event. This is accompanied by an increase in species diversity and absolute abundances, and also corresponds to a change in the assemblage composition from murolith- to placolith-dominated coccoliths. All these observations are consistent with data coming from other Tethyan settings although some local differences are observed.

The Pl/To represents a major turnover for several invertebrate groups, somehow more noteworthy than the T-OAE crisis, meaning that this event affected all marine biota and environments. Thus, the Pl/To corresponded to a key evolutionary period, occurring concomitantly with major geochemical perturbations, a prominent sea-level fall, likely glacio-eustatic in origin, followed by a rise. The upper Pliensbachian–lo-

wermost Toarcian successions are characterized by numerous depositional hiatuses and condensed intervals (e. g., Wignall 1991, Morard et al. 2003, Röhl and Schmid-Röhl 2005, Léonide et al. 2012, Pittet et al. 2014, Rocha et al. 2016). Because of the incomplete nature of the boundary strata in many Tethyan areas, it is still unclear if such a high origination rate is uniquely linked to the evolutionary history of marine invertebrates, or if there is a superimposed effect of hiatuses or condensations. If this is the case, it is not excluded that the Pl/To origination event was partly amplified in the sedimentary record. However, the glacio-eustatic sea-level fall in the uppermost Pliensbachian could also have been at the origin of an allopatric speciation, because geographical barriers likely appeared between Western Tethyan basins. Astrochronological studies should be applied in the future to such a high-resolution dataset in order to constrain diversification and turnover rates of calcareous nannofossils.

## Species list

List of the species identified in the present work, mentioned both in the text and in the plates. Taxonomy follows Bown (1987) for muroliths, Mattioli (1996) for *Lotharingius*, and Mattioli et al. (2004 b) for *Similiscutum/Biscutum*. Some remarks about taxonomic concepts have been added when needed.

*Axopodorhabdus atavus* (Grün et al., 1974) Bown, 1987
*Axopodorhabdus cylindratus* (Noël, 1965) Wind and Wise in Wise and Wind, 1977
*Biscutum dubium* (Noël, 1965) Grün in Grün et al., 1974
*Biscutum grande* Bown, 1987
*Biscutum intermedium* Bown, 1987
*Bussonius leufuensis* Bown and Kielbowicz, 1987 in Bown, 1987
Remarks**:** *Bussonius* is included in the Watznaueriaceae family, the same as for *Lotharingius*. However, the two genera are different because the two cycles composing the distal shield are equally bright in *Lotharingius* appearing white in color, whilst for *Bussonius* the inner cycle is slightly brighter than the outer, which is slightly grey. Also, the cross structure in the central area of *B. leufuensis* is thicker than the cross in *L. barozii* or in *L. crucicentralis*. The arms of the cross in *Bussonius* are offset, thus the cross appears asymmetrical.
*Bussonius prinsii* (Noël, 1973) Goy, 1979
Remarks: *B. prinsii* differs from *B. leufuensis* for its more elliptical shape and narrower central area.
*Calyculus* spp. Noël, 1973
Remarks: thin and narrowly elliptical specimens are recorded, as well as thicker and broadly elliptical forms. These last likely represent transitional forms between *Calyculus* and *Carinolithus*.
*Carinolithus poulnabronei* Mattioli, 1996
Remarks: these are forms with an extended tube between proximal and distal shields. In side view, the central opening has an elongated V-shape.
*Carinolithus superbus* (Deflandre in Deflandre and Fert, 1954) Prins in Grün et al., 1974
Remarks: the central opening is very reduced and, in side view, the coccolith has a general T-shape.
*Crepidolithus cavus* Prins ex Rood et al., 1973
Remarks: in Plate 1 we show a *C. cavus/impontus*. In fact, the difference between the two species is quite tenuous, and the bridge which caracterizes *C. impontus* is sometimes not preserved, although its insertions on the coccolith are visible.
*Crepidolithus crassus* (Deflandre in Deflandre and Fert, 1954) Noël, 1965
*Crepidolithus crucifer* Prins 1969
*Crepidolithus granulatus* Bown, 1987
Remarks: the specimens shown in Plate 1 is very thick, but we also have found forms with a much thinner wall.
*Diductius constan*s Goy in Goy et al., 1979
*Crucirhabdus primulus* Prins, 1969 ex Rood et al., 1973 emend.
*Crucirhabdus minutus* Jafar, 1983
*Discorhabdus ignotus* (Górka, 1957) Perch-Nielsen, 1968
*Ethmorhabdus crucifer* Noël, 1965
*Ethmorhabdus gallicus* Noël, 1965
*Lotharingius barozii* Noël, 1973
Remarks: *L. barozii* is distinguished from all other *Lotharingius* because of its thin rim and very wide central area. The outer and inner cycles of distal shield are of equal thickness. The cross spanning the central area is very rarely preserved.
*Lotharingius crucicentralis* (Medd, 1971) Grün and Zweili, 1980
Remarks: this is differentiated from *L. barozii* because of its more reduced central area, which is sub-rectangular or oval in shape. Central area is spanned by a cross which is often not preserved. When the cross is absent, the four insertions on the coccolith are still observed. *L. crucicentralis* displays small dimensions in upper Pliensbachian and lower Toarcian material,

but its size increased from the lower/middle Toarcian transition (Ferreira et al. 2016).

*Lotharingius frodoi* Mattioli, 1996

Remarks: small coccolith, broadly elliptical-to-elliptical in shape, and presenting a very reduced central area filled with two butresses mimicking a small bridge. If this central area stucture is lacking, the insertions of the butresses on both sides of the coccolith are still visible. It is differentiated from *L. barozii* and *L. crucicentralis* because of its reduced central area size.

*Lotharingius hauffii* Grün and Zweili in Grün et al., 1974

Remarks: small coccolith, elliptical-to-subcircular in shape, and presenting a reduced central area with a small button. It is differentiated from *L. barozii* and *L. crucicentralis* because of its reduced central area and more circular shape, and from *L. frodoi* because of less elliptical shape and central area structures.

*Lotharingius sigillatus* (Stradner, 1961) Prins in Grün et al., 1974

Remarks: elliptical coccolith, presenting a narrow and elongated central area, with a longitudinal butress bulging in its middle part. It is differentiated from *L. barozii* and *L. crucicentralis* because of its narrower central area, from *L. frodoi* and *L. hauffii* because of slightly larger dimensions of the coccolith and more elongated central area. In a way similar to *L. crucicentralis*, *L. sigillatus* dimension is small in upper Pliensbachian and lower Toarcian material, but its size increased from the lower/middle Toarcian transition (Ferreira et al. 2016).

*Lotharingius umbriensis* Mattioli, 1996

Remarks: this is a quite rare but easy to recognize coccolith. It possesses a subcircular shape, a reduced central area spanned by a little cross. The optical discontinuity between the inner and outer cycle of distal shield is well-marked.

*Lotharingius velatus* Bown and Cooper, 1989

Remarks: this is the largest *Lotharingius* species. The general shape of coccolith and central area are oval. The wide central area is spanned by granulations that sometimes are not preserved. Sometimes, specimens with the diagnostic characters, but with a thin rim are observed (*L.* aff. *velatus* of Plate 2). As for the other *Lotharingius* species, its size is smaller in lower Toarcian material and increased from the lower/middle Toarcian transition (Ferreira et al. 2016).

*Mazaganella protensa* Bown, 1987

*Mitrolithus elegans* Deflandre in Deflandre and Fert, 1954

*Mitrolithus lenticularis* Bown, 1987

*Mitrolithus jansae* (Wiegand, 1984) Bown and Young in Young et al., 1986

*Orthogonoides hamiltoniae* Wiegand, 1984

*Parhabdolithus liasicus* Deflandre in Grassé, 1952

*Parhabdolithus liasicus* subsp. distinctus Bown, 1987

*Parhabdolithus liasicus* subsp. *liasicus* Deflandre in Grassé, 1952

*Schizosphaerella* Deflandre & Dangeard, 1938

*Silimiscutum cruciulus* subsp. *avitum* Mattioli et al., 2004b

*Similiscutum cruciulus* subsp. *cruciulus* Mattioli et al., 2004b

*Similiscutum finchii* (Crux, 1984 emend. Bown, 1987) de Kænel and Bergren, 1993

Remarks: elliptical *Similiscutum* with light grey, striped birefringence colors. The central area is rectangular and elongated. It is differentiated from *S. cruciulus* group because of lighter grey colors, more elliptical shape and wider central area.

*Similiscutum novum* (Goy, 1979) Mattioli et al., 2004

Remarks: sub-circular *Similiscutum* with light grey, striped birefringence colors. The central area is subsquared. It is differentiated from *S. finchii* because of smaller size, less elliptical shape and more reduced central area size, and from *S. cruciulus* group because of lighter grey colors.

*Similiscutum precarium* de Kænel and Bergen, 1993

*Sollasites* sp. Black, 1967

*Sollasites arctus* (Noël, 1973) Bown, 1987

*Stradnerlithus* Black, 1971

*Tubirhabdus patulus* Prins ex Rood et al., 1973

Remarks: specimens very thin occur along with thicker forms.

*Zeugrhabdotus erectus* (Deflandre in Deflandre and Fert, 1954) Reinhardt, 1965

**Acknowledgements.** This study was supported by the projects INSU Syster/Interrvie, the LabEx LIO to AM, and IUF to EM. The authors wish to thank Mrs. Ghislaine Broillet for help with sampling preparation. The samples used in this study for nannofossil and geochemical analyses are cured in the Collections de Géologie de l'Université de Lyon (collection numbers FSL 768.213-768.269). We wish to warmly thank two anonymus reviewers, whose comments helped improving the overall quality of our manuscript.

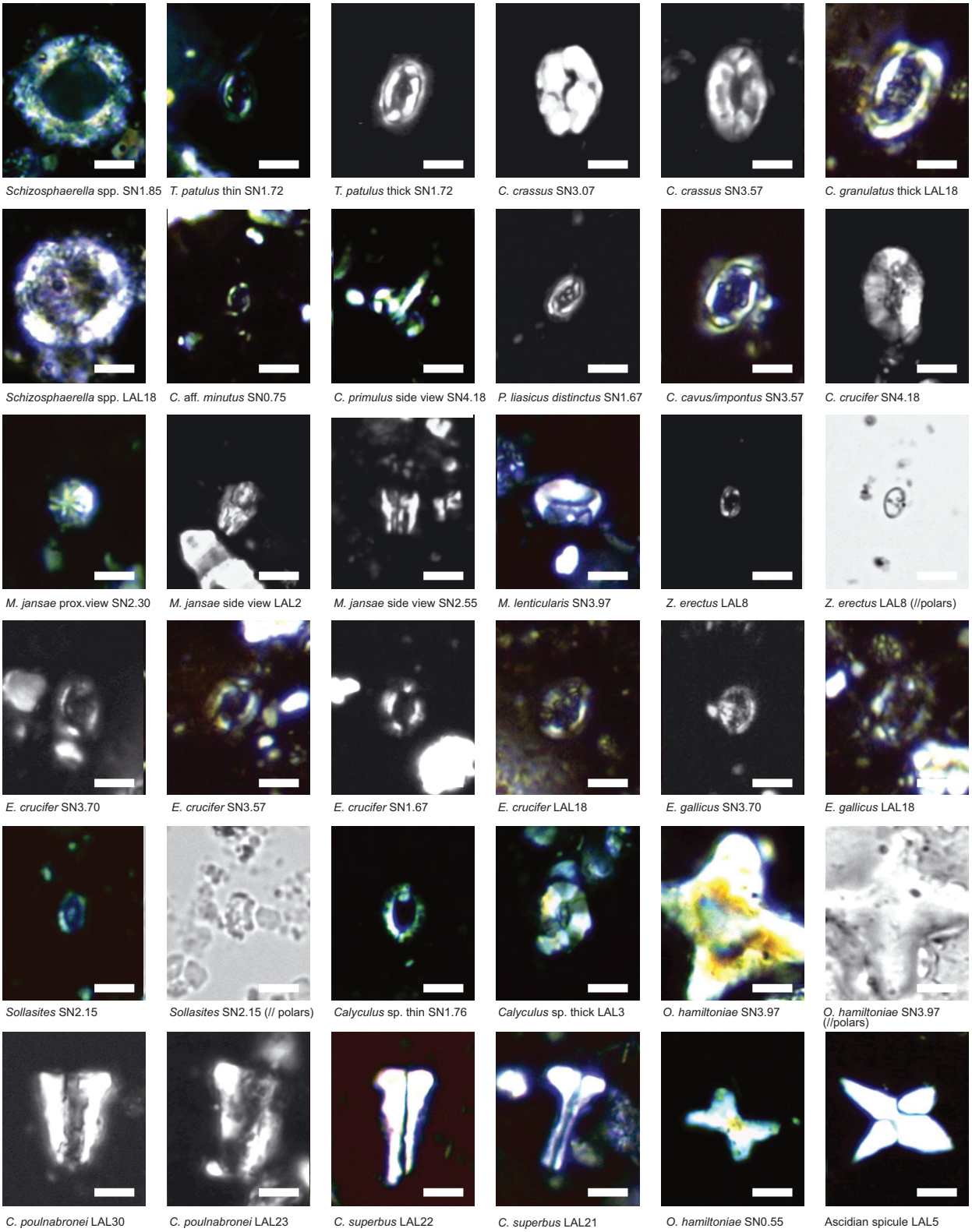


**Plate 1.** Microphotographs of common nannofossil taxa recored at La Almunia (LAL) and at Anse St. Nicolas (SN). Slight morphological differences may occur between nannofossils in the two regions. Scale bar is 5 microns.

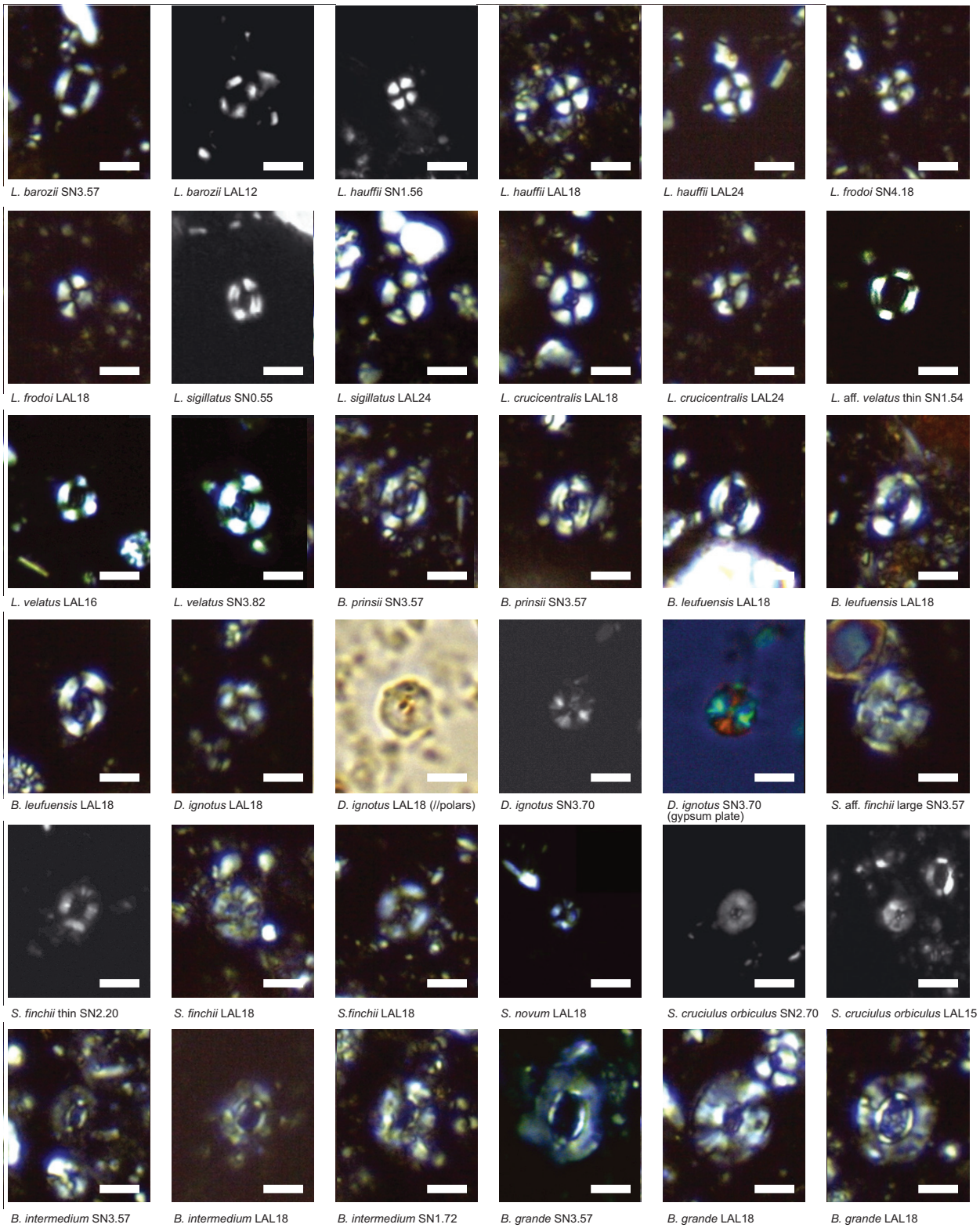


**Plate 2.** Microphotographs of common nannofossil taxa recored at La Almunia (LAL) and at Anse St. Nicolas (SN). Slight morphological differences may occur between nannofossils in the two regions. Scale bar is 5 microns.

Table 1. Stratigraphic distribution of calcareous nannofossils recorded at La Almunia section. Large-sized square symbol is used for abundant species (>10 % of the assemblage), intermediate-sized square is used for common species (1–10 %) and small-sized square represents frequent species (0–1 %). Species abundance concept is after Bown (1998).

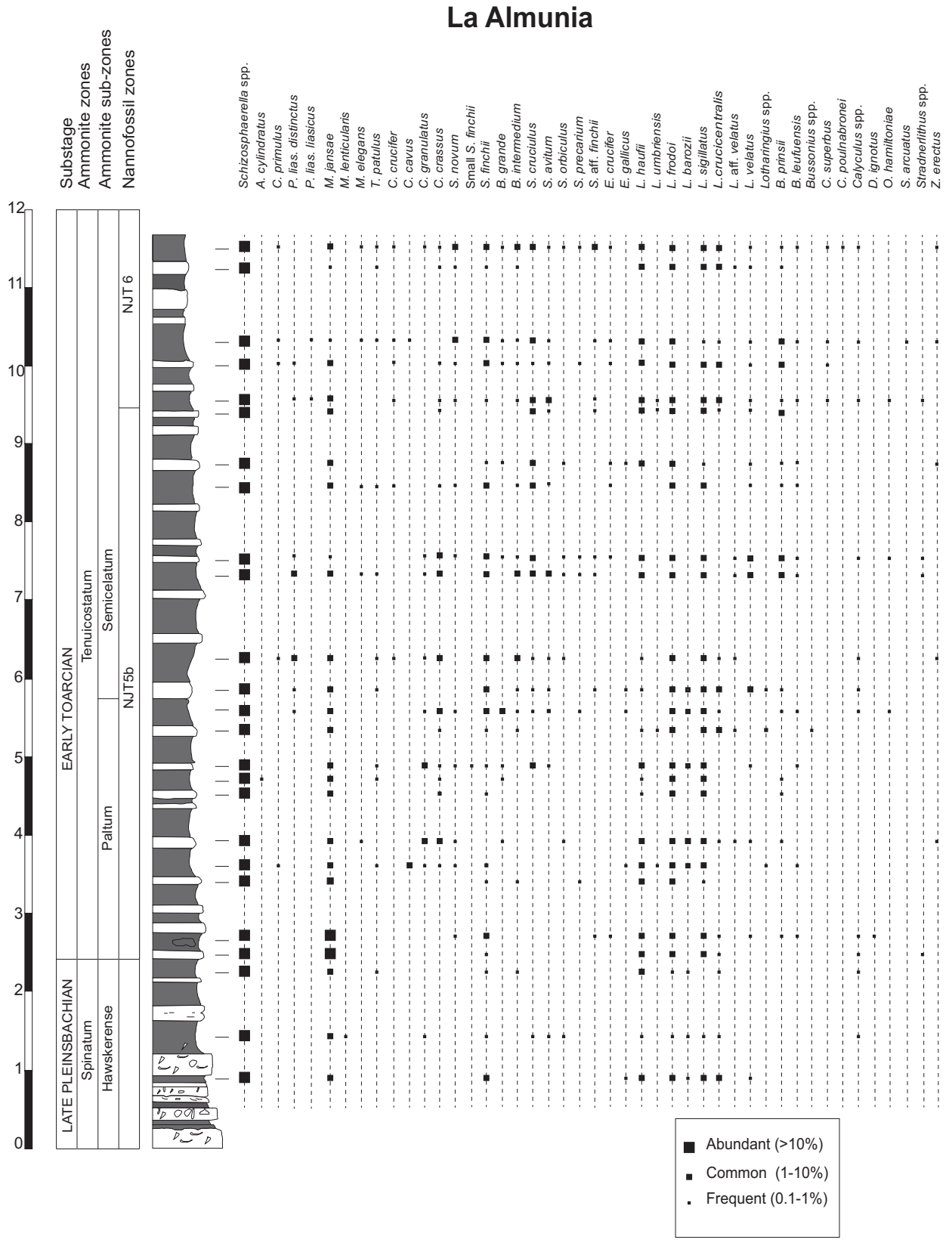

Table 2. Stratigraphic distribution of calcareous nannofossils recorded at Anse St. Nicolas section. Large-sized square symbol is used for abundant species (>10 % of the assemblage), intermediate-sized square is used for common species (1–10 %) and small-sized square represents frequent species (0–1 %). Species abundance concept is after Bown (1998).

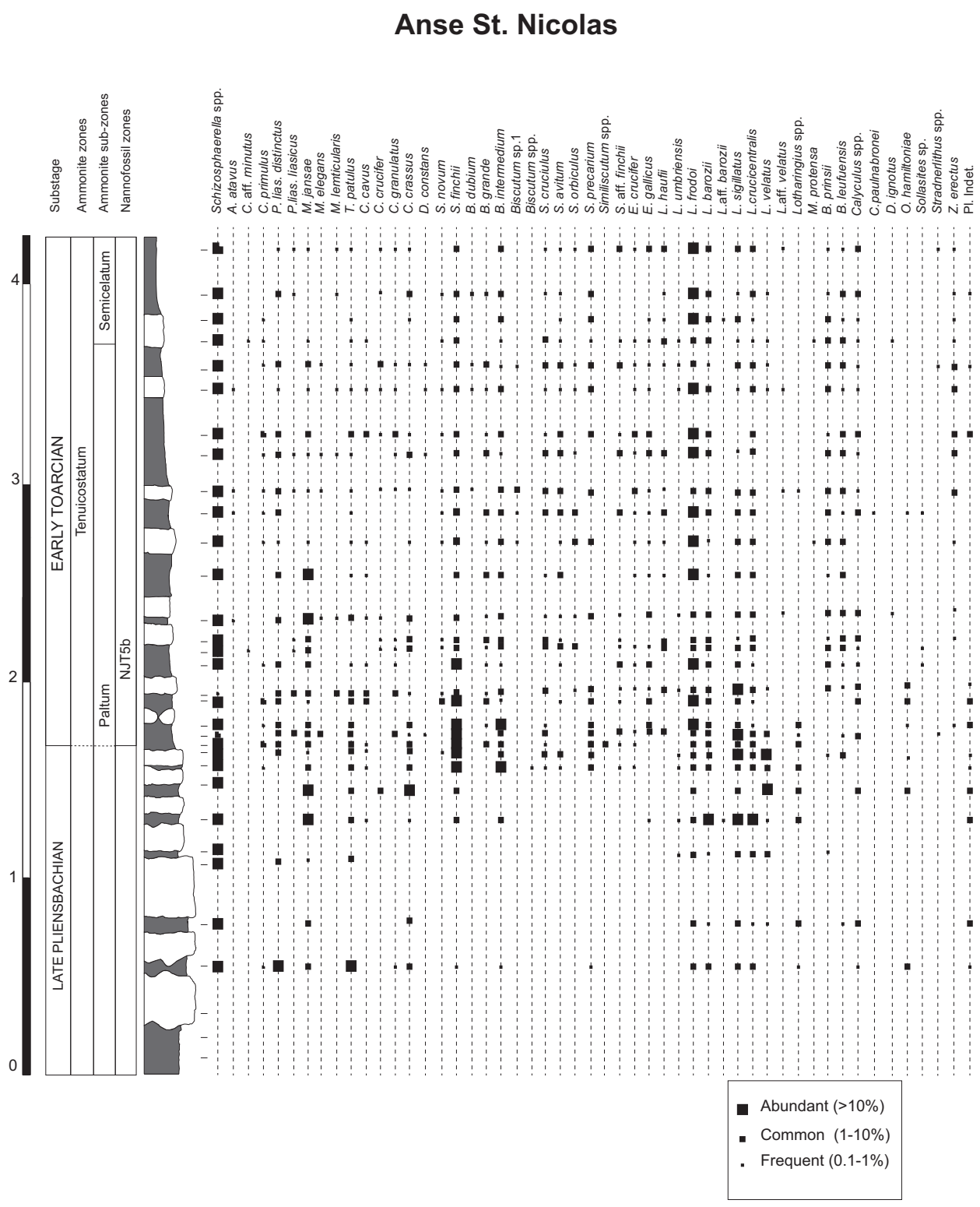

## References


Al-Suwaidi, A. H., Hesselbo, S. P., Damborenea, S. E., Manceñido, M. O., Jenkyns, H. C., Riccardi, A. C., Angelozzi, G. N., Baudin, F., 2016. The Toarcian Oceanic Anoxic Event (Early Jurassic) in the Neuquén Basin, Argentina: A Reassessment of Age and Carbon Isotope Stratigraphy. The Journal of Geology, doi: 10.1086/684831.

Arias, C. F., 1991. Las asociaciones de ostrácodos del Domeriense superior y Toarciense inferior de la Cordillera Ibérica. Coloquios de Paleontología 43, 79–99.

Arias, C. F., 1995. Los ostrácodos del Toarciense inferior en la Cordillera Ibérica. PhD Thesis, Fac. C. Geológicas. Univ. Complutense Madrid, Spain.

Bassoullet, J. P., Elmi, S., Poisson, A., Cecca, F., Bellion, Y., Guiraud, R., Baudin, F., 1993. Mid Toarcian. In: Dercourt, J., Ricou, L. E., Vrielynck, B. (Eds.), Atlas Tethys Paleoenvironmental Maps. BEICIPFRANLAB, Rueil-Malmaison.

Beaufort, L., Barbarin, N., Gally, Y., 2014. Optical measurements to determine the thickness of calcite crystals and the mass of thin carbonate particles such as coccoliths. Nature Protocols 9, 633–642.

Bécaud, M., 2002. Le Toarcien de la bordure sud et sud-est du Massif armoricain (Deux-Sèvres et Vendée). Le naturaliste vendéen 2, 3–33.

Bécaud, M., 2005. Ammonites peu connues du Toarcien inférieur du sud-ouest de la Vendée. Le naturaliste vendéen 5, 45–48.

Bécaud, M., 2006. Les Hildoceratidae (Ammonitina) du Toarcien de la bordure sud et sud est du Massif armoricain (France). Docum. Lab. Géologie Lyon 162, 1–148.

Blomeier, D. P. G., Reijmer, J. J. G., 1999. Drowning of a lower Jurassic carbonate platform: Jbel Bou Dahar, High Atlas, Morocco. Facies 41, 81–110.

Bodin, S., Krencker, F. N., Kothe, T., Hoffmann, R., Mattioli, E., Heimhofer, U., Kabiri, L., 2016. Perturbation of the carbon cycle during the late Pliensbachian – early Toarcian: New insight from high-resolution carbon isotope records in Morocco. Journal of African Earth Sciences 116, 89–104, https://doi.org/10.1016/j.jafrearsci.2015.12.018.

Bodin, S., Mattioli, E., Fröhlich, S., Marshall, J. D., Boutib, L., Lahsini, S., Redfern, J., 2010. Documentation of Early Toarcian (Jurassic) carbon isotope negative shifts and nutrient changes along the Northern Gondwana margin (High Atlas, Morocco): palaeoenvironmental implications. Palaeogeology, Palaeoclimatology, Palaeoecology 297, 377–390.

Boomer, I., Lord, A. R., Page, K. N., Bown, P. R., Lowry, F. M. D., Riding, J. B., 2009. The biostratigraphy of the Upper Pliensbachian–Toarcian (Lower Jurassic) sequence at Ilminster, Somerset. Journal of Micropalaeontology 28, 67–85.

Bown, P. R., 1987. Taxonomy, evolution and biostratigraphy of Late Triassic-early Jurassic calcareous nannofossils. Special Papers in Paleontology 38, 1–118.

Bown, P. R., Cooper, M. K. E., 1998. Jurassic. In: Bown, P. R. (Ed.), Calcareous Nannofossil Biostratigraphy, British Micropalaeontological Society Series. Chapman and Hall/Kluwer Academic Publishers, London, 86–131.

Brand, W. A., Coplen, T. B., Vogl, J., Rosner, M., Prohaska, T., 2014. Assessment of international reference materials for isotope-ratio analysis. Pure and Applied Chemistry 8866, 425–467.

Casellato, C. E., Erba, E., 2015. Calcareous nannofossil biostratigraphy and paleoceanography of the toarcian oceanic anoxic event at colle di sogno (Southern Alps, Northern Italy). Rivista Italiana di Paleontologia e Stratigrafia 121, 297–327.

Cecca, F., Macchioni, F., 2004. The two Early Toarcian (Early Jurassic) extinction events in ammonoids. Lethaia 3, 35–56, https://doi.org/10.1080/00241160310008257.

Comas-Rengifo, M. J., Gómez, J. J., Goy, A., Herrero, C., Osete, M. L., Palencia, A., 2010. A complementary section for he proposed Toarcian (Lower Jurassic) global stratotype: the Almonacid de la Cuba sections (Spain). Stratigraphy and Geological Correlation 18, 133–152.

Comas-Rengifo, M. J., Gómez, J. J., Goy, A., Herrero, C., Perilli, N., Rodrigo, A., 1999. El Jurásico Inferior en la sección de Almonacid de la Cuba (Sector central de la Cordillera Ibérica), Zaragoza, España. Cuad. Geol. Ibér. 25, 27–57.

Courtinat, B., Pittet, B., Mattioli, E., Rio, M., 2007. Marine microplankton and calcareous nannofossil palaeoecology of the Toarcian stratotype. Geobios 40, 785–800.

Dera, G., Neige, P., Dommergues, J.-L., Brayard, A., 2011. Ammonite paleobiogeography during the Pliensbachian–Toarcian crisis (Early Jurassic) reflecting paleoclimate, eustasy, and extinctions. Global and Planetary Change 78, 92–105.

Dera, G., Pellenard, P., Neige, P., Deconinck, J.-F., Pucéat, E., Dommergues, J.-L., 2009. Distribution of clay minerals in Early Jurassic Peritethyan seas: Palaeoclimatic significance inferred from multiproxy comparisons. Palaeogeography, Palaeoclimatology, Palaeoecology 271, 39–51.

Duncan, R. A., Hooper, P. R., Rehacek, J., Marsh, J. S., Ducan, A. R., 1997. The timing and duration of the Karoo igneous sevent, southern Gondwana. Journal of Geophysical Research 102, 127–138.

Elmi, S., 2007. Pliensbachian/Toarcian boundary: the proposed GSSP of Peniche (Portugal). Ciências da Terra (UNL) 16, 7–16.

Elmi, S., Rulleau, L., Gabilly, J., Mouterde, R., 1997. Ammonites: Toarcien. In: Cariou, E., Hantzpergue, P. (Eds.), Biostratigraphie du Jurassique ouest-européen et méditerranéen: Zonations parallèles et distribution des invertebrés et microfossiles. Groupe Français d'Etude du Jurassique. Bulletin du Centre de Recherches, Elf Exploration Production 17, 25–36 + 120–125.

Fantasia, A., Föllmi, K. B., Adatte, T., Bernárdez, E., Spangenberg, J. E., Mattioli, E., 2018. The Toarcian Oceanic Anoxic Event in southwestern Gondwana: An example from the Andean Basin, northern Chile. Journal of the

Geological Society, doi: https://doi.org/10.1144/jgs2018-008.

Fatela, F., Taborda, R., 2002. Confidence limits of species proportions in microfossil assemblages. Marine Micropaleontology 45, 169–174, 10.1016/S0377-8398(02)00021-X.

Ferreira, J., Mattioli, E., Pittet, B., Cachão, Spangenberg, J. E., 2015. Palaeoecological insights on Toarcian and lower Aalenian calcareous nannofossils from the Lusitanian Basin (Portugal). Paleogeography, Paleoclimatology, Paleoecology 436, 245–262.

Ferreira, J., Mattioli, E.van de Schootbrugge, B., 2016. Palaeoenvironmental vs. evolutionary control on size variation of coccoliths across the Lower-Middle Jurassic. Paleogeography, Paleoclimatology, Paleoecology, http://dx.doi.org/10.1016/j.palaeo.2016.10.029.

Fraguas, Á., Erba, E., 2010. Biometric analyses as a tool for the differentiation of two coccolith species of the genus Crepidolithus (Pliensbachian, Lower Jurassic) in the Basque-Cantabrian Basin (Northern Spain). Marine Micropaleontology 77, 125–136.

Fraguas, Á., Comas-Rengifo, M. J., Gómez, J. J., Goy, A., 2012. The calcareous nannofossil crisis in Northern Spain (Asturias province) linked to the Early Toarcian warming-driven mass extinction. Marine Micropaleontology 94–95, 58–71.

Fu, X., Wang, J., Feng, X., Wang, D., Chen, W., Song, C., Zeng, S., 2016. Early Jurassic carbon-isotope excursion in the Qiangtang Basin (Tibet), the eastern Tethys: Implications for the Toarcian Oceanic anoxic event. Chemical Geology 442, 62–72.

Gabilly, J., 1964. Stratigraphie et limite de l'étage Toarcien Thouars et dans les régions voisines. Coll. Jurassique, Luxembourg (1962). C. R. Mém. Inst. Grand Duc., Sect. Sci. Nat. Phys. Math., 193–201.

Gabilly, J., 1973. Le Toarcien du Poitou. Biostratigraphie de la région du stratotype. Évolution des Hildoceratacеae (Ammonitina). Doctoral dissertation, Poitiers, 546 p.

Gabilly, J., 1976. Le Toarcien à Thouars et dans le Centre-Ouest de la France. Biostratigraphie. Évolution de la faune (Harpoceratinae – Hildoceratinae); collection: Comité français de Stratigraphie. Les stratotypes français vol. 3. CNRS, Paris, 217 p.

Gautier, F., Mouterde, R., 1964. Stratigraphie – lacunes et irrégularités des dépôts à la limite du Jurassique inferieur et du jurassique moyen de la bordure nord des chaines ibériques (Espagne). Comptes rendus hebdomadaires des séances de l'académie des sciences 258, 3064.

Gómez, J. J., Comas-Rengifo, M. J., Goy, A., 2016. Palaeoclimatic oscillations in the Pliensbachian (Early Jurassic) of the Asturian Basin (Northern Spain). Climate of the Past 12, 1199–1214, doi: 10.5194/cp-12-1199-2016.

Gómez, J. J., Goy, A., Canales, M. L., 2008. Seawater temperature and carbon isotope variations in belemnites linked to mass extinction during the Toarcian (Early Jurassic) in Central and Northern Spain. Comparison with other European sections. Palaeogeography, Palaeoclimatology, Palaeoecology 258, 28–58.

Goy, A., Martínez, G., 1990. Biozonacion del Toarciense en el área de La Almunia de Doña Godina-Ricla (Sector Central de la Cordillera Ibérica). Cuadernos Geología Ibérica 14, 9–44.

Hammer, Ø., Harper, D. A. T., Ryan, P. D., 2001. Past: Paleontological Statistics Software Package for education and data analysis. Palaeoentologia Electronica 4 (1), 9, http://palaeo-electronica.org/2001_1/past/issue1_01.htm.

Hay, W. W., 1972. Probabilistic stratigraphy. Eclogae Geologicae Helveticae 65, 255–266.

Hermoso, M., Minoletti, F., Rickaby, R. E. M., Hesselbo, S. P., Baudin, F., Jenkyns, H. C., 2012. Dynamics of a stepped carbon-isotope excursion: Ultra high-resolution study of Early Toarcian environmental change. Earth and Planetary Science Letters 319–320, 45–54.

Herrero, C., 1992. Los foraminífero del Toarciense inferior de la Cordillera Ibérica. Tesis Doctoral. Facultad de Ciencias Geológicas, Universidad Complutense de Madrid, 523 pp.

Hesselbo, S. P., 2008. Sequence stratigraphy and inferred relative sea-level change from the onshore British Jurassic. Proceedings of the Geologists' Association 119, 19–34.

Hesselbo, S. P., Jenkyns, H. C., Duarte, L. V., Oliveira, L. C. V., 2007. Carbon-isotope record of the Early Jurassic (Toarcian) Oceanic Anoxic Event from fossil wood and marine carbonate (Lusitanian Basin, Portugal). Earth Planet. Sci. Lett. 253, 455–470.

Huang, C., Hesselbo, S. P., 2014. Pacing of the Toarcian Oceanic Anoxic Event (Early Jurassic) from astronomical correlation of marine sections. Gondwana Research 25, 1348–1356.

Jenkyns, H. C., 1988. The Early Toarcian (Jurassic) anoxic event: stratigraphic, sedimentary and geochemical evidence. Am. J. Sci. 288, 101–151.

Korte, C., Hesselbo, S., 2011. Shallow marine carbon and oxygen isotope and elemental records indicate icehouse-greenhouse cycles during the Early Jurassic. Paleoceanography 26, 1–18, PA4219, doi: 10.1029/2011PA002160.

Krebs, C. J., 1998. Ecological methodology (2nd edition). Addison Wesley Longman (Eds., Pearson Education), 620 pp.

Léonide, P., Floquet, M., Durlet, C., Baudin, F., Pittet, B., Lécuyer, C., 2012. Drowning of a carbonate platform as a precursor stage of the Early Toarcian global anoxic event (Southern Provence sub-Basin, South-east France). Sedimentology 59, 156–184.

Little, C. T. S., Benton, M. J., 1995. Early Jurassic mass extinction: a global long term event. Geology 23, 495–498.

Littler, K., Hesselbo, S. P., Jenkyns, H. C., 2010. A carbon-isotope perturbation at the Pliensbachian–Toarcian boundary: evidence from the Lias Group, NE England. Geological Magazine 147 (2), 181–192.

Mailliot, S., Mattioli, E., Guex, J., Pittet, B., 2006. The Early Toarcian anoxia, a synchronous event in the Western Tethys? An approach by quantitative biochronology (Unitary Associations), applied on calcareous nannofos-

sils. Palaeogeography, Palaeoclimatology, Palaeoecology 240 (3–4), 562–586, https://doi.org/10.1016/j.palaeo.2006.02.016.

Martindale, R. C., Aberhan, M., 2017. Response of macrobenthic communities to the Toarcian Oceanic Anoxic Event in northeastern Panthalassa (Ya Ha Tinda, Alberta, Canada). Palaeogeography, Palaeoclimatology, Palaeoecology 478, 103–120, https://doi.org/10.1016/j.palaeo.2017.01.009.

Martinez, M., Krencker, F.-N., Mattioli, E., Bodin, S., 2017. Orbital chronology of the Pliensbachian – Toarcian transition from the Central High Atlas Basin (Morocco). Newsletters on Stratigraphy 50 (1), 47–69, https://doi.org/10.1127/nos/2016/0311.

Mattioli, E., Erba, E., 1999. Synthesis of calcareous nannofossil events in tethyan lower and middle Jurassic successions. Rivista Italiana di Paleontologia e Stratigrafia 105, 343–376.

Mattioli, E., Pittet, B., Palliani, R., Rohl, H.-J., Schmid-Rohl, A., Morettini, E., 2004a. Phytoplankton evidence for the timing and correlation of palaeoceanographical changes during the early Toarcian oceanic anoxic event (Early Jurassic). Journal of the Geological Society 161 (4) (), 685–693, https://doi.org/10.1144/0016-764903-074.

Mattioli, E., Pittet, B., Petitpierre, L., Mailliot, S., 2009. Dramatic decrease of pelagic carbonate production by nannoplankton across the Early Toarcian anoxic event (T-OAE). Global and Planetary Change 65 (3–4), 134–145, https://doi.org/10.1016/j.gloplacha.2008.10.018.

Mattioli, E., Pittet, B., Suan, G., Mailliot, S., 2008. Calcareous nannoplankton changes across the early Toarcian oceanic anoxic event in the western Tethys. Paleoceanography 23 (3), 1–17, https://doi.org/10.1029/2007PA001435.

Mattioli, E., Pittet, B., Young, J. R., Bown, P. R., 2004b. Biometric analysis of Pliensbachian-Toarcian (Lower Jurassic) coccoliths of the family Biscutaceae: intra- and interspecific variability versus palaeoenvironmental influence. Marine Micropalaeontology 52, 5–27.

Mattioli, E., Plancq, J., Boussaha, M., Duarte, L. V., Pittet, B., 2013. Calcareous nannofossil biostratigraphy: new data from the Lower Jurassic of the Lusitanian Basin. Comunicacoes Geologicas T. 100, 100 (Especial I), 69–76.

McArthur, J. M., Donovan, D. T., Thirwall, M. F., Fouke, B. W., Mattey, D., 2000. Strontium isotope profile of early Toarcian (Jurassic) oceanic anoxic event, the duration of ammonite biozones, and belmnite palaeotemperature. Earth Planet. Sci. Lett. 179, 269–285.

Medd, A. W., 1982. Nannofossil zonation of the English Middle and Upper Jurassic. Marine Micropalentology 7, 73–95.

Mensik, H., 1965. Stratigraphie und Paläogeographie des marinen Jura in den nord-westlichen Iberischen Ketten (Spanien). Beih. Geol. Jb., 55–102.

Morard, A., Guex, J., Bartolini, A., Morettini, E., De Wever, P., 2003. A new scenario for the Domerian – Toarcian transition. Bull. Soc. géol. Fr. 4, 351–356.

Noël, D., 1965. Sur les Coccolithes du Jurassique Européen et d'Afrique du Nord. Éditions du Centre National de la Recherche Scientifique, Paris, 110–111.

Noël, D., 1972. Nannofossiles calcaires de sediments jurassiques finement laminés. Bull. Mus. Hist. Natur. 3 e sér. 75, 95–116.

Pálfy, J., Smith, P. L., 2000. Synchrony between Early Jurassic extinction, oceanic anoxic event, and the Karoo-Ferrar flood basalt volcanism. Geology 28, 747–750.

Peti, L., Thibault, N., Clémence, M.-E., Korte, C., Dommergues, J.-L., Bougeault, C., Pellenard, P., Jelby, M. E., Ullmann, C. V., 2017. Sinemurian–Pliensbachian calcareous nannofossil biostratigraphy and organic carbon isotope stratigraphy in the Paris Basin: Calibration to the ammonite biozonation of NW Europe. Palaeogeography, Palaeoclimatology, Palaeoecology 468, 142–161.

Philippe, M., Pujialon, S., Suan, G., Mousset, S., Thévenard, F., Mattioli, E., 2017. The palaeolatitudinal distribution of fossil wood genera as a proxy for European Jurassic terrestrial climate. Palaeogeography, Palaeoclimatology, Palaeoecology 466, 373–381.

Pittet, B., Suan, G., Lenoir, F., Vitor, L., Mattioli, E., 2014. Carbon isotope evidence for sedimentary discontinuities in the lower Toarcian of the Lusitanian Basin (Portugal): Sea level change at the onset of the Oceanic Anoxic Event. Sedimentary Geology 303, 1–14, https://doi.org/10.1016/j.sedgeo.2014.01.001.

Reggiani, L., Mattioli, E., Pittet, B., Duarte, L. V., Veiga de Oliveira, L. C., Comas-Rengifo, M. J., 2010. Pliensbachian (Early Jurassic) calcareous nannofossils from the Peniche section (Lusitanian Basin, Portugal): A clue for palaeoenvironmental reconstructions. Marine Micropaleontology 75 (1–4), 1–16, https://doi.org/10.1016/j.marmicro.2010.02.002.

Reolid, M., Emanuela, M., Nieto, L. M., Rodriguez-Tovar, F. J., 2014. The Early Toarcian Oceanic Anoxic Event in the External Subbetic (Southiberian Palaeomargin, Westernmost Tethys): Geochemistry, nannofossils and ichnology. Palaeogeography, Palaeoclimatology, Palaeoecology 411, 79–94, https://doi.org/10.1016/j.palaeo.2014.06.023.

Révész, K., Landwehr, J. M., 2002. $\delta^{13}C$ and $\delta^{18}O$ isotopic composition of $CaCO_3$ measured by continuous flow isotope ratio mass spectrometry: statistical evaluation and verification by application to Devils Hole core DH-11 calcite. Rapid Communications in Mass Spectrometry 16, 2102–2114.

Rocha, R., Mattioli, E., Duarte, L. V., Pittet, B., Elmi, S., Mouterde, R., Cabral, M. C., Comas-Rengifo, M. J., Gómez, J. J., Goy, A., Hesselbo, S. P., Jenkyns, H. C., Littler, K., Mailliot, S., Veiga, Oliveira, L. C., Osete, M. L., Perilli, N., Pinto, S., Ruget, C., Suan, G., 2016. Base of the Toarcian Stage of the Lower Jurassic defined by the Global Boundary Stratotype Section and Point (GSSP) at the Peniche section (Portugal). Episodes 39, 460–481.

Röhl, H. J., Schmid-Röhl, A., Wolfgang, O., Frimmel, A., Lorenz, S., 2001. The Posidonia Shale (Lower Toarcian) of SW-Germany: An oxygen-depleted ecosystem con-

trolled by sea level and palaeoclimate. Palaeogeogeography, Palaeoclimatology, Palaeoecology 165, 27–52, doi: 10.1016/S0031-0182(00)00152-8.

Rosales, I., Quesada, S., Robles, S., 2004. Paleotemperature variations of Early Jurassic seawater recorded in geochemical trends of belemnites from the Basque – Cantabrian basin, northern Spain. Palaeogeography, Palaeoclimatology, Palaeoecology 203, 253–275.

Roth, P. H., 1984. Preservation of calcareous nannofossils and fine-grained carbonate particles in mid-Cretaceous sediments from the southern Angola Basin. In: Hay, W. W. (Ed.), Initial Reports of Deep Sea Drilling Project 75. U. S. Government Printing Office, Washington, 651–655.

Sabatino, N., Neri, R., Bellanca, A., Jenkyns, H., Baudin, F., Parisi, G., Masetti, D., 2009. Carbon-isotope records of the Early Jurassic (Toarcian) oceanic anoxic event from the Valdorbia (Umbria–Marche Apennines) and Monte Mangart (Julian Alps) sections: palaeoceanographic and stratigraphic implications. Sedimentology 56, 1307–1328.

Sandoval, J., Bill, M., Aguado, R., O'Dogherty, L., Dogherty, L., Rivas, P., Morard, A., Guex, J., 2012. The Toarcian in the Subbetic basin (southern Spain): Bioevents (ammonite and calcareous nannofossils) and carbon-isotope stratigraphy. Palaeogeography, Palaeoclimatology, Palaeoecology 342–343, 40–63, https://doi.org/10.1016/j.palaeo.2012.04.028.

Shannon, C. E., Weaver, W., 1949. The Mathematical Theory of Communication. Univ. of Ill. Press, Urbana, Ill.

Spangenberg, J. E., Herlec, U., 2006. Hydrocarbon biomarkers in the Topla-Mežica zinc-lead deposits, northern Karavanke/Drau Range, Slovenia: Paleoenvironment at the site of ore formation. Economic Geology 101 (5), 997–1021.

Suan, G., Mattioli, E., Pittet, B., Lécuyer, C., Suchéras-Marx, B., Duarte, L. V., Martineau, F., 2010. Secular environmental precursors to Early Toarcian (Jurassic) extreme climate changes. Earth and Planetary Science Letters 290 (3–4), 448–458, https://doi.org/10.1016/j.epsl.2009.12.047.

Suan, G., Mattioli, E., Pittet, B., Mailliot, S., Lécuyer, C., 2008a. Evidence for major environmental perturbation prior to and during the Toarcian (Early Jurassic) oceanic anoxic event from the Lusitanian Basin, Portugal. Paleoceanography, 23, PA1202, doi: 10.1029/2007PA001459.

Them, T. R., Gill, B. C., Caruthers, A. H., Gröcke, D. R., Tulsky, E. T., Martindale, R. C., … Smith, P. L., 2017. High-resolution carbon isotope records of the Toarcian Oceanic Anoxic Event (Early Jurassic) from North America and implications for the global drivers of the Toarcian carbon cycle. Earth and Planetary Science Letters 459, 118–126, https://doi.org/10.1016/j.epsl.2016.11.021.

Thierry, J., Barrier, E., 2000. Middle Toarcian. In: Dercourt, J., Gaetani, M. E. A. (Eds.), Atlas Peri-Tethys. Palaeogeographical Maps CCGM/CGMW, Paris.

van de Schootbrugge, B., McArthur, J. M., Bailey, J. M., Rosenthal, Y., Wright, J. M., Miller, K. G., 2005. Toarcian oceanic anoxic event: An assessment of global causes using belemnite C isotope records. Paleoceanography 20, PA3008, doi: 10.1029/2004PA001102.

Wiggan, N. J., Riding, J. B., Fensome, R. A., Mattioli, E., 2018. The Bajocian (Middle Jurassic): A key interval in the early Mesozoic phytoplankton radiation. Earth-Science Reviews 180, 126–146.

Wignall, P. B., Hallam, A., Newton, R. J., Sha, J. G., Reeves, E., Mattioli, E., Crowley, S., 2006. An eastern Tethyan (Tibetan) record of the Early Jurassic (Toarcian) mass extinction event. Geobiology 4, 179–190.

Manuscript received: March 15, 2015
Revisions required: June 06, 2018
Revised version received: August 02, 2018
Manuscript accepted: August 06, 2018

**The pdf version of this paper includes an electronic supplement**
Please save the electronic supplement contained in this pdf-file by clicking the blue frame above. After saving rename the file extension to .zip (for security reasons Adobe does not allow to embed .exe, .zip, .rar etc. files).

**Table of contents – Electronic Supplementary Material (ESM)**
Calcareous nannofossils relative and absolute abundances as well as $\delta^{13}C$ bulk rock data are available as supplementary material. The file can be requested to the corresponding author.

# Chapitre 2.2. Calcareous nannofossil biostratigraphy across the Paleocene-Eocene Thermal Maximum

# Calcareous nannofossil biostratigraphy across the Paleocene-Eocene Thermal Maximum

Alessandro Menini[a*], Emanuela Mattioli[a,b], Arnauld Vinçon-Laugier[a], Guillaume Suan[a]

**Authors' addresses**

[a]Univ Lyon, Univ Lyon 1, ENSL, CNRS, LGL-TPE, F-69622, Villeurbanne, France.

Email : alessandro.menini@univ-lyon1.fr, emanuela.mattioli@univ-lyon1.fr, arnauld.vinçon-laugier@univ-lyon1.fr, guillaume.suan@univ-lyon1.fr

[b]Institut Universitaire de France (IUF), Paris, France. Email : emanuela.mattioli@univ-lyon1.fr

[*]**Corresponding author**

Alessandro Menini

Email: alessandro.menini@univ-lyon1.fr

Tel :0033 (0)4 72 44 83 82

Univ Lyon, Univ Lyon 1, ENSL, CNRS, LGL-TPE, F-69622, Villeurbanne, France

**Abstract**

The Paleocene-Eocene transition is charactirezed by a prominent negative carbon isotope excursion that corresponds to the Paleocene Eocene Thermal Maximum (PETM). The sharp negative shift of stable carbon isotopes has been retained as marker for the Paleocene/Eocene boundary. Although recorded in several oceanic and onland settings, the PETM phases namely the onset, the core of the event and the recovery, are not adequately dated by calcareous nannofossils because available standard biozonations do not provide us with a high-resolution

across the event. Here, we present new high-resolution biotratigraphic data from Sites 1209 (Shatsky Rise, Tropical Pacific Ocean) and 1263 (Walvis Ridge, South Eastern Atlantic Ocean) in order to precisely assess the succession of biostratigraphic events (first and last occurrences, changes in the assemblage composition), and to anchor them to the independent proxy represented by the $\delta^{13}C_{bulk\ carb}$ curve. A tidy comparison of our data with nannofossil events from six sections located at different (paleo)latitudes and in different geological settings (open ocean-to-shelf) revealed 26 calcareous nannofossil events across a 250 kyrs long-lasting interval spanning the PETM, and allowed a high-resolution biozonal subdivision of this interval. Calcareous nannofossil events plotted against available $\delta^{13}C_{bulk\ carb}$ curves show a certain degree of diachronism, even when considering previously established zonal markers. Also, unconformities occur at the onset of PETM in most oceanic sites, but to a lesser extent in onland sections. We propose here a new biozonation, based on reproducible events at different localities, to obtain a chronostratigraphic subdivision with a high-resolution for this short-lasting hyperthermal event. We define thus four new zones spanning the latest Paleocene and the earliest Eocene that allow correlation of shelf and open-ocean localities, and two subzones mainly useful in shelf environnements. These new zones correlate to the main trends of the $\delta^{13}C_{bulk\ carb}$ curve and define the pre-excursion interval (PE-1), the negative $\delta^{13}C_{bulk\ carb}$ shift defining the base of the Eocene (PE0), the core of the event, the recovery phase I (PE1) and the recovery phase II intervals (PE2).

**Keywords**; calcareous nannofossils, biostratigraphy, PETM, biozonation, shelf, open ocean

## 1. Introduction

The Paleocene-Eocene transition (56 Ma) is characterized by a brief but intense carbon isotope negative excursion (CIE) associated with a global warming of 5-7°C (Kennet and Stott 1991,

Zachos et al. 2001). This transition is known as the Paleocene Eocene Thermal Maximum (PETM). Recent models estimated that this event lasted approximatly 200 kyrs (Röhl et al. 2000, Röhl et al. 2007). The input of isotopically light carbon either from methane release or volcanism (Dickens et al. 1995, 1997) led to enhanced $pCO_2$ in the oceans, finally triggering acidification and shoaling of the carbonate compensation depth CCD (Zachos et al. 2004, Penman et al. 2014, Babila et al. 2018). Recent studies suggest that these changes happened during a 405 kyrs eccentricity maximum (Zeebe and Lourens 2019). Benthic communities suffered a dramatic extinction (Tjalsma and Lohmann 1983, Thomas and Shackleton 1996) and planktonic biota underwent a profound re-organisation (e.g., Bralower et al. 1995, Kelly et al. 1996, Bralower et al. 2002, Gibbs et al. 2006, Raffi et al. 2009).

The number of continuous late Paleocene-early Eocene successions is still relatively limited; consequently, only partial information exists about the biostratigraphic ranges of marker species. Because the PETM is characterized by intense carbonate dissolution, preservation problems have compromised a precise biostratigraphic information in several ODP/IODP settings and land sections (e.g., Wei and Zhong 1996, Kroon et al. 1998, Aubry et al. 2000). Thus, although the sequence of calcareous nannofossil bioevents (either the first or the last occurrence of taxa in a given stratigraphic section) is well-known across the PETM (Martini 1971, Bukry 1973, Perch-Nielsen 1985), the precise range and the reliability of the biostratigraphic markers are inadequately known. Up-to-date, important differences have been reported in the range of the species between various settings (e.g., Aubry et al. 2000, Bralower et al. 2002, Raffi et al. 2005, Agnini et al. 2007, Gibbs et al. 2006, Self-Trail et al. 2012). Furthermore, the repeated occurrence of condensation or hiatuses in both oceanic and onland settings makes the correlations difficult.

At ODP legs 198 (Site 1209, Shatsky Rise, Tropical Pacific Ocean) and 208 (Site 1263, Walvis Ridge, Southern-East Atlantic Ocean) intact composite sequences of the PETM from a wide

range of depths were recovered, providing very good material to establish a solid biostratigraphy. Site 1209 and 1263 are the shallowest sites in both Pacific and Atlantic Oceans and they are the best candidates for such a task. The close temporal succession of paleo-oceanographic and paleo-climatic events across the PETM (i.e., warming, C-isotope negative excursion, core of the event and recovery) call for a higher biostratigraphic resolution to be achieved, enabling us to more precisely date and more effectively correlate sections in various oceanic and onland areas.

Here, Sites 1209 and 1263 are compared to already published nannofossil data that we compiled, namely from the Sites 1260 (equatorial Atlantic; Mutterlose et al. 2007), 690 (South Atlantic; Bralower et al. 2002), South Dover Borehole (NW Atlantic; Self-Trail et al. 2012, Alamedilla (southern Spain; Monechi et al. 2000), and Cicogna (NE Italy; Agnini et al. 2016), TDP14 (Tanzania; Bown and Pearson 2009). All these sections and cores have been studied for calcareous nannofossil content and carbon isotope geochemistry and provide us with a supra-regional bio- and chemo-stratigraphic tool to precisely date the PETM in disparate localities.

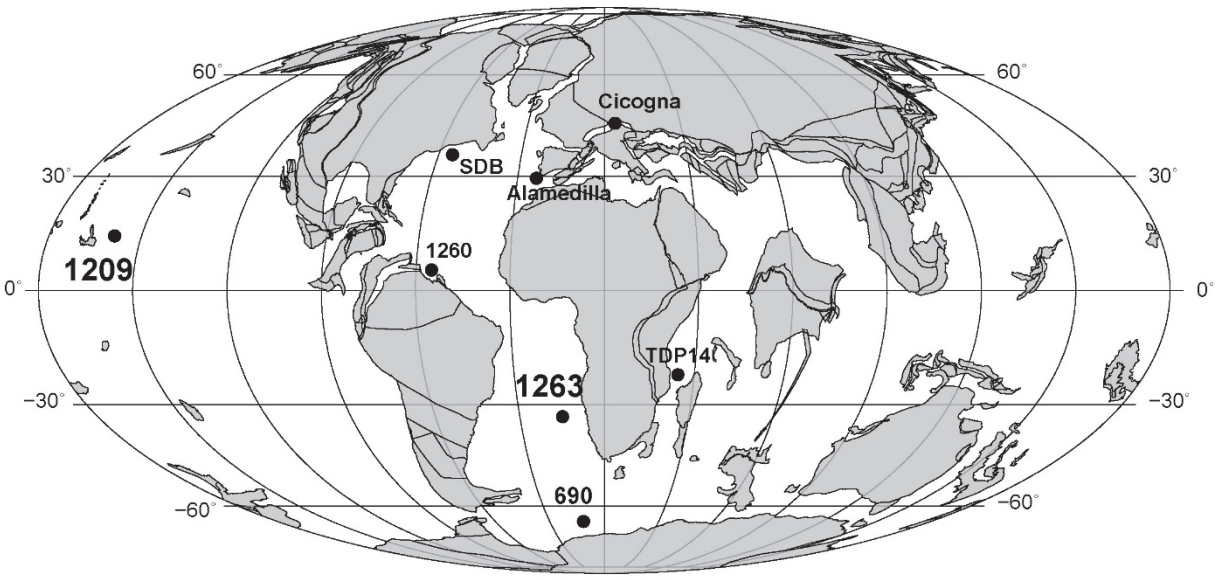


Figure 1

## 2. Materials and methods

### 2.1. Calcareous nannofossils

At Site 1209 (Fig. 1; 32°39.1'N, 158°30.4'E; 2387 water depth; 1900 paleodepth; Takeda and Kaiho 2007), we studied 20 samples over a 0.55 m interval spanning the PETM. The event lies in a ~25-cm-thick layer of clayey nannofossil ooze, with a sharp basal contact and a gradational contact with underlying and overlying chalk, respectively (Fig. 2). Samples were collected every 1-3 cm, with higher sampling rate across the PETM (1 cm). Core photos and carbonate concentration (Bralower et al., 2002; Farley, pers. comm.) are shown (Fig. 2).

At Site 1263 (Fig. 1, 28°32′S; 02°47′E; 2717 m water depth; 1500 m paleodepth; Zachos et al. 2004), we studied 30 samples over a ~2 m section spanning the PETM. The position of the site relative to the Paleocene-Eocene paleogeography is shown in Zachos et al. (2004). The PETM onset is marked by a sharp contact between grayish brown, ash-bearing clay overlying light gray nannofossil ooze. Samples were collected every 5-10 cm, with higher sampling rate across the PETM (5 cm). Given higher sedimentation rate at Site 1263 relative to Site 1209, sampling resolution between both sites is comparable. Core photos and carbonate concentration (Zachos et al. 2005) are shown (Fig. 2). Because of paucity of material in the PETM onset (~10 cm), this interval is undersampled. We analyzed the Hole 1263C between 333.61 and 335.20 rmcd, and Hole 1263D between 335.32 and 335.72 rmcd.

Calcareous nannofossil slides were prepared following the Random Settling method (Beaufort et al. 2014), slightly modified here. A cover slide was weighted before and after the settling (4 hours in a Petri-dish) of a homogeneous suspension of dry bulk sediment and water supersaturated with respect to $CaCO_3$. Water was carefully aspired with a water-pump connected to a micro-pipette to avoid any turbulence. After residual water drying, the cover slide was fixed on a microscope slide using Rhodopass B resin (Polyvinyl acetate). At least 500

nannofossils were counted in a total of 30 Fields of View (FOV) for each sample with a Leica DM750P microscope at 1000X magnification. Given the diameter of a single FOV (200 μm), the total studied area is 0.00942 $cm^2$.

Each slide was further scanned over 10 transects in order to detect the presence of rare but biostratigraphically significant species. 10 transects correspond to ~1600 FOV as we used 3.2x2.4 cm microscope slides. Each nannofossil slide was analysed twice over a year in order to check the consistency of the results.

To compare our data with previous studies, we generated relative abundance (%) data for all samples across the PETM using the formula:

$$y = \frac{n}{N} * 100 \quad (1)$$

where *y* is the relative abundance value; *n* in the number of counted specimens of a species in a slide and *N* is the total number of nannofossils counted in a slide.

On the basis of relative abundances of the species and genera, distribution charts for Site 1209 and 1263 were generated (Table 1, Table 2). Nannofossil abudances are expressed using the following notation: abundant (A, >10 %), common (C, 1-10 %), frequent (F, 1-0.1 %) and rare (R, <0.1 %).

The preservation of the studied nannofossil assemblages across the PETM at Sites 1209 and at 1263 was further investigated using a Phenom SEM G2PRO microscope. 20 samples were studied at Site 1209, and 7 at Site 1263 all across the PETM. Powdered dry bulk sediment was gently placed on a stub. The powder was then coated with gold by using a Leica EM ACE200 system.

Following Gradstein et al. (2012), the abbreviation FO (First Occurrence) is herein used for the first or stratigraphically lowest occurrence of a species in a section (or Base); LO (Last Occurrence) for the last or stratigraphically highest occurrence of a species in a section (or Top); FCO (First Consistent Occurrence) when a species previously discontinuous is recorded

in consecutive samples; LCO (Last Consistent Occurrence) when a species is no longer observed in consecutive samples; RI (Rapid Increase) for the stratigraphic horizon where a given taxon yields for the first time a relative abundance higher than 5% and maintains it throughout the subsequent samples; and RD (Rapid Decrease) when a quite common species decreases in relative abundance below the threshold of 5% (see also Ferreira et al., 2019).

### 2.2. Carbon stable isotope measurements

Stable isotope ratios of bulk-rock samples ($\delta^{13}C_{bulk\ carb}$) analyzed for their nannofossil content in the archive half of 1209B-22H-1 were determined using an autosampler MultiPrep™ system coupled to a dual-inlet GV IsoPrime™ isotope ratio mass spectrometer (IRMS) at the Laboratoire de Géologie de Lyon (Université Lyon 1). For each sample, an aliquot of about 100–500 µg (depending on the $CaCO_3$ content) of bulk-rock samples was reacted with anhydrous oversaturated phosphoric acid at 90°C for 20 min. Carbon isotope compositions are quoted in the δ notation inper mil (‰) relative to Vienna Pee Dee Belemnite standard (V-PDB). All samples were measured in duplicate and normalized to the VPDB scales with an in-house working standard Carrara Marble (CAM, $\delta^{13}C_{V\text{-}PDB}$ = 2.025) and international reference standards analyzed during the same session. The CAM was normalized with the international references NIST NBS19 limestone ($\delta^{13}C_{V\text{-}PDB}$ = +1.95‰) and NBS18 carbonatite ($\delta^{13}C_{V\text{-}PDB}$ = -5.01‰). External reproducibility is better than ±0.05 ‰ for $\delta^{13}C$ values (2 σ).

| Site | Hole | Core | Section | Interval | Depth relatively to LC | $\delta^{13}C_{bulk\ rock}$ | $\delta^{13}C_{bulk\ rock}$ SD | *Bomolithus aquilus* | *Bomolithus megastypus* | *Bomolithus supremus* | *Braarudosphaera* spp. | *Campylosphaera dela* | *Campylosphaera eodela* | *Coccolithus bownii* | *Coccolithus spp.* | *Cruci.+ Chiasmolithus* spp. | *Discoaster araneus* | *Discoaster multiradiatus* | *Discoaster salisburgensis* | *Discoaster* spp. |
|---|---|---|---|---|---|---|---|---|---|---|---|---|---|---|---|---|---|---|---|---|
| | | | | cm | m | ‰ | ‰ | | | | | | | | | | | | | |
| 1209 | B | 22H | 1A | 90-91 | 0.42 | 1.94 | 0.04 | R | | | | F | F | F | A | F | F | C | F | C |
| 1209 | B | 22H | 1A | 95-96 | 0.37 | 1.90 | 0.00 | | F | | | F | | F | A | F | F | C | | C |
| 1209 | B | 22H | 1A | 100-101 | 0.32 | 1.81 | 0.02 | | | | | F | F | F | A | F | F | C | | C |
| 1209 | B | 22H | 1A | 105-106 | 0.27 | 1.63 | 0.03 | R | F | | | F | F | F | A | F | F | C | | C |
| 1209 | B | 22H | 1A | 110-111 | 0.22 | 1.47 | 0.05 | R | | | C | C | F | C | A | F | C | C | | C |
| 1209 | B | 22H | 1A | 115-116 | 0.17 | 1.09 | 0.02 | | F | | C | F | | C | | F | F | C | F | C |
| 1209 | B | 22H | 1A | 120-121 | 0.12 | 1.00 | 0.02 | | F | | | F | F | C | A | C | F | C | F | C |
| 1209 | B | 22H | 1A | 125-126 | 0.07 | 0.39 | 0.03 | | | | | F | F | C | A | C | C | C | F | C |
| 1209 | B | 22H | 1A | 129-130 | 0.03 | 0.28 | 0.00 | | F | R | | F | | C | A | C | C | C | | F |
| 1209 | B | 22H | 1A | 130-131 | 0.02 | 0.47 | 0.00 | | F | F | | F | F | C | A | C | C | C | | C |
| 1209 | B | 22H | 1A | 131-132 | 0.01 | 1.02 | 0.03 | | F | | | F | F | C | A | C | C | C | | C |
| 1209 | B | 22H | 1A | 132-133 | 0 | 2.36 | 0.04 | | | F | | F | | | A | C | F | C | | C |
| 1209 | B | 22H | 1A | 133-134 | -0.01 | 2.34 | 0.03 | | F | | | C | F | C | A | F | C | C | | C |
| 1209 | B | 22H | 1A | 134-135 | -0.02 | 2.72 | 0.06 | | | | | F | F | C | A | F | F | C | | C |
| 1209 | B | 22H | 1A | 135-136 | -0.03 | 2.62 | 0.01 | | F | | | F | | F | A | C | C | C | | C |
| 1209 | B | 22H | 1A | 136-137 | -0.04 | 2.41 | 0.03 | | F | | | F | F | F | A | C | | C | | C |
| 1209 | B | 22H | 1A | 137-138 | -0.05 | 2.65 | 0.07 | | | | | C | F | | A | F | | C | | C |
| 1209 | B | 22H | 1A | 140-141 | -0.08 | 2.81 | 0.02 | | F | | | F | F | | A | C | | C | | C |
| 1209 | B | 22H | 1A | 142-143 | -0.1 | 2.82 | 0.02 | | F | | | | F | | A | F | | C | | C |
| 1209 | B | 22H | 1A | 145-146 | -0.13 | 2.82 | 0.02 | | F | R | | F | F | | A | F | | C | | C |

| Site | Hole | Core | Section | Interval | *Ericsonia* spp. | base/top *Fasciculithus* | *Fasciculithus clinatus* | *Fasciculithus involutus* | *Fasciculithus richardii* group | *Fasciculithus thomasii* | *Fasciculithus tympaniformis* | *Rhomboaster calcitrapa* group | *Rhomboaster cuspis* | *Sphenolithus* spp. | *Toweius + Prinsius* spp. | *Tribrachiatus bramlettei* | *Thoracosphaera* spp. | *Z. bijugatus* | Other nannofossils | Reworking Cretaceous |
|---|---|---|---|---|---|---|---|---|---|---|---|---|---|---|---|---|---|---|---|---|
| | | | | cm | | | | | | | | | | | | | | | | |
| 1209 | B | 22H | 1A | 90-91 | A | C | F | F | | F | F | R | F | C | A | F | F | C | C | |
| 1209 | B | 22H | 1A | 95-96 | A | C | | F | | | F | | F | C | A | F | F | C | C | |
| 1209 | B | 22H | 1A | 100-101 | A | C | F | C | | | C | | F | C | C | F | C | C | C | |
| 1209 | B | 22H | 1A | 105-106 | C | C | F | F | | | F | R | F | C | C | | F | A | C | |
| 1209 | B | 22H | 1A | 110-111 | A | C | F | C | | F | C | | F | A | C | | F | A | C | |
| 1209 | B | 22H | 1A | 115-116 | A | C | F | F | F | | F | | F | C | A | F | C | A | C | |
| 1209 | B | 22H | 1A | 120-121 | A | C | F | C | F | | C | R | F | C | C | | C | A | C | |
| 1209 | B | 22H | 1A | 125-126 | C | C | | F | C | F | F | | | C | C | F | C | C | C | |
| 1209 | B | 22H | 1A | 129-130 | C | C | F | C | C | | C | | F | C | C | | C | F | A | |
| 1209 | B | 22H | 1A | 130-131 | C | C | F | C | C | | C | R | F | C | C | F | C | F | C | C |
| 1209 | B | 22H | 1A | 131-132 | C | C | F | C | C | F | C | | | A | C | | C | C | C | C |
| 1209 | B | 22H | 1A | 132-133 | A | C | C | C | C | F | C | | | C | C | | F | F | C | F |
| 1209 | B | 22H | 1A | 133-134 | A | C | F | C | C | F | C | | F | C | C | | F | C | C | F |
| 1209 | B | 22H | 1A | 134-135 | A | C | F | C | C | C | C | | | C | C | | | F | C | F |
| 1209 | B | 22H | 1A | 135-136 | A | C | F | C | C | | C | | F | C | C | | F | F | C | |
| 1209 | B | 22H | 1A | 136-137 | A | C | F | C | C | F | C | | | C | C | | F | F | C | F |
| 1209 | B | 22H | 1A | 137-138 | A | C | F | C | C | F | C | | | C | C | | F | F | C | |
| 1209 | B | 22H | 1A | 140-141 | A | C | F | C | C | F | C | | | C | C | | | F | C | |
| 1209 | B | 22H | 1A | 142-143 | A | C | F | C | C | F | C | | | C | C | | F | F | C | |
| 1209 | B | 22H | 1A | 145-146 | A | C | F | C | C | | C | | | C | C | | | F | C | |

168

Table 1

| Site | Hole | Core | Section | Interval (cm) | Rmcd (m) | Depth to LC (m) | *Bomolithus megastypus* | *Bomolithus supremus* | *Calciosolenia aperta* | *Camplyosphaera dela* | *Camplyosphaera eodela* | *Cruci.* + *Chiasmolithus* spp. | *Coccolithus bownii* | *Coccolithus* spp. | *Discoaster araneus* | *Discoaster multiradiatus* | *Discoaster* spp. | *Fasciculithus involutus* | *Fasciculithus richardii* group | *Fasciculithus tympaniformis* | *Rhomboaster calcitrapa* gr. | *Rhomboaster cuspis* | *Sphenolithus* spp. | *Toweius*+*Prinsius* spp. | *Tribrachiatus bramlettei* | *Zygrhablithus* spp. | Other nannofossils |
|---|---|---|---|---|---|---|---|---|---|---|---|---|---|---|---|---|---|---|---|---|---|---|---|---|---|---|---|
| 1263 | C | 14H | 1A | 129-130 | 333.61 | 1.66 | R | | | C | F | C | | A | | C | C | C | | C | R | F | F | A | F | A | C |
| 1263 | C | 14H | 1A | 139-140 | 333.71 | 1.56 | | | | C | | C | | A | | C | C | C | | C | | | F | A | | A | C |
| 1263 | C | 14H | 1A | 149-150 | 333.81 | 1.46 | R | | | C | F | C | F | A | | C | C | C | | C | | | F | A | F | A | C |
| 1263 | C | 14H | 2A | 09-10 | 333.90 | 1.37 | R | | | C | F | C | F | A | C | C | C | A | | C | | F | F | A | | A | C |
| 1263 | C | 14H | 2A | 19-20 | 334.00 | 1.27 | | | F | F | | F | F | A | F | C | F | C | | C | | F | F | A | F | A | C |
| 1263 | C | 14H | 2A | 29-30 | 334.10 | 1.17 | R | | F | C | F | C | F | A | F | C | F | C | | C | | F | F | A | F | A | C |
| 1263 | C | 14H | 2A | 39-40 | 334.20 | 1.07 | R | | | C | F | C | F | A | F | C | F | C | | C | | F | F | A | | A | C |
| 1263 | C | 14H | 2A | 49-50 | 334.30 | 0.97 | | | | C | F | C | F | A | | C | C | C | F | C | R | C | F | A | F | A | C |
| 1263 | C | 14H | 2A | 59-60 | 334.40 | 0.87 | R | | F | C | F | C | F | A | F | C | C | C | F | C | | F | A | A | | A | C |
| 1263 | C | 14H | 2A | 69-70 | 334.50 | 0.77 | R | | | F | F | F | F | A | F | C | C | C | A | C | R | F | C | A | | C | C |
| 1263 | C | 14H | 2A | 79-80 | 334.60 | 0.67 | R | | F | C | F | C | F | A | F | C | F | C | A | A | | F | C | A | | C | C |
| 1263 | C | 14H | 2A | 89-90 | 334.70 | 0.57 | | | | F | F | F | F | A | C | C | C | A | A | A | | F | C | A | | C | C |
| 1263 | C | 14H | 2A | 99-100 | 334.80 | 0.47 | R | | | F | F | F | F | A | C | A | C | A | A | A | | | C | A | | C | C |
| 1263 | C | 14H | 2A | 104-105 | 334.85 | 0.42 | R | | | C | | C | F | A | C | C | C | A | A | A | R | F | A | A | | C | C |
| 1263 | C | 14H | 2A | 109-110 | 334.90 | 0.37 | | | | C | | F | C | A | C | C | C | A | A | A | | | C | C | | C | C |
| 1263 | C | 14H | 2A | 114-115 | 334.95 | 0.32 | R | | | F | F | F | F | A | F | C | F | A | A | A | | | C | A | | C | C |
| 1263 | C | 14H | 2A | 119-120 | 335.00 | 0.27 | R | | | F | F | F | F | A | F | C | C | A | A | A | R | F | C | A | | C | C |
| 1263 | C | 14H | 2A | 124-125 | 335.05 | 0.22 | R | | F | C | | C | F | A | C | C | F | C | C | C | | F | A | A | | F | C |
| 1263 | C | 14H | 2A | 129-130 | 335.10 | 0.17 | | R | | C | F | C | F | A | F | C | C | C | C | C | | | C | A | | C | F |
| 1263 | C | 14H | 2A | 134-135 | 335.15 | 0.12 | R | | | F | F | F | F | A | F | C | C | C | C | C | | R | C | A | | C | C |
| 1263 | C | 14H | 2A | 139-140 | 335.20 | 0.07 | R | | | C | | C | F | A | C | A | C | C | A | C | | | C | A | | C | C |
| 1263 | D | 4H | 1A | 72-73 | 335.32 | -0.05 | | R | C | C | | C | F | A | | A | C | C | C | C | | | C | A | | C | C |
| 1263 | D | 4H | 1A | 77-78 | 335.37 | -0.10 | R | | C | C | | C | F | A | | C | C | C | C | C | | | C | A | | C | C |
| 1263 | D | 4H | 1A | 82-83 | 335.42 | -0.15 | R | | | C | | C | F | A | | C | C | C | C | C | | | C | A | | C | C |
| 1263 | D | 4H | 1A | 87-88 | 335.47 | -0.20 | | R | | C | | C | F | A | | C | F | C | C | C | | | C | A | | C | A |
| 1263 | D | 4H | 1A | 92-93 | 335.52 | -0.25 | R | | | C | | C | | A | | C | C | C | C | C | | | C | A | | C | C |
| 1263 | D | 4H | 1A | 97-98 | 335.57 | -0.30 | | | | C | | C | | A | | C | C | C | C | C | | | C | A | | C | C |
| 1263 | D | 4H | 2A | 02-03 | 335.62 | -0.35 | R | | | C | | C | | A | | C | C | | C | C | | | C | A | | C | C |
| 1263 | D | 4H | 2A | 07-08 | 335.67 | -0.40 | R | R | | C | | C | | A | | C | C | F | C | F | | | C | A | | C | C |
| 1263 | D | 4H | 2A | 12-13 | 335.72 | -0.45 | R | | | F | | F | | A | | C | C | C | C | C | | | C | A | | C | C |

Table 2

## 3. Results

### 3.1. Preservation and assemblages at Site 1209 and Site 1263

At Site 1209, optical (OM) and Scanning Electron Microscope (SEM) pictures (Plates 1 to 3) reveal an overall good preservation, with the contemporaneous presence of limited etching (mainly on coccoliths) and overgrowth effects (mainly on fasciculiths and discoasters). A slight deterioration in nannofossil preservation occurs between 1 cm below and above the Lithological Contact (LC), as previously suggested by Bralower et al. (2014). In those samples, etching prevails consistently with the concomitant maximum in nannofossil fragmentation. At Site 1263, nannofossil preservation is moderate to good, but in a 6-cm thick interval from 0 to 6 cm above the LC, dissolution occurred as previously observed (Raffi et al. 2009). Although most of the coccoliths and nannoliths we observed in OM as well in SEM are moderately- to well-preserved, strongly etched specimens may coexist with fairly well preserved specimens in the same sample.

Calcareous nannofossil assemblages at both localities are similar in terms of percentage of different genera, although little disparities. Assemblages across the PETM at Site 1209 are rich except from the interval 1 cm below and 1 cm above the PETM. Assemblages are dominated by *Coccolithus* (abundant; Table 1) and *Ericsonia* (abundant) accompanied by *Toweius* (common to abundant). *Ericsonia* rapidly decreased from abundant to common at the onset of PETM. The rest of the assemblage is dominated by *Fasciculithus* (common to frequent), *Discoaster* (common) and *Sphenolithus* (common). *Zygrhablithus* rapidly increases from frequent to common 7 cm above the onset of PETM. Concomitantly, *Fasciculithus* decreases from common to frequent, as previously observed (Gibbs et al. 2006). These changes are not related with dissolution, as other robust taxa (e.g., *Discoaster* and *Sphenolithus*) do not increase in abundance.

At Site 1263, *Coccolithus* dominate the placolith-coccoliths (abundant; Table 2) as well as *Toweius* (abundant). Small *Ericsonia* referred to as *E. orbis* (Bown et al. 2016) are present but never reach abundance as high as at Site 1209. The rest of the assemblage is dominated by *Fasciculithus* (abundant to common), *Discoaster* (common) and *Sphenolithus* (common).. *Zygrhablithus* rapidly increases from common to abundant 0.87 cm above the onset of PETM, alongside a *Fasciculithus* decrease from abundant to common as previously reported (Raffi and De Bernardi 2008). These changes are not attributed to dissolution, as other robust taxa (e.g., *Discoaster* and *Sphenolithus*) do not increase in abundance.

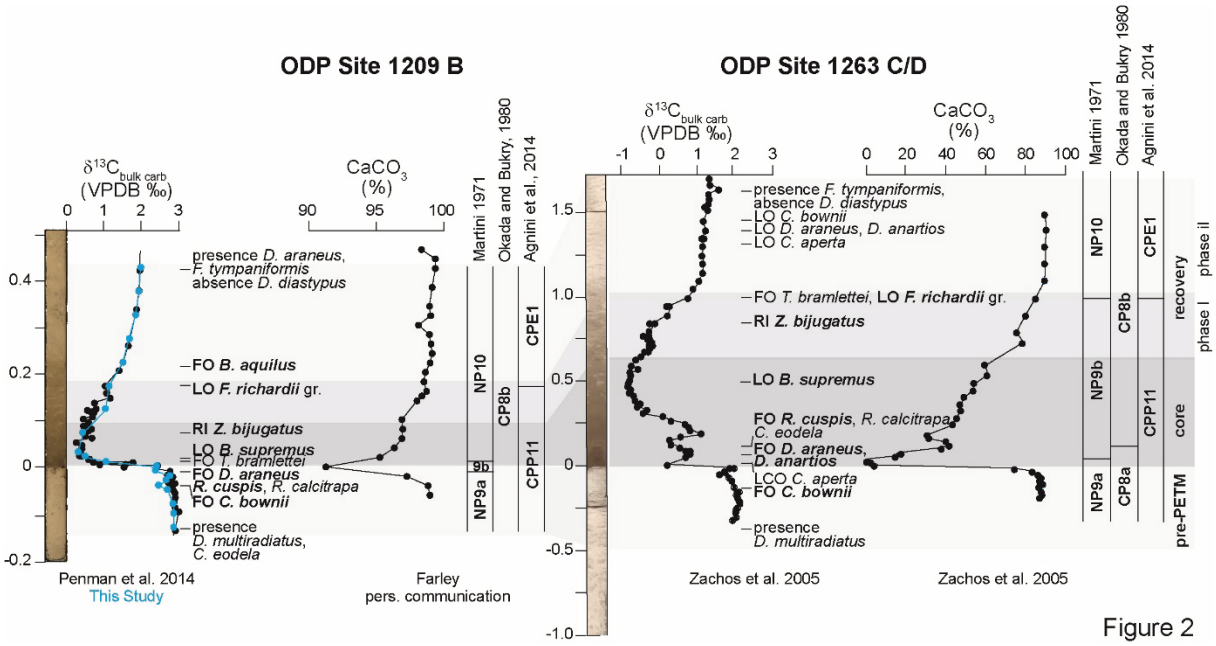


Figure 2

## 3.2. Biostratigraphy

Calcareous nannofossils biostratigraphy of late Paleocene and early Eocene is mostly based on standard zonations of Martini (1971) and Okada and Bukry (1980). Recent studies propose to subdivide the NP9 and NP10 of Martini (1971) in several subzones (Aubry et al. 1996, 1999) in order to improve the biostratigraphic resolution around the Paleocene/Eocene. Agnini et al. (2014) published a new biozonation frame for the Paleogene for low and middle latitudes. In order to effectively compare the results from the two sites, we express our data in function of

213 the depth below the LC, which marks the onset of the PETM. The biozonation of the two
214 sections is established following the different reference biozonations cited above.
215
216 **3.2.1. ODP Site 1209**
217 Several events were recorded spanning the Paleocene-Eocene transition (Fig. 2). *Discoaster*
218 *multiradiatus* and *Campylosphaera eodela* are present in the assemblage from the lowermost
219 sample. *Coccolithus bownii* first occurs at -0.04 m, just below the negative carbon excursion
220 marking the onset of the PETM. The very onset of the PETM is characterized by the FO of
221 *Discoaster araneus* in the same sample as *Rhomboaster cuspis* and *Rhomboaster calcitrapa* (-
222 0.03 m), shortly followed by the FO of *Tribrachiatus bramlettei* (0.02 m). The LO of
223 *Bomolithus supremus* is at 0.03 m. The RI of *Zygrhablithus bijugatus* (>5%) is observed at 0.07
224 m. The LO of *Fasciculithus richardii* group (see Appendix 1) at 0.17 m marks the inflexion of
225 $\delta^{13}C_{bulk\ carb}$ curve between the end of the PETM negative excursion and the return to steady
226 values. The uppermost part of the studied interval is characterized by the presence of *D. araneus*
227 and *Fasciculithus tympaniformis*, but the absence of *Discoaster diastypus* (Fig. 2).
228 The lower part of the section (-0.13 m to 0.01 m) is dated NP9 (Martini 1971) because of the
229 presence of *D. multiradiatus* from the lowermost sample and the absence of *T. bramlettei*.
230 Based on Aubry et al. (1999), who subdivided the NP9 of Martini (1971) into two subzones,
231 we attribute the lowest part of the section (-0.13 to -0.02 m) to the NP9a because of the presence
232 of *D. multiradiatus* and the FOs of *R. calcitrapa*, *D. araneus* and *D. anartios* at -0.03 m. From
233 -0.03 to 0.01 m, the section is dated NP9b (Aubry et al. 1996). According to Agnini et al. (2014),
234 the lower part of the section (-0.13 m to 0.17 m) is dated CNP11 because of the presence of *D.*
235 *multiradiatus* from the lowermost sample and the LO of *F. richardii* group in sample 1209B-
236 22H-1-115-116 (0.17 m).

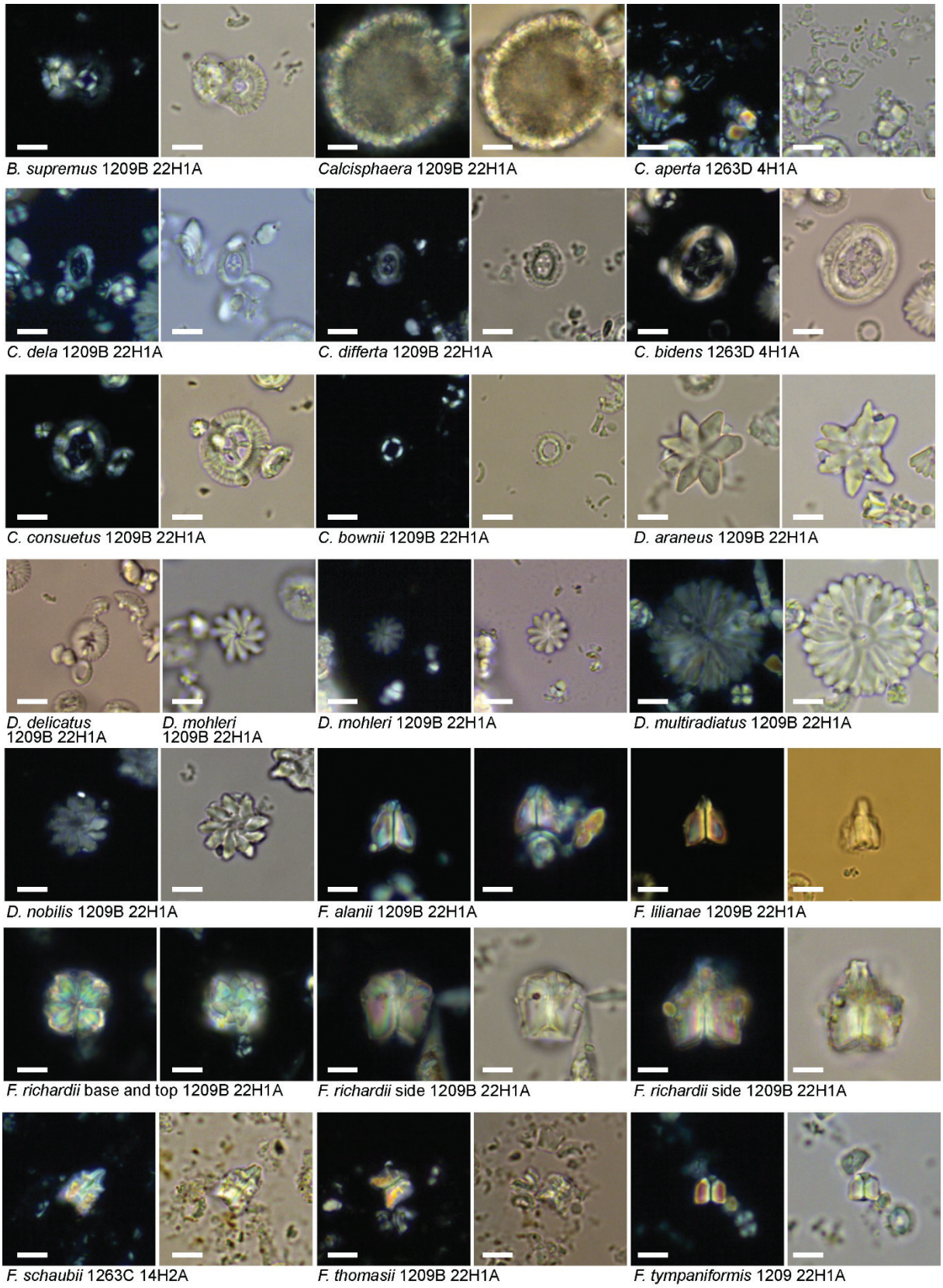
*B. supremus* 1209B 22H1A
*Calcisphaera* 1209B 22H1A
*C. aperta* 1263D 4H1A
*C. dela* 1209B 22H1A
*C. differta* 1209B 22H1A
*C. bidens* 1263D 4H1A
*C. consuetus* 1209B 22H1A
*C. bownii* 1209B 22H1A
*D. araneus* 1209B 22H1A
*D. delicatus* 1209B 22H1A
*D. mohleri* 1209B 22H1A
*D. mohleri* 1209B 22H1A
*D. multiradiatus* 1209B 22H1A
*D. nobilis* 1209B 22H1A
*F. alanii* 1209B 22H1A
*F. lilianae* 1209B 22H1A
*F. richardii* base and top 1209B 22H1A
*F. richardii* side 1209B 22H1A
*F. richardii* side 1209B 22H1A
*F. schaubii* 1263C 14H2A
*F. thomasii* 1209B 22H1A
*F. tympaniformis* 1209 22H1A

237

Plate 1

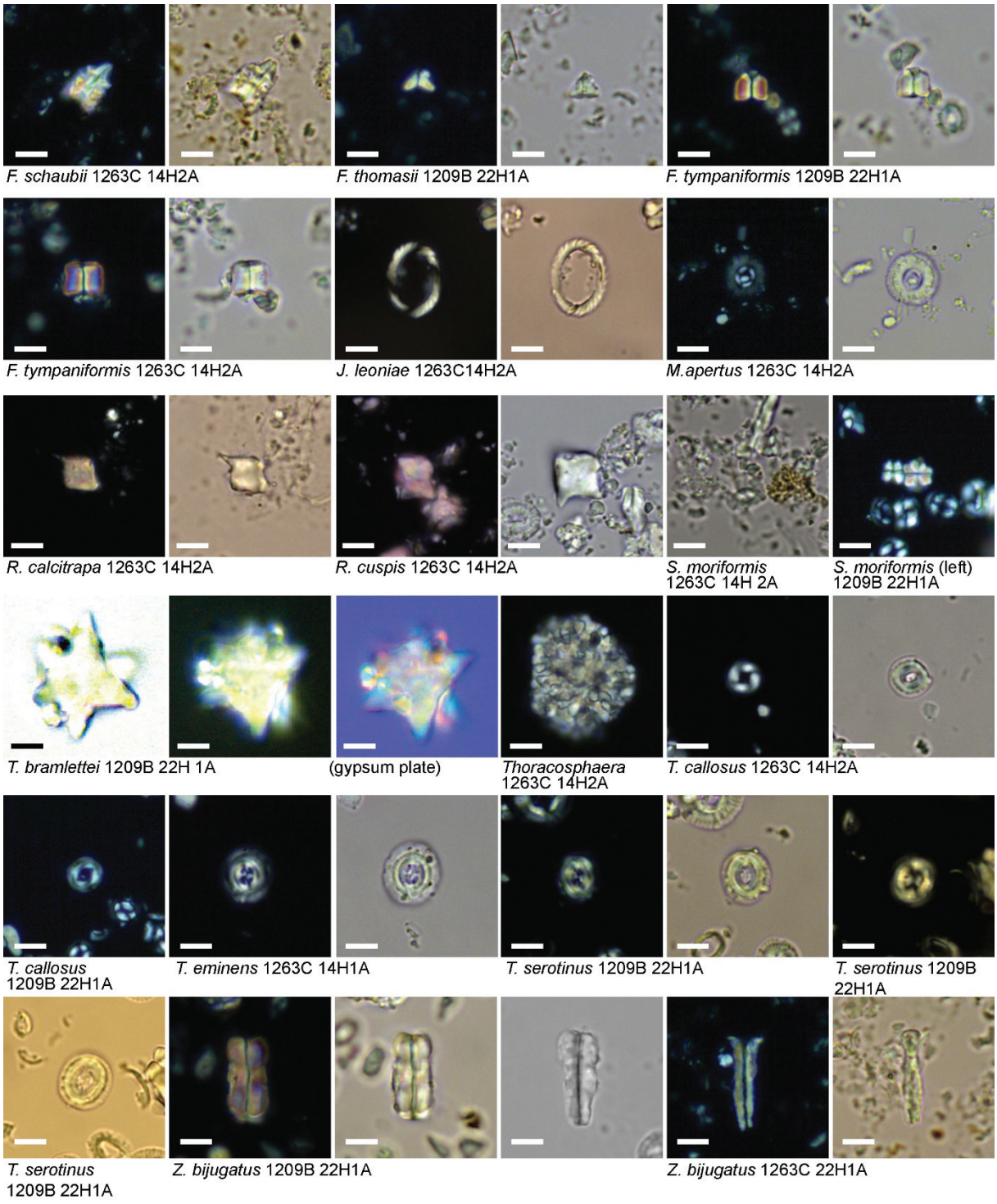


Plate 2

238

239

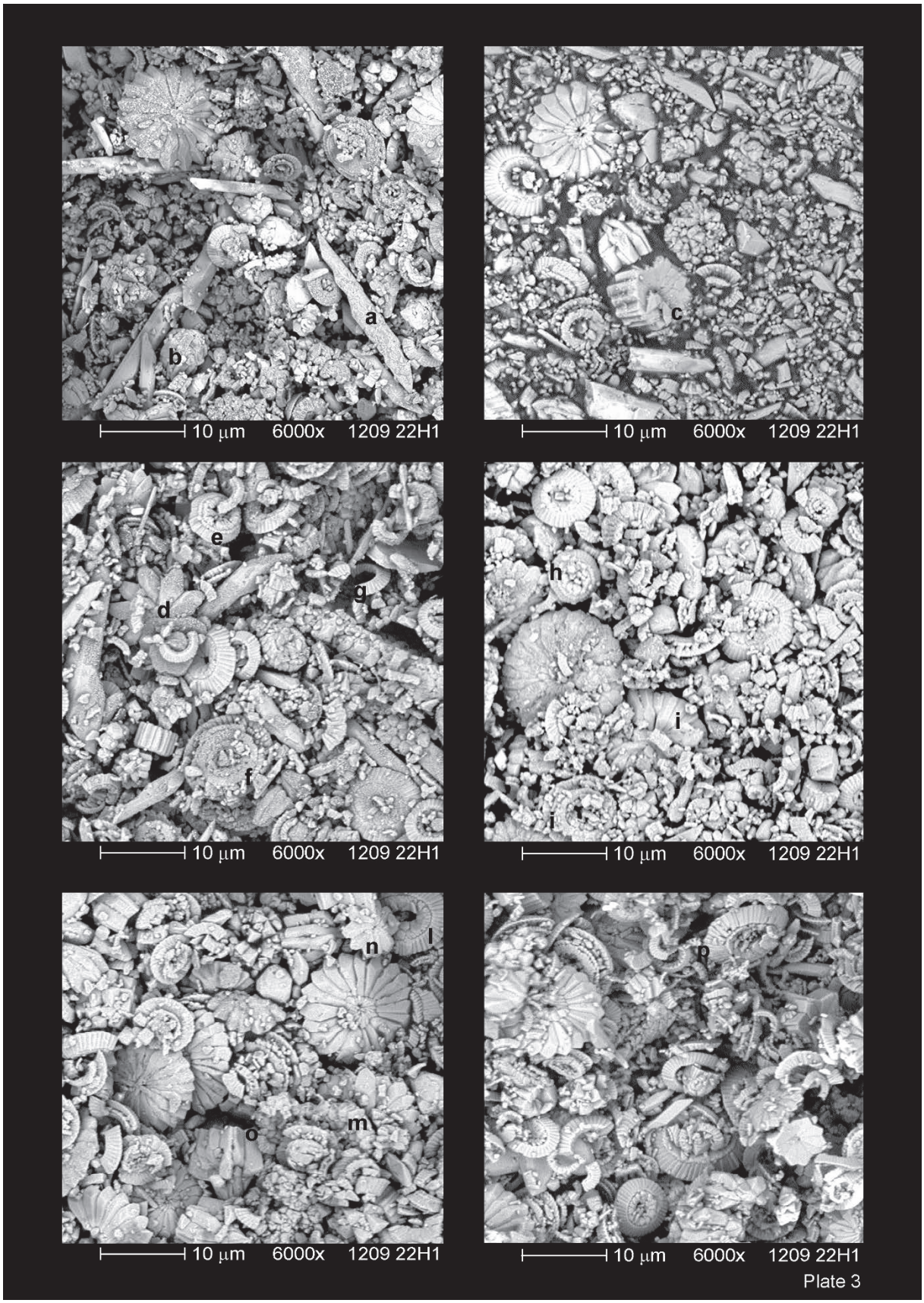
a
b
10 µm 6000x 1209 22H1
c
10 µm 6000x 1209 22H1
e
d
g
f
10 µm 6000x 1209 22H1
h
i
i
10 µm 6000x 1209 22H1
n
l
o
m
10 µm 6000x 1209 22H1
p
10 µm 6000x 1209 22H1
Plate 3

240

241

242 The interval comprised between 0.02 to 0.42 m is dated NP10 because of the FO of *T. bramlettei*
243 in sample 1209B-22H-1-130-131 and the absence of *Tribrachiatus contortus* in the uppermost
244 studied sample, whose FO marks the base of NP11. According to Aubry et al. (1996), this
245 interval corresponds to NP10a because of the absence of *Tribrachiatus digitalis*, whose FO
246 marks the base of NP10b. The upper part of the section (1.07-0.42 m) is dated CNE1 because
247 of the LO of *F. richardii* group (0.97 m) and the presence of *F. tympaniformis* in the uppermost
248 studied sample. According to Okada and Bukry (1980), the whole studied section is dated to
249 CP8b because of the presence of *D. multiradiatus*, *C. eodela* from the lowermost sample and
250 the absence of *D. diastypus* in the upper part of the studied section.
251
252 **3.2.2. ODP Site 1263**
253 Similar to Site 1209, *D. multiradiatus* is present from the base of the studied interval at Site
254 1263 (Fig. 2). The FO of *C. bownii* at -0.20 m also lies just below the negative carbon excursion
255 marking the onset of the PETM. The FOs of *D. araneus* and *D. anartios* are recorded at 0.07
256 m, at the onset of the PETM. Conversely, *C. eodela* is not present from the base of the studied
257 interval, but first occurs in the same sample as *R. cuspis*, at 0.12 m. The LO of *B. supremus* is
258 at 0.27 m. The RI of *Z. bijugatus* (>5%) is observed at 0.87 m, above the core of the PETM, in
259 an interval comparable to Site 1209. Also, similar to Site 1209, the LO of *F. richardii* group
260 (0.97 m) occurs in the interval where the inflexion of the $\delta^{13}C_{bulk\ carb}$ curve occurs, between the
261 end of the PETM negative excursion and the return to steady values. The FO of *T. bramlettei*
262 (0.97 m) is conversely very different from the Site 1209. In the upper part of the studied interval,
263 the successive LOs of *Calcisolenia aperta* (1.27 m) and of *D. araneus* and *D. anartios* (1.37
264 m) are recorded.
265 The NP9 zone (-0.45 to 0.87 m) is recognized because of the presence of *D. multiradiatus* from
266 the lowermost sample until the FO of *T. bramlettei* (0.97 m). Based on the subdivision of this

zone by Aubry et al. (1999), the NP9a subzone is recognized until the FOs of *D. araneus* and *D. anartios* (-0.45 to -0.05 m). From 0.07 to 0.87 m the section is dated NP9b (Aubry et al. 1996) until the FO of *T. bramlettei* (0.97 m). According to the zonation of Okada and Bukry (1980), the interval from -0.45 m to 0.07 m is dated CP8a because of the presence of *D. multiradiatus* from the lowermost sample until the FO of *C. eodela* (0.12 m). According to Agnini et al. (2014), the interval from -0.45 to 0.97 m is dated CNP11 because of the LO of *F. richardii* group in sample 1263C-14-2A-49-50 (0.97 m). The upper part of the section (0.97 to 1.66 m) is dated NP10 because of the FO of *T. bramlettei* in sample 1263C-14-2A-49-50 and the absence of *T.contortus* and of *T. digitalis*. The interval from 0.12 to 1.66 m is dated CP8b (Okada and Bukry 1980) because of the FO of *C. eodela* in sample 1263C-14-2A-134-135 (0.12 m) and the absence of *D. diastypus* in the upper part of the studied section. The upper part of the section (1.07 to 1.66 m) is dated CNE1 (Agnini et al. 2014) because of the absence of *F. richardii* group and the presence of *F. tympaniformis*.

### 3.3. Carbon isotopes at Sites 1209

We have measured the $\delta^{13}C_{bulk\ carb}$ on the samples analysed for their calcareous nannofossil content from the archive half of core 22H of Site 1209B to anchor them stratigraphically to already published $\delta^{13}C_{bulk\ carb}$ measurements (See Table 1). These measurements indicate that the working half has been offset downward by 25 mm relative to the archive half, consistently with the downward offset of 25 mm relative to the archive half during sampling mentioned in Colosimo et al. (2006). The depths of the samples investigated in this study have therefore been shifted downward by a constant offset of 25 mm to facilitate comparisons with previously published data.

In agreement with previously published $\delta^{13}C_{bulk\ carb}$ data (Colosimo et al. 2006, Penman et al. 2014), values are stable between -0.2 and 0 m with respect to the LC and range from 2.82 to

292 2.34 ‰. From 0 to 0.3 m, values drastically decrease to 0.28 ‰, with a 2 ‰ negative excursion.
293 Values stay low still up 0.10 m then recover from 0.10 to 0.40 m.
294 The $\delta^{13}C_{bulk\ carb}$ curve of Paleocene-Eocene interval has been published by Zachos et al. (2005).
295 The $\delta^{13}C_{bulk\ carb}$ trend is the same as Site 1263, but the values record a general offset of ~0.8‰
296 with respect to Site 1209.
297
298 **4. Discussion**
299
300 In order to check the reproducibility of nannofossil events and biostratigraphy from Sites 1209
301 and 1263, we compiled a synthesis of eight already published sections located in different
302 paleoceanographic settings and from several basins around the world, from low to high latitudes
303 across the PETM (Fig. 1). All the sections dispose of $\delta^{13}C$ isotopes measured on bulk-rock
304 samples ($\delta^{13}C_{bulk\ carb}$), besides detailed biostratigraphic data. The data used for comparison
305 come from Sites 690 (Southern Atlantic Ocean; Bralower 2002), 1260 (Equatorial Atlantic
306 Ocean; Mutterlose et al. 2007), that yield a reliable picture of open ocean records of the PETM.
307 The sections providing a PETM record in shelf areas are: South Dover Bridge (SDB; New
308 Jersey Coastal Plain; Self-Trail et al. 2012), Alamedilla (South-Spain; Monechi et al. 2000) and
309 Cicogna (North-Italy; Agnini et al. 2016), all of them being located in the Tethys Ocean, and
310 the Tanzania Drilling Project core 14 (TDP14; Bown and Pearson 2009). For TDP14 Site we
311 integrate $\delta^{13}C$ isotopes measured on *n*-alkanes because the CIE is not well expressed on bulk
312 rock (Handley et al. 2008, Aze et al. 2014).
313 Magnetostratigraphy is available for all the studied sections and shows that PETM encompasses
314 magnetochron C24r of Cande and Kent (1995) (see also Ali et al. 2000, Aubry et al. 2000,
315 Erbacher et al. 2004, Westerhold et al. 2007, Dallanave et al. 2009).

316 Differences and similarities between these sections provide us with a synthetic bio-
317 chemostratigraphic framework across the event (Fig. 3). A new biostratigraphic subdivision is
318 proposed here based on calcareous nannofossil FO and LO horizons, and on changes in
319 assemblage composition. These include RI and RD of taxa. Also, FCO and LCO and switchover
320 effects between taxa are taken into account.
321
322 **4.1. Age model**
323 Carbon isotope stratigraphy is extensively used to correlate upper Paleocene-lower Eocene
324 stratigraphic sections. Many records of magnetochron C24r have been "tuned" using the C-
325 isotope excursions (assumed to represent the CIE) but purposely avoiding biostratigraphic
326 datums because they are assumed to be somehow diachronous in nature (e.g., Pak and Miller
327 1992, Zachos el al. 1993, Thomas and Shackleton. 1996, Pak et al. 1997). However, a
328 comprehensive synthesis of nannofossil events and the carbon isotope curves in order to obtain
329 a precise overview and explain the supposed diachronism has never been attempted. Here, we
330 present the stratigraphic position of each event plotted against the $\delta^{13}C_{bulk\ carb}$ profiles of
331 different sites. Despite the broad similarities, the studied sites reveal marked differences in the
332 overall shape of their $\delta^{13}C$ profiles (Fig. 3). The most striking difference relates to the shape
333 and amplitude of the negative $\delta^{13}C_{bulk\ carb}$ excursion spanning the core of the PETM. This
334 excursion is indeed almost symmetrical at Alamedilla and Cicogna sections, but appears highly
335 asymmetrical at the other sites considered, where the negative $\delta^{13}C_{bulk\ carb}$ excursion is very
336 sharp. Assuming a comparable $\delta^{13}C_{bulk\ carb}$ variation in oceanic waters in times of global
337 perturbations, although local paleoceanography may produce isotopic offsets, the $\delta^{13}C_{bulk\ carb}$
338 values of the considered sites were compared to that of Alamedilla and Cicogna where the CIE
339 onset is more gradual (Fig. 3). This comparison clearly shows a very good consistency of
340 $\delta^{13}C_{bulk\ carb}$ values between the sites if considering the existence of unconformities. In particular,

341 the sharp negative shift toward negative $\delta^{13}C_{bulk\ carb}$ values in all the sites but Alamedilla and
342 Cicogna, most likely indicate very reduced sedimentation rates related to dissolution intervals
343 (i.e., Aubry et al. 2000, McCarren et al. 2008, Storme et al. 2012). Also, a major unconformity
344 is recorded in the recovery interval at South Dover and TDP14. Although the PETM has already
345 been reported as a period when sedimentary discontinuities did occur (e.g., Aubry et al. 2000)
346 the impact of such unconformities on biostratigraphic record has never been explored in detail
347 before.
348 The age model of Röhl et al. (2007) was applied. The authors proposed a state-of-the-art age
349 model for the PETM derived from a orbital chronology developed with cycle stratigraphic
350 records from sites drilled during ODP Leg 208 (Walvis Ridge, South-eastern Atlantic)
351 integrated with already published records from Site 690 (Weddell Sea, Southern Ocean, ODP
352 Leg 113). Bains et al. (1999) defined some carbon isotope tie points (from -B to H) from the
353 isotopic record at Site 690 and this nomenclature was adopted for tuning Site 1263 (Röhl et al.
354 2007). Here we integrate in Figure 3 the tie points defined by Röhl et al. (2007) for Site 690.
355 Ages are defined relatively to the PETM onset, fixed at 0 kyrs. On the basis of the previous
356 assumptions, we define four time intervals in agreement to Röhl et al. (2007) (Fig. 3): 1) the
357 pre-PETM prior to 0 kyrs; 2) the core of the PETM; 3) the recovery phase I; and 4) recovery
358 phase II. These intervals are tightly linked to the $\delta^{13}C_{bulk\ carb}$ profile across the event, as defined
359 by Zachos et al. (2005).
360 No detailed astrochronology exists for the PETM interval recovered during Leg 198 at Shatsky
361 Rise, as obliquity and precession-related cycles are not obvious due to low sedimentation rate
362 and bioturbational smoothing (Westerhold et al. 2008, Westerhold et al. 2018). Previous PETM
363 age models for ODP Site 1209 were therefore established using stable isotope correlations with
364 Atlantic Ocean and Southern Ocean sites (ODP Sites 1263 and 690).
365

366 **4.2. Calcareous nannofossil bioevents across the PETM at Sites 1209 and 1263**

367 Both Sites 1209 and 1263 represent a very good biostratigraphic record of the PETM interval.
368 Although the accumulation rate is almost twice at Site 1263 with respect to 1209, a very similar
369 succession of biostratigraphic events is observed in both sites. These events (in bold; Fig. 2)
370 seem therefore to be very reproducible because they occur in comparable intervals from remote
371 sites, both in the Atlantic and Pacific oceans. Namely, the FO of *C. bownii* in the pre-PETM
372 interval is closely followed by the FO of *D. araneus* and *D. anartios* very close to the onset of
373 the core of the PETM. *R. cuspis* is recorded in the same sample as these malformed discoasters
374 at Site 1209, very likely due to sedimentary condensation, but 5 cm higher at Site 1263. The
375 LO of *B. supremus* is also recorded within the core of the event in both sites. The RI of *Z.*
376 *bijugatus* is in the uppermost part of the PETM core at Site 1209, but in the recovery interval
377 at Site 1263. The LO of *F. richardii* group is recorded in the upper part of the recovery interval
378 in both 1209 and 1263 sites.

379 Conversely, other events appear to be slightly diachronous and, unfortunately, such events are
380 the ones used in standard biozonations. Thus, the FO of *T. bramlettei* occurring close to the
381 PETM onset at Site 1209, but at the end of the recovery phase I interval at Site 1263 makes
382 diachronous the base of the NP10 zone of Martini (1971). Also, the presence of *C. eodela* from
383 the lowermost studied sample at site 1209, while this species is first recorded at the PETM onset
384 at Site 1263 makes diachronous the base of CP8b Zone of Okada and Bukry (1980). Conversely,
385 the CPP11/CPE1 boundary, based on the LO of *F. richardii* group, is consistently synchronous
386 in both section occurring at the transition between the recovery phase I and the recovery phase
387 II intervals.

388

389

390

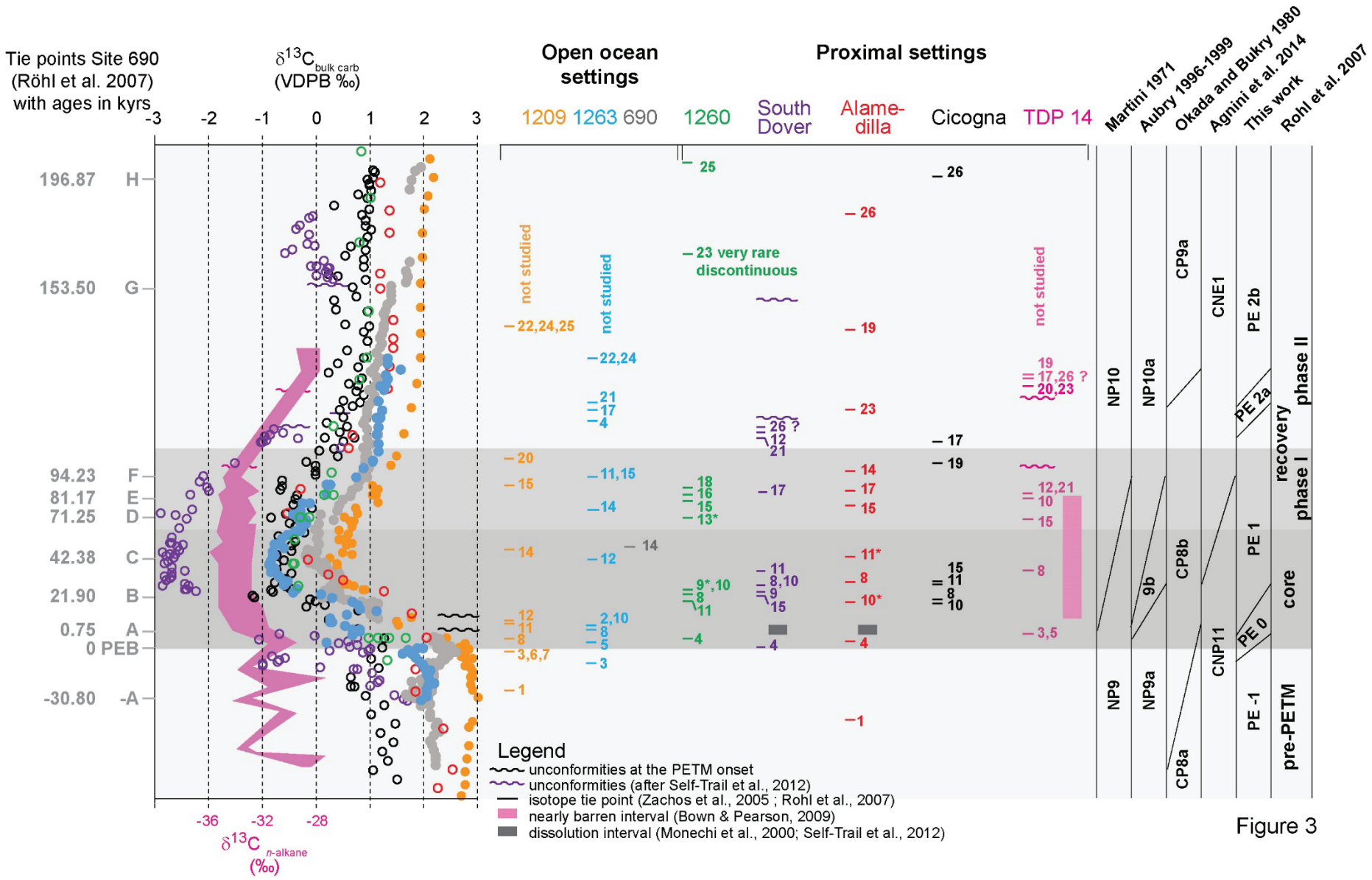
Tie points Site 690
(Röhl et al. 2007)
with ages in kyrs
δ13C bulk carb
(VDPB ‰)
-3 -2 -1 0 1 2 3
196.87 H
153.50 G
94.23 F
81.17 E
71.25 D
42.38 C
21.90 B
0.75 A
0 PEB
-30.80 -A
-36 -32 -28
δ13C n-alkane
(‰)
Open ocean settings
Proximal settings
1209 1263 690
1260
South Dover
Alame-dilla
Cicogna
TDP 14
Martini 1971
Aubry 1996-1999
Okada and Bukry 1980
Agnini et al. 2014
This work
Rohl et al. 2007
not studied
22,24,25
22,24
21
17
4
20
15
14
12
11
8
3,6,7
1
11,15
14
14
12
2,10
8
5
3
25
23 very rare discontinuous
18
16
15
13*
9*,10
8
11
4
26 ?
12
21
17
11
8,10
9
15
4
26
19
23
14
17
15
11*
8
10*
4
1
26
17
19
15
11
8
10
19
17,26 ?
20,23
12,21
10
15
8
3,5
NP10
NP9
NP10a
NP9a
9b
CP9a
CP8b
CP8a
CNE1
CNP11
PE 2b
PE 2a
PE 1
PE 0
PE -1
recovery phase II
recovery phase I
core
pre-PETM
Legend
unconformities at the PETM onset
unconformities (after Self-Trail et al., 2012)
isotope tie point (Zachos et al., 2005 ; Rohl et al., 2007)
nearly barren interval (Bown & Pearson, 2009)
dissolution interval (Monechi et al., 2000; Self-Trail et al., 2012)

Figure 3

392 **4.3. Comparison of Sites 1209 and 1263 with literature**

393 A synthesis of all biostratigraphic events reported across the Paleocene-Eocene is plotted
394 against $\delta^{13}C_{bulk\ carb}$ records for various localities considered here (Fig. 3). The age model used
395 is based on detailed foraminifer and calcareous nannofossil biostratigraphies available for each
396 site (Monechi et al. 2000, Bralower 2002, Mutterlose et al. 2007, Bown and Pearson 2009, Self
397 Trail et al. 2012, Agnini et al. 2016). The shape of isotopic curves allowed precise placement
398 of the different phases, namely pre-event, core of the PETM, recovery phase I and recovery
399 phase II. For all of the considered papers, we took into consideration the bioevents (namely,
400 FO, LO) reported in synthetic figures by the authors. However, in order to better integrate all
401 biostratigraphic information, we also carefully checked the distribution charts for single
402 species. We could therefore detect more biostratigraphic events than the ones indicated in
403 synthetic figures by the authors.

404 The synthesis we made is based upon a careful revision of taxonomic concepts used in various
405 papers, in order to ensure taxonomic stability. Thus, *T. bramlettei*, whose FO is used as zonal
406 marker by Martini (1971), was subdivided into various morphotypes by Monechi et al. (2000),
407 namely with short- and long-arms and variety T, which have successive FOs across the PETM.
408 A careful analysis of published images (plate 1, micrograph 20, p. 484) was thus necessary for
409 assessing that only *T. bramlettei* variety T of Monechi et al. (2000) corresponds to the forms
410 reported as *T. bramlettei* by other authors. Also, the specimens of *T. bramlettei* long-arms
411 figured by Monechi et al. (2000) (plate 1, micrographs 17 and 19, p. 484) very much resembles
412 to *R. calcitrapa*, and some of the specimens of *T. bramlettei* short arms (plate 1, micrographs 6
413 and 11, p. 484) might be attributed to *R. cuspis*. The FO or LO of these species is shown with
414 an asterisk in Figure 3 to mark the taxonomic choice we made. However, some papers show
415 the distribution of *Rhomboaster* instead of that of the different species of the genus (e.g., Bown
416 and Pearson 2009, Self-Trail et al. 2012). This is the reason why we also used *Rhomboaster* in

417 the synthesis of Figure 3. Also, according to Bown (2005a) we adopted the new combination
418 of *Scapholithus apertus* into *Calcisolenia aperta*, whose LO in considered in Monechi et al.
419 (2000). Also, *Scapholithus rhombiformis* reported in Mutterlose et al. (2007) is a synonym of
420 *C. aperta* (cf. Bown 2005a).
421 From comparison of biostratigraphic events in various localities, it results that two events,
422 namely the FO of *C. bownii* and the LCO or LO of *C. aperta* are recorded in almost all the sites
423 at the transition between the pre-PETM and the core of the PETM. This is a very new datum,
424 because *C. bownii* has been introduced only recently (Jiang and Wise 2007), therefore it was
425 not taken into account by Monechi et al. (2000), Bralower et al. (2002), or Mutterlose et al.
426 (2007), although this latter figured specimens of *C. subpertusus* (figure 5, micrograph 7, p. 19)
427 that can be ascribed to *C. bownii*. Mutterlose et al. (2007) consider these forms as typical of the
428 PETM negative CIE, thus we were able to tentatively place the RI and RD of *C. bownii* at Site
429 1260 (with an asterisk; Fig. 3), which likely stratigraphically corresponds to its FO and LO as
430 reported in various papers.
431 Contrarily to previous studies stating that *C. aperta* is absent in oceanic settings (Bown and
432 Pearson 2009), this species is recorded in almost all the onland sections and oceanic sites
433 considered here, unless Cicogna (Northern Italy; Agnini et al. 2016) and Site 1209 (central
434 Pacific; this study). *C. aperta* is also present in Equatorial Pacific Ocean, as confirmed by
435 preliminary observations of PETM sediments at Site 865 (Allyson Guyot, Alessadro Menini
436 unpublished). At 1260, South Dover and Alamedilla the LO of *C. aperta* is recorded below the
437 PETM onset. However, at Site 1263 and at TDP14 this species ranges up above the PETM,
438 despite discontinuously. The LO of *C. aperta* occurred in the recovery phase II interval at Site
439 1263. We postulate that the LO of *C. aperta* before the onset of the PETM in some sections is
440 very likely synchronous with the LCO in Tanzania and at ODP Site 1263, given that in both

these exceptionally preserved sections this species is still present during the recovery phase II of the event.

*C. bownii* has a short range, restricted to the PETM interval. In fact, in most of oceanic sites considered here and at South Dover, it disappears at the base of the recovery phase II interval, whilst at the TDP14 its LO is earlier, in the latest part of the recovery phase I interval. Interestingly, the RD of *C. pertusus* (~ *C. bownii*) occurs at the base of the recovery phase I interval at Site 1260 (Mutterlose et al. 2007). Previous studies also suggested that *C. bownii* is typical of the carbon negative excursion characterizing the PETM (Jiang and Wise 2007).

*D. araneus* and *D. anartios* are considered as malformed discoasters, probably corresponding to adaptation to variable environmental conditions (Bralower et al. 2016), as they are recorded with a different palaeogeographic distribution (Aubry 2001, Kahn and Aubry 2004, Self-Trail et al. 2012). These malformed discoasters first occurred within the PETM core interval in all the considered sections. They have a short range within the CIE, disappearing at the base of the recovery phase II interval. These specimens are thus very useful for supraregional correlations. The malformed discoaster often co-occur along with species of *Rhomboaster* (e.g., *R. calcitrapa*, *R. cuspis*, *R. spineus*). These latter first occur close to the base of the PETM core, unless at TDP 14 core, where they are restricted to a short interval between the upper part of the recovery phase I and the base of the recovery phase II (Fig. 3). The *Rhomboaster-Discoaster* (RD) assemblage is well-known to be characteristic of the PETM interval (Kahn and Aubry 2004). Both these forms can be sporadically present well after the PETM.

The FO of *T. bramlettei*, which is a marker used in the Martini (1971), seems to be consistently present in all the considered areas, but it is slightly diachronous within the interval corresponding to the PETM core, which lasts ~50 kyrs. The LO of *F. richardii* group *sensu* Agnini et al. (2014) (namely, *F. clinatus*, *F. aubertae*, *F. thomasii*, *F. involutus* and *F. tympaniformis*), approximates the transition between the recovery phase I and the recovery

466 phase II (~100 kyrs after the PETM onset ) in oceanic sites, whilst it occurs earlier within the
467 recovery phase I interval (at ~70 kyrs after the PETM onset) at Alamedilla and TDP14, and
468 even earlier in the Cicogna section (at the top of the core interval). The switchover between
469 fasciculiths and zygrhabliths is a well-known pattern occurring in the PETM interval (Bralower
470 2002, Tremolada and Bralower 2004, Gibbs et al. 2006, Agnini et al. 2007 2014), and it
471 corresponds to the LO of *F. richardii* group and the RI of *Z. bijugatus*. This last event is reported
472 at the boundary between the top of the PETM core and the base of the recovery phase I interval
473 in oceanic sites, whilst in the Alamedilla it occurs later, nearly at the end of the recovery phase
474 I interval. However, when considering the RI of *Z. bijugatus*, it might be somehow difficult to
475 precisely place this event without knowing which is the threshold percentage values for
476 different authors.
477 Other events having a supraregional significance are: the FO of *D. diastypus* in the middle part
478 of the recovery phase II interval (Alamedilla, TDP14, Site 1260); the LO of *F. tympaniformis*,
479 which seems to occur consistently at the top of the recovery phase II interval in proximal
480 settings, while this taxon is still present in the considered interval of oceanic settings.
481 The FO of *D. diastypus* is synchronous at TDP14 and Site 1260 while it is slightly offset at
482 Alamedilla (Fig. 3). However, the specimen figured by Monechi et al. (2000) and referred as to
483 *D. diastypus* (plate 2, micrograph 1, p. 486) is more likely *D. salisburgensis* given that it has
484 18 rays, whilst *D. diastypus* is reported to have maximum 16 rays (see Appendix 1). The
485 specimen illustrated by Monechi et al. (2000) has been found at 13.7 m while in their chart the
486 FO of both *D. salisburgensis* and *D. diastypus* occurs at 16.4 m. Given the poor preservation of
487 nannofossils at Alamedilla (Aubry et al. 2000) it could be difficult to systematically distinguish
488 between these two species. Some diachronism (~50 kyrs) between Alamedilla, TDP14 and Site
489 1260 cannot be completely ruled out but, given the concomitant FO of well-preserved *D.*
490 *diastypus* in disparate settings, this apparent diachronism might be explained by different

taxonomic concepts between authors. In any case, at Alamedilla, TDP14 and Site 1260 the FO of *D. diastypus* is reported in the recovery phase II interval and this record does not prevent its use in biostratigraphy.

Two other events are worth noticing, namely the LO of *Bomolithus supremus* and the FO of *Bomolithus aquilus*. These two species have been introduced, respectively, by Bown and Dunkley-Jones (2006) and by Bown (2010). Although these are not taken into account by older papers, the LO of *B. supremus* is recorded in both Sites 1209, 1263 and TDP 14 within the PETM negative CIE, while the FO of *B. aquilus* marks the base of recovery phase II interval in both Sites 1209 and TDP 14. These represent therefore promising events to be further confirmed in other localities.

### 4.4. Possible biases of preparation and counting methods

Before discussing the possible causes, e.g. paleoenvironmental factors or sedimentary features, of the observed similarities and differences amongst the studied localities, this section considers a basic issue concerning calcareous nannofossil studies, namely the preparation and counting methods used in different works.

As discussed above, our samples are prepared using the settling boxes method (Beaufort et al. 2014). Mutterlose et al. (2007) prepared the slides for ODP Site 1260 with a comparable settling method (Geisen et al. 1999). Settling provides slides with a very homogenous concentration of powder in each field of view (FOV) that is ideal for counting. Other datasets used here for comparison were acquired by studying standard smear-slides (Monechi et al. 2000, Bralower 2002, Bown and Pearson 2009, Self-Trail et al. 2012, Agnini et al. 2016).

Despite smear-slides remain the quickest sample preparation method, they do not consistently deliver a homogeneous preparation that should provide us with a rather constant number of nannofossils per FOV. This is quite possible when the sediment powder is let settle on the cover

516 slip resulting in a quasi-homogenous slide, whereas smear slides often provide alternating very
517 concentrated and poor FOVs.
518 In case of very poor FOV, it is certainly possible to recover all the species in a given assemblage
519 but this can be time-consuming. In very rich FOV, some species can be missed especially the
520 small-sized ones, which can be hidden by larger specimens.
521 Most papers dealing with nannofossil biostratigraphy count up to 300 or 500 specimens per
522 sample, independently on the number of analyzed FOV. However, this counting can be
523 problematic for biostratigraphic purposes, since 500 specimens can be easily achieved in very
524 few fields of view and the presence of rare but biostratigraphically important species can be
525 missed. Fatela and Taborda (2002) calculate that counting at least 300 specimens is statistically
526 robust to record all the species making up >1.7% of the total assemblage with a confidence
527 level of 99.5%. Because biostratigraphic markers are often rare and scattered after their first
528 occurrence, as well as close to their last occurrence, these precise horizons can be missed when
529 counting 300 or 500 specimens. This is particularly true for the time interval studied here, where
530 species such as *Coccolithus*, *Toweius* and *Fasciculithus* dominate the assemblages. We
531 performed empirical tests showing that the quantitative method we applied, which consists of
532 counting nannofossil specimens in 30 FOV plus 10 further transects scanned (~1600 FOV) is
533 far more accurate for recovering rare species. For example, the presence of *C. aperta* in open
534 ocean sections has been rarely reported. At Site 1263, previous studies did not report it (Raffi
535 and De Bernardi 2008, Raffi et al. 2009) while we could recover various specimens per sample
536 by scanning the slides over 10 transects.
537
538 **4.5. Paleoceanographic biases**
539 Previous studies showed that the distinctive association of *Rhomboaster* spp., *D. araneus* and
540 *D. anartios* (deformed *Discoaster*) has a marked provincialism, restricted to the Atlantic Ocean

and partially extending to the Tethys seaway and westernmost Indian Ocean (Kahn and Aubry 2004). Raffi (2005) found that the association *Rhomboaster* spp. and *D. araneus* also occurred in the paleo-equatorial Pacific Ocean. At Site 1209, we document that the *Rhomboaster* spp. and deformed *Discoaster* association also occurred in tropical Pacific. Thus these species colonized the world ocean across the PETM and were not restricted to the Tethys, Atlantic and Indian Oceans. Conversely, as shown by Bralower et al. (2016), *D. araneus* and *D. anartios* can be considered as morphotypes of the same biological species adapted to different oceanographic settings, thus occurring in different localities.

The LO of *F. richardii* group is recorded consistently earlier in proximal localities compared to open-ocean sites, probably reflecting environmental parameters. The genus *Fasciculithus* has been previously interpreted as a species adapted to warm and oligotrophic surface waters (Aubry 1998, Bralower 2002, Tremolada and Bralower 2004). Enhanced continental runoff during the PETM has been previously inferred (Ravizza et al. 2001, Kelly et al. 2005) likely triggering eutrophication of shelf areas. The demise of *F. richardii* group in oceanic settings corresponds to the beginning of the PETM recovery, where temperatures decreased to pre-event values. The absence of the group at high-latitudes might suggest that it was better adapted to warm waters (Bralower 2002, Tremolada and Bralower 2004), then became disadvantaged in times of decreased temperatures during the recovery phase (Raffi et al. 2005, 2009). Alternatively, the increase in abundance of *Zygrhablithus* concomitant with the extinction of *F. richardii* group could be linked to a decreased competition for the same ecological niche (Monechi et al. 2000), and environmental conditions in the early Eocene were probably more favorable to *Zygrhablithus*.

In some regions, a relevant increase in percentage of *Z. bijugatus* is observed concomitant with a drastic decline of fasciculiths (Bralower 2002, Tremolada and Bralower 2004, Gibbs et al. 2006, Agnini et al. 2007, 2014). The RI of *Z. bijugatus* is not recorded at Site 1260 but this is

566 coherent with other data from equatorial Atlantic (Raffi et al. 2005). In shelf sections, this event
567 is well documented at Cicogna (Agnini et al. 2016) and Alamedilla (Monechi et al. 2000), but
568 neither at TDP14 (Bown and Pearson 2009) nor at South Dover (Self-Trail et al. 2012) and
569 hence it cannot be used for supraregional correlations. *Z. bijugatus* is interpreted as a species
570 that thrived in oligotrophic conditions (Aubry 1998, Bralower 2002, Tremolada and Bralower
571 2004, Gibbs et al. 2006, Self-Trail et al. 2012). Meso-eutrophic conditions occurring in the
572 aftermath of the PETM were likely unfavourable to the development of this species (Self-Trail
573 et al. 2012), explaining its rarity in proximal sections. Whatever the environmental trigger, the
574 shift from *F. richardii* group ending with its LO and the RI of *Z. bijugatus* represents a reliable
575 event approximating the transition from the core of the event and the recovery interval in several
576 localities.
577 Contrarily to previous studies who stated that *C. aperta* is not present in oceanic localities
578 (Bown and Pearson 2009), this characteristic species has been recorded in oceanic sediments
579 from Site 1263 and Site 1260, as well as at Site 865 (Equatorial Pacific, Allyson Guyot,
580 Alessandro Menini, unpublished). The LO of *C. aperta* is approximatively 150 ky after the
581 PETM onset at Site 1263. This is coherent with the range presented by Bown and Pearson
582 (2009) at TDP14, where *C. aperta* is recorded within the PETM interval. This species is
583 however very tiny and rare (~1 specimen every 2 transects), thus it is not easily recovered. The
584 new record here should enable us to consider a paleogeographic distribution of *C. aperta* wider
585 than previously considered.
586 Previous studies pointed out that condensations or hiatuses frequently affected shelf PETM
587 settings, a sedimentary feature possibly introducing artifacts in the biostratigraphic record.
588 Short hiatuses have been reported at Alamedilla (Aubry et al. 2000), at South Dover (Aubry et
589 al. 2000, Self-Trail et al. 2012), and in TDP 14 (Bown and Pearson 2009, Aze et al. 2014) across
590 the PETM (Fig. 3), that could explain some of the apparent diachroneous events between shelf

591 and open-ocean sites. Unconformities are integral components of the PETM stratigraphic
592 record, both in shelves and deep-sea basins (Aubry et al. 2000). The contemporaneous
593 occurrence of *T. bramlettei*, the malformed *Discoaster* and *Rhomboaster* at Site 1260
594 (Mutterlose et al. 2007) is almost certainly due to the presence of an unconformity. Also, the
595 earlier LO of *C. bownii* at TDP14, within the core of the PETM, is possibly related to a
596 prolonged interval where samples are nearly barren. In any case, in both shelf and open-ocean
597 sections, this event is recorded in the core of the CIE. Other unconformities might be present,
598 although not detected on the basis of sedimentary features, that might affect the slightly
599 diachronous records of species. However, the method used in this paper, based on a precise
600 intercalibration of isotopic curves from various localities, should enable us to minimalize the
601 effect of unconformities on the timing of the events.
602
603 **4.6. Towards a new biozonation scheme for the PETM interval**
604 The comparison of nannofossil bioevents at Sites 1209 and 1263 with six other sections from
605 both open-ocean and shelves allows testing the reliability and the resolution power of the
606 existing standard zonations (i.e., Martini 1971, Okada and Bukry 1980, Agnini et al. 2014)
607 when applied to the very short time interval (<250 kyrs) represented by the PETM.
608 Some of the taxa used in standard zonations proved to be largely diachronous (Fig. 3). As an
609 example, the FO of *T. bramlettei* marking the NP9/NP10 boundary (Martini 1971), spans an
610 interval as long as the entire PETM negative CIE. Aubry et al. (1999) proposes a subdivision
611 of the Martini's zones into NP9a and NP9b subzones, based on the FO of malformed *Discoaster*
612 and of *Rhomboaster*. The boundary between these two subzones is also diachronous, but limited
613 to the core of the PETM. Such a diachronism might be only apparent to some extent, resulting
614 from the presence of unconformities, dissolution effects or barren intervals within the core of
615 the event. The FO of *D. diastypus*, marker of the CP8/CP9 boundary (Okada and Bukry 1980),

seems to be also largely diachronous. This event is recorded in some sites (e.g., 1209, 1263, Cicogna) very high stratigraphically, above the interval considered here, making the boundary diachronous across the recovery phase II interval. *C. eodela*, whose FO marks the base of CP8b (Okada and Bukry 1980), is not considered by some authors (e.g., Mutterlose et al. 2007, Bown and Pearson 2009, Self-Trail et al. 2012, Agnini et al. 2016), or when taken into account it has a very wide range, either first appearing before the pre-PETM interval (Site 1209; Alamedilla section) or in the core of the PETM (Site 1263). *C. eodela* resembles to *C. dela* but with a narrow central area largely filled by the axial cross. Its range matches with the lower part of the range of *C. dela* (e.g., Shamrock and Watkins 2012). Future biometry studies should test the robustness of differences between them in order to investigate their biostratigraphic value as markers. Agnini et al. (2014) considered open-ocean settings located at low-to-middle latitudes. The LO of *F. richardii* group used by Agnini et al. (2014) for the base CNE1 zone is also partly diachronous in various localities spanning all the recovery interval. Standard biohorizons appear therefore inaccurate to precisely dating and correlating the different phases of the PETM, as defined by $\delta^{13}C_{\text{bulk carb}}$ curve.

Most primary markers for GSSPs are biostratigraphic events, but some have utilized other global stratigraphic episodes (e.g., the CIE onset for the base-Eocene). Given that the $\delta^{13}C_{\text{bulk carb}}$ curve is an independent stratigraphic proxy, we subdivided the time interval spanning the PETM and anchored the zones we established to the different phases recognized in the $\delta^{13}C_{\text{bulk carb}}$ trends, namely the pre-event, core of the PETM, recovery phase I and recovery phase II. Criteria for the biozone definitions follow Agnini et al. (2014). We propose four new zones and two subzones for the Paleocene-Eocene transition that are defined as follows:

**PE-1**

Name: *Calcisolenia aperta* zone

Definition: Interval from FO of *D.multiradiatus* to FO of *C. bownii*

Reference section: Site 1209 (Shatsky Rise, Tropical Pacific; 32°39.1'N, 158°30.4'E).

Remarks: The FO of *C. bownii* is a very good marker approximating the top of the NP9 and the transition between the pre-excursion and the PETM onset in both shelves and oceanic sections. The sections we considered are stratigraphically above the extinction of *Ericsonia robusta* (morph. B, *sensu* Garzarella and Raffi 2018) in the lowermost CNP11 (Agnini et al. 2014), which shortly follows the base of magnetochron C24r (Garzarella and Raffi 2018). In this zone, it is also recorded the LCO or LO of *C. aperta*. This event is almost contemporaneous to the FO of *C. bownii* and can be used as auxiliary event.

This zone encompasses the upper part of NP9 of Martini (1971) and CP8a of Okada and Bukry (1980) and corresponds to an interval of background conditions according to the $\delta^{13}C_{bulk\ carb}$ curve, before the PETM onset. Assemblages are dominated by placoliths *Coccolithus* and *Toweius* as well as *Chiasmolithus*, *Campylosphaera* and *Cruciplacolithus*. In some sections, small *Ericsonia* are abundant (*E. orbis*, *E. aliquanta*). *Fasciculithus* are the most abundant nannoliths. Sphenoliths are represented by *S. moriformis* group (*sensu* Agnini et al. 2014) and *S. anarrhopus*. Several species of the genus *Discoaster* are present, such as *D. nobilis*, *D. falcatus, D. mohleri, D. lenticularis, D. delicatus.* and *D. multiradiatus*, whose FO is the standard marker for NP9 base (Martini 1971).

**PE0**

Name: *Discoaster araneus* zone

Definition: Interval from FO of *C. bownii* to FO of *D. araneus* or FO of malformed discoasters or FO of *Rhomboaster* spp..

Reference section: Site 1209 (Shatsky Rise, Tropical Pacific; 32°39.1′N, 158°30.4′E).

665 Remarks: This subzone approximates the uppermost part of NP9 and the PETM onset in both
666 shelves and open-ocean. $\delta^{13}C_{bulk\ carb}$ shows a drastic ~-3 ‰ negative excursion in all the
667 considered sections. Because of the definition of the Paleocene/Eocene, this zone also allows a
668 precise placement of the boundary. The only site where *D. araneus* first occurs later in the
669 PETM core is TDP14. However, most of the samples corresponding to the core of the event are
670 barren there and the biohorizons recorded are poorly reliable. Assemblages are similar to what
671 reported for the zone PE-1.
672 The sharp decrease of $\delta^{13}C_{bulk\ carb}$ values at the Paleocene/Eocene boundary very likely
673 corresponds to an unconformity (Fig. 3), future studies should thus consider to use the base of
674 PE0 as the marker for the Paleocene/Eocene.
675
676 **PE1**
677 Name: *Fasciculithus richardii* group zone
678 Definition: Interval from FO of *D. araneus* to the LO of *C. bownii* but also characterized by the
679 LO of *F. richardii* group
680 Reference section: Site 1263 (Walvis Ridge, Southern-East Atlantic; 28°32′S; 02°47′E).
681 Remarks:
682 The PE1 spans most of the PETM core and recovery interval phase I. The disappearance of the
683 *F. richardii* group represents an easily observable evolutionary change among the nannofossil
684 assemblages, where different species (*F. alanii*, *F. hayii*, *F. lilianae*, *F. mitreus*, *F. richardii,*
685 *F. schaubii* and *F. tonii*) concomitantly disappear. Agnini et al. (2014) used this event to define
686 the top of CNP11. The disappearance of the last species of the plexus is, however, slightly
687 diachronous within the recovery interval. This is the reason why we use the LO of *C. bownii*,
688 which shows a lower degree of diachronism between proximal and oceanic sites. The base of
689 PE1 is also characterized by the LO of *B. aquilus*, reported in a limited number of sites.

690 The fasciculiths group underwent an abrupt extinction across the PETM in Atlantic, Pacific and
691 Tethyan area (Monechi et al. 2000, Zachos et al. 2005, Raffi et al. 2005, Agnini et al. 2006,
692 2007). Despite their scarcity in shelf sections, both these taxa clearly last occurred during the
693 core of the PETM, as also observed at South Dover.
694 In some regions, *Z. bijugatus* occurred concomitant with the abundance decline of fasciculiths
695 (Bralower 2002, Tremolada and Bralower 2004, Gibbs et al. 2006, Agnini et al. 2007, 2014).
696 *Z. bijugatus* can attain 40% of total assemblage. This event can be useful for correlating high-
697 and low-latitude sections (e.g., Site 690) where the LO of *F. richardii* group is not well defined
698 due to its rarity.
699
700 **PE2**
701 Name: *Zygrhablithus bijugatus* zone
702 Definition: Interval from LO of *C. bownii* to LO of *F. tympaniformis*
703 Reference section: Site TDP 14 (Tanzania; 14 (9°16′59.89″S, 39°30′45.04″E)
704 Remarks: this zone is subdivided into two subzones described below.
705 **PE2a**
706 Name: *Coccolithus bownii* subzone
707 Definition: Interval from LO of *C. bownii* to FO of *D. diastypus*
708 Reference section: Site TDP 14 (Tanzania, 9°16′59.89″S, 39°30′45.04″E)
709 Remarks: This subzone represents the recovery phase II interval only in shelf sections.
710 The FO of *D. diastypus* also marks the base of CNP9a (Okada and Bukry 1980). It is sporadic
711 at the beginning of its range and its position relative to the $\delta^{13}C$ is somehow variable. This taxon
712 was not recorded neither at Sites 1263 or 1209. However, at Site 1209 Gibbs et al. (2006)
713 recorded its FO approximatively 1.5 m above the LC, and this is far above the interval we
714 studied here. Because the first occurrence of this species is recorded in the recovery phase II

interval only in proximal settings (Site 1260, Alamedilla, TDP 14), this zone has somehow a limited value and can be applied only locally.

**PE2b**

Name: *Fasciculithus tympaniformis* subzone

Definition: Interval from FO of *D. diastypus* to LO of *F. tympaniformis*

Reference section: Site TDP 14 (Tanzania; 14 (9°16′59.89″S, 39°30′45.04″E))

Remarks: This subzone represents the recovery phase II interval in both shelf sections and open-ocean localities. At Site 1260 and at TDP 14, the FO of *D. diastypus* is synchronous while at Alamedilla it occurs ~50 kyrs earlier. Different taxonomic concepts might explain this apparent diachronism. Thus, the base of PE2b is probably not diachronous upon a uniform taxonomic definition of *D. diastypus*. The LO of *F. tympaniformis* can be a slightly diachronous event, which due to the limited interval considered in this paper, has not been recorded at Sites 1209 and 1263.

## 5. Conclusions

Newly acquired biostratigraphic data from the Paleocene-Eocene Thermal Maximum (PETM) of ODP Sites 1209 (Tropical Pacific Ocean) and 1263 (South East Atlantic Ocean) were compared to available high-resolution records from various ODP cores and onland marine sections from Atlantic, Pacific, Southern oceans and Tethys region. All the considered records dispose of $\delta^{13}C_{bulk\ carb}$ geochemistry, which biostratigraphic data were plotted to. Such a tidy comparison revealed two main issues, namely: i) unconformities are present in all the considered sites but two onland localities (Alemadilla, Cicogna) at the onset of the PETM C-isotope negative excursion; ii) most of the considered bioevents, including the ones used in standard biozonations, are diachronous to some extent. These discoveries have profound implications, first because the C-isotope negative excursion is used to define the

740 Paleocene/Eocene boundary. Also, it appears that standard calcareous nannofossil biozonations
741 fail to bracket the PETM at an adequate resolution, because the zone duration averages 1-2
742 Myrs whilst the PETM is a short hyperthermal lasting some 250 kyrs. Because of the combined
743 effect of relatively low-resolution and diachronous nature of the events, standard calcareous
744 nannofossil biozonations may provide us with an apparent contradictory correlation of the
745 PETM in various sites. The inconsistency and partly diachronous nature of standard
746 biostratigraphic markers are either due to primary environmental factors or to preservation
747 biases. In fact, dissolution intervals are also well-known during the PETM.
748 The late Paleocene and early Eocene are characterized by several originations and extinctions,
749 and also by dominance shifts within the calcareous nannofossil communities. Some of these
750 events, never considered in earlier biozonations, proved to be consistent, with a lesser degree
751 of diachronism than the previously-used biostratigraphic markers. By reviewing the original
752 datasets available for each section, we end up with a new high-resolution biozonation scheme
753 with an average resolution of 50-100 kyrs per zone. More importantly, we anchor the
754 biostratigraphic events and new zones to the different phases characterizing the CIE defining
755 the Paleocene/Eocene. Thus, the pre-excursion interval is comprised in the PE-1 new
756 nannofossil zone. The onset of the CIE is bracketed by the PE0, which might be considered in
757 future works as the main marker for the Paleocene/Eocene boundary. The PE1 corresponds to
758 the core of the event and to the recovery interval phase I. The recovery interval phase II is
759 characterized by the PE2 zone, which can be subdivided into two subzones at least valable in
760 epicontinental areas.
761 For dating and correlating paleoceanographic events occurring on short-term geological time
762 scales (< 1 Myrs), an enhanced biostratigraphy is crucial. Because of diachronism of the events,
763 some studies on the PETM have avoided the use of calcareous nannofossil biostratigraphy in
764 order to recognize the PETM. However, precise biostratigraphy cannot be neglected and

765 remains fundament for modern research in paleoclimatology/paleoceanography studies aiming
766 at a better understanding of extreme events such as the PETM.
767
768 **Acknowledgements**
769 This study was supported by the projects LabEx LIO to AM, IUF and IODP France to EM and
770 ANR Oxymore (ANR-18-CE31-0020) to GS. The authors wish to warmly thank Pr. Kenneth
771 Farley (California Institute of Technology) for sharing unpublished %$CaCO_3$ data for Site
772 1209B. The authors wish to thank Mrs. Ghislaine Broillet for help in sampling preparation. The
773 samples used in this study for nannofossil and geochemical analyses are cured in the Collections
774 de Géologie de l'Université de Lyon (FSL number 717458).
775
776 **Appendix 1**
777 **Species list and taxonomic-stratigraphic remarks**
778 This list includes all the taxa cited in the paper. The taxonomy and bibliographical references
779 follow Perch-Nielsen (1985) and Bown (2005a). Potential biases when dealing with PETM
780 biostratigraphy may derive from the inconsistency between authors in the taxonomic concepts
781 adopted. We thus clarify the taxonomic concepts adopted here, which are consistently based on
782 the holotype of the species and its original description.
783
784 *Bomolithus* Roth 1973
785 *Bomolithus aquilus* Bown 2010
786 *Bomolithus megastypus* (Bramlette and Sullivan 1961) Bown 2010
787 *Bomolithus supremus* Bown and Dunkley Jones 2006
788 *Braarudosphaera* Deflandre 1957
789 *Calciosolenia aperta* (Hay and Mohler 1967) Bown 2005a

For synonimies prior to 2005, we refer to Bown 2005a

2007 *Scapolithus apertus* Mutterlose et al. 2007

We follow the taxonomic concept of Bown (2005a), who combined *S. apertus* and *S. rhombiformis* into *C.aperta*. The genus *Scapholithus* is a junior synonym of the extant genus *Calciosolenia* (see discussion by Bown in Kennedy et al. 2000; Young et al. 2003). This species of *Calciosolenia* has a central solid rod extending almost to the ends of the scapolith. This structure is very fragile and can be easily lost. However, this species cannot be confused with others of the same genus, because it is the only present in the late Paleocene. *C. aperta* can be easily recognized by using the gypsum plate: the four sides of the scapolith show an alternating extinction pattern every 90°. Namely, when the long sides of the lozenge show yellow birefringence colors, the short sides show blue-yellow colors and *vice-versa*.

Just below the onset of the CIE, several authors reported the last occurrence of *C. aperta* in shelf settings, but its presence in oceanic settings was never discussed so far. For the first time, we document the presence of *C. aperta* from the core of the PETM interval at Site 1263, following its LCO. Mutterlose et al. (2007) also observed this species in an Atlantic setting (ODP 1260). Thanks to its widespread distribution in Europe (Alamedilla), North Americ (South Dover) and Tanzania sections this event can be used in supraregional correlations. The last occurrence of *C. aperta* can be used to approximate the end of the NP9 of Martini (1971) and the NP9b of Aubry et al. (1999).

*Campylosphaera* Kamptner 1963

*Campylosphaera dela* (Bramlette and Sullivan 1961) Hay and Mohler 1967

*Campylosphaera differta* Bown 2010

*Campylosphaera eodela* Bukry 1971

*Chiasmolithus* Hay et al. 1966

*Chiasmolithus bidens* (Bramlette and Sullivan 1961) Hay and Mohler 1967

*Chiasmolithus consuetus* (Bramlette and Sullivan 1961) Hay and Mohler 1967

*Coccolithus* Schwarz 1894

*Coccolithus pelagicus* Schiller 1930

*Coccolithus bownii* Jiang and Wise 2007

2007 *Coccolithus subpertusus* Mutterlose et al. 2007 migrograph 7, figure 5.

Among the "excursion-taxa", Jiang and Wise (2007) described *C. bownii*. It is a broadly elliptical to subcircular *Coccolithus* with a large central opening, that occupies 40-50% of the coccolith diameter along the minor axis. In SEM, it possesses a very thin shield compared to *C.pelagicus*. This species possibly corresponds to the thin morphotypes of *C. pelagicus* oberseved at Bass River borehole (New Jersey) during the CIE (O'Dea et al. 2014).

Based on observation of the light microscope pictures of Mutterlose et al. (2007) (micrograph 7, figure 5), the specimens reported by the authors as *C.subpertusus* (= *Ericsonia subpertusa*) belong to *C. bownii*. *E. subertusa* has a narrow-to-closed central area, while the specimen figured by Mutterlose et al. (2007) has a clearly open central area that occupies at least 50% of the coccolith surface. If so, the range of *C. bownii* at Site 1260 is perfectly consistent with the record of Sites 1209, 1263, South Dover and TDP14.

*Cruciplacolithus* Hay and Mohler 1967

*Discoaster* Tan 1927

*Discoaster anartios* Bybell and Self-Trail 1995

*Discoaster araneus* Bukry 1971

Despite the recent taxonomic revision of PETM malformed discoasters by Bralower and Self-Trail (2016), here we refer to the original species concepts of *D. araneus* and *D. anartios* since in our sections we only found specimens that fit these two end-members. Given that *D. araneus* is more consistently recorded across our studied sections, we chose to adopt it as a zonal marker.

*D. araneus* is a large Discoaster (12-25 μm), with 7 to 9 tapering rays

that have a variable free length from 1/3 to 2/3 of the total ray length. The length of the individual rays, even on the same specimen, is not uniform and the angle between rays is likewise variable. The distinct taper of the rays, which terminate in points, and the large central knob are consistent characters in this morphologically plastic species. In overgrown specimens, the central knob is not easily recognizable, as overgrowth happens primarily in and around the central area of *Discoaster* (Adelsek et al. 1973). However, the tapering rays and the irregular angle between rays are still recognizable features. This taxon is typical in Pacific sediments and it corresponds to the specimens attributed to *Discoaster* cf. *araneus* by Bown (2005b) at Shatsky Rise. At Site 865 (Allyson Guyot), *D.* cf. *araneus* (*sensu* Bown 2005b) has been also found (Alessandro Menini preliminary observations), which we consider as *D. araneus*. This record indicates that this species was widespread in the Pacific Ocean. The specimens reported as *D.* cf. *araneus* (Bown 2005b) have exactly the same stratigraphic range as *D. araneus* in the sections studied here.

As already stated by Bukry (1971), *D. araneus* is easily distinguished from other Lower Tertiary species, such as *D. multiradiatus* or *D. nobilis* which show consistently regular ray arrangements, because of long tapering rays and large central knob, and the variability of the general proportions of the rays in a single specimen.

Previous studies stated that the distinctive *Rhomboaster* spp. - *D. araneus* association is considered to have a marked provincialism, restricted to the Atlantic Ocean and partially extending into the Tethys seaway and westernmost Indian Ocean (Kahn and Aubry 2004). Raffi (2005) reported that the distinct *Rhomboaster* spp. - *D. araneus* association also occurs in the paleo-equatorial Pacific Ocean. Thanks to our record from Site 1209, located in the Tropical Pacific Ocean, we can attest that the *Rhomboaster* spp. - *D. araneus* association also occurs in tropical Pacific settings. Thus possibly these organisms colonized the world ocean across the PETM and were not restricted to the Tethys, Atlantic and Indian Oceans.

*Discoaster delicatus* Bramlette and Sullivan 1961

*Discoaster diastypus* Bramlette and Sullivan 1961

*non* 2000 *Discoaster diastypus* Monechi et al. 2000 plate 2, micrograph 1, p. 486

*D. diastypus* is a large to very large species (11 to 20 µm in diameter) of rosette-shaped discoaster with 9 to 16 pointed rays. The rays are joined through most of their length (1/2 to 2/3) and typically they are curving. This species has two central knob, thus side views are diagnostic and very peculiar. *D. diastypus* is distinguished from *D. salisburgensis* (Stradner 1961) by an overall higher number of rays in the latter (12 to 24) and presence of prominent knob of one side only.

*Discoaster lenticularis* Bramlette and Sullivan 1961

*Discoaster multiradiatus* Bramlette and Riedel 1954

*Discoaster mohleri* Bukry and Percival 1971

*Discoaster nobilis* Martini 1961

*Discoaster salisburgensis* Stradner 1961

*Ericsonia* Black 1964

*Ericsonia aliquanta* Bown 2016

*Ericsonia orbis* Bown 2016

*Ericsonia robusta* (Bramlette and Sullivan 1961) Edwards and Perch-Nielsen 1975

*Ericsonia subpertusa* Hay and Mohler 1967

*Fasciculithus* Bramlette and Sullivan 1961

*Fasciculithus alanii* Perch-Nielsen 1971

*Fasciculithus hayi* Haq 1971

*Fasciculithus involutus* Bramlette and Sullivan 1961

*Fasciculithus mitreus* Gartner 1971

*Fasciculithus richardii* Perch-Nielsen 1971

890 *Fasciculithus schaubii* Hay and Mohler 1967

891 *Fasciculithus thomasii* Perch-Nielsen 1971

892 *Fasciculithus tonii* Perch-Nielsen 1971

893 *Fasciculithus tympaniformis* Hay and Mohler 1967

894 *Fasciculithus richardii* group *sensu* Agnini et al. 2014

895 Close to the top of the CIE, the Paleocene genus *Fasciculithus* drastically decreased in
896 abundance. Such a decrease is driven by the successive extinctions of *F. richardii*, *F. hayi*, *F.*
897 *lilianae F. schaubii*, *F. mitreus*, *F. tonii* (Romein 1979, Perch-Nielsen 1985, Agnini et al. 2007,
898 Agnini et al. 2014). These species constitute the third and last major radiation event among the
899 fasciculiths in the upper Thanetian. These taxa are here all included in the single *F. richardii*
900 group, according to Agnini et al. (2014) given their similar conical shape and their very similar
901 stratigraphic range. Some species have fenestrae (i.e., *F. schaubii, F. richardii*) and other do
902 not (i.e., *F. alanii*, *F. lilianae*) but the lack/presence of fenestrae is not of stratigraphic value
903 (Romein 1979, Perch-Nielsen et al. 1985, Raffi et al. 2005, Agnini et al. 2014). Previous studies
904 found that all these species have a similar stratigraphic range, with a common first appearance
905 close to Chron C25n/C24r boundary and a last occurrence in correspondence with the onset of
906 the PETM and hence the Paleocene-Eocene boundary (Raffi et al. 2005, Agnini et al. 2007,
907 2014). In both ODP Sites 1209 and 1263 studied here, and in marine onland sections, the last
908 occurrence of the different species of the genus *Fasciculithus* occurs in the core of the event
909 (between 50-100 ky after the PETM).

910 *Fasciculithus tympaniformis* Hay and Mohler *in* Hay et al. 1967

911 It possesses a peculiar morphology consisting of a small-to-medium sized (5-7 μm in lenght),
912 squat cylindrical fasciculith, almost square in side-view, with gently convex upper surface. *F.*
913 *tympanifomis* is distinguished from *F. involutus* because it is lacking of fenestrae. Wise and
914 Wind (1977) showed that the *F. tympaniformis* morphotype could be produced through

915 overgrowth of *F. involutus* and considered the two forms as conspecific. Following this
916 interpretation, they considered *F. tympaniformis* to be a junior synonym of *F. involutus*.
917 However, most authors keep separated the two forms, and arguably the forms with fenestrae
918 only occur in the upper part of the range of the group.
919 *Jakubowskia leoniae* Varol 1989
920 *Markalius apertus* Perch Nielsen 1979
921 *Rhomboaster* (Bramlette and Sullivan 1961) and *Tribrachiatus bramlettei* (Bronnimann and
922 Stradner 1960) Proto-Decima et al. 1975
923 The taxonomy of most PETM taxa is generally well established, except for the much-debated
924 genera *Rhomboaster* and *Tribrachiatus* (Perch-Nielsen 1985, Bybell and Self-Trail 1997,
925 Aubry et al. 2000, Wei and Zhong 1996, von Salis et al. 2000, Raffi et al. 2005). Within the
926 CIE, the genus *Rhomboaster* evolved with several species, finally giving rise to *Tribrachiatus*
927 *bramlettei*. Although some investigators have gathered the two taxa under the genus
928 *Rhomboaster* and recombined all the species within *Tribrachiatus* into *Rhomboaster*, we prefer
929 to distinguish both genera, only recognizing the following *Rhomboaster* taxa: *R.cuspis* (with
930 short rays) and *R. calcitrapa* group, which includes the species *R. calcitrapa*, *R. intermedia*, *R.*
931 *bitrifida* and *R. spineus* (all possessing long rays). In literature *Rhomboaster* spp. are either
932 distinguished at a specific level or lumped together. Despite the ray length could be partially
933 due to a diagenetic artefact (Bybell and Self-Trail 1995, Wei and Zhong 1996), we prefer to
934 distinguish morphotypes with short arms from long arms as previously proposed (Aubry et al.
935 2000), and hence *R. cuspis* from *R. calcitrapa* in order to avoid misrepresentation of the original
936 data.
937 Despite the considerable debate on morphologic and evolutionary relationships between
938 *Rhomboaster* and *Tribrachiatus* (e.g., Perch-Nielsen 1985, Bybell and Self-Trail 1995, 1997,
939 Aubry 1995, Aubry et al. 1996, 2000; Angori and Monechi 1995, Wei and Zhong 1996, von

940 Salis et al. 2000), biostratigraphic studies have improved our understanding of known ranges
941 of the different species (e.g., Bralower and Mutterlose 1995, Bybell and Self-Trail 1997,
942 Monechi et al. 2000). By combing SEM and optical microscope study of type material where
943 the holotypes of several *Rhomboaster* and *Tribrachiatus* species were described, Wei and
944 Zhong (1996) showed that the transition from *Rhomboaster* to *Tribrachiatus* is expressed by a
945 general flattening of the nannolith. The distinction between *Rhomboaster* and *Tribrachiatus* is
946 justified by the existence of shape gradation between the two genera and the morphologic
947 difference is very important in most cases (for example *T. orthostylus* from *R. cuspis*). Besides,
948 different stratigraphic ranges exist between *Rhomboaster* and *Tribrachiatus*: while
949 *Rhomboaster* are restricted to the PETM interval, *Tribrachiatus* evolve in the lower Eocene (*T.*
950 *contortus*, *T. digitalis*, *T. orthostylus*, *T. absidatus*, *T. lunatus*) and, given that the nomenclature
951 stability is still strongly encouraged by the IBCN, we keep separated the two genera.
952 *Rhomboaster cuspis* (Bramlette and Sullivan 1961)
953 2000 *Rhomboaster bramlettei* var. short arms Monechi et al. 2000 plate 3, micrograph 4, p. 488
954 *R. cuspis* (Bramlette and Sullivan 1961) is a rhombic-shaped nannolith with little or no
955 extension from the points of the rhomb. Faces are depressed and strongly concave. Polarized
956 light shows that it is composed of a unique mass of calcite.
957 *Rhombiaster calcitrapa* group *sensu* Raffi et al. 2005
958 2000 *Rhomboaster bramlettei* var. long arms Monechi et al. 2000 plate 1, micrograph 17-19, p.
959 484
960 *R. calcitrapa*, *R. intermedia*, *R. bitrifida* and *R. spineus* are all rhombic-shaped nannolith with
961 long extensions from the points of the rhomb. *Rhomboaster bitrifida*, *R. intermedia* and *R.*
962 *spineus* are rarely reported in the literature (Bybell and Self-Trail 1995, Wei and Zhong 1996)
963 justifying our choice to lump these species into the *R. calcitrapa* group.
964 *Sphenolithus* Deflandre *in* Grassé, 1952

965 *Sphenolithus anarrhopus* Bukry and Bramlette 1969

966 *Sphenolithus moriformis* group *sensu* Agnini et al. 2014

967 *Prinsius* Hay and Mohler 1967

968 *Thoracosphaera* Kamptner 1927

969 *Toweius* Hay and Mohler 1967

970 *Toweius callosus* Perch-Nielsen 1971

971 *Toweius eminens* (Bramlette and Sullivan, 1961) Perch-Nielsen, 1971

972 *Toweius serotinus* Bybell and Self Trail 1995

973 *Tribrachiatus* Shamrai 1963

974 *Tribrachiatus bramlettei* (Bronnimann and Stradner 1960) Proto-Decima et al. 1975

975 2000 *Rhomboaster bramlettei* var. T Monechi et al. 2000 plate 3, micrograph 1-2-3, p. 488.

976 *T. bramlettei* is a nannolith with two symmetrically offset and superimposed tri-radiate cycles.

977 These are very easy to observe by focusing under microscope in plane-polarized light or in XPL

978 light. In side view, it is flatter than species of *Rhomboaster* genus (Romein 1979, Wei and

979 Zhong 1996). The first occurrence of *T. bramlettei* defines the Subzone NP10a (=base NP10)

980 of Aubry et al. (1999).

981 *Zygrhablithus* Deflandre 1959

982 *Zygrhablithus bijugatus* Deflandre 1959

983

984 **References**

985 • Adelseck, C.G., Geehan, G.W., Roth, P.H., 1973. Experimental evidence for the selective

986 dissolution and overgrowth of calcareous nannofossils during diagenesis. Geological Society

987 of America Bulletin 84, 2755–2762.

988 • Agnini, C., Muttoni, G., Kent, D. V., Rio, D., 2006. Eocene biostratigraphy and magnetic
989 stratigraphy from Possagno, Italy: The calcareous nannofossil response to climate
990 variability. Earth and Planetary Science Letters 241, 815–830.
991 • Agnini, C., Fornaciari, E., Rio, D., Tateo, F., Backman, J., Giusberti, L., 2007. Responses of
992 calcareous nannofossil assemblages, mineralogy and geochemistry to the environmental
993 perturbations across the Paleocene/Eocene boundary in the Venetian Pre-Alps. Marine
994 Micropaleontology 63, 19–38.
995 • Agnini, C., Fornaciari, E., Raffi, I., Catanzariti, R., Pälike, H., Backman, J., Rio, D., 2014.
996 Biozonation and biochronology of Paleogene calcareous nannofossils from low and middle
997 latitudes. Newsletters on Stratigraphy 47, 131–181
998 • Agnini, C., Spofforth, D.J.A., Dickens, G.R., Rio, D., Pälike, H., Backman, J., Muttoni, G.,
999 Dallanave, E., 2016. Stable isotope and calcareous nannofossil assemblage record of the late
1000 Paleocene and early Eocene (Cicogna section). Climate of the Past 12, 883–909.
1001 • Ali, J. R., Kent, D. V., Hailwood, E. A., 2000. Magnetostratigraphic reinvestigation of the
1002 Palaeocene/Eocene boundary interval in Hole 690B, Maud Rise, Antarctica. Geophysical
1003 Journal International 141(3), 639–646.
1004 • Angori, E., Monechi, S., 1995. High-resolution calcareous nannofossils biostratigraphy
1005 across the Paleocene/Eocene boundary at Caravaca (southern Spain). Israel Journal of Earth
1006 Sciences 44, 197– 206.
1007 • Aubry, M.-P., 1995. Towards an upper Paleocene–lower Eocene high resolution stratigraphy
1008 based on calcareous nannofossils stratigraphy. Israel Journal of Earth Sciences 44, 239– 253.
1009 • Aubry, M.-P., 1998. Early Paleogene calcareous nannoplankton evolution: a tale of climatic
1010 amelioration. In: Aubry, M.-P., Lucas, S., Berggren, W.A. (Eds.), Late Paleocene and Early
1011 Eocene Climatic and Biotic Evolution. Columbia University Press, New York, 158–203.

1012 • Aubry, M.-P., 1999. Late Paleocene–early Eocene sedimentary history in western Cuba:
1013 implications for the LPTM and for regional tectonic history. Micropaleontology 45, 5 –18.
1014 • Aubry, M.-P., 2001. Provincialism in the photic zone during the LPTM. In: Ash, A., Wing,
1015 S. (Eds.), Climate and Biota of the Early Paleogene. International Meeting, Powell,
1016 Abstract Volume, Powell, p. 6.
1017 • Aubry, M.P., Cramer, B.S., Miller, K.G., Wright, J.D., Kent, D. V., Olsson, R.K., 2000. Late
1018 Paleocene event chronology: Unconformities, not diachrony. Bulletin de la Societé.
1019 Geologique de France 171 (3), 367–378
1020 • Aze, T., Pearson, P.N., Dickson, A.J., Badger, M.P.S.S., Bown, P.R., Pancost, R.D., Gibbs,
1021 S.J., Huber, B.T., Leng, M.J., Coe, A.L., Cohen, A.S., Foster, G.L., 2014. Extreme warming
1022 of tropical waters during the Paleocene-Eocene thermal maximum. Geology 42 (9),739–742
1023 • Babila, T.L., Penman, D.E., Hönisch, B., Kelly, D.C., Bralower, T.J., Rosenthal, Y., Zachos,
1024 J.C., 2018. Capturing the global signature of surface ocean acidification during the
1025 Palaeocene–Eocene Thermal Maximum. Philosophical Transactions A 376.
1026 • Bains, S., R. Corfield, M., Norris, R. D., 1999. Mechanisms of climate warming at the end
1027 of the Paleocene, Science 285, 724–727.
1028 • Beaufort, L., Barbarin, N., Gally, Y., 2014. Optical measurements to determine the thickness
1029 of calcite crystals and the mass of thin carbonate particles such as coccoliths. Nature
1030 Protocols 9 (3), 633–642
1031 • Blair, S., Watkins, D. K., 2009. High-resolution calcareous nannofossil biostratigraphy for
1032 the Coniacian/Santonian Stage boundary, Western Interior Basin. Cretaceous Research 30,
1033 367–384.
1034 • Bown, P. R., 2005a. Palaeogene calcareous nannofossils from the Kilwa and Lindi areas of
1035 coastal Tanzania (Tanzania Drilling Project 2003-4). J. Nannoplankton Res. 27 (1), 2005,
1036 21–95.

- Bown, P.R., 2005b. Cenozoic calcareous nannofossils biostratigraphy, ODP Leg 198 Site 1208 (Shatsky Rise, northwest Pacific Ocean). In Bralower, T.J., Premoli Silva, I., and Malone, M.J. Proceedings of the Ocean Drilling Program. Scientific Results 198, 1– 44.
- Bown, P. R., 2010. Calcareous nannofossils from the Paleocene/Eocene Thermal Maximum interval of southern Tanzania (TDP Site 14). Journal of Nannoplankton Research. 31(1), 11–38.
- Bown, P.R., 2016. Paleocene calcareous nannofossils from Tanzania (TDP sites 19, 27 and 38). J. Nannoplankton Res, The calcareous nannofossil genus Ericsonia in the upper Paleocene 149 36 (1), 1–32.
- Bown, P. R., Dunkley Jones, T., 2006. New Paleogene calcareous nannofossil taxa from coastal Tanzania: Tanzania Drilling Project Sites 11 to 14. Journal of Nannoplankton Research 28 (1), 17–34.
- Bown, P., Pearson, P., 2009. Calcareous plankton evolution and the Paleocene/Eocene thermal maximum event: New evidence from Tanzania. Marine Micropaleontology 71, 60–70.
- Bralower, T.J., 2002. Evidence of surface water oligotrophy during the Paleocene–Eocene Thermal Maximum: nannofossil assemblage data from Ocean Drilling Program Site 690 Maud Rise, Weddell Sea. Paleoceanography 17, 1–13.
- Bralower, T.J., Mutterlose, J., 1995. Calcareous nannofossil biostratigraphy of ODP Site 865, Allison Guyot, Central Pacific Ocean: a tropical Paleogene reference section. In: Winterer, E.L., Sager, W.W., Firth, J.V. (Eds.), Proceedings of the Ocean Drilling Program. Scientific Results 143, 31– 72.
- Bralower, T.J., Self-Trail, J.M., 2016. Nannoplankton malformation during the Paleocene-Eocene Thermal Maximum and its paleoecological and paleoceanographic significance. Paleoceanography 31, 1423–1439.

1062 • Bralower, T.J., Kelly, D.C., Gibbs, S., Farley, K., Eccles, L., Lindemann, T.L., Smith, G.J.,
1063 2014. Impact of dissolution on the sedimentary record of the Paleocene-Eocene thermal
1064 maximum. Earth and Planetary Science Letters 401, 60–72
1065 • Bramlette, M. N., Sullivan, F. R., 1961. Coccolithophorids and related nannoplankton of the
1066 early Tertiary in California. Micropaleontology, 129-188.
1067 • Bukry, D., 1973. Low-latitude coccolith biostratigraphic zonation. In: Edgar, N.T.,
1068 Saunders, J.B., et al. Initial Reports of the Deep Sea Drilling Project 15. U.S. Government
1069 Printing Office, Washington, 685–703.
1070 • Bukry, D., 1975. Coccolith and silicoflagellate stratigraphy, northwestern Pacific Ocean,
1071 Deep Sea Drilling Project Leg 32. In: Larson, R.L., Moberly, R., et al. Initial Reports of the
1072 Deep Sea Drilling Project 32. U.S. Government Printing Office, Washington, 677– 701.
1073 • Bybell, L.M., Self-Trail, J.M., 1995. Evolutionary, biostratigraphic, and taxonomic study of
1074 calcareous nannofossils from a continuous Paleocene-Eocene boundary section in New
1075 Jersey. US Geological Survey Professional Paper 1554.
1076 • Bybell, L.M., Self-Trail, J.M., 1997. Late Paleocene and early Eocene calcareous
1077 nannofossils from three boreholes in an onshore-offshore transect from New Jersey to the
1078 Atlantic Continental Rise. Proceedings of the Ocean Drilling Program. Scientific results 150,
1079 91–110.
1080 • Cande, S.C., Kent, D.V., 1995. Revised calibration of the geomagnetic polarity timescale
1081 for the Late Cretaceous and Cenozoic. Journal of Geophysical Research 100, 6093– 6095.
1082 • Colosimo, A.B., Bralower, T.J., Zachos, J.C., 2006. Evidence for lysocline shoaling at the
1083 Paleocene/Eocene thermal maximum on Shatsky rise, northwest Pacific. Proceeding of the
1084 Ocean Drilling Program. Scientific Results 198, 1–36.

- Dallanave, E., Agnini, C., Muttoni, G., Rio, D., 2009. Magneto-biostratigraphy of the Cicogna section (Italy): Implications for the late Paleocene-early Eocene time scale. Earth and Planetary Science Letters 285, 39–51.
- Dickens, G.R., O'Neil, J.R., Rea, D.K., Owen, R.M., 1995. Dissociation of oceanic methane hydrate as a cause of the carbon isotope excursion at the end of the Paleocene. Paleoceanography 10, 965–971
- Dickens, G.R., Castillo, M.M., Walker, J.G.C., 1997. A blast of gas in the latest Paleocene: Simulating first-order effects of massive dissociation of oceanic methane hydrate, Geology 25, 259–262.
- Dickson, A.J., Cohen, A.S., Coe, A.L., Davies, M., Shcherbinina, E.A., Gavrilov, Y.O., 2015. Evidence for weathering and volcanism during the PETM from Arctic Ocean and Peri-Tethys osmium isotope records. Palaeogeography, Palaeoclimatology, Palaeoecology 438, 300–307.
- Erbacher, J., Mosher, D.C., Malone, Berti, D., Bice, K. L., Bostock, H., Jürgen Brumsack, H., Danelian, T., Glatz, C., Heidersdorf, F., Henderiks, J., Janecek, T., Junium, C., Le Callonec, L., MacLeod, K., Meyers, P. A., Mutterlose, J., Nishi, H., Norris, R., Ogg, J. G., O'Regan, M., Rea, B., Sexton, P., Sturt, H., Suganuma, Y., Thurow, J.W., Wilson, P. A., Wise, S. W., 2004. Demerara rise: equatorial cretaceous and Paleogene paleoceanographic transect, Western Atlantic (Leg 207, Sites 1257–1261). Proceedings of the Ocean Drilling Program 207, 1–89.
- Fatela, F., Taborda, R., 2002. Confidence limits of species proportions in microfossil assemblages. Marine Micropaleontology 45, 169–174.
- Ferreira, J., Mattioli, E., Suchéras-Marx, B., Giraud, F., Duart, L., V., Pitter, B., Hassler, A., Spangenberg, J., 2019. Western Tethys Early and Middle Jurassic calcareous nannofossils biostratigraphy. Earth-Science Reviews 197, 1–19.

1110 • Garzarella, A., Raffi, I., 2018. Taxonomy and evolutionary relationships within the
1111 calcareous nannofossil genus Ericsonia in the upper Paleocene. Rivista Italiana di
1112 Paleontologia e Stratigrafia 124 (1), 129–150.
1113 • Geisen, M., Bollmann, J., Herrle, J.O., Mutterlose, J., Young, J.R., 1999. Calibration of the
1114 random settling technique for calculation of absolute abundances of calcareous
1115 nannoplankton. Micropaleontology 45, 437– 442.
1116 • Gibbs, S.J., Bralower, T.J., Bown, P.R., Zachos, J.C., Bybell, L.M., 2006. Shelf and open-
1117 ocean calcareous phytoplankton assemblages across the Paleocene–Eocene thermal
1118 maximum: implication for global productivity gradients. Geology 34 (4), 233–236.
1119 • Gradstein, F.M., Ogg, J.G., Schmitz, M.D., Ogg, G.M., 2012. The geologic time scale, The
1120 Geologic Time Scale 2012.
1121 • Handley, L., Pearson, P., McMillan, I.K., Pancost, R.D., 2008. Large terrestrial and marine
1122 carbon and hydrogen isotope excursions in a new Paleocene/Eocene boundary section from
1123 Tanzania. Earth and Planetary Science Letters 275, 17–25.
1124 • Jiang, S., Wise, S.W., 2006. Surface-water chemistry and fertility variations in the tropical
1125 Atlantic across the Paleocene/Eocene Thermal Maximum as evidenced by calcareous
1126 nannoplankton from ODP Leg 207, Hole 1259B. Revue de Micropaléontologie 49, 227–244.
1127 • Kahn, A., Aubry, M.P., 2004. Provincialism associated with the Paleocene/Eocene thermal
1128 maximum: Temporal constraint. Marine Micropaleontology 52, 117–131.
1129 • Kelly, D.C., Bralower, T.J., Zachos, J.C., Premoli Silva, I., Thomas, E., 1996. Rapid
1130 diversification of planktonic foraminifera in the tropical Pacific (ODP Site 865) during the
1131 late Paleocene thermal maximum. Geology 24, 423– 426.
1132 • Kelly, D.C., Zachos, J.C., Bralower, T.J., Schellenberg, S.A., 2005. Enhanced terrestrial
1133 weathering/runoff and surface ocean carbonate production during the recovery stages of the
1134 Paleocene-Eocene thermal maximum. Paleoceanography 20, 1–11.

- Kennedy, J., Gale, A.S., Bown, P.R., Caron, M., Davey, R.,Gröcke, D., Wray, D.S. 2000. Integrated stratigraphy of the Aptian-Albian boundary interval in the Marnes Bleues, at the Col de Pré-Guittard, Arnayon (Drôme), and at Tartonne (Alpes-de-Haute-Provence), France, a candidate Global Boundary Stratotype Section and Boundary Point for the base of the Albian stage. Cretaceous Research 21, 591–720.
- Kennett, J.P., Stott, L.D., 1991. Abrupt deep-sea warming, palaeoceanographic changes and benthic extinctions at the end of the Palaeocene. Nature 353, 225–229.
- Kroon, D., Norris, R.D., Klaus, A., 1998. Proceeding of the Ocean Drilling Program. Initial Reports 171B.
- Lu G., Keller, G., Adattte T., Ortiz, N., Molina, E., 1996. Long-term ($10^5$) or short-term ($10^3$) $\delta^{13}C$ excursion nearthe Palaeocene-Eocene transition: evidence from the Tethys. Terra Nova 8, 347-355.
- Martini, E., 1971. Standard Tertiary and Quaternary calcareous nannoplankton zonation. In: Farinacci, A., Proceedings of the 2nd International Conference on Planktonic Microfossils 2, 739– 785
- McCarren, H., Thomas, E., Hasegawa, T., Röhl, U., Zachos, J.C., 2008. Depth dependency of the Paleocene-Eocene carbon isotope excursion: Paired benthic and terrestrial biomarker records (Ocean Drilling Program Leg 208, Walvis Ridge). Geochemistry, Geophysics, Geosystems 9, 1–10.
- Monechi, S., Angori, E., von Salis, K., 2000. Calcareous nannofossil turnover around the Paleocene/Eocene transition at Alamedilla (southern Spain). Bulletin de la Soceté Géologique de France 171 (4), 477–489.
- Mutterlose, J., Linnert, C., Norris, R., 2007. Calcareous nannofossils from the Paleocene-Eocene Thermal Maximum of the equatorial Atlantic (ODP Site 1260B): Evidence for tropical warming. Marine Micropaleontology 65, 13–31.

1160 • O'Dea, S.A., Gibbs, S.J., Bown, P.R., Young, J.R., Poulton, A.J., Newsam, C., Wilson, P.A.,
1161 2014. Coccolithophore calcification response to past ocean acidification and climate change.
1162 Nature Communcations 5 (5363).
1163 • Okada, H., Bukry, K., 1980. Supplementary modification and introduction of code numbers
1164 to the low-latitude coccolith biostratigraphic zonation. Marine Micropaleontology 5, 321–
1165 325.
1166 • Pak, D. K., Miller, K. G., 1992. Paleocene to Eocene benthic foraminiferal isotopes and
1167 assemblages: Implications for deep water circulation, Paleoceanography 7, 405– 422.
1168 • Pak, D., Miller, K., Browning, J., 1997. Global significance of an isotopic record from the
1169 New Jersey coastal plain: linkage between the shelf and deep sea in the late Paleocene to
1170 early Eocene. In Proceedings of the Ocean Drilling Program. Scientific results 156, 305–
1171 315.
1172 • Penman, D.E., Hönisch, B., Zeebe, R.E., Thomas, E., Zachos, J.C., 2014. Rapid and
1173 sustained surface ocean acidification during the Paleocene-Eocene Thermal Maximum.
1174 Paleoceanography 29, 357–369.
1175 • Penman, D.E., Turner, S.K., Sexton, P.F., Norris, R.D., Dickson, A.J., Boulila, S., Ridgwell,
1176 A., Zeebe, R.E., Zachos, J.C., Cameron, A., Westerhold, T., Röhl, U., 2016. An abyssal
1177 carbonate compensation depth overshoot in the aftermath of the Palaeocene-Eocene Thermal
1178 Maximum. Nature Geosciece 9, 575–580.
1179 • Perch-Nielsen, K., 1985. Cenozoic calcareous nannofossils. In: Bolli, H.M., Saunders, J.B.,
1180 Perch-Nielsen, K. Plankton Stratigraphy. Cambridge University Press, Cambridge, 427–554.
1181 • Raffi, I., De Bernardi, B., 2008. Response of calcareous nannofossils to the Paleocene–
1182 Eocene thermal maximum: observations on composition, preservation and calcification in
1183 sediments from ODP Site 1263 (Walvis Ridge -SW Atlantic). Marine Micropaleontology
1184 69, 119–138.

- Raffi, I., Backman, J., Pälike, H., 2005. Changes in calcareous nannofossil assemblages across the Paleocene/Eocene transition from the paleo-equatorial Pacific Ocean. Palaeogeography, Palaeoclimatology, Palaeoecology 226, 93–126.
- Raffi, I., Backman, J., Zachos, J.C., Sluijs, A., 2009. The response of calcareous nannofossil assemblages to the Paleocene Eocene Thermal Maximum at the Walvis Ridge in the South Atlantic. Marine Micropaleontology 70, 201–212.
- Ravizza, G., Norris, R.N., Blusztajn, J., Aubry, M.P., 2001. An osmium isotope excursion associated with the late Paleocene thermal maximum: Evidence of intensified chemical weathering. Paleoceanography 16 (2), 155–163
- Röhl, U., L. J. Abrams, 2000, High-resolution, downhole and non-destructive core measurements from Sites 999 and 1001 in the Caribbean Sea: Application to the late Paleocene thermal maximum, Proceedings of the Ocean Drilling Program Sci. Results 165, 191–203.
- Röhl, U., Westerhold, T., Bralower, T.J., Zachos, J.C., 2007. On the duration of the Paleocene–Eocene thermal maximum (PETM). Geochemistry, Geophysics, Geosystems 8,
- Romein, A.J.T., 1979. Lineages in early Paleogene calcareous nannoplankton (Doctoral dissertation, Utrecht University), 76–78.
- Self-Trail, J. M., Powars, D. S., Watkins, D. K., Wandless, G., 2012. Calcareous nannofossil assemblage changes across the Paleocene-Eocene thermal maximum: Evidence from a shelf setting, Marine Micropaleontology 92–93, 61–80,
- Shamrock, J. L., Watkins, D. K., 2012. Eocene calcareous nannofossil biostratigraphy and community structure from Exmouth Plateau, Eastern Indian Ocean (ODP Site 762). Stratigraphy 9 (1), 1–11.

- Stradner, H., Papp, A., 1961. Tertiäre Discoasteriden aus Österreich und deren stratigraphische Bedeutung mit Hinweisen auf Mexico, Rumanien und Italien. Jahrbuch der Geologischen Bundesanstalt (Wien) 7, 1–159.
- Storme, J.Y., Devleeschouwer, X., Schnyder, J., Cambier, G., Baceta, J.I., Pujalte, V., Di Matteo, A., Iacumin, P., Yans, J., 2012. The Palaeocene/Eocene boundary section at Zumaia (Basque-Cantabric Basin) revisited: New insights from high-resolution magnetic susceptibility and carbon isotope chemostratigraphy on organic matter ($\delta^{13}C_{org}$). Terra Nova 24, 310–317.
- Takeda, K., Kaiho, K., 2007. Faunal turnovers in central Pacific benthic foraminifera during the Paleocene-Eocene thermal maximum. Palaeogeography, Palaeoclimatology, Palaeoecology 251, 175–197.
- Thomas, E., Shackleton, N.J., 1996. The latest Paleocene benthic foraminiferal extinction and stable isotope anomalies. In: Knox, R.O., Corfield, R.M., Dunay, R.E. Correlation of the Early Paleogene in Northwest Europe. Geological Society of London Special Publication 101, 40–441.
- Tjalsma, R. C., Lohmann, G. P., 1983. Paleocene-Eocene bathyal and abyssal benthic foraminifera from the Atlantic Ocean. Micropaleontology Special Publication 4, 1–90.
- Tremolada, F., Bralower, T.J., 2004. Nannofossil assemblage fluctuations during the Paleocene-Eocene Thermal Maximum at Sites 213 (Indian Ocean) and 401 (North Atlantic Ocean): Palaeoceanographic implications. Marine Micropaleontology 52, 107–116.
- von Salis, K., Monechi, S., Bybell, L.M., Young, J., 2000. Remarks on the calcareous nannofossil markers Rhomboaster and Tribrachiatus around the Paleocene/Eocene boundary. Journal of the Geological Society of Sweden 122, 138–140.
- Wei, W., Zhong, S., 1996. Taxonomy and magnetobiochronology of Tribrachiatus and Rhomboaster, two genera of calcareous nannofossils. Journal of Paleontology 70, 7– 22.

- Westerhold, T., Röhl, U., Donner, B., Zachos, J.C., 2018. Global Extent of Early Eocene Hyperthermal Events: A New Pacific Benthic Foraminiferal Isotope Record From Shatsky Rise (ODP Site 1209). Paleoceanography and Paleoclimatology 33, 626–642.
- Westerhold, T., Röhl, U., Laskar, J., Raffi, I., Bowles, J., Lourens, L.J., Zachos, J.C., 2007. On the duration of magnetochrons C24r and C25n and the timing of early Eocene global warming events: Implications from the Ocean Drilling Program Leg 208 Walvis Ridge depth transect. Paleoceanography 22, 1–19.
- Westerhold, T., Röhl, U., Raffi, I., Fornaciari, E., Monechi, S., Reale, V., Bowles, J., Evans, H.F., 2008. Astronomical calibration of the Paleocene time. Palaeogeography, Palaeoclimatology, Palaeoecology 257, 377–403.
- Wise, S.W., Wind, F.H., 1977. Mesozoic and Cenozoic calcareous nannofossils recovered by DSDP Leg 36 drilling on the Falkland Plateau, south-west Atlantic sector of the Southern Ocean. Initial Reports of the Deep Sea Drilling Project 36, 269–491.
- Zachos, J.C., Lohmann, K.C., Walker, J.C.G., Wise, S.W. Jr., 1993. Abrupt climate change and transient climates during the Paleogene: A marine perspective, J. Geol. 101, 191 – 213.
- Zachos, J.C., Kroon, D., Blum, P., Bowles, J., Gaillot, P., Hasegawa, T., Hathorne, E.C., Hodell, D. A., Kelly, D. C., Jung, J. H., Keller, S. M., Lee, Y. S., Leuschner, D. C., Lohmann, K. C., Lourens, L., Monechi, S., Nicolo, M., Raffi, I., Riesselman, C., Röhl, U., Schellenber, S. A., Schmidt, D., Slujis A., Thomas, D., Thomas, E., Vallius, H. , 2004. Early Cenozoic extreme climates: the Walvis Ridge transect. Proceedings of the Ocean Drilling Program. Initial Reports 208.
- Zachos, J.C., Pagani, M., Sloan, L.C., Billups, K., Thomas, E., 2001. Trends, rhythms, and aberrations in global climate 65 Ma to present. Science 292, 686–693.

1256 • Zachos, J.C., Röhl, U., Schellenberg, S.A., Sluijs, A., Hodell, D.A., Kelly, D.C., Thomas,
1257 E., Nicolo, M., Raffi, I., Lourens, L.J., McCarren, H., Kroon, D., 2005. Rapid acidification
1258 of the ocean during the Paleocene–Eocene thermal maximum. Science 308, 1611–1615.
1259 • Zeebe, R.E., Lourens, L.J., 2019. Solar System chaos and the Paleocene–Eocene boundary
1260 age constrained by geology and astronomy. Science 365, 926–929.
1261
1262
1263 **Figure captions**
1264
1265 Fig. 1. Location of the two studied sections on a paleogeographic map at 56 Ma
1266 (http://www.odsn.de/odsn/services/paleomap/paleomap.html): Site 1209 (Shatsky Rise,
1267 Tropical Pacific), and Site 1263 (Walvis Ridge, South Eastern Atlantic). Location of the sites
1268 used for comparison is also shown: Site 690 (Southern Ocean) Site 1260 (Equatorial Atlantic),
1269 SDB (New Jersey), TDP 14 (Tanzania), Cicogna (North Italy), Alamedilla (Spain).
1270
1271 Fig. 2. Core photo, $\delta^{13}C_{bulk\ carb}$, $CaCO_3$ (%) and calcareous nannofossil bioevents for Sites 1209
1272 (left side) and 1263 (right side) in function of depth. Depth is expressed as relative to the
1273 lithological contact (LC: from white nannofossils ooze to brown clayey nannofossil ooze).
1274 Calcareous nannofossil biozonations are after Martini (1971), Okada and Bukry (1980) and
1275 Agnini et al. (2014). The subdivision of NP9 (Martini 1971) in NP9a and NP9b is after Aubry
1276 et al. 1999. Shaded area are used to subdivide the PETM interval in pre-PETM, core of the
1277 PETM and recovery phase I and II according to Röhl et al. (2007).
1278
1279 Fig. 3. Compilation of biostratigraphic events in all the studied sections relative to the $\delta^{13}C_{bulk}$
1280 $_{carb}$ record (Alamedilla (red) Lu al. 1996, ODP 690 (grey) Bains et al. 1999 , ODP 1209 (orange)

Penman et al. 2014, ODP 1263 (light blue) Zachos et al. 2005, ODP 1260 (green) Mutterlose et al. 2007, South Dover (violet) Self Trail et al. 2012, Cicogna (black) Agnini et al. 2016). For TDP 14 (pink) we used $\delta^{13}C_{n\text{-alkane}}$ record (isotopes of C-25, C-27, C-29 and C-31 alkanes), since $\delta^{13}C_{bulk\ carb}$ did not provide satisfacting results (Bown and Pearson 2009, Aze et al. 2014). Tie-points of the $\delta^{13}C_{bulk\ carb}$ at Site 690 as defined by Zachos et al. (2005) and Röhl et al. (2007) from –A to H are shown. These authors reviewed the original definition of the $\delta^{13}C_{bulk\ carb}$ inflection points of Site 690 by Bains et al. (1999). Ages of tie-points ages are after Röhl et al. (2007). Biostratigraphic events from 1 to 26 are expressed as first or last occurrence (FO, LO), LCO (last consistent occurrence), RI, RD (rapid increase, rapid decrease) according to Gradstein et al. (2012). These events are from the earliest to the latest: 1. Presence of *C. eodela*; 2. FO *C. eodela*; 3. FO *C. bownii*; 4. LO *C. aperta*; 5. LCO *C. aperta*; 6. FO *R. cuspis*; 7. FO *R. calcitrapa*; 8. FO malformed *Discoaster* (*D. araneus*, *D. anartios*); 9. RI *C. bownii*; 10. FO *Romboaster* spp.; 11. FO *T. bramlettei*; 12. LO *B. supremus*; 13. RD *C. bownii*; 14. RI *Z. bijugatus*; 15. LO *F. richardii*; 16. LCO malformed *Discoaster*; 17. LO malformed *Discoaster*; 18. LCO *Rhomboaster* spp.; 19. LO *Rhomboaster* spp.; 20. FO *B. aquilus*; 21. LO *C. bownii*; 22. Absence of *D. diastypus*; 23. FO *D. diastypus*; 24. Presence of *D. araneus*; 25. Presence of *F. tympaniformis*; 26. LO *F. tympaniformis*. The presence of uncorformities is also represented based on literature data. On the left side we show the biostratigraphic synthesis across the PETM after Martini (1971), Aubry et al. (1999), Okada and Bukry (1980), Agnini et al. (2014) and the new PETM zones and sub-zones (PE)

Plate. 1. Micrographs under optical microscope, crossed polars, at 1000X magnification of selected specimens in alphabetic order. Scale bar is 5 μm

Plate. 2. Micrographs under optical microscope, crossed and parallel polars, at 1000X magnification of selected spcimens in alphabetic order. Scale bar is 5 μm

Plate. 3. SEM pictures from selected samples from Site 1209B-22H-1A. Photos were acquired with Phenom SEM G2 PRO microscope at 6000X magnification. Overgrown is clearly visible on *Discoaster* specimens. Early overgrowth occurs in and around the central area of the discoasters then it proceeds outwards along the rays, until the entire ray becomes overgrown (Adelsek et al. 1973). a. Calcite blade; b. Overgrown *Fasciculithus*; c. *F. tympaniformis*; d. Overgrown *D. nobilis*; e. *T. pertusus*; f. Overgrown placolith; g. Nannofossil fragment; h. Overgrown *Toweius*; i., Overgrown *D. multiradiatus*; l. *C. pelagicus*; m. Broken *Calcisphaera*; n. Overgrown *D. mohleri*; o. Overgrown *Fasciculithus*; p. Overgrown placolith

**Table captions**

Table. 1. Distribution of the counted calcareous nannofossils at Site 1209 B. Nannofossil abudances are expressed as follows: abundant (A, >10 %), common (C, 1-10 %), frequent (F; 1-0.1 %) and rare (R; <0.1 %). Stable isotope ratios of bulk-rock samples ($\delta^{13}C_{bulk\ carb}$) measured on the archive-half of core 22H-1 (see text for details).

Table. 2. Distribution of the counted calcareous nannofossils at Site 1263 C/D. Nannofossil abudances are expressed as follows: abundant (A, >10 %), common (C, 1-10 %) %), frequent (F; 1-0.1 %) and rare (R; <0.1 %).

# Chapitre 3. 1. Primary and carbonate productivity changes across the Pliensbachian-Toarcian interval in Mochras Borehole

# Primary and carbonate productivity changes across the Pliensbachian-Toarcian interval in Mochras Borehole

[1]Alessandro Menini, [1,2]Emanuela Mattioli, [3]Stephen P. Hesselbo, [4]Micha Ruhl, [1]Guillaume Suan

[1]Univ Lyon, Univ Lyon 1, ENSL, CNRS, LGL-TPE, F-69622, Villeurbanne, France
[2]Institut Universitaire de France, Paris, France
[3]University of Exter, Camborne School of Mines, UK
[4] Trinity College Dublin, The University of Dublin, Ireland

## 1. Abstract

**The classical scenario for interpreting the lower Toarcian anoxic event (T-OAE; ~183 Ma) and the associated negative carbon isotope event is commonly related to the massive release of $^{12}C$ to the surface reservoirs, because of the emplacement of Karoo-Ferrar LIP, the destabilization of methane hydrates from continental margins, or the thermogenic methane release due to sill emplacement in Karoo-Ferrar. Whatever the cause, this massive carbon release is thought to have favored greenhouse conditions, enhanced hydrological cycle and continental weathering. These conditions finally promoted the delivery of nutrients to shallow basins, supporting the primary productivity and, because of $O_2$ consumption by organic matter respiration, the development of oceanic anoxia.**

**However, several works showed that primary producers, like calcareous nannoplankton and dinoflagellates, experienced a severe crisis during the T-OAE, culminating with a phytoplankton blackout. Also, organic matter fluxes seem to be not exceptional. The analysis of nannofossil size in the Mochras borehole (drilled by the BGS) can help us to solve this conundrum. The sedimentary recovery of the core is excellent, the section is continuous and well-dated and has been the object of high-resolution analyses, that makes it an ideal spot where to analyze the combined evolution of carbonate and primary production. Through combination of biometry and absolute abundances**

**(specimens per g of rock) we can estimate the fluxes of nannofossil-derived carbonates and organic matter to the sediments. We can compare these results to the total organic content of sediments and to the $\delta^{13}C$, which reflects the perturbations of the carbon cycle occurred in the lower Toarcian. This study should enable us to better assess the mechanisms of mineral and organic carbon export from the upper ocean to the sediments during the major climate and environmental changes that occurred in the Toarcian.**

## 2. Introduction

The Early Jurassic was a time of extreme environmental changes: there are well-documented examples of rapid transitions from cold climates to greenhouse events (Price, 1999; Dera et al., 2009; Suan et al., 2010; Korte and Hesselbo, 2011), such as the early Toarcian oceanic event (T-OAE) (~183 Ma ago). The T-OAE (Jenkyns, 1988) is one of the most intense and geographically extensive events of oceanic redox change and organic-carbon burial in the Mesozoic era. A perturbation of the carbon cycle is evidenced by carbon isotopes excursions as recorded in marine carbonate, organic matter, biomarker and fossil wood (e.g., Jenkyns and Clayton, 1997; Hesselbo et al., 2007; Xu et al., 2017-2018, Storm et al., 2020). Organic rich deposits are found across the T-OAE especially in the northern Tethys and these may have resulted from enhanced primary productivity, either from intensified upwelling (Jenkyns, 1988) or from increased continental weathering and runoff (Cohen et al., 2004; Brazier et al., 2015). The alternation between icehouse and greenhouse events caused global sea-level changes (Hesselbo et al., 2000; Hesselbo, 2008; Suan et al., 2010; Pittet et al., 2014) and major biological changes in marine ecosystems (Little and Benton, 1995; Menini et al., 2019). Then, sea-level changes led to condensations and or hiatus in many localities (Pittet et al., 2014; Menini et al., 2019). However, there are evidences that paleoenvironmental perturbations started before the T-OAE, namely at the Pliensbachian-Toarcian boundary (Pl-To) (Bodin et al., 2016; Martinez et al., 2017; Menini et al., 2019). There are several proofs that the paleoenivornmental changes occurring at the time were driven by increased volcanism, linked to the emplacement of large igneous provinces in the Karoo-Ferrar region (Duncan et al., 1997; Hesselbo et al., 2000; Kemp et al., 2005; McElwain et al., 2005; Svensen et al., 2007; Percival et al., 2015). Besides volcanism, other mechanisms might explain the excess of light

carbon inferred by $\delta^{13}C$ records across the T-OAE. Namely, this might be due to thermogenic methane ($CH_4$) from sill intrusion into Gondwanan coal and organic-rich shale, and/or biogenic methane from dissociation of sub-seafloor methane clathrates. The early Toarcian CIE is supposed to have induced a wetter climate in mid latitudes: this drove to an accelerated hydrological cycle that caused an increase in silicate weathering on the continents, and consequent increased fluvial supply of nutrients to the oceans and large inland lakes (Jenkyns et al., 2002; Cohen et al., 2004; Jenkyns, 2010; Dera et al., 2011
; Kemp et al., 2011; Brazier et al., 2015; Xu et al., 2017; Izumi et al., 2018). Enhanced nutrient fluxes caused an increase in primary productivity in the oceans and large lakes as well as enhanced burial of organic matter in these reservoirs, facilitated by local water-column stratification. Organic-carbon burial, coupled to an increase in silicate weathering, eventually drew down the excess of $CO_2$, conducting to an inverse greenhouse effect and global cooling (Schouten et al., 2000; Cohen et al., 2004). There are evidences, especially in northern Europe, of widespread development of anoxic–euxinic (sulphide-rich) bottom waters in restricted basins which intensely affected marine ecosystems (Jenkyns, 2003, 2010; Caswell and Coe, 2013; Hermoso et al., 2013; Ullmann et al., 2014; Danise et al., 2015). Also, globally significant burial of photosynthetically derived (12C-rich) organic matter took place, and this gave rise to a positive (higher δ13C) carbon-isotope excursion (CIE) of ~3‰ in marine carbonate and ~4 ‰ in bulk sedimentary organic matter (Jenkyns et al., 2002; Gradstein et al., 2012; Hermoso et al., 2013). This observed early Toarcian positive CIE was interrupted by the characteristic abrupt negative shift (to lower $\delta^{13}C$) that occurred synchronously with the T-OAE (Jenkyns and Clayton, 1997). Important changes are documented among primary producers at the Pl-To and across the T-OAE. Namely, a turnover in calcareous nannofossil communities is reported at the Pl-To (Menini et al., 2019), while a significant decrease and temporary disappearance in calcareous nannofossil abundance is recorded across the T-OAE (Bucefao Palliani et al., 2002; Mattioli et al., 2004b; Mattioli et al., 2008; Fraguas et al., 2012). During the T-OAE, primary productivity was solely sustained by phototrophic bacteria (Chlorobiaceae) (van de Schootbrugge et al., 2005) or by green algae (*Tasmanites*) (Bucefalo Palliani et al., 2002).

In the last decades several studies focused on the response of calcareous nannofossils to the Late Pliensbachian-Early Toarcian environmental perturbations in the Southern Tethys Ocean (Fig. 1), where several onshore marine sections provide excellent stratigraphic records of this time interval (e.g., Mattioli et al., 2004b; Mattioli et al., 2008; Fraguas et al., 2012; Casellato et al., 2015; Menini et al., 2019). Recent studies have focused on remote settings such as the Néquen Basin (Argentina) (Al-Suwaidi et al., 2016), Andean Basin (Fantasia et al., 2018) or Tibet (Wignall et al., 2006; Fu et al., 2016). However, calcareous nannofossils records in the northern Tethyan margin remain by now less studied. Mochras borehole, in the Cardigan Bay Basin (Wales), is the thickest complete Early Jurassic section, with a total thickness of 1300 m for the Early Jurassic: this time interval is three times thicker at Mochras than coeval onshore sections (Hesselbo et al., 2013) and many sedimentological, geochemical and cyclostratigraphic data are available (e.g., Ruhl et al., 2016; Xu et al., 2018; Storm et al., 2020).

Here, we present new calcareous nannofossils data from the Mochras borehole in order to track changes in primary and carbonate production in response to paleoenvironmental changes across the Late Pliensbachian and Early Toarcian. To do this, we present nannofossil absolute abundance and fluxes and we compare them to available geochemical and sedimentological records. Ultimately, by comparing Mochras with other coeval sections, we discuss the relationship between paleoenvironmental changes and primary production across the Late Pliensbachian-Early Toarcian.

## 3. Geological setting

In the Early Jurassic the western Tethys consisted of shallow epicontinental basins extending between the Laurasian and African landmasses (Fig. 1). Several evidences point to consistent paleoclimatic and paleoceanographic differences between (~27-35 °N) and the southern tropical margin (~17-23 °N). Water masses with distinctive properties have been interpreted for the two domains to explain the different ammonite faunas (Cecca and Macchioni, 2004 and references herein) and the dissimilar calcareous nannofossil assemblages (Bown, 1987; Mattioli et al., 2008). Evidences of more humid climate conditions in the northern margin opposed to a more arid climate in the southern part come from belemnite oxygen isotope composition, clay minerals

and fossil wood assemblages (van de Schootbrugge et al., 2005; Rosales et al., 2006; Dera et al., 2009; Philippe et al., 2017). Thus, the northern margin is characterized by siliciclastic deposits while the southern one is dominated by carbonates. Besides, paleoceanographic reconstructions show that the northern margin corresponded to the wide north European epicontinental shelf while the southern one comprised relatively shallow basins separated by large carbonate platforms (Bassoulet et al., 1993). In the Early Jurassic, Mochras borehole belonged to the Cardigan Bay Basin, at the southern end of the European epicontinental seaway that linked the north-western Tethys to the Boreal Sea (Fig. 1). The core covers some 27 Myr of Early Jurassic history, from the Hettangian to the Toarcian. It was drilled onshore by the British Geological Survey (BGS) and Arberys-coast University, between 1967 and 1969, on the Cardigan Bay cosast, at Llamber, Gwynnedd, northwest Wales (Woodland, 1971; Gradstein et al., 2012; Hesselbo et al., 2013). The Lower Jurassic succession recovered at Mochras (~1300m) is much thicker than coeval onshore sections (Ruhl et al., 2016). All Pliensbachian and Toarcian ammonite zones and sub-zones are present at Mochras (Ivimey-Cook, 1971; Page, 2003; Simms et al., 2004; Copestake and Johnson, 2014). Here the ammonite zones and sub-zones are named by a typifying species (e.g *tenuicostatum* Zone). Calcareous nannofossils occur consistently throughout the core. Besides, belemnites, bivalves, brachiopods and benthic foraminifera occur regularly throughout the core and crinoid ossicles are locally common, but only up to the Pliensbachian. Macroscopic plant debris commonly occurs throughout the Pliensbachian and the Toarcian successions: their occurrence is coeval with levels rich in siliciclastic silt and sand, suggesting relatively close proximity to nearby landmasses (Cope, 1984). The predominant lithology characterized by dark grey mudstones and marl beds, alternated with pale grey limestone beds, suggests a relative open-marine sedimentary environment (Sellwood and Jenkyns, 1975).

## 4. Materials and methods

Forty-seven samples for calcareous nannofossils were prepared following the method described by Beaufort et al., 2014, slightly modified here. A cover slide is weighted before and after a homogenous suspension of dried rock-powder and water (supersaturated with respect to $CaCO_3$ and with a basic *p*H) is let to settle on the cover

slides for 2 hours in a Petri-dish. After settling of the powder, water is carefully aspired with a water pump connected to a micro-pipette in order to avoid any turbulence in the Petri-dish. The residual water on the cover slide is dried, the cover slide is recovered and then attached on a microscope slide using Rhodopass resine. This method allows the quantification od absolute abundances of nannofossils per gram of rock (n/g), using the following formula:

$$x = \frac{n * l * h}{m * A}$$

Where x is the absolute abundance value, n is the number of counted specimens in a slide, l is the length of the cover slide, h is the height of the cover slide, m is the mass of the weighted sample and A is the studied surface of the sample.

Fluxes are calculated by using the following formula:

$$F = X * AR * d$$

where F is the flux (n/m$^2$/yr); X is the absolute abundance of nannofossils (n/g); AR is the accumulation rates calculated on the basis of the age model of Ruhl et al., 2016 for the Late Pliensbachian and new AR for the Early Toarcian, d (g/cm3) is the calcite density (d=2.71).

Sample richness is generally low at Mochras, so we did not count 300 nannofossils for each sample. We counted 200 calcareous nannofossils with a Leica DM750P microscope with a 1000X magnification. Counts of 200 specimens per sample provides us with a probability of ~10 % not to recover a rare species which has relative abundance of 1% in the total assemblage (Hay 1972). Depending of the richness a minimum of 50 up to 100 specimens has been counted in some samples. In 4 samples (820.55, 830.62, 832.61, 880.52m), less than 50 specimens were counted. Six samples are almost barren of calcareous nannofossils (5 specimens over 2 tranverses) and were excluded for the successive data treatment. Particularly, these samples produced artificial peaks in the relative abundance of some species as a consequence of closed-sum effects. However, they were scanned over 4 additional transverses in order to check the presence of biostratigraphically important species. Fatela and Taborda 2002 demonstrate that, for palaeoceanographic studies, counts of 100 specimens have a satisfactory statistical reliability. Each sample was further scanned over two transects to detect rare but biostratigraphically important species. Also, we constructed rarefaction plots based on the method described by Krebs (1998) and Hammer et al., 2001. Through these graphs it is possible to evaluate the theoretical

diversity of samples with respect to a reference sample where species richness is higher. It is possible to estimate when sample size is significant. Namely, when the confidence interval of the tested samples is superimposed to the confidence interval of the reference sample the result can be considered as satisfactory.

The relative abundances of species expressed as percentages are calculated for *Schizosphaerella*, an *incertae sedis* but probably a dinoflagellate cyst (Bown, 1987), respectively to the total nannofossil counts (i.e., coccoliths plus *Schizosphaerella*), while the percentage of coccoliths is calculated with respect to the total coccoliths. Fatela and Taborda (2002) calculated the confidence interval for species with a proportion of 0.1 (i. e., 1 %) when counting 100 individuals. The confidence interval extends from 0.041 to 0.159 around the value of 1 %. This is the reason why in the rest of the manuscript we only discuss taxa representing more than 5 % in the assemblage.

Nannofossil preservation was investigated using a Phenom SEM G2 PRO; on the basis of the degree of etching and overgrowth (Roth et al., 1984), three classes are recognized: poor nannofossil assemblages if strong etching and overgrowth or fragmentation are observed; moderate and good when *Schizosphaerella* fragmentation is limited and delicate coccoliths still preserve intact structures. The nannofossil biostratigraphic record is compared to standard ammonite zones.

The nannofossil biostratigraphic record has been compared to the standard ammonite zones taking into account data available in the literature for the studied sections. Following Gradstein et al. (2012), the abbreviation FO (First Occurrence) is herein used for the first or stratigraphically lowest occurrence of a species in a section (or Base) and LO (Last 140 Occurrence) for the last or stratigraphically highest occurrence of a species in a section (or Top).

# 5. Results

## 5.1. Biostratigraphy

Several first occurrences (FO) and some last occurrences (LO) are recorded across the Late Pliensbachian and the Early Toarcian. *Crepidolithus cavus* (868.32 m),

*Crepidolithus impontus* (872.36 m), *Zeugrhabdothus erectus* (868.32 m), *Lotharingius sigillatus* (884.45 m), *Lotharingius crucicentralis* (868.32 m), *Ethmorhabdus crucifer* (880.52 m) and *Ethmorhabdus gallicus* (870.53 m) appear in the Late Pliensbachian. Much of the FO are recorded around the Pl-To boundary as previous studies observed in other sections (Mattioli et al., 2013; Menini et al., 2019): namely, *B. intermedium* (870.53 m), *Lotharingius velatus* (870.53 m), *Discorhabdus ignotus* (858.55 m), at the Pl-To. The FO of *C. superbus* (842.62 m) is in the Early Toarcian, in the *tenuicostatum* zone. This a crucial moment for the evolutionary history of calcareous nannofossils since it represents the turnover murolith-coccoliths: placolith become increasingly more abundant in the Early Toarcian and will become the most dominant group of the Mesozoic (Bown, 1987; Menini et al., 2019). The FO of *Carinolithus poulnabronei* (822.55 m) is recorded across the T-OAE. In the *falciferum* zone we find the LO of *E. crucifer* and the genus *Watznaueria* appears (774.47 m).

### 5.2. Absolute abundance and flux

Total absolute abundance and flux are calculated by summing absolute abundance and flux values of all the counted species. At Mochras, absolute abundance and flux show the same trend ($R^2$=0.86). Absolute abundance ranges from 1E^6 to 150 E^6 and flux ranges from 6E^6 to 1E^9 (Fig. 2). An overall increasing trend is observed up in the section, with a peak in correspondence of the Pliensbachian-Toarcian boundary (Pl-To), across the 2 ‰ negative excursion in $\delta^{13}C_{org}$ defining the Pl-To. Values are low from 884.45 m to 870.53 m (5E^6 and 50 E^6 respectively) and start to increase at 868.32 m (20 E^6 and 200 E^6 respectively). At the Pl-To we observe an abrupt peak in both absolute abundance and flux (140 E^6 and 1 E^9).

Values decrease after the Pl-To till up going down almost to 0 in some samples corresponding to the T-OAE (*exaratum* Subzone), defined on the base of the negative excursion of both carbonate and organic carbon (Katz et al., 2005; van de Schootbrugge et al., 2005; Xu et al., 2018). In the aftermath of the T-OAE absolute abundance and flux increase relatively to pre-T-OAE values but they are highly fluctuating, similarly to other localities (Mattioli et al., 2004b-2008; Menini et al., 2019).

### 5.3. Assemblages

Despite the presence of slight overgrowth, as observable on the basis of SEM pictures (Bown, 1987), coccoliths' fragile structures, such as spines in *Crucirhabdus primulus* and in *Parhadolithus liasicus*, are intact (This study; Bown, 1987) suggesting an overall good preservation relatively to other coeval sections. Generally Early Toarcian samples are richer than Late Pliensbachian ones. However, Toarcian samples that span the T-OAE present low richness and some are barren.

Calcareous nannofossil assemblages are dominated by *Schizosphaerella* spp., *Lotharingius* spp., *Crepidolithus crassus* and *Similiscutum finchii* (Fig. 3). This is evidenced by both relative and absolute abundances. Other taxa, such as *P. liasicus*, *Crepidolithus* spp., *Bussonius* spp. ecc… are rarer, and usually do not overcome 5%. Here, we decided to separated small-size *Lotharingius* to large-size *Lotharingius*. *L. hauffii*, *L. frodoi* and *L. umbriensis* are grouped into "small-size *Lotharingius*". *L. crucicentralis*, *L. sigillatus* and *L. velatus* are included in "large-size *Lotharingius*". We refer to Menini et al., 2019 for the taxonomic concepts adopted here. Ferreira et al., 2017 show that *Lotharingius* spp. increase in size from the Upper Pliensbachian to the Upper Toarcian and this is related to paleoenvironmental factors. Given that species of the genus *Biscutum* and *Similiscutum* show the same trend in both relative and absolute abundance, we chose to group the whole family Biscutaceae.

We will subdivide the section analyzed here in three parts on the basis of trends in relative and absolute abundance and in the high-resolution $\delta^{13}C_{org}$ isotopes record measured on organic matter (Xu et al., 2018; Storm et al., 2020) similarly to Mattioli et al., 2008

Then section is subdivided as follows:

1. Late Pliensbachian=> up to the Pl-To (900.43- 866.42 m);
2. Lower Toarcian => from the Pl-To to the T-OAE (864.59- 794.56 m);
3. Lower Toarcian=> recovery from the T-OAE (792.33-770.69 m)

1. The Late Pliensbachian corresponds here to the *spinatum* ammonite zone. Samples are generally poor in richness: assemblages are dominated by *Schizosphaerella* spp., small size-*Lotharingius* and Biscutaceae. *Schizosphaerella* spp. relative abundance varies from 30 to 50 %. The most abundant coccoliths are small-size *Lotharingius,* which represent 20 up to 40% of coccolith percentage. Biscutaceae are also abundant in the Late

Pliensbachian and range from 20% to 40 %. Despite of the elevated values of relative abundance, absolute abundance of these species is low from 884.45 m to 870. 53 m, where it never overcomes 1 Eˆ6. Absolute abundance of *Schizosphaerella*, small *Lotharingius* and Biscutaceae start increase at 868.32 m until 858.55 m where they reach in 30 E^6 for *Schizosphaerella*,12 E^6 for small *Lotharingius* and 20 E^6 for Biscutaceae. *Crucirhabdus primulus*, is locally abundant in the Late Pliensbachian (15-20%) but progressively decreases upward in the section. The Pl-To is recognized on the basis of the negative $\delta^{13}C_{org}$ excursion at the boundary between the *spinatum* and the *tenuicostaum* ammonite zones (Xu et al., 2018; Storm et al., 2020; Fig. 3) All taxa show a peak in absolute abundances at the Pl-To (858.55 m) and values are 4 times higher than in the Late Pliensbachian. However, this is not observed in relative abundances: *Schizosphaerella* spp. and Biscutaceae show a decrease followed by an increase across the Pl-To while small-size *Lotharingius* gently increase across the Pl-To. Also large-sized *Lothriangius* increase considerably in percentage across the Pl-To but absolute abundance does not increase in this interval. However, from this moment large-size *Lotharingius* start to become significantly more abundant and relative abundance attain values up to 40%.

2. The negative shift of $\delta^{13}C_{org}$ corresponding to the Pl-To is followed by a gentle positive excursion (860.20-839.44 m) across the *tenuicostaum* zone that precedes the T-OAE (Fig. 3; Xu et al., 2018). *Schizosphaerella* spp. relative and absolute abundances progressively decrease at this stage, small-size *Lotharingius* and Biscutaceae are relatively constant, while *C. crassus* and large-size *Lotharingius* start to increase. Then, $\delta^{13}C_{org}$ values show an abrupt negative shift of ~-5‰ (~ 820 m) across the *exaratum* subzone of *serpentinum* zone (Fig. 3) due to the T-OAE (e.g., Jenkyns et al., 1988; Xu et al., 2018). Absolute abundance of all taxa decrease at this point, attaining lowermost vales (E^6). However relative abundances are different. *Schizosphaerella* spp. show a progressive decrease. The same is for Biscutaceae. Small-size *Lotharingius* relative abundances are more or less constant, while large-size ones show a progressive increase up in the section (Fig. 3a). Also, *C. crassus* shows an increase in abundance from the T-OAE up to the recovery, passing from 3 E^6

at 808.38 m to 20 E^6 at 804.52 m (Fig. 3b). Across the T-OAE we observe a peak in the family Calyculaceae, which features *Calyculus* spp., *C. poulnabronei* and *C. superbus*. The peak is more evident when looking at relative abundance: Calyculaceae are rare or absent before and after the T-OAE but here they attain values of more than 30%.

3. In the aftermath of the T-OAE (800.94-770.69 m), $\delta^{13}C_{org}$ values return to pre-event ones. This is observed in both relative and absolute abundances. At this stage, the most abundant taxa are *C. crassus* and both small and large-size *Lotharingius* spp. (Fig. 3b). While relative abundance of small Lotharingius decrease, absolute one still increase in the aftermath of the T-OAE. Large-size Lotharingius increase in both relative and absolute abundance. This indicates that the increase in large-size *Lotharingius* is not counterbalanced by the decrease in small-sized ones. After the T-OAE, *C. crassus* and large-size *Lotharingius* continue to increase and reach values up to 60%. However, they show a fluctuating trend; namely, in samples where *C. crassus* is dominant, *Lotharingius* are rarer and viceversa. *Schizosphaerella* spp. and Biscutaceae show their lowest values here.

# 5. Discussion

## 5.1. Calcareous nannofossils bioevents: stratigraphic implications

Mochras is the thickest and one of the most-distal Lower Jurassic marine section available up to date (Hesselbo et al., 2003). This is also noticeable by relatively high (l) sedimentation intervals (on average 2.7 cm/kyrs for the studied interval; Ruhl et al., 2016; This work). Theoretically, it should be less affected by condensation problems, which have an impact on the ranking of the bioevents in several Tethyan sections (Menini et al., 2019). Calcareous nannofossils biostratigraphy for the whole Mochras borehole (Hettangian to Toarcian) was previously presented by Bown, 1987, who defined eight nannofossils zones and eleven subzones. The pivotal work by Bown, 1987, slightly modified by Bown, 1988, allowed to refine the Early Jurassic calcareous nannofossil biostratigraphy in the north-Western Tethys and is still today one of the

standard schemes. However, recent advances as by more solid taxonomic concepts (Mattioli and Erba, 1999; Mattioli et al., 2013; Menini et al., 2019; Ferreira et al., 2019) allow us to achieve a higher-resolution than two-decades ago. Several first occurrences (FO) are reported around the Pliensbachian-Toarcian boundary, similarly to southern Tethyan settings (Mattioli et al., 2013; Menini et al., 2019; Ferreira et al., 2019). Also, placolith-coccoliths rapidly increase in abundance through the Late Pliensbachian-Early Toarcian as previously observed (Bown, 1987).

The lowest part of the section belongs to the CN zone NJ-5a, because of the presence of *Lotharingius hauffii* and the absence of *Crepidolithus cavus*. The FO of *C. cavus* marks the base of CN zone NJ-5b: this is recorded just before the onset of the negative excursion of the PI-To. We found this horizon at 868.32 m while Bown, 1987 found it at 866 m, or two meters above our record. The difference between our record and the one by Bown, 1987 can be easily explained by different sampling resolution. However, the taxonomy of this taxon is somehow problematic: Bown, 1987 consider *C. cavus* and *C. impontus* as synonyms while we consider them as the two distinct species (Menini et al., 2019). In our record, *C. impontus* occurs 2 m below *C. cavus* then, regardless of the taxonomic concept adopted, this does not impact the results since the two species occur almost simultaneously. The FO of *Carinoltihus superbus* is a very distinct event at Mochras and marks the zone NJ-6: we found it at 842.62 m while Bown,1987 found it at 824 m. This event is recorded across the positive carbon isotope excursion that follows the PI-To and precedes the T-OAE. Several papers have questioned the synchronism of this biohorizon in northern and in southern Tethys. Mattioli et al., 2004b show that the FO of *C. superbus* is just before the onset of the T-OAE and Menini et al., 2019 reported that is synchronous in both Tethyan and remote ones. While several studies focused on the southern Tethyan margin (e.g., Fraguas et al., 2012; Mattioli et al., 2008; Casellato et al., 2015), few data are available for the northern one. The FO of *C. superbus* at Mochras is also recorded across the positive carbon isotopes excursion, after the PI-To and before the T-OAE. This is coherent with other records coming from both Tethyan and remote sections. The FO of *C. superbus* reported by Bown, 1987 at 824 m coincides in our dataset with an acme of Calyculaceae during the T-OAE (Fig. 3). It is reasonable that, due to the rarity of this species when it firstly appears, Bown, 1987, placed the FO of this taxon in correspondence of this acme of Calyculaceae (Fig. 3b), where *C. superbus* suddenly attains ~15% and Calyculaceae reach 30 % in relative abundance.

Also, Bown, 1987 defines the NJ-7 at Mochras on the base of the FO of *Discorhabdus ignotus* but this has been lately replaced by the FO of *D. striatus*. (Bown, 1998). Previous studies evidenced that the FO of *D. ignotus* occurs at the Pliensbachian-Toarcian boundary (Mattioli et al., 2002; Mattioli et al., 2013; Bodin et al., 2016; Martinez et al., 2017; Menini et al., 2019) but these data mostly come from southern Tethyan sections. At Mochras, we find the FO of *D. ignotus* at 858.55 m, exactly across the Pl-To.

The biostratigraphic marker defining the NJ-7 is the FO of *D. striatus*. We find the FO of *D. striatus* at 770.69 m depth, in the last samples that we analyzed. This is toward the end of the falciferum zone, as previously reported (Bown, 1987).

2)Total calcareous nannofossils absolute abundance and flux

Absolute abundance and flux are five times higher passing from the Pliensbachian to the Toarcian (Fig. 2). A similar increase has already been observed by other authors (Mattioli et al., 2004-2008; Menini et al., 2019) and this is probably due to an increase in primary productivity (Mattioli et al., 2008). An abrupt peak is observed in correspondence of the Pl-To, which is difficult to explain in terms of enhanced primary productivity. The Late Pliensbachian is characterized by relatively cold sea-water temperatures (Morard et al., 2003; Suan et al., 2008a; Korte et al., 2011) and sea level experienced a prominent fall followed by a rapid transgression in the early Toarcian (e.g., Pittet et al., 2014). The alternation between regressions and transgressions gave rise to many condensation levels and/or hiatus in several localities (Menini et al., 2019) which could be at the basis of the observed peak in nannofossil absolute abundances and fluxes. Previous studies documented several episodes of fast regressions in the *polymorphum* zone and the quantification of nannofossil absolute abundance and flux allows to recognize condensed intervals, as aberrant peaks in these parameters are likely due to sediment starvation (Pittet et al., 2014; Menini et al., 2019). Here, we document the presence of condensed intervals at the Pl-To in northern localities and we show that the fast transgression at the Pl-To produced condensed intervals even in more expanded depositional settings, such as Mochras.

Both absolute abundance and flux collapse across the T-OAE (some samples are even barren) and recover in the aftermath of the event (Fig. 2), in agreement with previous studies in other Tethyan sections (Mattioli et al., 2008-2009). Size decrease of

433 *Schizosphaerella* spp. and Biscutaceae also support the crisis of pelagic environments
434 (Mattioli et al., 2004a; Tremolada et al., 2005; Suan et al., 2008a; Mattioli et al., 2008-
435 2009). Besides, shallow-water carbonate platforms recorded a dramatic crisis at the
436 same time and this begun by the Pl-To spanning the entire Early Jurassic (e.g.,
437 Dromart et al., 1996; Blomeier and Reijmer, 1999; Mallarino et al., 2002 add reference
438 papier emanuela 2009). The crisis of neritic environments started about 0.6 Ma before
439 the biocalcification decrease in the pelagic realm, before the T-OAE (Suan et al.,
440 2008b). At Mochras, nannofossil fluxes show the lowest values during the T-OAE (Fig.
441 2) but values start to decrease well below the onset of the event (17 m below), in
442 agreement with data from sections in the UK (Bucefalo-Palliani et al., 2002), N Spain
443 (Tremolada et al., 2005), Portugal, Germany and Italy (Mattioli et al., 2004b-2008-
444 2009; Casellato et al., 2015). This is also coherent with recent data coming from more
445 remote settings, which point to a crisis of pelagic environments even if absolute
446 abundances are not available (e.g., Fraguas et al., 2012; Bodin et al., 2016). We
447 postulate that the T-OAE represents the acme of a longer trend difficulty of marine
448 organisms to calcify that begun around the Pliensbachian-Toarcian boundary (Pl-To
449 event).
450 The marked negative excursion in $\delta^{13}C$ associated with the T-OAE has been explained
451 in several ways. Some authors inferred that this is the result of an injection of $CO_2$ (with
452 light isotope carbon) in the marine and atmospheric carbon reservoirs due to a sudden
453 dissociation of large amounts of metastable methane hydrate from the seabed
454 (Hesselbo et al., 2000; Beerling et al., 2002; Cohen et al., 2007). It seems that the
455 release of methane occurred in pulses (Kemp et al., 2005). Alternatively, the input of
456 isotopically light carbon from the release of thermogenic methane occurred because
457 of magma intrusion of Gondwana coals by Toarcian aged Karoo-Ferrar dolerites
458 (McElwain et al., 2005; Svensen et al., 2007). During the T-OAE, both mechanisms
459 are consistent with elevated $pCO_2$ (900-100 ppmv; Beerling et al., 2002; McElwain et
460 al., 2005). Effectively elevated $pCO_2$ could account for biocalcification crisis. Studies
461 on modern corals show that calcification is hampered by elevated marine and
462 atmospheric $CO_2$ (Gattuso et al., 1998). However, studies on modern coccolithophores
463 do not indicate a direct effect of increased $pCO_2$ on calcification, since the response is
464 species specific (Bollman, 1997; Hendiriks and Renaud, 2004; Iglesias-Rodriguez et
465 al., 2008). An indirect role of increased $pCO_2$ on nannofossils has also been
466 demonstrated for PETM (Gibbs et al., 2016). The hypothesis that high *p*CO2 was

responsible for the nannofossils biocalcification crisis during the T-OAE has already been advanced by Mattioli et al., (2004b), Erba (2004) and Tremolada et al., (2005) and evidences exist that increased $CO_2$ levels were likely responsible for the drastic decrease in nannofossil fluxes across the Weissert OAE (Valanginian) and the OAE 1a (Aptian) (Erba and Tremolada, 2004). As observed by Mattioli et al., 2009, this doesn't explain the reason why, for the T-OAE, the carbonate crisis affected earlier neritic environments than planktonic ones.

Blomeier and Rejimer, 1999 suggest that the demise of a carbonate platform in Morocco was due to an environmental deterioration in platform settings owing to either a nutrient input or a decrease in sea-surface temperature.

Several evidences indicate a climatic deterioration from the Pliensbachian to the Toarcian. Temperature decreased in various Tethyan settings (McArthur et al., 2000; Bailey et al., 2003; Rosales et al., 2004; Suan et al., 2008a; Gómez et al., 2008). The decrease in temperature likely caused sedimentary condensations and-or hiatus in many Tethyan settings that expanded till up the first Toarcian ammonite zone (Guex et al., 2001; Morard et al., 2003; Pittet et al., 2014). This was probably driven by glacioeustaic mechanisms (Guex et al., 2001; Morard et al., 2003; Pittet et al., 2014). Therefore, the crisis in neritic settings seems to be due to both cooling and nitrification of surface waters. Sea level low caused a reduction of space where carbonate platforms could develop. Then the crisis of carbonate platforms is not directly related to an increase in *p*CO2 and the subsequent decrease in oceanic carbonate saturation state (Mattioli et al., 2009).

An increase in $pCO_2$ might have in turn caused ocean acidification, as suggested for the PETM (Zachos et al., 2005). The shallowing of the lysocline and the calcite compensation depth (CCD) during the T-OAE might be responsible for the observed demise in nannofossil abundance. If this is true for deep oceanic sites, as the one studied by Zachos et al., 2005 for the PETM, it must be noticed that all Early Jurassic sections belonged to epicontinental basins that were always above the CCD during the Early Jurassic (<200m). If we assume, as for the PETM, that the CCD shallowed of ~2 km in open oceanic settings, it is improbable that Mochras and other Tethyan sections were above it during the event. Moreover, delicate coccoliths are always present during the event and this is at the odds with the hypothesis of dissolution.

So, we can ask ourselves if the low nannofossil fluxes during the T-OAE are directly related to an increase of $pCO_2$ and the subsequent sea-water carbonate saturation

501 decrease. Alternatively, the reduction in pelagic carbonate production was indirectly
502 controlled by environmental changes induced by the $pCO_2$ increase. Namely,
503 increased hydrological cycle and the discharge of freshwater into the epicontinental
504 basins of the western Tethys. The development of a more humid climate during the
505 event might associated to an increase in sea water temperature from the second half
506 of the *tenuicostatum* ammonite zone, could have favored a general sea level rise. This
507 might have facilitated the connections between the Arctic Ocean and the western
508 Tethys. Bjerrum et al., (2001) already discussed the southward flow of low-saline water
509 masses from the Arctic Ocean over the Tethyan high-saline ones. This phenomenon
510 might have then amplified the effect of a more humid climate, drastically reducing the
511 surface water salinity (mostly in NW Tethys, that was connected to the Arctic Ocean
512 through the Laurasian seaway). This is coherent with our data at Mochras, where low-
513 salinity tolerant species show a peak in abundance during the T-OAE (see following
514 section for details) while other species temporarily either disappear or drastically
515 decrease in abundance.
516 It must be said that few modern coccolith species tolerate low-salinity environments
517 (Bukry, 1974). Salinity can be an important factor controlling coccolith both abundance
518 and size. Also, coccospheres with a reduced number of coccoliths are typical of Arctic
519 and Subartic regions where weakly saline waters form in response to seasonal melt
520 water (Winterer et al., 1994).
521
522 3) Nannofossil assemblages across the Late Pliensbachian and the Early Toarcian
523
524 The Late Pliensbachian and Early Toarcian represent a significant acceleration in the
525 evolution rate in the history of calcareous nannofossils (Bown et al., 2004). At Mochras,
526 that values abruptly increase at the Pl-To similarly to other northern and southern
527 Tethyan sections (Mattioli et al., 2008; Fraguas et al., 2012; Ferreira et al., 2015;
528 Menini et al., 2019). While the originations of placolith coccoliths are numerous in this
529 time interval, there are not originations of murolith coccoliths. Biscutaceae and
530 *Lotharingius* spp. become dominant assemblage components in the aftermath of the
531 Pl-To. Then, across the T-OAE, *C. crassus* and large-size *Lotharingius* become
532 dominant components.
533 Nannofossil assemblages change significantly across the early Toarcian CIE; as also
534 suggested for other Tethyan localities (Mattioli et al., 2008) this parallels the long-term

(~2Ma) evolution of environmental conditions (Suan et al., 2008b). We exclude a control on differential preservation on the nannofossil trends observed, since preservation is overall good across the section. The only samples where signs of poor preservation are present were removed from the data set. Here we will discuss changes in nannofossils assemblages over the studied interval.

*Pre-event*

Pre-event conditions correspond to the Late Pliensbachian and Lower Toarcian, including the Pl-To CIE and the positive CIE in the aftermath of the Pl-To. Assemblages are here dominated by *Schizosphaerella* spp., small-size *Lotharingius* and Biscutaceae, which are taxa with nutrient affinity (Mattioli et al., 2004a; Mattioli et al., 2008). Also, taxa with northern affinity (i.e., *C. primulus, P. liasicus, T. patulus, C. cavus*) are abundant in this interval (Bown, 1987; Mattioli et al., 2008). Therefore, this record can be interpreted in terms of the occurrence of cool surface waters associated with high productivity and fertility. Several evidences of relatively cool sea water temperature exist for the Tethys during this time. The Late Pliensbachian is interpreted as a cooling period (Morard et al., 2003; Suan et al., 2008a-b; Korte et al., 2011; Gómez et al., 2016). Oxygen isotopes measured on Late Pliensbachian belemnites rostra indicate sea-temperature of 12-13° in northern Spain (Rosales et al., 2004; Gómez et al., 2008) and brachiopod shells (Suan et al., 2008a) suggest temperature of 13-16° for bottom waters in the Lusitanian basin (Portugal). Also, evidences of a severe cooling event at that time come from fossil wood (Philippe and Thevenard, 1996; Philippe et al., 2017). These authors show that *Xenoxylon*, a taxon adopted to cold, wet conditions, extended his distribution southward. Indirect proxies also suggest cold conditions at the time: the stomatal index measured on mesofossil leaves from the eastern Danish basin suggest low $pCO_2$ across the first Toarcian ammonite zone (*tenuicostatum*) (McElwain et al., 2005). Moreover, glendonites and dropstones in Late Pliensbachian sediments from high latitudes, suggest low temperature and continental ice (Price, 1999; Suan et al., 2015). Likely high sea water fertility happened at the time, since assemblages are dominated by schizospherellids and small-size coccoliths. This is in agreement with what observed in other settings (Mattioli et al., 2004b, Mattioli et al., 2008). A decoupling in *Schizosphaerella* spp. relative and absolute abundances is observed at the Pl-To: while relative abundances suggest a decrease in

*Schizosphaerella* spp. across the Pl-To, absolute abundances show a peak (Fig. 3). The decrease in *Schizosphaerella* spp. relative abundance is coherent with Tremolada et al., 2005 but, as stressed by Mattioli et al., 2008 and Menini et al., 2019, this result might be due to close-sum effects. A peak in absolute abundances of all species is observed at the Pl-To as well as in the total absolute abundance as described in the previous chapter and this is probably due to condensation levels or hiatus. High surface water in this interval is also indicated by the occurrence of mesotrophic taxa such as Biscutaceae, in agreement with Mattioli and Pittet, 2002 and Tremolada et al., 2005. This is coherent with the $\delta^{13}C$ records at Mochras by Xu et al., 2018 and Percival et al., 2016 and with the one of other sections (e.g., Hesselbo et al., 2007).

*T-OAE*

In correspondence of the T-OAE, there is a remarkable peak in *Calyculaceae*, since they attain 30% of coccoliths. Absolute abundances and fluxes are the lowest in this interval similarly to what observed by Mattioli et al., 2008 at Dotternhausen (Germany). Mattioli et al., 2008 interpreted the peak of *Calyculaceae* in other Tethyan settings during the T-OAE as due to low salinity. Studies on dynoflagellates are in agreement with this both at Mochras (van de Schootbrugge et al., 2005) and in other Tethyan sites (Bucefalo-Palliani et al., 2002; Mattioli et al., 2004b). At Mochras, during the event, the primary productivity was solely sustained by prasinopythes (green algae) and in other sites it was both sustained by prasinopythes and Chlorobiaceae (phototrophic bacteria) (van de Schootbrogge et al., 2005). These organisms replaced nannofossils (Mattioli et al., 2008) and dynoflagellates during the event (Bucefalo-Palliani et al., 2002; van de Schootbrugge et al., 2005) and they can thrive in conditions of extremely low salinity. Few modern species can tolerate low-salinity (S<15-20ppt) environments (Paasche, 1968). Evidences of low salinity from the northern Tethyan margin is also supported by belemnite rostra data from both UK and German sections (after correction using Mg/Ca) (McArthur et al., 2000; Bailey et al., 2003) and from Dotterhausen (Germany) extremely low $\delta^{18}O$ values of bulk sediment (Röhl et al., 2001; Schmid-Röhl et al., 2002).

Low surface water salinity during the event might be due to increased river inflow (Röhl et al., 2001) or southward flow of low density Arctic waters into the Tethys (Bjerrum et al., 2001). At Mochras, evidences of increased continental weathering during the T-

OAE also come from osmium isotopes ($\delta^{187}Os$) (Percival et al., 2015-2016) and from elevated kaolinite/illite ratio (Xu et al., 2018). The low salinity might have produced stratification of surface waters, favoring anoxia (Farrimond et al., 1989; Prauss et al., 1991; Bucefalo-Palliani et al., 2002) that sometimes reached the photic zone. At Mochras, high pyrite concentrations and limited presence of the biomarkers gammacerane and isorenieritane in the sediment corresponding to the T-OAE, suggest transient photic zone euxininia and episodic anoxia at the seafloor (Xu et al., 2018). Intermittent anoxia could have further hampered nannofossils and dynoflagellate production. It is reasonable that salinity fluctuated significantly during the event and that when it approached "normal" conditions, a diverse nannofossils assemblage could develop.

If the photic zone was low saline and occasionally attained anoxic conditions this has a consequence on the interpretation of species of the family Calyculaceae, namely *Calyculus spp*., *C. superbus* and *C. poulnabronei*. Bufefalo Palliani and Mattioli, 1998 and Erba 2004 interpreted *Calyculus* as deep and intermediate dweller, respectively. More reasonably, it was a shallow dweller, tolerant to low salinity conditions and anoxia (Mattioli et al., 2008-2009; Clémence et al., 2015). The same for *Carinolithus*, in agreement with Clémence et al., 2015. It is reasonable that *Calyculus* and *Carinolithus* had similar palaeoecological affinities since *Carinolithus* evolved from *Calyculus* in the lower Toarcian (Mattioli et al., 1996). Besides, Calyculaceae closely resemble to modern coccolith *Umbellosphaera*. The species belonging to this genus, thrive in very shallow water (<80-100 m) in contexts of very low nitrate concentrations (Thierstein et al., 2004). *Umbellosphaera* is characterized by a "double-layered" coccosphere, with an extra cellular space that may serve to store nutrients or trap water (Young, 1994). Mattioli et al., 2008 state that the coccosphere of *Calyculus* might have functioned for similar purposes. Otherwise, it is also possible that the additional space served to reduce the overall hydrodynamic density of the organism by trapping water of relatively low density. This could have helped *Calyculus* to keep their position in proximity of the surface in presence of stratified waters.

This might also be true for *Carinolithus*, given that the structure of the two coccoliths is similar. *Carinolithus* is characterized by more developed vertical elements, and a progressive closing of the axial canal from *C. poulnabronei* to *C. superbus* (Mattioli, 1996). Given that the coccoliths of the genus *Carinolithus* present more developed vertical elements, the coccosphere might have been even further adapted to trap

635 water, store nutrients or ultimately reduce hydrodynamic density in low salinity
636 conditions.
637 Site belonging to the southern Tethyan margin are characterized by high proportion of
638 *Mitrolithus jansae* (Mattioli et al., 2008 and references herein) while it is nearly absent
639 along the northern Tethyan margin. *M. jansae* presumably was a deep dweller (Mattioli
640 and Pittet, 2004a; Mattioli et al., 2008; Casellato et al., 2015), that dominated over
641 other coccoliths in times of stratification of the water column but when anoxia still did
642 not reach the lower photic zone. It is possible that in northern settings anoxia expanded
643 more frequently into the photic zone (Pancost et al., 2004). Alternatively, temperature
644 or light penetration were not adequate, and irradiance was not sufficient to support the
645 development of *M. jansae*. Modern coccolith species *Florisphaera profunda*, which is
646 a deep dweller, exhibits a similar sharp decrease in abundance between 30° and 40°
647 N in the Pacific (Okada and Honjio, 1973).
648
649 *Post T-OAE*
650
651 After the CIE of the T-OAE, assemblages are dominated by *Lotharingius* and
652 *Crepidolithus crassus*, a deep dweller (Bour et al., 2007; Mattioli et al., 2008). These
653 observations are generally in agreement with what has already been observed by other
654 authors in other both northern and southern Tethyan settings (e.g., Tremolada et al.,
655 2005; Mattioli et al., 2008; Fraguas et al., 2012; Casellato et al., 2015). Namely, we
656 observe successive pulses of *Lotharingius* and *C. crassus* and here these are
657 interpreted in terms of gradual recovery to “normal” conditions, after the widespread
658 eunixia-anoxia. This could also be facilitated by more effective connections between
659 the different basins due to the high sea level at the time (Pittet et al., 2014). Alongside
660 with the increase in abundance, *Lotharingius* start to increase in size at the time
661 (Ferreira et al., 2017). In the aftermath of the T-OAE, more stable conditions might
662 have favored *Lotharingius* increase in size, as already observed for Cenozoic
663 foraminifera and palaeoceanographic perturbations (Ferreira et al., 2017 and
664 references herein)
665 *Lotharingius* probably dwelled in shallow water with high-moderate nutrient
666 concentrations (Pittet and Mattioli, 2002; Mattioli and Pittet, 2004; Mattioli et al., 2008;
667 Casellato et al., 2015) and the pulse of these species in the aftermath of the T-OAE
668 signifies increased nutrient input to surface waters. Then, *C. crassus* definitely

dominates the assemblages in the aftermath of the T-OAE, in times of reduced species diversity. Given that *C. crassus* was a deep dweller (Bour et al., 2007; Mattioli et al., 2008), this might suggest a progressive deepening of anoxia and a restoration of the deep photic zone communities, in agreement with the recovery interval of marine inverterbrates (Harries and Little, 1999) Absolute abundances and fluxes are elevated in this time interval (~100 E^6) and this is coherent with the positive $\delta^{13}C$ positive excursion of the late Early Toarcian (Jenkyns, 1988) also observed at Mochras (Xu et al., 2018). Accordingly, to literature data, this can be interpreted in terms of high productivity in the surface water of the western Tethys.

Also, taxa with northern affinity such as *P. liasicus*, *C. cavus* and *C. primulus* (Bown, 1987; Mattioli et al., 2008) drastically decrease in abundance in this time interval at Mochras and this might be due to the rapid radiation of placolith coccoliths, such as *Lotharingius*. This phenomenon already started at the Pl-To event, where placolith-coccolith rapidly conquer the nannofossil assemblages (Menini et al., 2019). Perhaps more effective connections between western Tethys basins, coupled to a more greenhouse climate, facilitated the spread of placolith-coccoliths which increased both in abundance and in size. Ultimately, the favorable conditions for placolith-coccoliths might also be at the origin of the first occurrence of species of the genus *Watznaueria*, that will finally dominate the oceans for the rest of the Mesozoic era.

4) Comparison with an independent proxy: magnetostratigraphy and Karoo traps volcanism

Xu et al., 2018 published a magnetostratigraphic record of the entire Toarcian stage for the Mochras core. The Pliensbachian-Toarcian boundary is characterized by the inversion of the magnetic polarity from reverse to normal (T-R0-T-N1). The first two Toarcian ammonite zones (*tenuicostatum* and *serpentinum*) are characterized by two normal and two reverse chrons. Comas-Rengifo et al., 2010 studied magnetostratigraphy at the Almunacid de la Cuba section (Spain), located at a few kilometers from La Almunia section and high-resolution calcareous nannofosil data and C-isotopes stratigraphy exist for this section (Menini et al., 2019). Almunacid de la Cuba section has also been used in Rocha et al., 2016 as an additional section to define the Toarcian GSSP at Peniche (Portugal), since magnetostratigraphy did not provide satisfactory results at Peniche (see Rocha et al., 2016 for details). Xu et al.,

2018 show that there is a good correlation between Almunacid de la Cuba and Mochras magnetostratigraphic record: this provides us with an independent proxy to compare Tethyan sections to the Karoo Large Igneous Province reversed/normal polarity succession, and hence the possible projection of Karoo ages onto the Pl-To (Fig. 4). The carbon cycle perturbations at the Pl-To and in the Early Toarcian have been linked to the emplacement of Karoo traps and associated release of volcanogenic $CO_2$ and methane from biogenic sources and sub-seafloor clathrates (Duncan et al. 1997; McElwain et al. 2005; Svensen et al. 2007; Percival et al. 2015, 2016). Increased sedimentary mercury concentrations at the Pl-To and during the T-OAE further support enhanced volcanic activity at the time (Percival et al., 2015-2016). Across the Pl-To CIE and the positive CIE just below the T-OAE, several nannofossil species show their first occurrence and this has been found in several Tethyan and remote settings (Menini et al., 2019). The most relevant for supraregional correlations are the first occurrence of *D. ignotus a*cross the Pl-To CIE, and *C. superbus* across the positive C isotopes excursion preceding the T-OAE CIE (Fig. 4). Bio- and magnetostratigraphic correlation of the Pliensbachian-Toarcian boundary at Mochras and Almonacid De La Cuba, and consequent magnetostratigraphic correlation to the Karoo volcanic succession from the Lebombo volcanic rift margin and the Drakensberg Group in northern Lesotho, southern Africa, suggest that the three normal-polarity magnetozones there correspond to the N1 and N2 magnetozones in the Mochras core (Fig. 4; Riley et al. 2004; Comas-Rengifo et al. 2010; da Rocha et al. 2016). In all Tethyan, sections, the FO of *D. ignotus* is recorded in correspondence of this inversion of the magnetic polarity (from reverse to normal) at the Pliensbachian-Toarcian boundary. This allows to correlate Tethyan sections to Karoo lavas and to project Karoo ages onto the FO of *D. ignotus*: $^{40}Ar/^{38}Ar$ which provides an age of 182.7±0.8 Ma for the Pliensbachian-Toarcian boundary (Duncan et al., 1997) and this age ca be projected onto the FO of this species (Fig. 4). Similarly, the FO of *C. superbus*, is recorded in the middle of a normal chron in Tethyan sections (TN1 at Mochras, N3 at La Almunia) and this chron is also well represented at Karoo (Fig. 4. Radiometric ages of basalts belonging to this chron provide an age of 181. 2 ±1.0 Ma. Menini et al., 2019 have highlighted that the FO of *C. superbus* is synchronous in both tethyan and remote settings and, on the basis of radiometric ages and magnetostratigraphy, we can anchor this bioevent to the Karoo record.

Our age model for the Early Toarcian at Mochras, indicates that the timing between the FO of *D. ignotus* and *C. superbus* is approximately 770 kyrs, and this is coherent (within the error bars) with the results provided by radiometric ages. Previous studies suggested that the timing between the FO of these two taxon is either 500 in Morocco or 433 kyrs at Peniche (Martinez et al., 2017). A slightly longer interval at Mochras could be the result sedimentological artefacts, a primary difference between northern and southern tethyan sections or both factors. At Peniche, Pittet et al., 2014 discuss the presence of a hiatus near the FO of *C. superbus*. Moreover, the Pl-To boundary in the Peniche section is condensed (Pittet et al., 2014; Martinez et al., 2017). Martinez et al., 2017 evidenced that at Foum Tillicht section some condensation levels exist from the FO of *D. ignotus* to the FO of *C. superbus*, affecting the timing between the events. Alternatively, differences could reflect the slight diachronous nature of these biohorizons from northern to southern Tethyan sections.

Being the thickest Lower Jurassic section, characterized by the highest sedimentation rates, we support the idea that longer timing between the FO of these taxa are due to the presence of condensation levels or hiatus, that in sections characterized by lower sedimentation rates (e.g., Peniche), lead to a more imprecise estimation of timings. In any case, at Mochras we evidenced the presence of condensation levels at the Pl-To, meaning that sea-levels changes affected the stratigraphic record also in this locality.

In any case, the correlation between Mochras, Almunacid de la Cuba (and in turn the GSSP at Peniche, Portugal) with Karoo lavas allows to unambiguously relate calcareous nannofossils events to magnetic chrons. Finally, the integration of high-resolution calcareous nannofossils biostratigraphy and magnetostratigraphy provide us with a powerful tool to link Late Pliensbachian-Early Toarcian environmental perturbations recorded in both northern and southern Tethyan sediments to the emplacement of the Karoo Large Igneous Province and to project Karoo ages onto the micropaleontological record.

## 6. Conclusions

We presented new calcareous nannofossils data from the Mochras borehole (Cardigan Bay Basin, UK), the thickest Lower Jurassic sections. The good preservation and abundance of nannofossils allows the establishment of a refined biostratigraphy in the northern Tethyan margin, which remains by now less studied than the southern one.

Thanks to the quantification nannofossil absolute abundance and fluxes we show that these organisms were very sensible to changes in paleoenvironmental conditions spanning the Late Pliensbachian and the Early Toarcian. This time interval saw the rise in abundance of placolith-coccoliths through the Pliensbachian-Toarcian boundary. During the T-OAE assemblages were typically dominated by Calyculaceae, which could sustain stressed environments. As previously reported, this time interval is a fundamental step in the evolution of this group of marine algae: large-size *Lotharingius* increased in abundance in the aftermath of the T-OAE as previously reported for other Tethyan sections. The correlation between Mochras, the GSSP in Peniche and La Almunia with Karoo lavas allows to unambiguously relate CN events to magnetic chrons and to finally link the environmental perturbations recorded in the western Tethys to Karoo volcanism.

## References


- Al-Suwaidi, A.H., Hesselbo, S.P., Damborenea, S.E., Manceñido, M.O., Jenkyns, H.C., Riccardi, A.C., Angelozzi, G.N., Baudin, F., 2016. The Toarcian Oceanic Anoxic Event (Early Jurassic) in the Neuquén Basin, Argentina: A Reassessment of Age and Carbon Isotope Stratigraphy. The Journal of Geology.
- Bailey, T. R., Y. Rosenthal, McArthur, J.M., van de Schootbrugge, B., Thirlwall M. F., 2003. Paleoceanographic changes of the late Pliensbachian- early Toarcian interval: A possible link to the genesis of an oceanic anoxic event, Earth and Planetary Sciences Letters 212, 307–320.
- Bassoullet, J.P., Elmi, S., Poisson, A., Cecca, F., Bellion, Y., Guiraud, R., Baudin, F., 1993. Mid Toarcian. In: Dercourt, J., Ricou, L.E., Vrielynck, B. (Eds.), Atlas Tethys Paleoenvironmental Maps, BEICIP-FRANLAB, Rueil-Malmaison. 63–80.
- Beaufort, L., Barbarin, N., Gally Y, 2014. Optical measurements to determine the thickness of calcite crystals and the mass of thin carbonate particles such as coccoliths. Nature Protocols 9, 633-642.
- Blomeier, D.P.G., Reijmer, J.J.G., 1999. Drowning of a lower Jurassic carbonate platform: Jbel Bou Dahar, High Atlas, Morocco. Facies 41, 81–110.
- Bodin, S., Krencker, F. N., Kothe, T., Hoffmann, R., Mattioli, E., Heimhofer, U., Kabiri, L., 2016. Perturbation of the carbon cycle during the late Pliensbachian - early Toarcian: New insight from high-resolution carbon isotope records in Morocco. Journal of African Earth Sciences 116, 89–104.
- Bour, I., Mattioli, E., Pittet, B.,2007. Nannofacies analysis as a tool to reconstruct paleoenvironmental changes during the Early Toarcian anoxic event. Palaeogeography, Palaeoclimatology, Palaeoecology 249(1–2), 58–79.
- Bown, P.R., 1987. Taxonomy, evolution and biostratigraphy of Late Triassic-early Jurassic calcareous nannofossils. Special Papers in Paleontology 38, 1–118.

- Bown, P.R., Cooper, M.K.E., 1998. Jurassic. In: Bown, P.R. (Ed), Calcareous Nannofossil Biostratigraphy, British Micropalaeontological Society Series. Chapman and Hall/Kluwer Academic Publishers, London, 86–131.
- Brazier, J. M., Suan, G., Tacail, T., Simon, L., Martin, J. E., Mattioli, E., and Balter, V., 2015. Calcium isotope evidence for dramatic increase of continental weathering during the Toarcian oceanic anoxic event (Early Jurassic). Earth and Planetary Science Letters 411, 164–176.
- Bucefalo Palliani, R. B., Cirilli S., Mattioli E., 1998. Influences of the relative sea level fluctuations on the primary productivity, an example from the early Toarcian Umbria-Marche basin (central Italy), Palaeogeogeography, Palaeoclimatology and Paleoecology 142, 33–50.
- Casellato, C.E., Erba, E., 2015. Calcareous nannofossil biostratigraphy and paleoceanography of the toarcian oceanic anoxic event at colle di sogno (Southern Alps, Northern Italy). Rivista Italiana di Paleontologia e Stratigrafia 121, 297–327.
- Cecca, F., Macchioni, F., 2004. The two Early Toarcian (Early Jurassic) extinction events in ammonoids. Lethaia 3, 35–56.
- Clémence, M. E., Gardin, S., Bartolini, A. 2015. New insights in the pattern and timing of the Early Jurassic calcareous nannofossil crisis. Palaeogeography, Palaeoclimatology, Palaeoecology 427, 100–108.
- Cohen, A. S., Coe, A. L., Harding, S. M., & Schwark, L. (2004). Osmium isotope evidence for the regulation of atmospheric CO2 by continental weathering. Geology, 32(2), 157–160.
- Comas-Rengifo, M. J., Gómez, J. J., Goy, A., Herrero, C., Osete, M. L., Palencia, A., 2010. A complementary section for he proposed Toarcian (Lower Jurassic) global stratotype: the Almonacid de la Cuba sections (Spain). Stratigraphy and Geological Correlation 18, 133–152.
- Cope, J.C.W., 1984. The Mesozoic history of Wales. Proc. Geol. Assoc.95, 373–385.
- Copestake, P., Johnson, B., 2014. Lower Jurassic Foraminifera from the Llanbedr (Mochras Farm) Borehole, North Wales, UK. Monograph of the Palaeontographi-cal Society 167.

- Dera, G., Neige, P., Dommergues, J. L., Brayard, A., 2011. Ammonite paleobiogeography during the Pliensbachian–Toarcian crisis (Early Jurassic) reflecting paleoclimate, eustasy, and extinctions. Global and Planetary Change, 78(3-4), 92–105.
- Dera, G., Pucéat, E., Pellenard, P., Neige, P., Delsate, D., Joachimski, M. M., et al., 2009. Water mass exchange and variations in seawater temperature in the NW Tethys during the Early Jurassic: evidence from neodymium and oxygen isotopes of fish teeth and belemnites. Earth and Planetary Science Letters 286(1–2), 198–207.
- Dromart, G., Allemand, P., Garcia, J.-P., Robin, C., 1996. Variation cyclique de la production carbonatée au Jurassique le long d'un transect Bourgogne-Ardèche, Est-France. Bulletin de la Société Géologique de France 167, 423–433.
- Duncan, R. A., Hooper, P. R., Rehacek, J., Marsh, J. S., Ducan, A. R., 1997. The timing and duration of the Karoo igneous sevent, southern Gondwana. Journal of Geophysical Research 102, 127–138.
- Erba, E., 2004. Calcareous nannofossils and Mesozoic oceanic anoxic events. Marine Micropaleontology 52 (1–4), 85–106.
- Fantasia, A., Föllmi, K. B., Adatte, T., Spangenberg, J. E., Montero-Serrano, J. C., 2018. The Early Toarcian oceanic anoxic event: Paleoenvironmental and paleoclimatic change across the Alpine Tethys (Switzerland). Global and Planetary Change 162, 53–68.
- Farrimond, P., G. Eglington, and S. C. Brassel, 1989. Toarcian anoxic event in Europe: An organic geochemical study, Marine and Petroleum Geology 6, 136–147.
- Fatela, F., & Taborda, R., 2002. Confidence limits of species proportions in microfossil assemblages. Marine Micropaleontology 45(2), 169–174.
- Ferreira, J., Mattioli, E., Suchéras-Marx, B., Giraud, F., Duarte, L. V. et al., 2019. Western Tethys Early and Middle Jurassic calcareous nannofossil biostratigraphy. Earth-Science Review 197.
- Ferreira, J., Mattioli, E., van de Schootbrugge, B., 2017. Palaeoenvironmental vs. evolutionary control on size variation of coccoliths across the Lower-Middle Jurassic, Paleogeography, Paleoclimatology, Paleoecology. 465, 177–192.

- Fraguas, Á., Comas-Rengifo, M. J., Gómez, J. J., Goy, A., 2012. The calcareous nannofossil crisis in Northern Spain (Asturias province) linked to the Early Toarcian warming-driven mass extinction. Marine Micropaleontology 94–95, 58–71.
- Fu, X., Wang, J., Feng, X., Wang, D., Chen, W., Song, C., Zeng, S., 2016. Early Jurassic carbon-isotope excursion in the Qiangtang Basin (Tibet), the eastern Tethys: Implications for the Toarcian Oceanic anoxic event. Chemical Geology 442, 62–72.
- Gradstein, F. M., Ogg, J. G., Schmitz, M. B., Ogg, G. M., 2012. The geologic time scale.
- Hay, W.W., 1972. Probabilistic stratigraphy. Eclogae Geologicae Helveticae 65, 255–266.
- Hesselbo, S. P., Bjerrum, C. J., Hinnov, L. A., MacNiocaill, C., Miller, K. G., Riding, J. B., van de Schootbrugge, B., 2013. Mochras borehole revisited: a new global standard for Early Jurassic earth history.
- Hesselbo, S. P., Gröcke, D. R., Jenkyns, H. C., Bjerrum, C. J., Farrimond, P., Bell, H. S. M., Green, O. R., 2000. Massive dissociation of gas hydrate during a Jurassic oceanic anoxic event. Nature 406(6794), 392–395.
- Hesselbo, S. P., Jenkyns, H. C., Duarte, L. V., & Oliveira, L. C. (2007). Carbon-isotope record of the Early Jurassic (Toarcian) Oceanic Anoxic Event from fossil wood and marine carbonate (Lusitanian Basin, Portugal). Earth and Planetary Science Letters 253(3–4), 455–470.
- Hesselbo, S.P., 2008. Sequence stratigraphy and inferred relative sea-level change from the onshore British Jurassic. Proceedings of the Geologists' Association 119, 19–34.
- Ivimey-Cook, H.C., 1971. Stratigraphical palaeontology of the Lower Jurassic of the Llanbedr (Mochras Farm) Borehole. In: Woodland, A.W. (Ed.), The Llanbedr (Mochras Farm) Borehole. Institute of Geological Sciences, 87–92.
- Izumi, K., Kemp, D. B., Itamiya, S., Inui, M.,2018. Sedimentary evidence for enhanced hydrological cycling in response to rapid carbon release during the early Toarcian oceanic anoxic event. Earth and Planetary Science Letters 481, 162–170.

- Jenkyns, H. C., 2010. Geochemistry of oceanic anoxic events. Geochemistry, Geophysics, Geosystems 11(3).
- Jenkyns, H. C., Jones, C. E., Gröcke, D. R., Hesselbo, S. P., Parkinson, D. N., 2002. Chemostratigraphy of the Jurassic System: applications, limitations and implications for palaeoceanography. Journal of the Geological Society 159(4), 351–378.
- Jenkyns, H.C., 1988. The Early Toarcian (Jurassic) anoxic event: stratigraphic, sedimentary and geochemical evidence. Am. J. Sci. 288, 101–151.
- Jenkyns, H.C., Clayton, C.J., 1997. Lower Jurassic epicontinental carbonates and mudstones from England and Wales: chemostratigraphic signals and the early Toarcian anoxic event. Sedimentology, 44: 687–706.
- Katz, M. E., Wright, J. D., Miller, K. G., Cramer, B. S., Fennel, K., Falkowski, P. G., 2005. Biological overprint of the geological carbon cycle. Marine Geology 217(3-4), 323–338.
- Kemp, D. B., Coe, A. L., Cohen, A. S., & Weedon, G. P. (2011). Astronomical forcing and chronology of the early Toarcian (Early Jurassic) oceanic anoxic event in Yorkshire, UK. Paleoceanography 26(4).
- Kemp, D.B., Coe, A.L., Cohen, A.S., Schwark, L., 2005. Astronomical pacing of methane release in the Early Jurassic period. Nature 437, 396–399.
- Korte, C. and Hesselbo, S. P, 2011. Shallow-marine carbon- and oxygen isotope and elemental records indicate icehouse-greenhouse cycles during the Early Jurassic, Paleoceanography 26, PA4219.
- Little, C.T.S., Benton, M.J., 1995. Early Jurassic mass extinction: a global long term event. Geology 23, 495–498.
- Mallarino, G., Goldstein, R.H., Di Stefano, P., 2002. New approach for quantifying water depth applied to the enigma of drowning of carbonate platforms. Geology 30, 783–786.
- Martinez, M., Krencker, F.-N., Mattioli, E., Bodin, S., 2017. Orbital chronology of the Pliensbachian – Toarcian transition from the Central High Atlas Basin (Morocco). Newsletters on Stratigraphy 50(1), 47–69.
- Mattioli, E. 1996. New calcareous nannofossil species from the Early Jurassic of Tethys. Rivista Italiana di Paleontologia e Stratigrafia 102(3).

- Mattioli, E., Erba E., 1999. Synthesis of calcareous nannofossil events in tethyan lower and middle Jurassic successions. Rivista Italiana di Paleontologia e Stratigrafia 105, 343–376.
- Mattioli, E., Pittet, B., 2002. Contribution of calcareous nannoplankton to carbonate deposition: a new approach applied to the Lower Jurassic of central Italy. Marine micropaleontology 45(2), 175–190.
- Mattioli, E., Pittet, B., Palliani, R., Rohl, H.-J., Schmid-Rohl, A., Morettini, E., 2004a. Phytoplankton evidence for the timing and correlation of palaeoceanographical changes during the early Toarcian oceanic anoxic event (Early Jurassic). Journal of the Geological Society 161(4), 685–693.
- Mattioli, E., Pittet, B., Petitpierre, L., Mailliot, S., 2009. Dramatic decrease of pelagic carbonate production by nannoplankton across the Early Toarcian anoxic event (T-OAE). Global and Planetary Change 65(3–4), 134–145.
- Mattioli, E., Pittet, B., Suan, G., Mailliot, S., 2008. Calcareous nannoplankton changes across the early Toarcian oceanic anoxic event in the western Tethys. Paleoceanography 23(3), 1–17.
- Mattioli, E., Pittet, B., Young, J.R., Bown, P.R., 2004b. Biometric analysis of Pliensbachian-Toarcian (Lower Jurassic) coccoliths of the family Biscutaceae: intra- and interspecific variability versus palaeoenvironmental influence. Marine Micropalaeontology 52, 5–27.
- Mattioli, E., Plancq, J., Boussaha, M., Duarte, L.V., Pittet, B., 2013. Calcareous nannofossil biostratigraphy: new data from the Lower Jurassic of the Lusitanian Basin. Comunicacoes Geologicas T. 100, 100 (Especial I), 69–76.
- McArthur, J. M., D. T. Donovan, M. F. Thirwall, B. W. Fouke, and D. Mattey, 2000. Strontium isotope profile of early Toarcian (Jurassic) oceanic anoxic event, the duration of ammonite biozones, and belmnite palaeotemperature, Earth and Planetary Sciences Letters 179, 269–285.
- McElwain, J.C.,Wade-Murphy, J., Hesselbo, S.P., 2005. Changes in carbon dioxide during an oceanic anoxic event linked to intrusion into Gondwana coals. Nature 435, 479–482.
- Menini, A., Mattioli, E., Spangenberg, J. E., Pittet, B., and Suan, G., 2019. New calcareous nannofossil and carbon isotope data for the Pliensbachian/Toarcian

boundary (Early Jurassic) in the western Tethys and their paleoenvironmental implications. Newsletters on Stratigraphy, 173–196.

- Morard, A., Guex, J., Bartolini, A., Morettini, E., De Wever, P., 2003. A new scenario for the Domerian - Toarcian transition. Bull. Soc. géol. Fr. 4, 351–356.
- Okada, H., and Honjo, S., 1973. The distribution of oceanic coccollithophorids in the Pacific,Deep Sea Res. Oceanogr. Abstr., 20, 355– 374.
- Paasche, E., 1968. Biology and physiology of coccolithophorids, Annual Review of Microbiology 22, 71–86.
- Page, K.N., 2003. The Lower Jurassic of Europe: its subdivision and correlation. Geological Survey of Denmark and Greenland1, 23–59.
- Palliani, R. B., Mattioli, E., Riding, J. B., 2002. The response of marine phytoplankton and sedimentary organic matter to the early Toarcian (Lower Jurassic) oceanic anoxic event in northern England. Marine micropaleontology 46(3–4), 223–245.
- Pancost, R. D., Crawford, N., Magness, S., Turner, A., Jenkyns, H. C., Maxwell, J. R., 2004. Further evidence for the development of photic-zone euxinic conditions during Mesozoic oceanic anoxic events, Journal of the Geological Society of London 161, 1–12.
- Percival, L. M. E., Witt, M. L. I., Mather, T. A., Hermoso, M., et al., 2015. Globally enhanced mercury deposition during the end-Pliensbachian extinction and Toarcian OAE: A link to the Karoo–Ferrar Large Igneous Province. Earth and Planetary Science Letters 428, 267–280.
- Percival, L.M.E., Cohen, A.S., Davies, M.K., Dickson, A.J., Hesselbo, S.P., Jenkyns, H.C., Leng, M.J., Mather, T.A., Storm, M.S., Xu, W., 2016. Osmium isotope evidence for two pulses of increased continental weathering linked to Early Jurassic volcan-ism and climate change. Geology 44, 759–762.
- Philippe, M., Pujialon, S., Suan, G., Mousset, S., Thévenard, F., Mattioli, E., 2017. The palaeolatitudinal distribution of fossil wood genera as a proxy for European Jurassic terrestrial climate. Palaeogeography, Palaeoclimatology, Palaeoecology 466, 373 -381.
- Pittet, B., Suan, G., Lenoir, F., Duarte, L. V., Mattioli, E., 2014. Carbon isotope evidence for sedimentary discontinuities in the lower Toarcian of the Lusitanian

Basin (Portugal): Sea level change at the onset of the Oceanic Anoxic Event. Sedimentary geology 303, 1–14.

- Price, G. D., 1999. The evidence and implications of polar ice during the Mesozoic, Earth-Sciences Reviews 48, 183–210.
- Riley, T. R., Millar, I. L., Watkeys, M.K., Curtis, M. L., Leat, P.T., Klausen, M. B., Fanning, C. M., 2004. U–Pb zircon (SHRIMP) ages for the Lebombo rhyolites, South Africa: refining the duration of Karoo volcanism. Journal of the Geological Society 161(4), 547–550.
- Rocha, R. Mattioli, E., Duarte, L.V., Pittet, B., Elmi, S., Mouterde, R., Cabral, M.C., Comas-Rengifo, M.J., Gómez, J.J., Goy, A., Hesselbo, S.P., Jenkyns, H.C., Littler, K., Mailliot, S., Veiga de Oliveira, L.C., Osete, M.L., Perilli, N., Pinto, S., Ruget, C. and Suan, G., 2016. Base of the Toarcian Stage of the Lower Jurassic defined by the Global Boundary Stratotype Section and Point (GSSP) at the Peniche section (Portugal). Episodes 39, 460-481.
- Rohl, H. J., Schmid-Rohl, A., O. Frimmel, Wolfgang, A., Lorenz, S., 2001. The Posidonia Shale (Lower Toarcian) of SW-Germany: An oxygen-depleted ecosystem controlled by sea level and palaeoclimate, Palaeogeogeogry, Palaeoclimatology, Palaeoecology 165, 27–52.
- Rosales, I., Quesada, S., Robles, S., 2004. Paleotemperature variations of Early Jurassic seawater recorded in geochemical trends of belemnites from the Basque - Cantabrian basin, northern Spain. Palaeogeography, Palaeoclimatology, Palaeoecology 203, 253–275.
- Roth, P.H., 1984. Preservation of calcareous nannofossils and fine-grained carbonate particles in mid-Cretaceous sediments from the southern Angola Basin. In: Hay, W.W. (Ed.), Initial Reports of Deep Sea Drilling Project 75. U.S. Government Printing Office, Washington, 651–655.
- Ruhl, M., Hesselbo, S. P., Hinnov, L., Jenkyns, H. C., Xu, W., et al., 2016. Astronomical constraints on the duration of the Early Jurassic Pliensbachian Stage and global climatic fluctuations. Earth and Planetary Science Letters 455, 149–165.
- Schmid-Rohl, A., Rohl, H. J., O. Frimmel, W., A., Schwark L., 2002, Palaeoenvironmental recontruction of lower Toarcian epiconrinental black

shales (Posidonia Shale, SW Germany): Global versus regional control, Geobios (Jodhpur India) 35, 13– 20.

- Sellwood, B.W., Jenkyns, H.C., 1975. Basins and swells and the evolution of an epeiric sea (Pliensbachian–Bajocian of Great Britain). Journal of the Geological Society of London 131, 373–388.
- Simms, M.J., Chidlaw, N., Morton, N., Page, K.N., 2004. British Lower Jurassic Stratigraphy. Geological Conservation Review Series 30. Joint Nature Conservation Committee, Peterborough.
- Storm, M. S., Hesselbo, S. P., Jenkyns, H. C., Ruhl, M., Ullmann, C. V., Xu, W. et al., 2020. Orbital pacing and secular evolution of the Early Jurassic carbon cycle. Proceedings of the National Academy of Sciences 117(8), 3974–3982.
- Suan, G., Mattioli, E., Pittet, B., Lécuyer, C., Suchéras-Marx, B., Duarte et al., 2010. Secular environmental precursors to Early Toarcian (Jurassic) extreme climate changes. Earth and Planetary Science Letters 290 (3–4), 448–458.
- Suan, G., Mattioli, E., Pittet, B., Mailliot, S., Lécuyer, C., 2008a. Evidence for major environmental perturbation prior to and during the Toarcian (Early Jurassic) oceanic anoxic event from the Lusitanian Basin, Portugal, Paleoceanography 23, PA1202.
- Suan, G., Pittet, B., Bour, I., Mattioli, E., Duarte, L. V., Mailliot, S., 2008b. Duration of the Early Toarcian carbon isotope excursion deduced from spectral analysis : consequence for its possible causes. Earth and Planetary Science Letters 267(3–4), 666–679.
- Svensen, H., Planke, S., Chevallier, L., Malthe-Sorenssen, A., Corfu, F., Jamtveit, B., 2007. Hydrothermal venting of greenhouse gases triggering Early Jurassic global warming. Earth and Planetary Sciences Letters 256, 554–566.
- Thierstein, H. R., Corte`s, M. Y., Haidar, A. T., 2004. Plankton community behaviour on ecological and evolutionary timescales: When models confront evidence, in Coccolithophores From Molecular Processes to Global Impact, edited by H. R. Thierstein and J. R. Young, 455– 480.
- Tremolada, F., Van de Schootbrugge, B., & Erba, E. (2005). Early Jurassic schizosphaerellid crisis in Cantabria, Spain: implications for calcification rates and phytoplankton evolution across the Toarcian oceanic anoxic event. Paleoceanography 20(2).

- van de Schootbrugge, B., McArthur, J.M., Bailey, J.M., Rosenthal, Y., Wright, J.M., Miller, K.G., 2005, Toarcian oceanic anoxic event: An assessment of global causes using belemnite C isotope records, Paleoceanography 20.
- Wignall, P.B., Hallam, A., Newton, R.J., Sha, J.G., Reeves, E., Mattioli, E., Crowley, S., 2006. An eastern Tethyan (Tibetan) record of the Early Jurassic (Toarcian) mass extinction event. Geobiology 4, 179–190.
- Woodland, A. W., 1971. The Llanbedr (Mochras Farm) Borehole,Report 71/18, Institute of Geological Sciences.
- Xu, W., Ruhl, M., Jenkyns, H. C., Hesselbo, S. P., Riding, J. B., et al., 2017. Carbon sequestration in an expanded lake system during the Toarcian oceanic anoxic event. Nature Geoscience 10(2), 129-134.
- Xu, W., Ruhl, M., Jenkyns, H. C., Leng, M. J., Huggett, J. M., et al., 2018. Evolution of the Toarcian (Early Jurassic) carbon-cycle and global climatic controls on local sedimentary processes (Cardigan Bay Basin, UK). Earth and Planetary Science Letters 484, 396–411.
- Young, J. R., 1994. Functions of coccoliths, in Coccolithophores, edited by A. Winter and W. Siesser, 63–82.

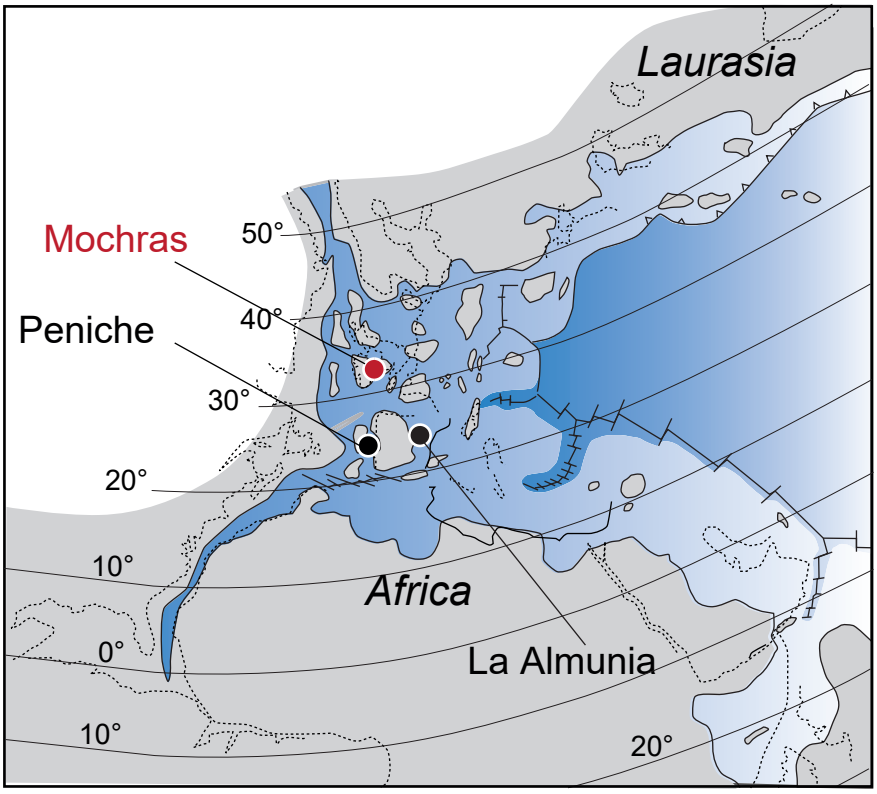


Figure 1. Paleoceanographic reconstruction of the western Tethys at about 183 Ma (after Bassoullet et al., 1993) showing the location of Mochras core and the two sections used for comparison. Mochras (Wales, UK) is located in the Northern Tethyan margin while La Almunia (Central Spain) is located in the Southern Tethyan margin. Peniche was located in the Lusitanian Basin, a N-S corridor in connexion with both Tethyan and NW European regions.

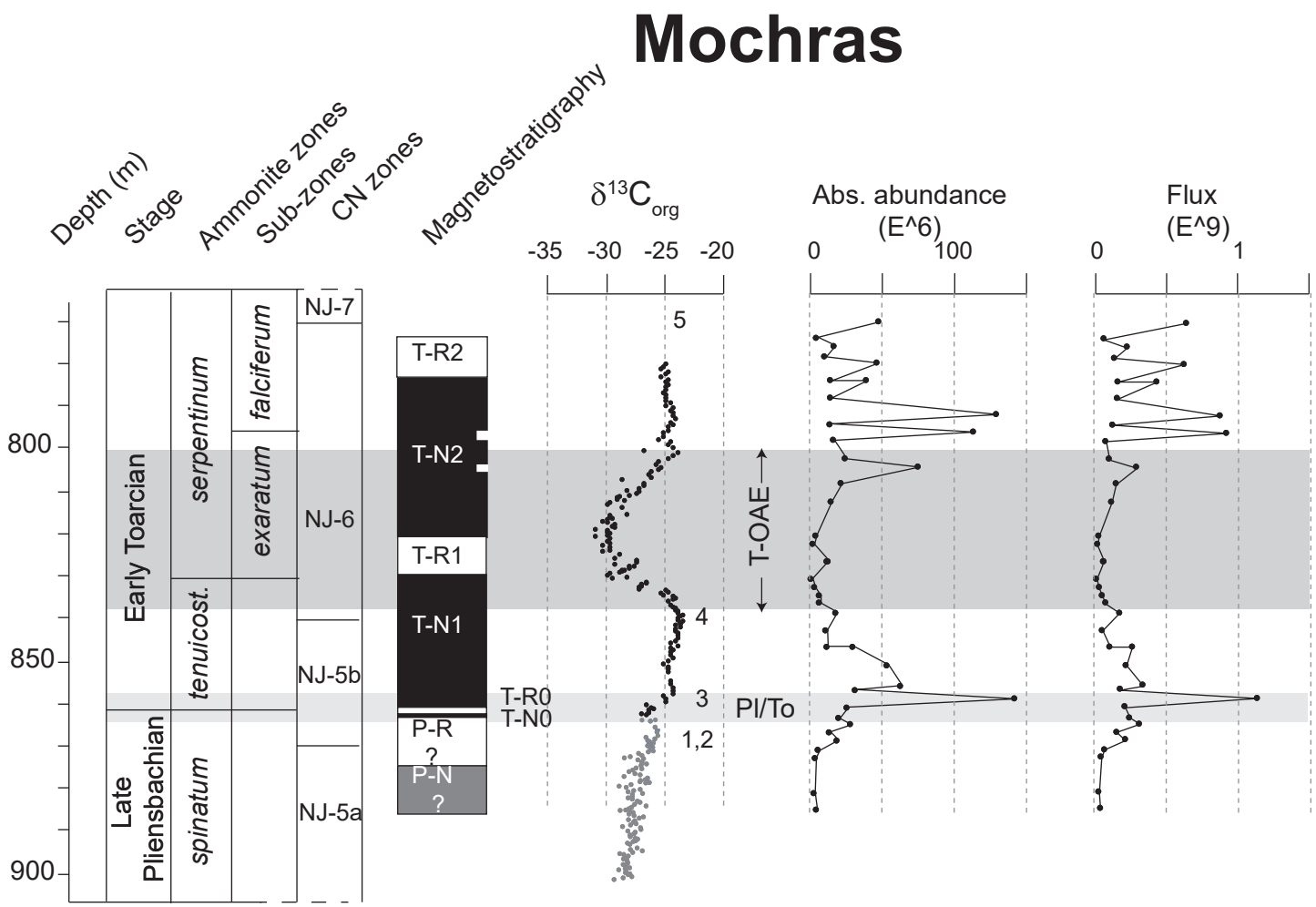


Figure 2. Absolute abundance of nannofossils per gram of rock and flux of nannfossils (nannofossils/m2/year). On the right, ammonite biostratigraphy (Tippan et al., 1994). Calcareous nannofossil biostratigraphy based on Bown, 1987 and Bown, 1998. First occurences of biostratigraphically important species (1. C. cavus, 2. Z. erectus, 3. D. ignotus, 4. C. superbus, 5., D. striatus). Magnetostratigraphy after Xu et al., 2018. δ13Corg for the Lower Toarcian (black dots) after Xu et al., 2018 and for the Late Pliensbachian (grey dots) after Storm et al., 2020.

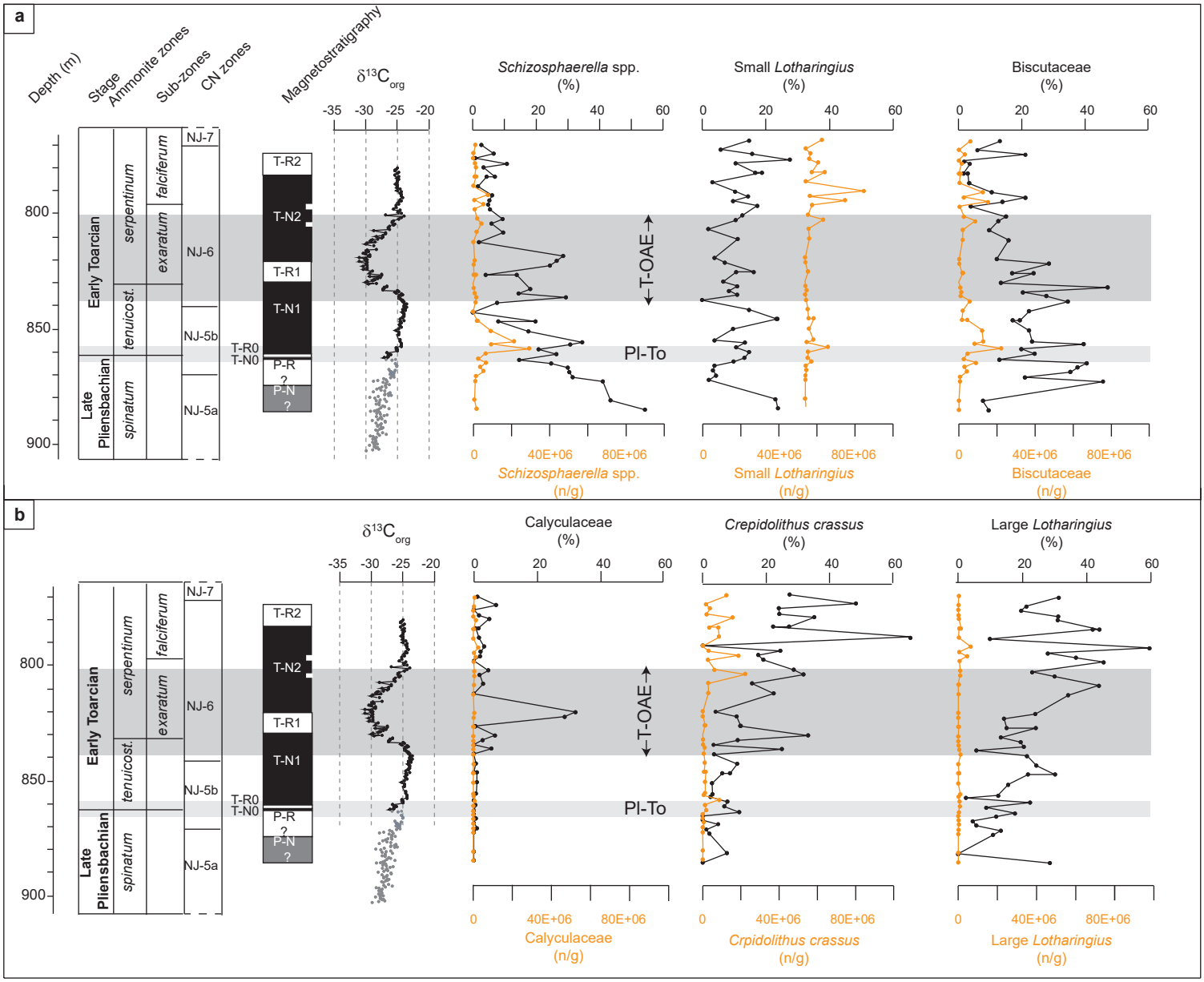


Figure 3. Relative and absolute abundance of main taxa. Ammonite biostratigraphy after Tappin et al., 1994. a., Nannofossil assemblages from the Late Pliensbachian and earliest Toarcian (*spinatum* to *tenuicostatum* ammonite zones, below the T-OAE). b., Nannofossil assemblages from the T-OAE and after the event (corresponding to *serpentinum* zone)

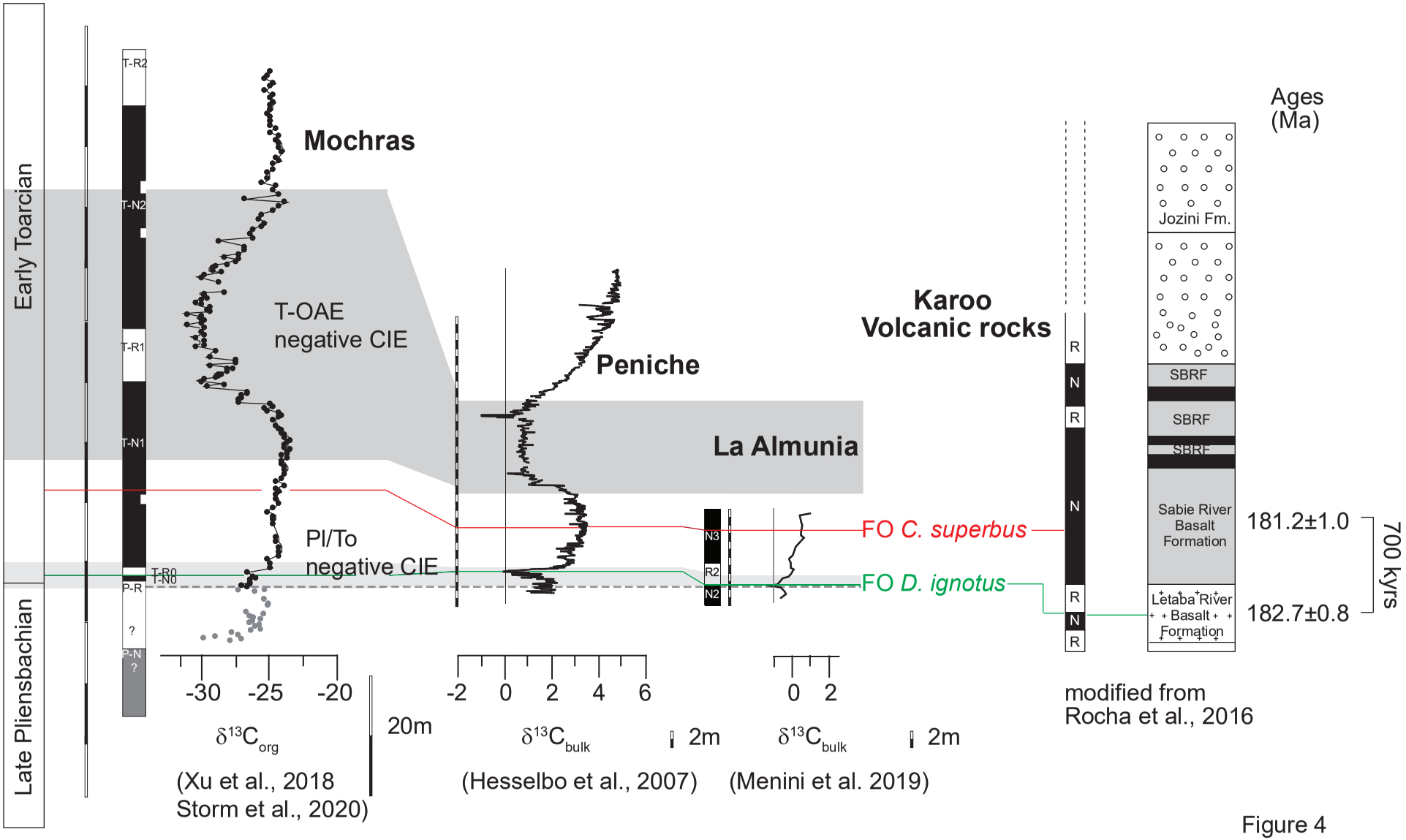


Figure 4

Figure 4. Correlation between Mochras (Wales, Cleveland Basin), Peniche (Portugal, Lusitanian Basin), La Almunia (Central Spain) and Karoo lavas. Magnetostratigraphy at La Almunia is from Almunacid de La Cuba section (see text for details). Litostra-tigraphy at Karoo is after Riley et al., 2004 Magnetostratigraphy at Karoo is after Hargreaves et al., 1997

# Chapitre 3.2. Calcareous nannofossil response to PETM: a comparison between shelf and open-ocean settings.

**Calcareous nannofossil response to PETM: a comparison between shelf and open-ocean settings**

Alessandro Menini[1], Ilef Belhadj Taher[1,2,3], Jorge Ferreira[1], Jorge Spangenberg[4], Arnauld Vinçon-Laugier[1], Mohamed Soussi[3], Guillaume Suan[1], Emanuela Mattioli[1,5]

[1] Univ Lyon, Univ Lyon 1, ENSL, CNRS, LGL-TPE, 69622 Villeurbanne, France

[2] Université de Tunis El Manar, Faculté des Sciences de Tunis, Département de Géologie, LR18ES07, Campus Universitaire, 2092, Tunis, Tunisie

[3] Entreprise Tunisienne des Activités pétrolières (ETAP), 54 Avenue Mohamed V- 1002, Tunis, Tunisia

[4] Institute of Earth Surface Dynamics (IDYST), University of Lausanne, Building Géopolis, CH-1015 Lausanne, Switzerland

[5] Institut Universitaire de France (IUF)

## 1. Introduction

The Paleocene-Eocene transition is characterized by a brief but intense carbon isotope excursion (CIE) associated with a global warming of 5-7 °C (Kennet and Stott, 1991; Zachos et al., 2001). This transition is known as the Paleocene-Eocene Thermal Maximum (PETM). The input of light carbon either from methane release or volcanism (Dickens et al., 1995, 1997; Dickson et al., 2005) led to enhanced $pCO_2$ levels in the oceans, finally triggering ocean acidification (Penman et al., 2014; Babila et al., 2018) and the shoaling of the CCD (Kroon et al., 2004; Penman et al., 2016). Recent studies suggest that all these changes happened during a 405 kyrs eccentricity maximum (Zeebe and Lourens, 2009), and recent models estimated the duration of the event at ca. 200 kyrs (Rohl et al., 2000; Rohl et al., 2007). Benthic communities

suffered a dramatic extinction (Tjalsma and Lohmann, 1983; Thomas and Shackleton, 1996) and planktonic biota underwent a profound re-organization (e.g., Bralower et al., 1995; Kelly et al., 1996; Bralower et al., 2002; Gibbs et al., 2006b; Raffi et al., 2009).

Plankton assemblages are profoundly different in shelf or open-ocean sites. This pattern makes the interpretation on ecological preference of taxa difficult and sometimes contradictory from a paper to another. At open-ocean sites, the turnover which occurred during the PETM is thought to reflect warmer and nutrient-depleted conditions during the onset and peak of the event caused by thermally enhanced stratification (Kelly et al., 1998; Bralower, 2002). However, in proximal sites, local conditions such as high precipitation rates and possible increase in storm events may have resulted in increased continental runoff that affected assemblage response to the PETM (Self-Trail et al., 2012). Previous studies showed that there is also an impact of paleotemperatures on the size of some taxa, such as *Discoaster multiradiatus*, that can be used to infer water mass stratification (Tremolada et al., 2008).

Geochemical and ~~other~~ biotic proxies at some of the ~~same~~ most studied oceanic sites and at shelf locations challenge the micropaleontological interpretations, as they preferentially support increased primary productivity as a consequence of intensified continental weathering and nutrient runoff (e.g., Thomas and Shackleton, 1996; Bains et al., 2000; Crouch et al., 2001; Stoll and Bains, 2003; Stoll et al., 2007b, c). Since elevated primary production, along with enhanced weathering, has been proposed as a major negative feedback of the carbon cycle perturbation after the onset of the PETM (Bains et al., 2000; Ravizza et al., 2001), it is critical to determine the global distribution of productivity at different stages of the event and thereby assess its role in carbon export and subsequent sequestration.

Calcareous nannofossils are exoskeletal microalgae and represent one of the most important sources of carbonate to deep-sea sediments. These organisms thriving in the upper photic zone are very sensitive to environmental parameters. The distribution of individual species in surface

waters is controlled by temperature, salinity, and, especially, availability of nutrients (e.g., Winter et al., 1994). The paleoecology of extinct nannofossil species can be inferred from biogeography, paleoenvironmental proxy data, and comparison with extant taxa. Despite of limitations to these interpretations, calcareous nannofossils allow global productivity reconstruction since they are almost ubiquitous in the oceans.

So far, only a few open ocean sites with complete Paleocene/Eocene transitions and relatively well-preserved nannofossil assemblages have been studied in detail (Bralower, 2002; Tremolada and Bralower, 2004; Gibbs et al., 2006; Raffi et al., 2009), thus our knowledge of the response of calcareous nannofossils to the PETM remains partially unclear. Moreover, almost no data exist on nannofossil absolute abundance (nannofossils/grams of rock) or fluxes (per $cm^2$ and per year) and most of the paleoenvironmental interpretations are inferred from relative turnovers between species or genus, which do not represent effective changes in assemblage composition but only relative switchovers.

Here we present detailed nannofossil assemblage records of the PETM across disparate paleoceanographic settings (Fig. 1) in order to unravel global *versus* local environmental influences upon primary production during the PETM. We studied a proximal section (Kharouba, Tunisia), the South Eastern Atlantic Site ODP 1263 and a central gyre location in the Pacific Ocean (ODP Site 1209). All three studied sections display the C isotope anomaly, namely the negative excursion of carbon stable isotopes that characterizes the PETM (Kennet and Stott, 1991; Zachos et al., 2001). These records are compared to already published data from both proximal and distal localities, namely South Dover Bridge core (New Jersey Coastal Plain, SDB), ODP 690, ODP 1260, Cicogna section (North East Italy), Alamedilla (South Spain) and Tanzania Drilling Project core 14 (TDP14). Such a comparison should enable us to obtain a more comprehensive framework of calcareous nannoplankton distribution and of

ecological preferences of taxa across a major paleoceanographic event, and to discriminate between local *versus* global trends in assemblage changes.

## 2. Materials and methods

### 2.1 Carbon isotope measurements

Carbon isotope data are already available for Sites 1209 and 1263 (Penman et al., 2014; Zachos et al., 2005). We studied 37 samples of the Kharouba section for stable carbon isotopes measured on bulk rock carbonates ($\delta^{13}C_{bulk\ rock}$). 25 samples were analysed at the Institute of Earth Surface Dynamics of the University of Lausanne, Switzerland (UNIL) and 12 were analysed at the Laboratoire de Géologie de Lyon (Université Lyon 1, LGL-TPE). At UNIL, sample powders were analysed using a Thermo Fisher Scientific Gas Bench II (Bremen, Germany) carbonate preparation device connected to a Delta Plus XL isotope ratio mass spectrometer that was operated in the continuous helium flow mode (Révész and Landwehr 2002). At LGL-TPE, stable isotopes were determined using an autosampler MultiPrep™ system coupled to a dual-inlet GV IsoPrime™ isotope ratio mass spectrometer (IRMS).

Samples with clear evidence of diagenetically neoformed or recrystallized carbonates (calcite or dolomite) were not analysed. For each sample, an aliquot of about 100–500 µg (depending on the $CaCO_3$ content) of bulk-rock samples was reacted with anhydrous oversaturated phosphoric acid at 90°C for 20 min. Carbon isotope compositions are quoted in the δ notation in per mil (‰) relative to Vienna Pee Dee Belemnite standard (V-PDB). All samples were measured in duplicate and normalized to the V-PDB scales with an in-house working standard Carrara Marble (UNIL-CAM, $\delta^{13}C_{V\text{-}PDB}$ = 2.05; LGL-TPE-CAM, $\delta^{13}C_{V\text{-}PDB}$ = 2.025) and international reference standards (RMs) in each run. The $\delta^{13}C$ values of the reference gas and the UNIL-CAM and LGL-TPE-CAM were normalized with the RMs NBS-19 limestone with

100 $\delta^{13}C$ = +1.95‰, NBS-18 carbonatite with $\delta^{13}C$ = –5.04‰, and LSVEC lithium carbonate with
101 $\delta^{13}C$ = –46.65‰ (Brand et al., 2014). The repeatability and intermediate precision of the
102 analyses (2σ), monitored by replicate analyses of the laboratory standard UNIL-CAM and
103 LGL-TPE-CAM and the RMs was better than ±0.05‰. The accuracy of the analyses was
104 checked periodically through the analyses of the RMs.
105
106 **2.2 Calcareous nannofossils**
107 At Site 1209 (Fig. 1; Shatsky Rise, Tropical Pacific; 32°39.1′N, 158°30.4′E, 2387 water depth,
108 1900 paleodepth; Takeda and Kaiho, 2007), we studied 20 samples over 0.54 m transect
109 spanning the PETM. The event lies in a ~25-cm-thick layer of clayey nannofossil ooze with a
110 sharp basal contact and a gradational upper contact with underlying and overlying chalk,
111 respectively (Fig. 2A). Samples were collected every 1-3 cm, with higher sampling rate across
112 the PETM (1cm).
113 At Site 1263 (Fig. 1; Walvis Ridge, Southern-East Atlantic; 28°32′S; 02°47′E; 2717 m water
114 depth; 1500 m paleodepth; Zachos et al., 2004), we studied 26 samples over ca. 2 m transect
115 across the PETM. The PETM onset is marked by a sharp contact between grayish brown ash-
116 bearing clay above, and light gray nannofossil ooze below (Fig. 2B). Samples were collected
117 every 5-10 cm, with higher sampling rate across the PETM (5 cm). Given higher sedimentation
118 rates at Site 1263 relatively to Site 1209, we adopted a relatively coarser sampling resolution.
119 However, because of paucity of material in the PETM core interval (~10 cm), this interval is
120 undersampled. We analyzed the Hole 1263C between 333.61 and 335.15 rmcd, and Hole 1263D
121 between 335.20 and 335.65 rmcd.
122 At Kharouba section (Fig.1; Tunisian Atlas) upper Paleocene to lower Eocene sediments
123 outcrop over 30 meters and 51 samples were collected, selected as fresh and unaltered as
124 possible and studied for their calcareous nannofossil content. The lower part of the section is

125 constituted by 10 meters of dark marls and continues with 20 meters of alternations of marls
126 and calcareous marls (Fig. 2C). Samples were collected on average every 1 meter.
127 All calcareous nannofossil slides were prepared following the settling method (Beaufort et al.,
128 2014). A cover slide was weighted before and after the settling of a homogeneous suspension
129 of dry bulk sediment and water supersaturated with respect to $CaCO_3$ for 4 hours in a Petri-dish.
130 Water was carefully aspired with a water-pump connected to a micro-pipette to avoid any
131 turbulence. After residual water drying, the cover slide was fixed on a microscope slide using
132 Rhodopass B resin (Polyvinyl acetate). At least 500 specimens of calcareous nannofossils were
133 counted for each sample with a Leica DM 750 P microscope with 1000X magnification. Each
134 slide was further scanned over 10 transects (ca. 1500 FOV, 0.471 $cm^2$) in order to detect the
135 presence of rare species. Each slide was observed twice over a year in order to check
136 consistency of the results. Five replicates per sample were studied at Site 1209 for absolute
137 abundance in order to test statistical differences, thus average values with an error bar of (2 SD)
138 were calculated.
139 Absolute nannofossil abundance per gram of sediment were calculated as follows:
140 $$x = \frac{n*(l*h)}{m*A} \quad (1)$$
141 where is $x$ is the absolute abundance value, $n$ is the number of counted specimens in a slide, $l$
142 is the length of the cover slide, $h$ is the height of the cover slide, $m$ is the mass of the weighted
143 sample and $A$ is the studied surface of the sample.
144 We calculated nannofossil accumulation rates (NAR) using the formula:
145 $$NAR=X*AR*d \quad (2)$$
146 where $NAR$ is is in n/$cm^2$/yr, $X$ is the absolute abundance of nannofossils (n/g), $AR$ is the
147 accumulation rate (cm/ky), $d$ is the dry bulk density of the sediment. The accumulation rate at
148 Sites 1209 and 1263 has been calculated according to Menini et al. (submitted, 2020b). For
149 Kharouba, we used the duration of 5 kyrs for the base of the section until the base of NP10

nannofossil zone, according to Zachos et al. (2005; calculated for Site 1263). For the core of the event and the recovery interval, we used the duration of the PE1 and PE2a nannofossil zones as defined by Menini et al. (submitted, 2020a), namely ~85 kyrs and ~15 kyrs respectively. The dry density of rock for Sites 1209 and 1263 was calculated according to the ship data (REFS); for Kharouba, as calcium carbonate measurements of samples showed they are mainly marls, we used the average value of 2.73 g/cm$^3$ provided for marls.

In order to compare our data with previous studies we generated relative abundance data for the three sections (Supplementary Material). The preservation was further investigated using a Phenom SEM G2 PRO microscope. In order to obtain a consistent dataset, only samples showing good preservation are retained for statistical analyses.

Principal components analysis (PCA) was applied to nannofossil assemblages on the entire dataset composed of samples from the 3 sections, and eventually to datasets of individual sections. This multivariate statistical method allows analysis of the entire nannofossils community, instead of changes in single taxa abundance. Also, this method permits a better interpretation of complex datasets and reduces a large data matrix composed of several variables to a small number of factors representing the main modes of variations (Beaufort and Heussner, 2001).

PCA was computed with PAST 4.0 software (Hammer et al., 2001). The extraction method for eigenvalues was Orthotran/Varimax. We introduced the $\log_2$ of relative abundance values in the matrix in order to reduce the influence of outliers. Some species (such as *Fasciculithus richardii, F. alanii*, *F. lilianae*, *F. mitreus* and *F. tonii* or genera belonging to the family Zygodiscales) were grouped because they display abundance peaks in the same samples. Also, *Discoaster araneus* and D. *anartios* were grouped because both they co-occur in the same samples and they are interpreted as morphotypes of the same species (Bralower and Self-Trail, 2016). The matrix consists of 13 to 18 taxa according to the different sections. Error bars in Fig.

175 3 represent lower and upper limits for 95% confidence intervals, using 9999 bootstrap
176 replicates.
177 SIMPER (Similarity Percentage) was applied to counting data in order to test the degree of
178 similarity between the sections we studied and already published sections. Detailed distribution
179 charts were available in the literature for Alamedilla section in South Spain (Monechi et al.,
180 2000), Cicogna in NE Italy (Agnini et al., 2016), Site 1260, central Atlantic off South America
181 (Mutterlose et al., 2007), the TDP 14 core, Tanzania (Bown and Pearson, 2009), South Dover
182 core in the mid-Atlantic Coastal Plain (Self-Trail et al., 2012), Site 690, Weddel Sea, South
183 Atlantic (Bralower et al., 2002). Before applying SIMPER, a taxonomic revision was
184 undertaken in order to make homogeneous the dataset. In this paper, the counting at the genus
185 level was introduced in order to avoid eventual biases linked to different taxonomic concepts
186 used in various works. SIMPER is a simple method for assessing which taxa are primarily
187 responsible for an observed difference between groups of samples belonging to different
188 sections. The overall significance of the difference has been assessed by ANOSIM. The Bray-
189 Curtis similarity measure was used with SIMPER. Additionally, the hierarchical clustering was
190 used to produce a dendrogram showing how data points (rows) can be clustered. Both SIMPER
191 and cluster analysis were computed with PAST 4.0 software (Hammer et al., 2001).
192
193 ## 3. Results
194
195 ### 3.1 Depth definitions and PETM subdivision
196 At both Site 1209 and 1263 we express our data relatively to the lithological contact of the
197 PETM and carbon isotopes stratigraphy (Fig. 2A and B). We follow Zachos et al. (2005) in the
198 definition on the PETM and we refer to pre-PETM below the carbon isotope excursion (CIE),
199 to “core of the PETM” all through the $\delta^{13}C$ CIE (-3‰) and to the recovery phase above it, where

200 $\delta^{13}C$ values recover to pre-PETM ones (Fig. 2A and B). At Kharouba, the lithology is constantly
201 dominated by marls in this interval and no lithological contact exists for the basal Eocene. The
202 base of the section is fixed at 0 m (Fig. 2C).
203 We express all the data at the same scale, in order to avoid visual erroneous interpretations.
204 In agreement to Zachos et al. (2005) and Röhl et al. (2007) we subdivide the PETM interval in
205 pre-PETM, core of the PETM and recovery phase.
206

207 **3.2 Carbon isotopes**

208 At Site 1263, the $\delta^{13}C_{bulk\ rock}$ curve of Paleocene-Eocene interval has been published by Zachos
209 et al. (2005). At both sites 1209 and 1263, a prominent negative carbon excursion can be seen
210 from ~3 ‰ to ~0.2 ‰ and from ~2 ‰ to ~-1‰, respectively (Fig. 2A and B). The $\delta^{13}C_{bulk\ rock}$
211 trend is the same as at Site 1209, but the values record a general offset towards more
212 negative/positive values of ~0.8‰. We have measured the $\delta^{13}C_{bulk\ rock}$ of 37 samples from the
213 Kharouba section (Fig. 2C). From 0 to 1 m, values are stable and range from 0.8 to 0.9 ‰. At
214 4.4 m values drastically decrease to -2.5 ‰, with a 2 ‰ negative excursion (Fig. 2C).
215 Biostratigraphic and chemostratigraphic data allow us to recognize the onset of the PETM at
216 1.1 m. Values stay low till up 4.4 m and recover at 6.2 m. These data are in agreement with
217 previously published $\delta^{13}C_{bulk\ rock}$ data for the PETM in both oceanic Sites 1209 (Colosimo et al.,
218 2006; Penman et al., 2014; Menini et al., under revision) and 1263.
219

220 **3.3 Preservation and biostratigraphy**

221 At Site 1209, nannofossil preservation is good overall but it declines between 1 cm below and
222 above the LC, as previously indicated by Bralower et al. (2014). Coccoliths in those samples
223 are mostly affected by dissolution, consistently with the coeval maximum of nannofossil
224 fragmentation, while *Discoaster* are slightly overgrown.

225 At Site 1263, SEM pictures reveal moderate to good preservation but increased dissolution is
226 observed from 0 to 0.6 cm above the LC, as previously observed (Raffi et al., 2009). Although
227 most of the coccoliths and nannoliths we observed in the slides as well in SEM are moderately
228 to well preserved, etched and overgrown specimens coexist with fairly well preserved
229 nannofossils in the same sample.
230 At Kharouba, nannofossil preservation is excellent throughout the section, and even the
231 assemblages of the PETM interval include fragile coccoliths: delicate structures that are
232 normally lacking in less well-preserved coeval material are present in Kharouba samples e.g.,
233 holococcoliths (*Semihololithus*, *Holodiscolithus*, *Gladiolithus*) similarly to exceptional
234 preserved sections of Tanzania (Bown 2005; Bown and Pearson, 2009).
235 At all the three localities, a typical and very rich late Paleocene and early Eocene calcareous
236 nannofossil assemblage is recorded. The presence of *Discoaster multiradiatus* from the
237 lowermost sample (- 0.13 m, at site 1209; -0.45 m, at site 1263; 0 m, at Kharouba) in the three
238 sections allows us to recognize the NP9 zone of Martini (1971) and the CP8a subzone of Okada
239 and Bukry (1980) (Fig. 2).
240 The first occurrence (FO) of *Tribrachiatus bramlettei* allows the recognition of the base of the
241 NP10 at 0.02 m at 1209, at 0.97 m at Site 1263, and at 3 m at Kharouba. The FO of *Rhomboaster*
242 *cuspis* or *R. calcitrapa* allows the recognition of subzone CP8b (Okada and Bukry, 1980) in all
243 the sections, namely at -0.03 m at 1209, at 0.12 m at 1263, and at 2.2 m at Kharouba.
244 At Kharouba, the FO of *Discoaster diastypus* is recorded at 13.2 m and it marks the CP9a of
245 Okada and Bukry (1980). The section is dated to as CP9a from 13.2 to 28.2 m because of the
246 absence of *Tribrachiatus contortus* until the uppermost studied sample (at 28.2 m). *D. diastypus*
247 is absent at both 1263 and 1209, and the FO of this species is reported stratigraphically higher
248 in these sections (Gibbs et al., 2006; Raffi et al., 2009).

249 The studied interval encompasses the zone CNP11 and CNE1 of Agnini et al. (2014) (Fig. 2).
250 The last occurrence of *Fasciculithus richardii* group (0.17 m, site 1209; 0.97 m, site 1263; 13.2
251 m, Kharouba) is recorded in the three sections across the recovery phase (Rohl et al., 2007) of
252 the PETM.
253 The cumulative graphs of the assemblage composition show as common trend the dominance
254 of coccoliths over other nannofossils. However, *Fasciculithus* spp. are abundant at Sites 1209
255 and 1263 in the pre-excursion interval and the core of the event while they are in low
256 proportions at Kharouba. Also, *Zygrhablithus* spp. that are abundant starting from the core of
257 the event and in the post-event interval at Sites 1209 and 1263 are rare at Kharouba. In this last
258 section, small holococcoliths (*Gladiolithus flabellatus*, *Holodiscolithus* spp., *Semihololithus*
259 *kanungoi*, *S. tentorium*, *S. biskayae*, *S. dimidius*) have small peaks just before and at the end of
260 the PETM CIE (Fig. 2). The cumulative curves for the coccolith assemblage composition show
261 a dominance in the three studied sites of *Coccolithus* spp. A major difference concerns
262 *Ericsonia* spp., which is abundant at Site 1209 but absent or very rare at Site 1263 and
263 Kharouba, respectively (Fig. 2).
264
265 **3.4 Absolute abundances and fluxes of calcareous nannofossils**
266 At Site 1209, absolute abundance decreases from 4.5 E^9 to 3.5 E^9 starting at -0.20 m up to
267 the lithologic change corresponding to the PETM event (Fig. 4A). Minimum values are
268 recorded (2 E^9) at 0.1 m. Values recover from 0.1 to 0.4 m up to 3 E^9 but never attain pre-
269 PETM records. One-way ANOVA test indicates that pre-PETM values are statistically different
270 from the ones belonging to the core of the PETM and from those belonging to the recovery
271 interval (Supplementary material). Fluxes measured as Nannofossil Accumulation Rates (NAR;
272 number of specimens per square centimeter per year) overall match absolute abundance values.
273 Overall values are very low, being in the range of 0 to 0.05 E^¨9.

At Site 1263 (Fig. 4B), absolute abundance is in the same order of magnitude as at Site 1209 (E^9) although values are slightly more fluctuating (Fig. 4). Values are about 4 E^9 in the interval below the PETM, then decrease down to ~2 E^9 from - 0.2 m and stay low during core of the event (0.07 m to 0.57 m). A return to pre-PETM values is observed during the recovery phase (from 0.67 to 1.66). One-way ANOVA test indicates that pre-PETM values are statistically different than the ones belonging to the core of the PETM and from those belonging to the recovery interval (Supplementary material). NAR values well match absolute abundance. Overall values are quite low, being in the range of 0 to 0.5 E^9.

At Kharouba absolute abundance values are lower respectively to ocean sites (Fig. 4C). Values are constant below the event from 0 to 3 m (0.1 E^9). Despite a highly fluctuating trend, from 3.2 to 28.2 m values show an almost 3-times increase. One-way ANOVA test indicates that values belonging to the recovery phase are statistically different with respect of those of pre-PETM and core of the event. NAR values are quite high compared to the oceanic sites, being in the range of 0 to 50 E^9. NAR is relatively high in the pre-PETM interval, very low in the core of the event, and high again in the recovery interval and in the post-PETM. However, the sharp increase observed at ~7.5m might be an artifact due to the accumulation rate values used in this work.

### 3.5 Principal Component Analysis

Only species with a high sampling adequacy (that are recorded in a continuous way after their first occurrence) and having a loading higher than ±0.5 on one of the extracted factors are considered here. Factors are regarded as significant only when they have a contribution to the variance higher than 10 %. First, we performed a PCA on the whole dataset from the three sections, then for each studied section separately.

299 Principal component analysis (PCA) performed on the whole dataset gives four main factors
300 accounting for 79 % of total variance (Fig. 3A). The first factor (27 % of the variance) has an
301 important positive loading of malformed *Discoaster*, *Rhomboaster* and *C. bownii*. The second
302 factor (22 % of the variance) has strong negative loading of *Tribrachiatus bramlettei* opposed
303 to *C. bownii*. The third factor (19 % of the variance) has strong loading of *Prinsius* and
304 *Rhomboaster*. The fourth factor (11 % of the variance) has strong positive loading of
305 *Thoracosphaera.*
306 For samples from Site 1209 when analyzed separately (Fig. 3B), three factors were extracted
307 by PCA. The first one accounts 61 % of total variance and, similar to PCA applied to the whole
308 dataset, has an important positive loading of malformed *Discoaster*, *Rhomboaster* and *C.*
309 *bownii*. The second factor (13 % of total variance) has a strong loading for *T. bramlettei* like
310 PCA applied to the whole dataset. The third factor (10 % of total variance) has a strong loading
311 for *Thoracosphaera,* like the PC4 applied to the whole dataset.
312 At Site 1263 (Fig. 3C), PCA provides four factors. The first factor (43% of total variance) has
313 a strong positive loading of malformed *Discoaster*, *Rhomboaster* and *C. bownii* like at Site
314 1209, but at Site 1263 these are opposed to *Prinsius*. The second factor (43% of total variance)
315 has a strong loading for *T. bramlettei* like at Site 1209 and PCA applied to the whole dataset,
316 but here it is opposed to *Thoracosphaera*. At 1263, the third and fourth factor account both for
317 10 % of total variance. PC4 has a strong positive loading for *Thoracosphaera* and compares to
318 PC3 at both 1209 and Kharouba (see below). Here, *Thoracosphaera* is highly opposed to
319 *Prinsius*.
320 The PCA at Kharouba (Fig. 3D) provides three factors representing 63 % of total variance. The
321 second factor (22 % of total variance) has a strong (0.6) loading of malformed *Discoaster*,
322 *Rhomboaster* and *C. bownii* like at both Site 1209 and 1263 but these are opposed to
323 *Hornibrookina*, which is absent at both 1209 and 1263. The first factor (29 % of total variance)

has an important negative loading (-0.6) of *T. bramlettei* and it compares to the first PC factor at 1263 and 1209. Here, *T. bramlettei* it is opposed to *C. bownii* (like in PCA applied to the whole dataset) and *Prinsius*. The third factor displays negative (-0.5) loading for *Thoracosphaera*, but here this taxon is strongly opposed to *Hornibrookina*. This factor compares to PC3 of PCA applied to the whole dataset and of Site 1209, and to PC4 of Site 1263.

### 3.6 Stratigraphic changes in PCA scores

PCA scores show some common stratigraphic features in the three sections, although the variance contribution of correlative factors is different in each section. Score values are generally more stable in open-ocean localities relatively to proximal ones. Namely, values are very stable at Site 1209, fluctuating at Site 1263, and highly fluctuating at Kharouba (Fig. 4A, B, C). In oceanic localities, we observe that the decrease of all factors begins well before the PETM and lithological change (Fig. 4A, B, C). At Kharouba, values are stable in the pre-PETM and highly fluctuate from the core of the PETM until the end of the recovery. It is worth noticing that even in the aftermath of the PETM values remain highly fluctuating at Kharouba.

The most striking similarity occurs between the first factor of oceanic sections (1209 and 1263) and the second one of Kharouba. These factors ~~begin to~~ display high positive values during the core of the PETM and persist at least until the end of the recovery phase (Fig. 4 A, B, C). At Site 1209, the first factor remains high until the last studied sample (0.42 m; Fig. 4A), while at Site 1263 and at Kharouba they decrease and are more fluctuating just above the end of the recovery phase (Fig. 4B, C). This is in perfect agreement with the fact that at Site 1209, the last studied sample belongs to the recovery phase (Fig. 4A), while at Site 1263 and at Kharouba the studied interval extends above the recovery phase. The most important taxa loading on these factors are *C. bownii*, malformed *Discoaster* and *Rhomboaster*.

A decreasing trend is observed for PCA factors 2 at 1209 and 1263 and factor 1 at Kharouba respectively. Minimum values are recorded in the post-PETM. In all sections, the most important taxa loading on these factor is *T. bramlettei*. While at Site 1263 this taxon is strongly opposed to *Thoracosphaera* at Kharouba it is opposed to *Prinsius* and *C. bownii*.

The third factor at Site 1209 and Kharouba and the fourth at 1263 present all high loading for *Thoracosphaera*. The stratigraphic pattern of this factor differs from open ocean localities to proximal ones. At Site 1209 is fluctuating in the pre-PETM but it is very stable during the core of the event, where it reaches highest values and is still very stable the recovery phase. At Site 1263, albeit being less stable than at Site 1209, this factor displays higher values during the core of the event and is highly fluctuating in the post-PETM. Here, *Thoracosphaera* is strongly opposed to *Prinsius*. At Kharouba this factor is highly fluctuating. *Thoracosphaera* is here strongly opposed to *Hornibrookina.*

### 3.7 SIMPER and cluster analysis used for comparisons between sites

The similarities and dissimilarities between localities are evaluated by using multivariate analyses like SIMPER and cluster analysis applied to the three sections studied here and to six other sites used for comparison. The species accounting for the dissimilarities and their percentage contribution are also shown in the SIMPER graph. The percentages of similarity between localities are shown in the cluster analysis dendrogram. The results of SIMPER and cluster analysis show that *Coccolithus*, which is the most abundant species alongside with *Toweius*, is very abundant at Site 1263 as well as in the other localities, but at Site 690. Conversely, *Chiasmolithus* spp. are very abundant at Site 690. Also, *F. richardii* group is absent at Site 690, while it is very abundant at Site 1263 and other sites. This makes Site 690, which is located at high latitudes in the Southern Ocean, the most dissimilar location as far as calcareous nannofossils are concerned. *Ericsonia* spp. is very abundant at Site 1209, conversely

374 *Semihololithus*, which is interpreted as a holococcolith (Bown, 2005) is absent at Site 1209 (N
375 Pacific gyre), but it is present only in proximal settings (TDP 14, Kharouba, Alamedilla). This
376 peculiar assemblage composition makes Site 1209 very different from other localities. TDP 14,
377 located in Tanzania, is also a quite peculiar site in which *Zygrhablithus* spp. is absent. This site
378 is also known to be a sort of coccolith lagerstätt. The differences between Site 1263 and
379 Kharouba section are mainly explained by the rarity of *Fasciculithus* spp. in this last location.
380 Kharouba section is also different from Site 1260 because of the abundance of *Discoaster* spp.
381 *Toweius* spp. is a very common taxon, its higher proportion at Kharouba explains the
382 dissimilarity with respect to Alamedilla, in spite of the proximity between the two areas, and
383 the similarity with respect to Atlantic sites, where *Toweius* is relatively more abundant than in
384 Tethys or in the Pacific. The differences between Alamedilla (Spain) and Cicogna (Italy) are
385 mainly explained by the more consistent presence of *Thoracosphaera* in this latter.
386
387 **4. Discussion**
388 **4.1 Preservation**
389 Before discussing trends in nannofossil assemblages, preservation issues potentially affecting
390 assemblage composition have to been carefully considered. In fact, the PETM is classically
391 considered as an event of shoaling of both lysocline and CCD inducing dissolution of delicate
392 forms and, finally, diversity loss. The three studied sections were all deposited well above the
393 CCD, and carbonate dissolution likely occurred a few centimeters around the lithological
394 contact, as shown by a poor nannofossil preservation there also attested by previous studies
395 (Bralower et al., 2014; Raffi et al., 2009). However, at Site 1209 nannofossil preservation is
396 moderate to good unless the very thin interval across the LC, and slightly overgrowth
397 *Discoaster* specimens are commonly observed in the studied samples, indicating that overall
398 burial diagenesis was operating (Adelseck et al., 1973), but dissolution in the water column or

399 at the water/sediment interface were rather limited phenomena (unless around the LC interval).
400 At Site 1263, poorly preserved coccoliths are observed in the same sample as pristinely
401 preserved specimens of the same species. This peculiar pattern may indicate that a high-
402 frequency (probably seasonal?) fluctuation in accumulation rate occurred at this location. In
403 times of low accumulation rates, nannofossil assemblage was poorly preserved because of a
404 longer exposure at the sediment/water interface (Schneidermann, 1977). Conversely, when
405 sedimentary input was higher, nannofossils were rapidly buried and escaped to the corrosive
406 action of waters at the sea-floor. At Kharouba, overall preservation is moderate-to-good likely
407 due to the presence of clay minerals in marly lithologies, which inhibited corrosive water
408 circulation more efficiently than in limestones. In fact, commonly the best preservation of
409 nannofossils is recorded in marly lithologies (Thierstein and Roth, 1991). A common pattern in
410 Kharouba samples is the presence of delicate holococcoliths, which also show abundance peaks
411 just before and at the end of the PETM CIE. Holococcoliths would be easily dissolved if
412 corrosive waters occurred or intense burial diagenesis. In synthesis, after carefully
413 consideration of preservation issues, it seems likely that dissolution in the water column or at
414 the water/sediment interface or within the sediment overall poorly impacted nannofossil
415 assemblage composition, unless in discrete and stratigraphically circumscribed intervals.
416
417 **4.2 Global *versus* local features**
418 The three studied sections were located in very different paleoceanographic settings during the
419 late Paleocene and the early Eocene: while Sites 1209 and 1263 provide us with excellent
420 records from tropical gyres in the Pacific and the Atlantic Ocean respectively (Bralower et al.,
421 2002; Zachos et al., 2004), Kharouba section was located in a proximal setting in the southern
422 Tethys (Karoui-Yaakoub et al., 2011). Although situated in a tropical gyre, Site 1263 was
423 located on Walvis Ridge off Namibia coast. In the modern ocean, nutrient depleted tropical

gyres are characterized by very stable conditions (Milliman et al., 1993), contrarily to more unstable coastal localities, where the environmental parameters can undergo rapid changes.

The ecology of calcareous nannofossils is inferred from their paleogeographic distributions; tropical species are thought to be adapted to warm-waters and high-latitude species to cold water, coastal species are adapted to eutrophic or unstable conditions and open-ocean species to oligotrophic environments (Haq and Loqmann, 1976; Gibbs et al., 2004; Bown and Pearson, 2009). We discuss here similarities and differences in nannofossil assemblages between the three localities in order to track global *versus* local features in response to environmental perturbations across the PETM.

The most striking feature when comparing the three studied sites is that, although absolute abundances are in the same order of magnitude at Sites 1209 and 1263, and lower and quite steady at Kharouba, when taking fluxes into consideration the same trend is observed but with huge differences in the magnitude (Fig. 4). Kharouba records fluxes 3-to-4 orders of magnitude higher than at the oceanic sites. As general trend, both absolute abundance, fluxes and PCA scores show gradual and regular changes at Site 1209, are slightly more fluctuating at Site 1263 and more irregularly fluctuating in the most coastal site (Kharouba), suggesting more unstable conditions there. Higher fluxes and more intensely fluctuating parameters at Kharouba may indicate that environmental conditions were more unstable there and that continent-delivered nutrients were in higher concentrations supporting a more vigorous nannoplankton productivity. Such an interpretation is further supported by the C-isotope trends, which although similarly record in the three sections the negative CIE related to PETM, display a very prominent offset. In fact at Site 1209, supposed to represent the most oligotrophic area, C-isotope values are comprised between 0 and 3 ‰, at Site 1263 between -1 and 2, and at Kharouba between -2.5 and 1. $^{12}C$ uptake by primary producers was therefore much more

efficient in the proximal Kharouba section than in the oceanic site and, especially, the Pacific gyre.

In all the sections, the change in absolute abundance and fluxes (i.e., the significant decrease) and in nannofossil assemblages as indicated by PCA factors slightly predates the onset of the PETM. This pattern may be linked to a differential diagenesis according to lithology. At Site 1209, the lithology is constantly dominated by nannofosils oozes and $CaCO_3$ never goes below 90 % even during the core of the PETM (Colosimo et al., 2006). This could explain why both absolute abundances, fluxes and PCA factors are very stable. At Site 1263, the onset of the PETM is marked by an increase in clay content and a decrease almost to 0 % in $CaCO_3$ (Zachos et al., 2005). However, no major shifts in absolute abundances, fluxes and PCA factors is observed, while both parameters start to vary before the PETM. At Kharouba, PCA values are very stable below the PETM, but during the PETM they become more fluctuating. PCA factors begin to fluctuate at 3.4 m, which is above the onset of the PETM, while fluxes are highly fluctuating from the recovery interval upsection. No lithological change is observed at Kharouba, since the lithology is always constituted by marls. Finally, different diagenetic or lithological conditions among the sections fail to explain increased fluctuating signals from open ocean localities to proximal ones.

In the three studied localities, environmental perturbations began before the PETM.-In the core of the PETM, an increase in factors characterized by strong loadings of malformed *Discoaster*, *Rhomboaster* and *C. bownii* is observed in all sections. Previous studies suggested that these taxa are restricted to the PETM interval and have an affinity for warm waters and oligotrophic environments (Bown and Pearson, 2009). Strongly oligotrophic conditions persisted in oceanic localities but in coastal environments, such as Kharouba, it is reasonable that increased nutrient influx and more humid conditions triggered more unstable conditions, as also suggested by mineralogical analyses (Karoui-Yaakoub et al., 2011). Bralower and Self-Trail (2016)

suggested that malformation of *Discoaster* across the PETM is due to a low saturation state of oceanic waters with respect to carbonates, proposing ocean acidification as the main cause. *Coccolithus bownii* has a peculiar morphology displaying a wider central area than other *Coccolithus* species and an overall smaller mass (see chapter 4). This feature would also be compatible with a low ocean saturation state of oceanic waters, but this remains highly speculative. Despite the ecological affinity of malformed *Discoaster*, *Rhomboaster* and *C. bownii* cannot be unequivocally discerned because there are extinct taxa with no living counterpart, PCA results indicate a global pattern across all the Oceans and in disparate environmental conditions.

PC3 at 1209, PC4 at 1263 and PC3 at Kharouba are characterized by strong loadings of *Thoracosphaera*, a taxon adapted to nutrient-depleted environments in modern oceans (Vink et al., 2002). PC3 is very stable at Site 1209, particularly from the core of the PETM to the recovery (Fig. 4A) and this suggests very stable oligotrophic conditions across the event, in agreement to previous studies (Gibbs et al., 2006). At Site 1263, PC3 is more fluctuating and *Thoracosphaera* is opposed to *Prinsius* (Fig. 4B), a cold-water taxon adapted to eutrophic environments (Haq and Loqmann, 1976; Bown and Pearson, 2009; Self-Trail et al., 2012).

Previous studies showed that during the PETM, cold-water and eutrophic taxa (*Prinsius*, *Hoornibrookina*) are replaced by warm ~~waters~~ and oligotrophic species (*Thoracosphaera*, *C. bownii*; Gibbs et al., 2006; Self-Trail et al., 2012; Bown and Pearson, 2009). A direct temperature control explaining the response of *Prinsius* to the PETM is unlikely at both 1263 and Kharouba, given that both localities were located in low-latitude contexts (Zachos et al., 2004; Karoui-Yaakoub et al., 2011). The strong opposition between oligotrophic-adapted taxa and eutrophic-ones suggests fluctuating nutrient conditions in these settings, that due to their proximity to emerged lands, were more prone to record shifting environmental conditions than Site 1209 situated in an oligotrophic gyre. Peaks in taxa indicative of cool and high-fertility

conditions suggest a relatively shallow nutricline and well mixed surface waters; conversely, peaks of taxa indicative of warm and low-fertility waters suggest a relatively deep nutricline and more stratified waters (Vink et al., 2002). Site 1263, shifted from oligotrophic to under more eutrophic conditions in the course of Paleogene, favoring the development of meso-eutrophic taxa (Bordiga et al., 2015). Then, alternating peaks of *Prinsius* and *Thoracosphaera* (PC4) suggest more unstable conditions compared to Site 1209 with alternating stratified and mixed waters.

At Kharouba, environmental conditions where even more unstable as indicated by higher fluxes, highly fluctuating absolute abundances and PCA factors (Fig. 4C). Here, *Thoracosphaera* is highly opposed to *Hornibrookina*. The similarity of their construction to specimens of the Cretaceous and Tertiary genus *Biscutum*, and their first occurrence immediately following the Cretaceous/Paleogene boundary, suggests that *Hornibrookina* may have evolved from *Biscutum*, a genus long thought to be indicative of high paleoproductivity (Watkins, 1989; Self-Trail et al., 2012). Thus, high fluctuating values of PC3 at Kharouba further support unstable conditions in this locality. In agreement to mineralogical analyses (Karoui-Yaakoub et al., 2011). Increased continental weathering due to more humid conditions favored eutrophic taxa, while during arid climatic phases (and reduced riverine nutrient discharge) oligotrophic taxa thrive.

PC2 at Site 1209 and 1263 and PC1 at Kharouba have strong loadings of *T. bramlettei*, pointing to a global trend across all oceans and different paleoenvironments. At Site 1263, PC2 markedly decreases at 0.97m, in correspondence of the appearance of *T. bramlettei* and at Kharouba PC1 is constant below the appearance of *T. bramlettei* and starts to decrease at 3 m. Such an observation supports an evolutionary control on this factor. Even if at Site 1263 *T. bramlettei* is opposed to *Thoracosphaera* and at Kharouba it is opposed to *Prinsius*, the fact that at both localities these factors start to decrease in correspondence of the appearance of *T. bramlettei*

means that this is related to the emergence of the genus *Tribrachiatus*, that will thereafter evolve in the lower Eocene.

### 4.3 Comparison with other sites

The biogeographic patterns of Neogene calcareous nannofossils was already explored by Haq and Lohmann (1976) by using quantitative methods, namely Q-mode Varimax Factor and Oblique Factor Analyses. In this account, a quantification of similarities and dissimilarities of the sites we studied with respect to already published nannofossil data from various oceanic sites and proximal seas is attempted by using multivariate analyses. According to calcareous nannofossil assemblages, the most dissimilar section is Site 690 located in Antarctic waters. This pattern is also reported for modern assemblages that show a reduced diversity and a dominance of opportunistic species in sub-polar waters, where the limiting factors are the low-temperature and poor light availability in winter season, while surface waters are enriched in nutrients (Winter, 1994). Another locality which is very different from all the other settings is the TDP 14 core, located in Tanzania. This corresponds to a nannofossil lagerstätte, showing exceptionally well-preserved coccolith structures (Bown and Pearson, 2009). TDP 14 has some features typical of equatorial sites (e.g., the absence of *Zygrhablithus*) but, because of pronounced differences concerning the overall assemblage composition, this locality might correspond to a cul-de-sac, poorly connected with the open-ocean. Similarly, Alamedilla (Spain) and Cicogna (Italy) display nannofossil assemblages which are markedly different from the other oceanic sites, probably because of their proximal position with respect to emerged lands, and location in very restricted stretch of sea. Also, Site 1209 is fairly different from all the other sites, and this is probably due to its position within an oceanic gyre. There, oligotrophic conditions dominated and the gyre probably represented a physical barrier preventing mixing of waters with the rest of Pacific Ocean. Interestingly, Kharouba shows less

548 pronounced dissimilarities with Atlantic sites, which were located relatively close to emerged
549 lands (namely, South Dover core, Sites 1260 and 1263), than with other Tethys settings (such
550 as Alamedilla and Cicogna) in spite of geographic proximity. This pattern attests for the
551 existence of effective oceanic connections between the south-western part of Tethys, where
552 Kharouba is located, and the Atlantic Ocean. These novel results show that oceanic connections
553 and surface circulation played a major control on upper Paleocene-lower Eocene calcareous
554 nannofossil assemblage composition.
555
556 **4.4 Comparison with other proxies**
557 The negative C-isotopes excursion at the PETM, despite its origin is still matter of debate
558 (Dickens et al., 1995; Gutjahr et al., 2017), has been previously globally recorded and allows
559 us to produce effective correlation of open ocean and proximal sections across different
560 localities (Fig. 6; modified after Menini et al., submitted). Irrespectively of its source, the input
561 of isotopically light carbon led to an increase of 5-8° C in seawater temperatures, as indicated
562 by oxygen isotopes measured in planktonic and benthic foraminifera. Other
563 paleothermomethers such as the Mg/Ca ratio (Zachos et al., 2003; Penman et al., 2014) and
564 $TEX^{86}$ (Suijs et al., 2007) confirm this pattern. Ultimately, excess $pCO_2$ lead to ocean
565 acidification, as shown by boron isotopes (Penman et al., 2014; Penman et al., 2014; Babila et
566 al., 2018). Enhanced continental weathering is thought to be the principal negative feedback
567 responsible for the removal of the excess in $pCO_2$ and this is supported by both experimental
568 data (Osmium isotopes; Ravizza et al., 2001) and models (Zeebe et al., 2012). The PETM is
569 associated to perturbations in all the major geochemical cycles, and this prominently impacted
570 on the response of marine ecosystems. All microfossils groups were affected by environmental
571 perturbations induced by the PETM: calcareous nannofossils, living in the mixed-layer photic
572 zone (uppermost 200 m in oceanic environment or lesser) were very sensitive to these changes.

In open-ocean localities (Fig. 6) dramatic decreases in absolute abundances and PCA are most probably related to reduced nutrient supply in the photic zone as a consequence of warming-driven oligotrophy (see above). Cold-water taxa decreased in abundance during the event and warm-water ones increased (Bralower et al., 2002; Gibbs et al., 2006; Self-Trail et al., 2012). However, some taxa (malformed *Discoaster*, *Rhomboaster*, *Thoracosphaera*) took advantage of these stressful conditions in all localities and at all latitudes. In proximal localities, nannofossils assemblages suggest highly fluctuating trophic conditions from the PETM until the recovery (Fig. 6) and absolute abundances increased. Meso-eutrophic species flourished in times of enhanced nutrient discharge into the basins, in agreement with enhanced continental weathering during the event (Ravizza et al., 2001).

The environmental perturbations occurring along with the C-isotopes excursion of the PETM also affected other organisms, such as planktonic and benthic foraminifera and dinoflagellates. At both low and high latitudes, planktonic foraminifer assemblages shifted from cold-water taxa before the PETM to warm-water ones during the event, returning to pre-event conditions during the recovery phase (Clay Kelly et al., 2002; Petrizzo, 2007). Similar to nannofossils, the rapid diversification of planktonic foraminifer excursion taxa (Clay Kelly et al., 1996, 1998) is recorded in tropical localities, but these taxa are absent at high latitudes. Benthic foraminifera suffered a dramatic excursion at the base of the PETM and this is not only due to reduced carbonate preservation (Alegret et al., 2009). Another prominent example of biotic change associated with the onset of the PETM is recorded along continental margins, where sediment sequences from all latitudes contain high abundances of dinoflagellate cysts (dinocysts) belonging to the subtropical genus *Apectodinium* (e.g., Sluijs et al., 2006; Crouch et al., 2013). Previous studies have shown that a basic requirement for *Apectodinium* acme was high-temperature conditions, but it is also reasonably associated to meso-eutrophic conditions in proximal localities (Sluijs et al., 2007). However, our nannofossil data do not support this

hypothesis, namely reduced nannofossil fluxes during the event suggest decreased nannofossil production, while the flux increase in the recovery phase suggests enhanced nannofossil production and thereby nutrient supply in the aftermath of the PETM. However, pulses of eutrophic taxa, such as *Hornibrookina* and *Prinsius*, are observed in the proximal Kharouba section, suggesting that oligotrophy was sporadically interrupted because of continent-derived nutrient inputs. Previous studies have brought evidences that environmental perturbations preceded the light carbon injection (Sluijs et al., 2007; Frieling et al., 2019) and this is supported by our data, albeit the causes of early warming remain still uncertain.

## 5. Conclusions

The high-resolution study of calcareous nannofossil assemblages at three sections located in different paleoceanographic settings allowed us to track regional *versus* global features in response to the Paleocene Eocene Thermal Maximum. In both oceanic tropical oceanic localities from the Pacific and Atlantic oceans (Sites 120 and 1263) and in proximal settings Kharouba we show that changes in calcareous nannofossil assemblages predate the carbon isotopes excursion. PCA shows that the PETM interval is characterized by strong loadings of malformed *Discoaster*, *Rhomboaster* and *C. bownii* (excursion taxa). Despite of a global fingerprint, the three sections present some peculiarities as far as nannofossil assemblages are concerned and these are related to different paleoceanographic contexts.

At Site 1209, in the middle of a tropical gyre and far from emerged lands, very stable oligotrophic conditions characterize the PETM, as indicated by the consistent occurrence of *Thoracocosphaera*, and the very low nannofossil fluxes. This locality was the less affected by environmental changes induced by the event and overall low productivity conditions are attested further by the positive offset of C-isotope values across the studied interval. At Site

623 1263, despite of the analogies with Site 1209, nannofossil assemblages record less stable
624 conditions than at Site 1209. The proximity of emerged lands (Zachos et al., 2004) and the
625 influence of upwelling (Bordiga et al., 2015) may explain the fluctuating trend from
626 oligotrophic to eutrophic conditions at this site. At Kharouba, a proximal Tethys section,
627 nannofossils assemblages indicate strongly fluctuating environments, namely an alternation of
628 phases of stratification and mixing of surface waters. At this locality, PCA shows a strong
629 opposition of eutrophic (*Hoornibrookina*) to oligotrophic (*Thoracosphaera*) taxa. This locality
630 was also the most productive, as shown by very high nannofossil fluxes and negative overall
631 offset of C-isotope values. Sporadic increased nutrient input also occurred during the PETM,
632 as also pointed out by osmium isotopes (Ravizza et al., 2001), and modulated the response of
633 nannofossils in proximal localities, which are more easily affected by changes in nutrient
634 discharge because of their proximity to emerged lands.
635 An increase in nannofossil fluxes in all the studied localities during the recovery phase of the
636 event suggests that primary productivity returned to pre-event levels. Recent studies on Barium
637 isotopes evidenced that, in oceanic localities, export production either remained unchanged or
638 decreased during the PETM (Bridgestock et al., 2019), before increasing during the recovery
639 phase and this is coherent with our results. With this regard, calcareous nannofossil production,
640 along with enhanced continental weathering and, to a more limited degree, increased organic
641 carbon production and burial in shelf areas, likely contributed to $CO_2$ drawdown and ultimately
642 climatic recovery in the aftermath of the PETM.
643
644
645 Figures captions
646

Figure 1. Fig. 1. Location of the three studied sections on a paleogeographic map at 56 Ma : (http://www.odsn.de/odsn/services/paleomap/paleomap.html): Kharouba section (Tunisia), Site 1209 (Shatsky Rise, Tropical Pacific), and Site 1263 (Walvis Ridge, South Eastern Atlantic). Location of the sites used for comparison is also shown: Site 690 (Southern Ocean) Site 1260 (Equatorial Atlantic), SDB (New Jersey), TDP 14 (Tanzania), Cicogna (North Italy), Alamedilla (Spain).

Figure 2. Cumulative graphic of main nannofossil genus for the three studied sections in function of depth. Horizontal scale is the same but vertical one is different because of important differences in the thickness between oceanic sites and Kharouba. Also, nannofossil biostraigraphy and lithostratigraphic column. Total assemblage composition (coccoliths, nannoliths) and coccolith assemblages for the three sections.

Figure 3. Principal components analysis loading plots. Only species with a high sampling adequacy and having a loading higher than ±0.5 on one of the extracted factors are considered here. Factors are regarded as significant only when they have a contribution to the variance higher than 10 %. A; loading plot resulting from the PCA performed on the three studied sections.,B; loading plot resulting from the PCA performed on ODP Site 1209, C; ODP Site 1263, D; Kharouba. Error bars irepresent lower and upper limits for 95% confidence intervals, using 9999 bootstrap replicates.

Figure 4. Stratigraphical evolution of PCA scores, absolute abundance (black) and NAR (grey) in function of depth against nannofossil biostratigraphy and carbon isotopes curve ($\delta^{13}C$) in the three studied sections. Note that the vertical scale is different from a section to another. The correlative factors, i.e., those on which the same taxa load, are shown in the same order for the

three sections, irrespective of their variance values. The species with important loadings on the different factorial axes are reported.

Figure 5. Cluster analysis (right) and SIMPER analysis (left) applied on the three studied sections (Site 1209, 1263 and Kharouba) and 6 other sections that provide excellent stratigraphic records of the PETM calcareous nannofossils (See text for further details).

Figure 6. Synthesis of the main geochemical and biotic events occurring across the PETM relative to the δ13C bulk carbonate record (Alamedilla (red) Lu al. 1996, ODP 690 (grey) Bains et al. 1999, ODP 1209 (orange) Penman et al. 2014, ODP 1263 (light blue) Zachos et al. 2005, ODP 1260 (green) Mutterlose et al. 2007, Kharouba (brown), This work, South Dover (violet) Self Trail et al. 2012, Cicogna (black) Agnini et al. 2016). For TDP 14 (pink) we used δ13Cn-alkane record (isotopes of C-25, C-27, C-29 and C-31 alkanes), since δ13Cbulk carb did not provide satisfacting results (Bown and Pearson 2009, Aze et al. 2014). Tie-points of the $\delta^{13}$Cbulk carb at Site 690 as defined by Zachos et al. (2005) and Röhl et al. (2007) from –A to H are shown. Envelope curve of oxygen isotope records (extracted from the database of Cramer et al., 2009) from individual cores from the North Atlantic (ODP1051), and Southern Oceans (ODP690). Osmium isotopes record after Ravizza et al., 2001 at DSP Site 541. Planctonic foraminfera data after Petrizzo et al., 2008 (warm water=Morozovella spp., cold water=Subbotina spp.). Dynocists data after Sluijs et al., 2006. See text for details.

# Supplementary data

### 3.4 Relative and absolute abundances of Nannofossils

At Kharouba, placolith assemblages compose most of the assemblage: *Toweius* (30-50 %) and *Coccolithus* (30-40 %) are the most abundant genus. *Toweius serotinus* is particularly abundant from 5.3 to 7.6 m (15 %), across the recovery phase of the PETM. During the core of the PETM (from 0.9 m to 2.5 m) we observe increased abundances of *Hornibrookina* spp., *Coccolithus bownii*, *Discoster araneus* and *D. anartios* and *Rhomboaster*. *Prinsius* spp. attain up 10 % in relative abundance before the event and become more scattered up in the section. *Cruciplacolithus* and *Chiasmolithus* never overcome 5 % in abundance. Nannoliths are mainly composed by *Fasciculithus* (10%), *Discoaster* (10 %) and *Sphenolithus* (10 %). *Fasciculithus* relative abundance drastically decreases to 1% at 14 m. *Zygrhablithus bijugatus* never overcomes 10 % but it increases up in the section starting at 12 m A peak (15 %) is observed at 15.2 m.

Absolute abundance of all genus is constant below the PETM for all genus values increase during the event at 3.2 m and remain high through the section until the last studied samples

721 (28.2 m). It is worth noticing that values decrease from 2.2 m to 3 m but this is not statistically
722 significant, since one-way ANOVA indicates that only values belonging to the recovery interval
723 are statistically different from the ones of the core and from the ones of the pre-PETM (Table
724 S1).
725 *Coccolithus* and *Toweius* are the most abundant genera and account up to half of total absolute
726 abundance. Values of each genues are stable below the PETM (60 E^6) and display a two-times
727 increase at 3.2 m.
728
729 *Coccolithus* abundance is constant (60 E^6) below the PETM. Vthe PETM values decrease to.
730 *Prinsius* absolute abundance is higher below the PETM (20 E^6) until 3.2 m and then it
731 gradually decreases.
732 Absolute abundance of *Discoaster* is constant from 0 to 3 m and from (20 E^6) and it displays
733 a two-fold increase (40 E^6) at 3.2 m until the last studied sample.
734 Despite two peaks at 12.3 and 28.2 m, *Sphenolithus* absolute abundance is constant s through
735 the section (20 E^6). *Fasciculithus* absolute abundance are low at Kharouba in comparison to
736 ODP 1209 and 1263. Maximum values are recorded during the core of the event at 3.4 m and
737 then a gradual decrease is observed from 3.4 m to 14. 2 m, where values drastically decrease
738 to 2 E^6 and will never recover.
739 At Site, 1263 *Coccolithus* dominates the placolith-coccolith part of the assemblage (30-40 %)
740 as well as *Toweius* (25 %). Small *Ericsonia* referred to as *E. orbis* (Bown et al., 2016) are
741 present but never reach high abundance like at Site 1209. *Prinsius* are consistently present and
742 account up to 2% of total assemblage. The rest of the assemblage is dominated by *Fasciculithus*
743 (40 % to 5%), *Discoaster* (10 %) and *Sphenolithus* (10%). During the core of the PETM (from
744 0 m to 0.47 m) we observe increased abundances of *Coccolithus bownii*, *Discoster araneus* and
745 *D. anartios* and *Rhomboaster*.

*Zygrhablithus* rapidly increases from 1 to 30 % at 0.57 m. At Site 1263 *Fasciculithus* increase in relative abundance from 10 % to 40 % from -0.45 m to 0.67m

Afterwards (0.67 m), *Fasciculithus* decreases from 40 % to 5%, as previously observed (Raffi and De Bernardi, 2008; Raffi et al., 2009).

*Coccolithus* is the most abundant genus and it accounts up to half of total absolute abundance (Fig. 3) and values are stable across the PETM. *Toweius* is the second placolith most abundant genus at Site 1263 and neither displays changing in abundance. *Fasciculithus* absolute abundance increases from -0.45 m to 0.67 m, where they reach maximum values.

At the same time, *Zygrhablithus* spp. rapidly increases. Similarly, to Site 1209 *Sphenolithus* and *Discoaster* absolute abundance remain constant all through the event.

At site 1209, Placolith assemblages are dominated by *Coccolithus* (30-40 %) and *Ericsonia* (20 %) accompanied by lower abundances of *Toweius* (10-15 %). *Ericsonia* rapidly decreases from 40% to 10% at 0 cm above the PETM. During the core of the PETM (from -0.03 m to 0.07 m) we observe increased abundances of *Coccolithus bownii*, *Discoster araneus* and *D. anartios* and *Rhomboaster*.

The rest of the assemblage is composed by *Fasciculithus* (40 % to 5%), *Discoaster* (10 %) and *Sphenolithus* (10%). *Zygrhablithus* rapidly increases from 1 to 20 % at 7 cm above the lithological contact. In parallel, *Fasciculithus* decreases from 40 % to 10%, as previously observed (Gibbs et al., 2006b).

*Coccolithus* is the most abundant genus and it accounts up to half of total absolute abundance (Fig. 3). Values are generally stable across the PETM except at the onset of the event, where absolute abundance show a distinct two-fold peak. *Ericsonia* is very abundant below the PETM but rapidly decreases starting from the onset of the event. Similarly, *Fasciculithus* decrease from the pre-PETM to the recovery phase but this is far less spectacular than the drastic decrease

770 in relative abundance. At the same time, *Zygrhablithus* spp. rapidly increase. Interestingly,

771 *Sphenolithus* and *Discoaster* absolute abundance remain constant all through the event.

## References


- Agnini, C., Fornaciari, E., Raffi, I., Catanzariti, R., Pälike, H., Backman, J., Rio, D., 2014. Biozonation and biochronology of Paleogene calcareous nannofossils from low and middle latitudes. Newsletters on Stratigraphy 47, 131–181
- Alegret, L., Ortiz, S., and Molina, E., 2009. Extinction and recovery of benthic foraminifera across the Paleocene–Eocene Thermal Maximum at the Alamedilla section (Southern Spain). Palaeogeography, Palaeoclimatology, Palaeoecology, 279(3–4), 186–200.
- Babila, T.L., Penman, D.E., Hönisch, B., Kelly, D.C., Bralower, T.J., Rosenthal, Y., Zachos, J.C., 2018. Capturing the global signature of surface ocean acidification during the Palaeocene–Eocene Thermal Maximum. Philosophical Transactions A 376.
- Bains, S., Norris, R. D., Cordfield, R. M., Faul, K. L., 2000. Termination of global warmth at the Palaeocene/Eocene boundary through productivity feedback. Nature 407, 171–174.
- Beaufort L., Barbarin, N., Gally Y., 2014. Optical measurements to determine the thickness of calcite crystals and the mass of thin carbonate particles such as coccoliths. Nature protocols 9(3), 633–642.
- Beaufort, L., Heussner, S., 2001. Seasonal dynamics of calcareous nannoplankton on a West European continental margin: The Bay of Biscay. Marine Micropaleontology 43(1–2), 27–55.
- Bown, P. R., 2005. Palaeogene calcareous nannofossils from the Kilwa and Lindi areas of coastal Tanzania (Tanzania Drilling Project 2003-4). J. Nannoplankton Res. 27 (1), 2005, 21–95.

- Bown, P. R., Pearson, P., 2009. Calcareous plankton evolution and the Paleocene/Eocene thermal maximum event: New evidence from Tanzania. Marine Micropaleontology 71, 60–70.
- Bralower, T., Clay Kelly, D., Gibbs, S., Farley, K., Eccles, L., Lindemann, T.L., Smith, G. S., 2014. Impact of dissolution on the sedimentary record of the Paleocene–Eocene thermal maximum. Earthy and Planetary Sciences Letters 401, 70–82.
- Bralower, T.J., 2002. Evidence of surface water oligotrophy during the Paleocene–Eocene Thermal Maximum: nannofossil assemblage data from Ocean Drilling Program Site 690 Maud Rise, Weddell Sea. Paleoceanography 17, 1–13.
- Bralower, T.J., Mutterlose, J., 1995. Calcareous nannofossil biostratigraphy of ODP Site 865, Allison Guyot, Central Pacific Ocean: a tropical Paleogene reference section. In: Winterer, E.L., Sager, W.W., Firth, J.V. (Eds.), Proceedings of the Ocean Drilling Program. Scientific Results 143, 31– 72.
- Bralower, T.J., Premoli Silva, I., Malone, M.J., et al., 2002. Proc. ODP, Initial Reports., 198: College Station, TX (Ocean Drilling Program).
- Bralower, T.J., Self-Trail, J.M., 2016. Nannoplankton malformation during the Paleocene-Eocene Thermal Maximum and its paleoecological and paleoceanographic significance. Paleoceanography 31, 1423–1439.
- Brand, W. A., Coplen, T.B., Vogl, J., Rosner, M., Prohaska, T., 2014. Assessment of international reference materials for isotope-ratio analysis. Pure and Applied Chemistry 8866, 425–467.
- Colosimo, A.B., Bralower, T.J., Zachos, J.C., 2006. Evidence for lysocline shoaling at the Paleocene/Eocene thermal maximum on Shatsky rise, northwest Pacific. Proceeding of the Ocean Drilling Program. Scientific Results 198, 1–36.

- Crouch, E. M., Dickens, G. R., Brinkhuis, H., Aubry, M. P., Hollis, C. J., Rogers, K. M., and Visscher, H., 2003. The Apectodinium acme and terrestrial discharge during the Paleocene–Eocene thermal maximum: new palynological, geochemical and calcareous nannoplankton observations at Tawanui, New Zealand. Palaeogeography, Palaeoclimatology, Palaeoecology 194(4), 387–403.
- Crouch, E., Heilmann-Clausen, C., Brinkhuis H., Morgans H. E.G., Rogers K.M., Egger, H., Schmitz, B., 2001. Global dinoflagellate event associated with the late Paleocene thermal maximum. Geology 29(4), 315–318.
- Dickens, G.R., Castillo, M.M., Walker, J.G.C., 1997. A blast of gas in the latest Paleocene: Simulating first-order effects of massive dissociation of oceanic methane hydrate, Geology 25, 259–262.
- Dickens, G.R., O'Neil, J.R., Rea, D.K., Owen, R.M., 1995. Dissociation of oceanic methane hydrate as a cause of the carbon isotope excursion at the end of the Paleocene. Paleoceanography 10, 965–971
- Dickson, A.J., Cohen, A.S., Coe, A.L., Davies, M., Shcherbinina, E.A., Gavrilov, Y.O., 2015. Evidence for weathering and volcanism during the PETM from Arctic Ocean and Peri-Tethys osmium isotope records. Palaeogeography, Palaeoclimatology, Palaeoecology 438, 300–307.
- Frieling, J., Peterse, F., Lunt, D. J., Bohaty, S. M., Sinninghe Damsté, J. S., Reichart, G. J., Sluijs, A., 2019. Widespread warming before and elevated barium burial during the Paleocene-Eocene Thermal Maximum: Evidence for methane hydrate release ?. Paleoceanography and paleoclimatology, 34(4), 546–566.
- Gibbs, S., Shackleton, N., Young, J., 2004. Orbitally forced climate signals in mid-Pliocene nannofossil assemblages. Marine Micropaleontology 51(1–2), 39–56.

- Gibbs, S.J., Bralower, T.J., Bown, P.R., Zachos, J.C., Bybell, L.M., 2006. Shelf and open-ocean calcareous phytoplankton assemblages across the Paleocene–Eocene thermal maximum: implication for global productivity gradients. Geology 34 (4), 233–236.
- Hammer, Ø., Harper, D. A., Ryan, P. D., 2001. PAST: Paleontological statistics software package for education and data analysis. Palaeontologia electronica, 4(1), 9.
- Haq, B. U., Loqmann G. P., 1976. Early Cenozoic calcareous nannoplankton biogeography of the Atlantic ocean. Marine Micropaleontology 1, 119–194.
- Karoui-Yaakoub, N., M'barek-Jemaï, M. B., Cherni, R., 2011. Le passage Paléocène/Eocène au nord de la Tunisie (Jebel Kharouba): foraminifères planctoniques, minéralogie et environnement de dépôt. Revue de Paléobiologie 30(1), 105–121.
- Kelly, D. C., 2002. Response of Antarctic (ODP Site 690) planktonic foraminifera to the Paleocene–Eocene thermal maximum: faunal evidence for ocean/climate change. Paleoceanography 17(4), 23–1.
- Kelly, D.C., Bralower, T., J., Zachos, J.C., 1998. Evolutionary consequences of the latest Paleocene thermal maximum for tropical planktonic foraminifera. Palaeogeography, Palaeoclimatology, Palaeoecology 141, 139–161.
- Kennett, J.P., Stott, L.D., 1991. Abrupt deep-sea warming, palaeoceanographic changes and benthic extinctions at the end of the Palaeocene. Nature 353, 225–229.
- Martini, E., 1971. Standard Tertiary and Quaternary calcareous nannoplankton zonation. In: Farinacci, A., Proceedings of the 2nd International Conference on Planktonic Microfossils 2, 739– 785.
- Milliman, J. D., 1993. Production and accumulation of calcium carbonate in the ocean: budget of a nonsteady state. Global geochemical cycles 7(4), 927–957.

- Okada, H., Bukry, K., 1980. Supplementary modification and introduction of code numbers to the low-latitude coccolith biostratigraphic zonation. Marine Micropaleontology 5, 321–325.
- Penman, D.E., Hönisch, B., Zeebe, R.E., Thomas, E., Zachos, J.C., 2014. Rapid and sustained surface ocean acidification during the Paleocene-Eocene Thermal Maximum. Paleoceanography 29, 357–369.
- Penman, D.E., Turner, S.K., Sexton, P.F., Norris, R.D., Dickson, A.J., Boulila, S., Ridgwell, A., Zeebe, R.E., Zachos, J.C., Cameron, A., Westerhold, T., Röhl, U., 2016. An abyssal carbonate compensation depth overshoot in the aftermath of the Palaeocene-Eocene Thermal Maximum. Nature Geosciece 9, 575–580.
- Raffi, I., Backman, J., Zachos, J.C., Sluijs, A., 2009. The response of calcareous nannofossil assemblages to the Paleocene Eocene Thermal Maximum at the Walvis Ridge in the South Atlantic. Marine Micropaleontology 70, 201–212.
- Ravizza G., Norris R. N., Blusztajn J., Aubry M.P., 2001. An osmium isotope excursion associated with the late Paleocene thermal maximum: Evidence of intensified chemical weathering. Paleoceanography and Paleoclimatology 16(2), 155–163
- Révész, K., Landwehr, J.M., 2002. $\delta^{13}C$ and $\delta^{18}O$ isotopic composition of $CaCO_3$ measured by continuous flow isotope ratio mass spectrometry: statistical evaluation and verification by application to Devils Hole core DH-11 calcite. Rapid Communications in Mass Spectrometry 16, 2102–2114.
- Röhl, U., L. J. Abrams, 2000, High-resolution, downhole and non-destructive core measurements from Sites 999 and 1001 in the Caribbean Sea: Application to the late Paleocene thermal maximum, Proceedings of the Ocean Drilling Program Sci. Results 165, 191–203.

- Röhl, U., Westerhold, T., Bralower, T.J., Zachos, J.C., 2007. On the duration of the Paleocene–Eocene thermal maximum (PETM). Geochemistry, Geophysics, Geosystems 8
- Schneidermann, N., 1977. Selective dissolution of recent coccoliths in the Atlantic Ocean. In: Ramsay, A.T.S. (Ed.), Oceanic Micropaleontology 2, 1009–1053.
- Self-Trail, J. M., Powars, D. S., Watkins, D. K., Wandless, G., 2012. Calcareous nannofossil assemblage changes across the Paleocene-Eocene thermal maximum: Evidence from a shelf setting, Marine Micropaleontology 92–93, 61–80.
- Sluijs, A., Brinkhuis, H., Schouten, S., Bohaty, S. M., John, C. M., Zachos, J. C. et al., 2007. Environmental precursors to rapid light carbon injection at the Palaeocene/Eocene boundary. Nature, 450(7173), 1218–1221.
- Sluijs, A., Schouten, S., Pagani, M., Woltering, M., Brinkhuis, H., Damsté, J. S. S., et al., 2006. Subtropical Arctic Ocean temperatures during the Palaeocene/Eocene thermal maximum. Nature, 441(7093), 610–613.
- Stoll, H. M., Bains, S., 2003. Coccolith Sr/Ca records of productivity during the Paleocene-Eocene thermal maximum from the Weddell Sea. Paleoceanography 18(2), 1–11.
- Stoll, H. M., Shimizu N., Archer D., Ziveri P., 2007. Coccolithophore productivity response to greenhouse event of the Paleocene–Eocene Thermal Maximum. Earth and Planetary Science Letters 258, 192–206.
- Stoll, H. M., Shimizu N., Arevalos A., Matell N., Banasiak A, Zeren S., 2007. Insights on coccolith chemistry from a new ion probe method for analysis of individually picked coccoliths. Geochemistry, Geophysics, Geosystems 8 (6), 1–8.

- Takeda, K., Kaiho, K., 2007. Faunal turnovers in central Pacific benthic foraminifera during the Paleocene-Eocene thermal maximum. Palaeogeography, Palaeoclimatology, Palaeoecology 251, 175–197.
- Thierstein, H.R., Roth, P.H., 1991. Stable isotopic and carbonate cyclicity in Lower Cretaceous deep-sea sediments: Dominance of diagenetic effects. Marine Geology 97, 1–34.
- Thomas, E., Shackleton, N.J., 1996. The latest Paleocene benthic foraminiferal extinction and stable isotope anomalies. In: Knox, R.O., Corfield, R.M., Dunay, R.E. Correlation of the Early Paleogene in Northwest Europe. Geological Society of London Special Publication 101, 40–441.
- Tjalsma, R. C., Lohmann, G. P., 1983. Paleocene-Eocene bathyal and abyssal benthic foraminifera from the Atlantic Ocean. Micropaleontology Special Publication 4, 1–90.
- Tremolada, F., Bralower, T.J., 2004. Nannofossil assemblage fluctuations during the Paleocene-Eocene Thermal Maximum at Sites 213 (Indian Ocean) and 401 (North Atlantic Ocean): Palaeoceanographic implications. Marine Micropaleontology 52, 107–116.
- Vink, A., Brune, A., Höll, C., Zonneveld, K. A., Willems, H., 2002. On the response of calcareous dinoflagellates to oligotrophy and stratification of the upper water column in the equatorial Atlantic Ocean. Palaeogeography, Palaeoclimatology, Palaeoecology 178(1–2), 53–66.
- Winter, A., Siesser W.G., 2006. Coccolithophores. Cambridge University Press.
- Zachos, J.C., Kroon, D., Blum, P., Bowles, J., Gaillot, P., Hasegawa, T., Hathorne, E.C., Hodell, D. A., Kelly, D. C., Jung, J. H., Keller, S. M., Lee, Y. S., Leuschner, D. C., Lohmann, K. C., Lourens, L., Monechi, S., Nicolo, M., Raffi, I., Riesselman, C., Röhl, U., Schellenber, S. A., Schmidt, D., Slujis A., Thomas, D., Thomas, E., Vallius, H. ,

2004. Early Cenozoic extreme climates: the Walvis Ridge transect. Proceedings of the Ocean Drilling Program. Initial Reports 208.

- Zachos, J.C., Pagani, M., Sloan, L.C., Billups, K., Thomas, E., 2001. Trends, rhythms, and aberrations in global climate 65 Ma to present. Science 292, 686–693.
- Zachos, J.C., Röhl, U., Schellenberg, S.A., Sluijs, A., Hodell, D.A., Kelly, D.C., Thomas, E., Nicolo, M., Raffi, I., Lourens, L.J., McCarren, H., Kroon, D., 2005. Rapid acidification of the ocean during the Paleocene–Eocene thermal maximum. Science 308, 1611–1615.
- Zeebe, R.E., Lourens, L.J., 2019. Solar System chaos and the Paleocene–Eocene boundary age constrained by geology and astronomy. Science 365, 926–929.

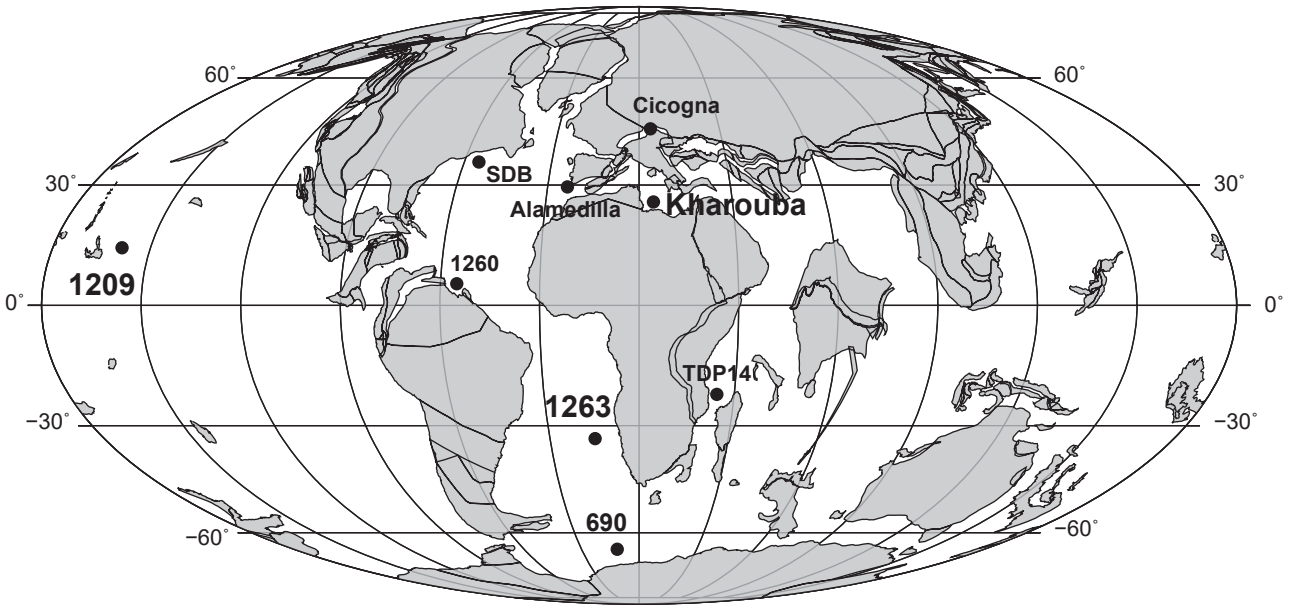


Figure 1. Location of the three studied sections on a paleogeographic map at 56 Ma : (http://www.odsn.de/odsn/services/paleomap/paleomap.html): Kharouba section (Tunisia), Site 1209 (Shatsky Rise, Tropical Pacific), and Site 1263 (Walvis Ridge, South Eastern Atlantic). Location of the sites used for comparison is also shown: Site 690 (Southern Ocean) Site 1260 (Equatorial Atlantic), SDB (New Jersey), TDP 14 (Tanzania), Cicogna (North Italy), Alamedilla (Spain).

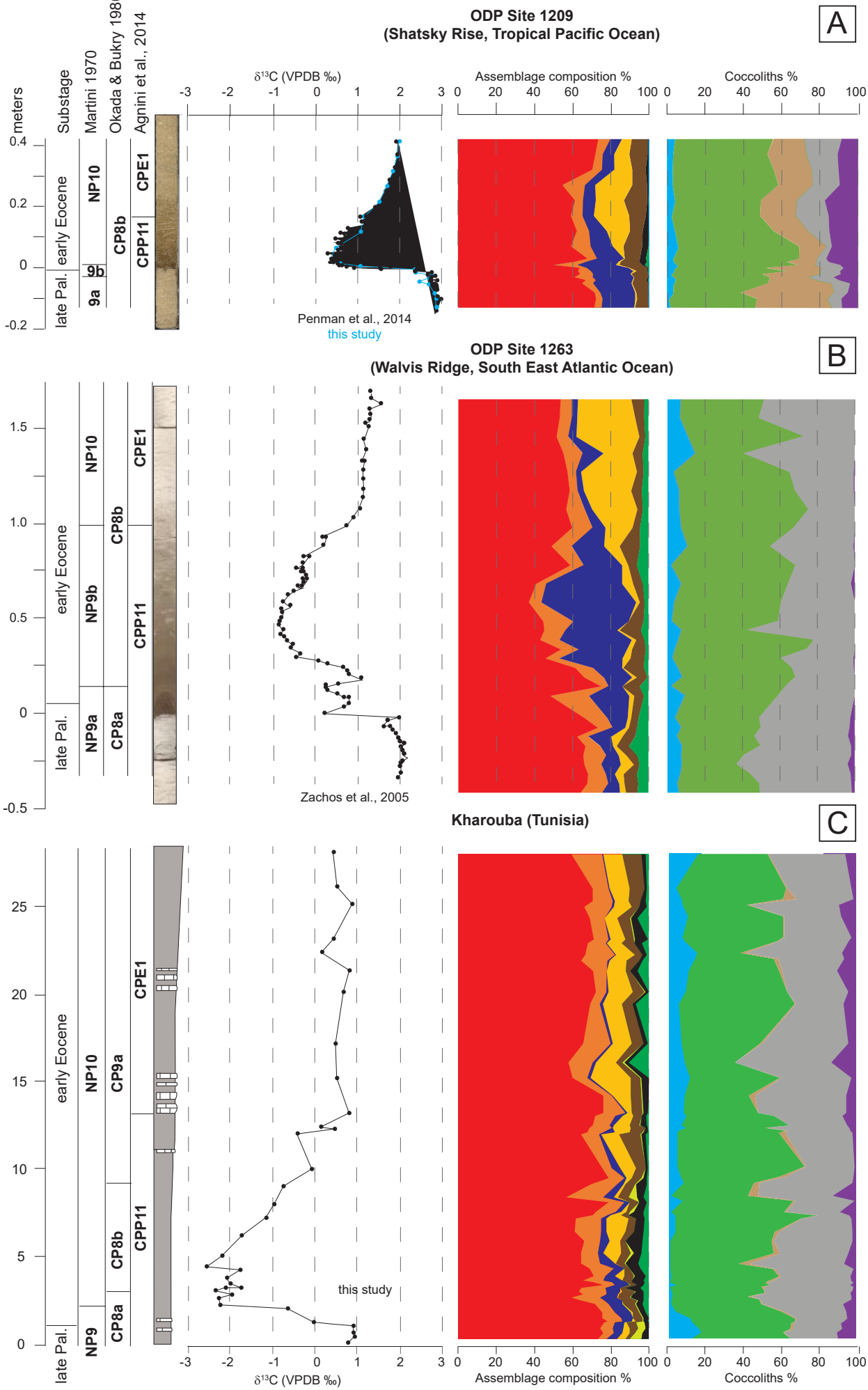


Fig. 2. Cumulative graphic of main nannofossil genus for the three studied sections in function of depth. Hrizontal scale is the same but vertical one is different because of important differences in the thickness betwee oceanic sites and Kharou-ba. Alson nannofossil biostratigraphy and lithostratigraphic column. Total assemblage composition (coccoliths, nanno-liths) and coccolith assemblages for the three sections.

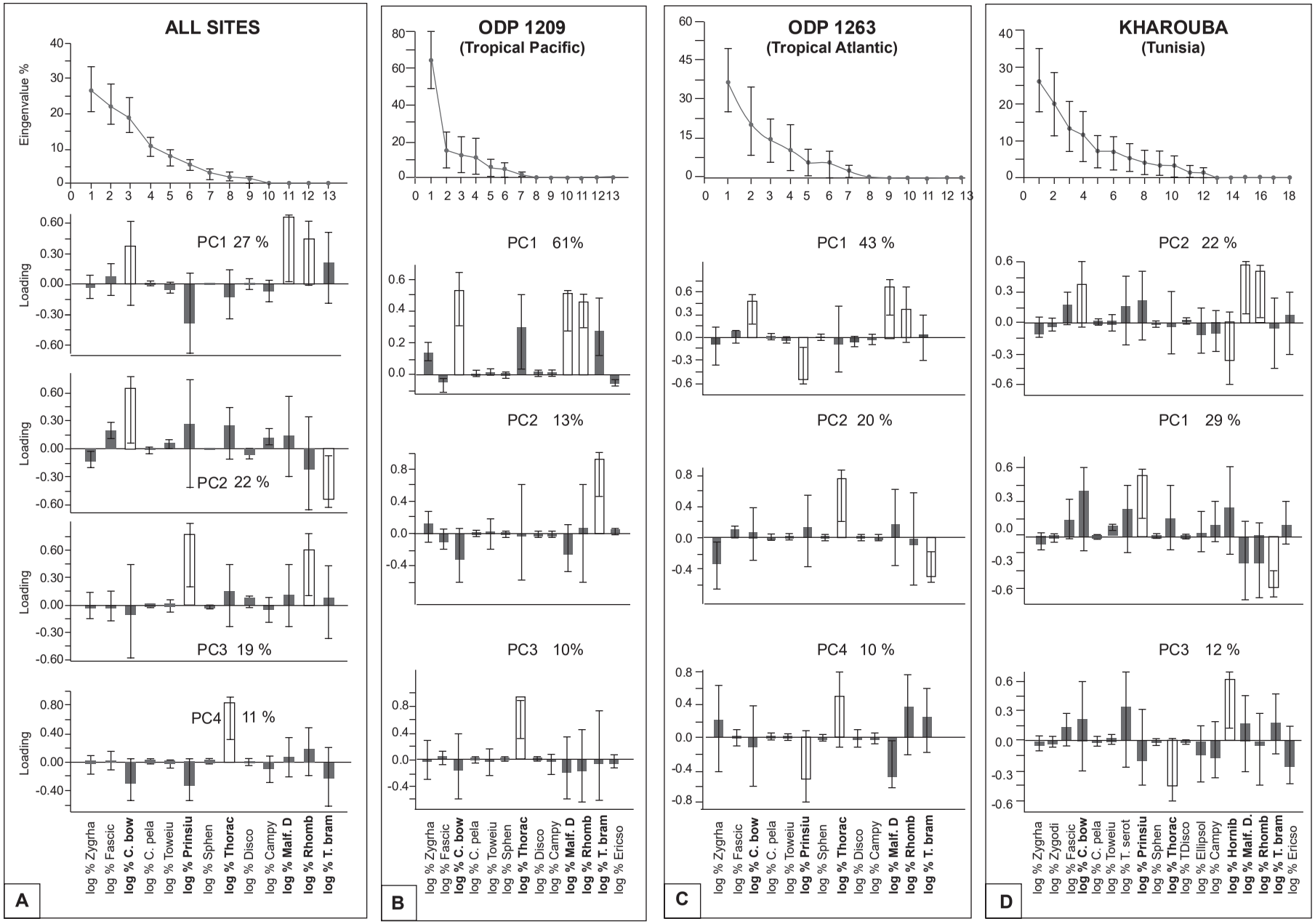


Fig.3. Principal components analysis loading plots. Only species with a high sampling adequacy and having a loading higher than ±0.5 on one of the extracted factors are considered here. Factors are regarded as significant only when they have a contribution to the variance higher than 10 %. A; loading plot resulting from the PCA performed on the three studied sections.,B; loading plot resulting from the PCA performed on ODP Site 1209, C; ODP Site 1263, D; Kharouba. Error bars irepresent lower and upper limits for 95% confidence intervals, using 9999 bootstrap

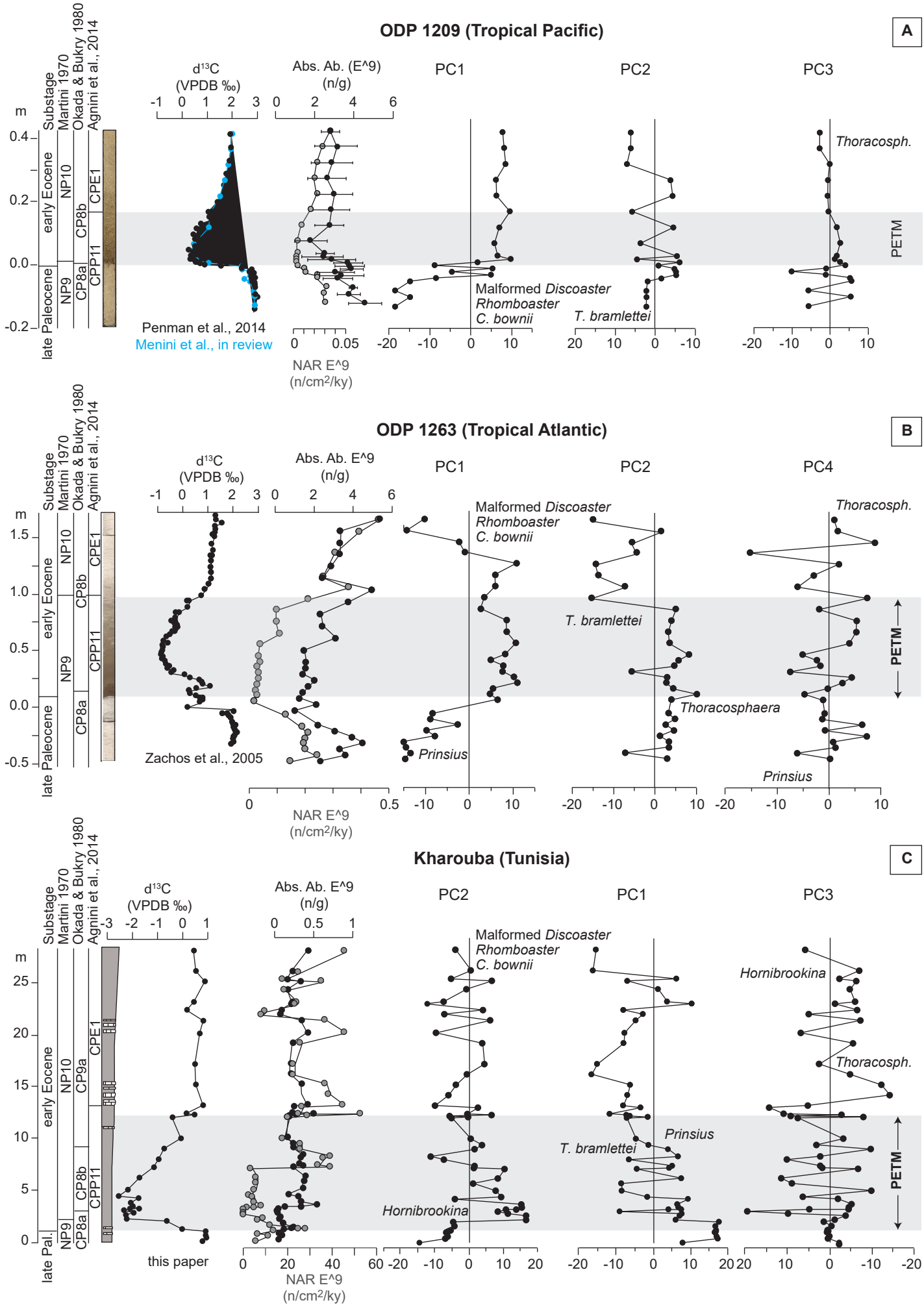


Figure 4. Stratigraphical evolution of PCA scores, absolute abundance (black) and NAR (grey) in function of depth against nannofossil biostratigraphy and carbon isotopes curve in the three studied sections. Note that the vertical scale is different from a section to another. The correlative factors, i.e., those on which the same taxa load, are shown in the same order for the three sections, irrespective of their variance values. The species with important loadings on the different factorial axes are reported.

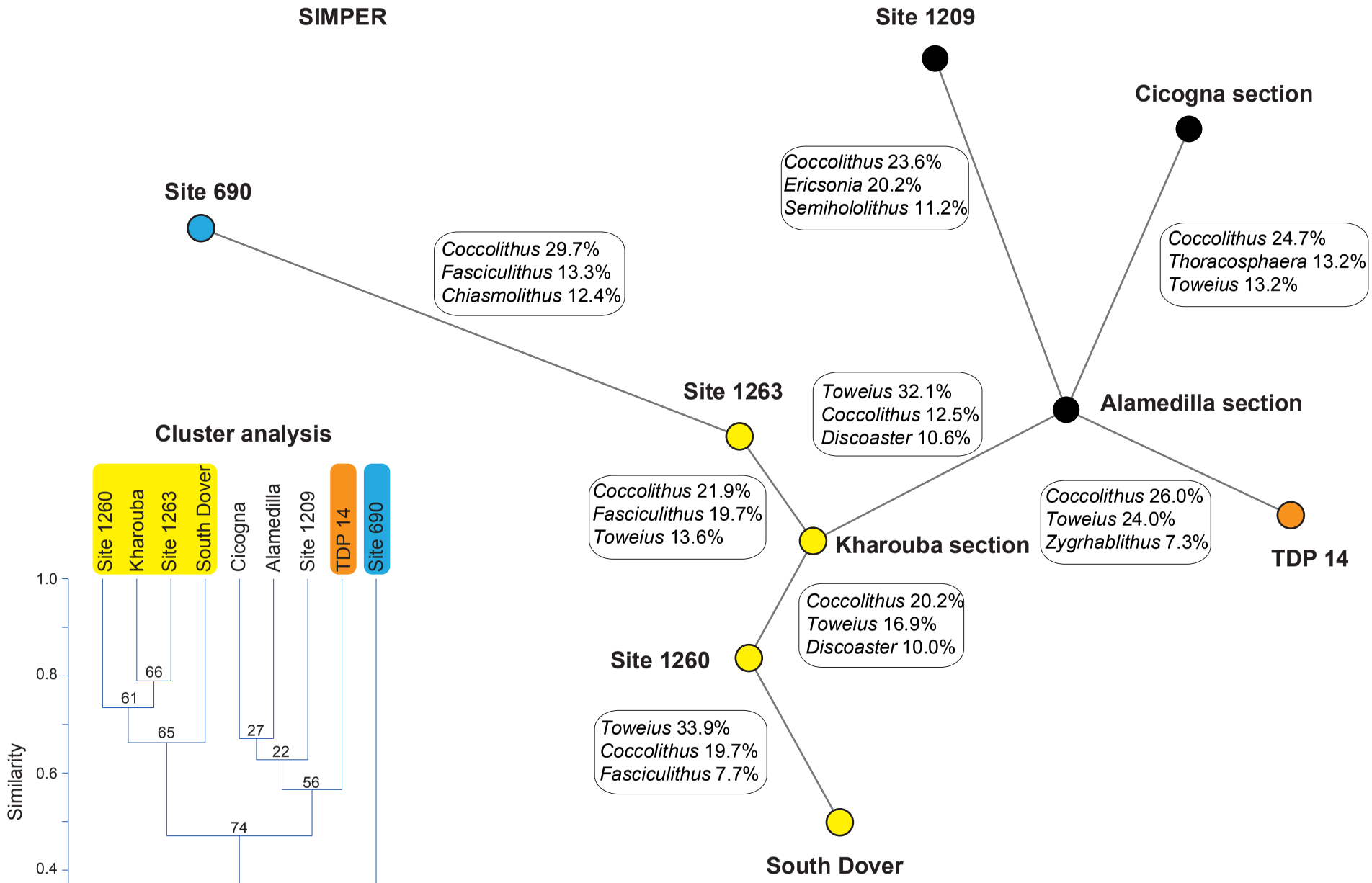


Figure 5. Cluster analysis (right) and SIMPER analysis (left) applied on the three studied sections (Site 1209, 1263 and Kharouba) and 6 other sections that provide excellent stratigraphic records of the PETM calcareous nannofossils .

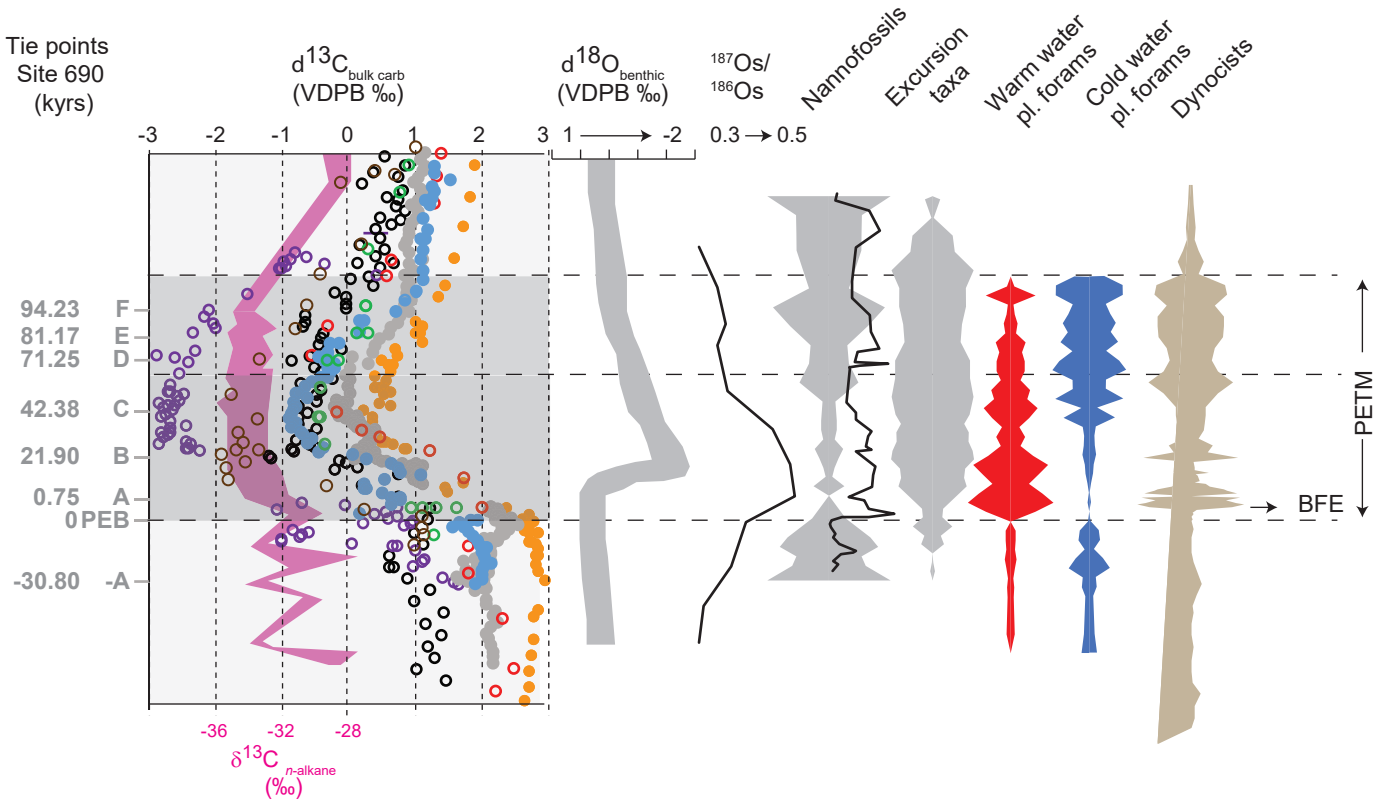


Figure 6. Synthesis of the main geochemical and biotic events occurring across the PETM relative to the δ13C $_{\text{bulk carbonate}}$ record (Alamedilla (red) Lu al. 1996, ODP 690 (grey) Bains et al. 1999 , ODP 1209 (orange) Penman et al. 2014, ODP 1263 (light blue) Zachos et al. 2005, ODP 1260 (green) Mutterlose et al. 2007, Kharouba (brown), This work, South Dover (violet) Self Trail et al. 2012, Cicogna (black) Agnini et al. 2016). For TDP 14 (pink) we used δ13Cn-alkane record (isotopes of C-25, C-27, C-29 and C-31 alkanes), since δ13Cbulk carb did not provide satisfacting results (Bown and Pearson 2009, Aze et al. 2014). Tie-points of the δ13Cbulk carb at Site 690 as defined by Zachos et al. (2005) and Röhl et al. (2007) from –A to H are shown. Envelope curve of oxygen isotope records (extracted from the database of Cramer et al., 2009) from individual cores from the North Atlantic (ODP1051), and Southern Oceans (ODP690). Osmium isotopes record after Ravizza et al., 2001 at DSP Site 541. Planctonic foraminfera data after Petrizzo et al., 2008 (warm water=*Morozovella* spp., cold water=*Subbotina* spp.). Dynocists data after Sluijs et al., 2006. See text for details.

**1209** — **A**

Test for equal means

| | Sum of sqrs | df | Mean square | F | p (same) |
|---|---|---|---|---|---|
| Between gro | 3.08E+19 | 2 | 1.54E+19 | 19.9 | 4.02E-08 |
| Within group | 8.65E+19 | 112 | 7.73E+17 | Permutation | p (n=99999) |
| Total: | 1.17E+20 | 114 | 1.00E-05 | | |

Components of variance (only for random effects):

| | | | | | |
|---|---|---|---|---|---|
| Var(group): | 4.10E+17 | Var(error): | 7.73E+17 | ICC: | 0.346497 |

| | |
|---|---|
| omega2: | 0.2474 |

| | | |
|---|---|---|
| Levene´s test | p (same): | 0.2017 |
| Levene´s test | p (same): | 0.3046 |

Welch F test in the case of unequal variances: F=20.13, df=48.22, p=4.409E-07

**B**

| | recovery | core | pre-petm |
|---|---|---|---|
| recovery | | 0.8246 | 1.16E-07 |
| core | 0.8375 | | 0.0002514 |
| pre-petm | 8.348 | 5.765 | |

**KHAROUBA** — **E**

Test for equal means

| | Sum of sqrs | df | Mean square | F | p (same) |
|---|---|---|---|---|---|
| Between gro | 1.92E+17 | 2 | 9.62E+16 | 7.542 | 0.002007 |
| Within group | 4.21E+17 | 33 | 1.28E+16 | Permutation | p (n=99999) |
| Total: | 6.13E+17 | 35 | 0.00203 | | |

Components of variance (only for random effects):

| | | | | | |
|---|---|---|---|---|---|
| Var(group): | 8.14E+15 | Var(error): | 1.28E+16 | ICC: | 0.389581 |

| | |
|---|---|
| omega2: | 0.2666 |

| | | |
|---|---|---|
| Levene´s test | p (same): | 0.03867 |
| Levene´s test | p (same): | 0.1161 |

Welch F test in the case of unequal variances: F=39.88, df=17.31, p=3.305E-07

**1263** — **C**

Test for equal means

| | Sum of sqrs | df | Mean square | F | p (same) |
|---|---|---|---|---|---|
| Between gro | 2.01E+19 | 2 | 1.00E+19 | 17.87 | 1.14E-05 |
| Within group | 1.52E+19 | 27 | 5.61E+17 | Permutation | p (n=99999) |
| Total: | 3.52E+19 | 29 | 4.00E-05 | | |

Components of variance (only for random effects):

| | | | | | |
|---|---|---|---|---|---|
| Var(group): | 9.50E+17 | Var(error): | 5.61E+17 | ICC: | 0.62861 |

| | |
|---|---|
| omega2: | 0.5293 |

| | | |
|---|---|---|
| Levene´s test | p (same): | 0.08227 |
| Levene´s test | p (same): | 0.1267 |

Welch F test in the case of unequal variances: F=29.58, df=14.62, p=7.255E-06

**D**

| | pre petm | Core | recovery |
|---|---|---|---|
| pre petm | | 0.0001708 | 0.871 |
| core | 6.719 | | 2.24E-05 |
| recovery | 0.7097 | 7.796 | |

**F**

| | pre petm | core | recovery |
|---|---|---|---|
| pre petm | | 0.2723 | 0.007764 |
| core | 2.221 | | 0.01708 |
| recovery | 4.562 | 4.12 | |

Table S1: One-way ANOVA applied on nannofossil absolute abundance for Site 1209, 1263 and Kharouba(A,C,E). In B,D,F the table of "post-hoc" pairwise comparisons, based on the Tukey-Kramer test. The Studentized Range Statistic Q is given in the lower left triangle of the array, and the probabilities p(equal) in the upper right.

# Chapitre 4. Carbon cycle modulation by phytoplankton during the Paleocene-Eocene Thermal Maximum

# Carbon cycle modulation by phytoplankton during the Paleocene-Eocene Thermal Maximum

Alessandro Menini[1], Guillaume Suan[1], Luc Beaufort[2], Nicolas Pige[1], Jeremy E. Martin[1], Auguste Hassler[1], Frédéric Quillévéré[1], Maria Rose Petrizzo[3], Kenneth A. Farley[4] , Emanuela Mattioli[1,5]

[1] Univ Lyon, Univ Lyon 1, ENSL, CNRS, LGL-TPE, F-69622, Villeurbanne, France

[2] CEREGE, Université Aix-Marseille, Aix-en-Provence, France

[3] Earth Science Department 'Ardito Desio', University of Milan, Italy

[4] Division of Geological and Planetary Sciences, California Institute of Technology, USA

[5] IUF, Paris, France

**The Paleocene Eocene Thermal Maximum (PETM, ~56 My ago), is considered as one of the best analogues for anthropogenic $CO_2$ emissions. Yet, the key negative feedbacks that removed the excess carbon during the PETM termination remain controversial. Higher deep-sea $CaCO_3$ saturation and burial due to enhanced silicate weathering are commonly accepted as the main driving processes. Alternatively, a $CO_2$-induced drop in net algal $CaCO_3$ production could have triggered the alkalinity buildup and oversaturation, but this mechanism remains unsupported by proxy evidence. Here, we present a multiproxy study of tropical Pacific and Atlantic deep-sea records demonstrating that $CaCO_3$ burial recovered to pre-PETM levels about 30 000 years later than saturation. We attribute this decoupling to a dramatic (>60%) and sustained (>80 000 years) collapse in net $CaCO_3$ production due to warming-induced ocean stratification and lowered nutrient availability. Our records show that the resulting excess alkalinity was rapidly consumed when $CaCO_3$ production and burial eventually recovered, triggering a rapid and massive drawdown of both inorganic and organic carbon. Our findings elucidate some of the key biogeochemical mechanisms that drove the PETM recovery and emphasize the overlooked but crucial importance of biological thresholds in the regulation of past and ongoing events of greenhouse warming.**

Past greenhouse events, such as the PETM, provide deep geological insight into the critical biogeochemical consequences of ongoing anthropogenic $CO_2$ emissions. PETM marine

carbonates record a global 3-4‰ carbon isotope ($\delta^{13}C$) negative excursion (CIE) coeval with a >5°C temperature increase indicating the massive input of $^{13}C$-depleted carbon into the ocean-atmosphere system (Kennett and Stott, 1991; Zachos et al., 2003). The increase in atmospheric $pCO_2$ led to a drastic drop in ocean *p*H and carbonate ion content [$CO_3^{2-}$] (Penman et al., 2014; Babila et al., 2018). Such dramatic changes in ocean chemistry are reflected by widespread dissolution horizons in deep oceanic sediments, which record a global shoaling of the lysocline – the depth where [$CO_3^{2-}$] falls below calcite saturation – and of calcite compensation depth (CCD) – the depth where the dissolution becomes sufficiently rapid to exactly balance the calcite rain flux (Ridgwell and Zeebe, 2005; Zachos et al., 2005). Model simulations for the PETM suggest that the warming-induced increase in continental weathering favored a long-term (10-100 ky) increase in bicarbonate ion [$HCO_3^-$] ultimately leading to an overshoot of the lysocline and CCD, and enhanced $CO_2$ drawdown (Penman et al., 2016).

Crucially, most previous simulations implicitly assumed constant $CaCO_3$ production and export across the PETM (Dickens et al., 1997; Ridgwell, 2007; Zeebe et al., 2009), leaving seafloor dissolution/preservation of $CaCO_3$ as the central oceanic carbon-cycle controlling feedback. In deep-sea sediments, $CaCO_3$ export-flux is predominantly provided by calcareous phytoplankton (mainly coccolithophores), whose tiny (<30 μm) calcite remains form nannofossil ooze, and subordinately, by larger (>63 μm) shells of planktonic foraminifera. Previous studies of PETM nannofossils have shown that the drop of surface ocean *p*H and [$CO_3^{2-}$] had little effects on both coastal- and open-ocean calcareous phytoplankton calcification (the ratio of inorganic carbon to photosynthetically derived organic carbon) and diversity (Gibbs et al., 2006b). However, changes in net open-ocean pelagic $CaCO_3$ production, despite their outstanding biogeochemical and ecological importance, remain virtually unconstrained by empirical data. The seldom attempts to constrain phytoplankton productivity using Sr/Ca ratios or Ba contents have proven controversial, due largely to the complex dependence of these proxies to several environmental forcing factors (Stoll and Bains, 2003; Ma et al., 2014; Bridgestock et al., 2019). Model simulations suggest that the input of >6500 Gt of $CO_2$ accompanied by a sustained 50% drop in net $CaCO_3$ production could adequately reproduce $CaCO_3$ depth transects at Walvis Ridge (S Atlantic)(Luo et al., 2016). Although yet unsupported by other quantitative evidence, such a drop in net $CaCO_3$ production implies, through a long term alkalinity buildup, a decoupling between $CaCO_3$ saturation and burial that should be detectable in PETM deep-sea sediments (Luo et al., 2016). By contrast, $CaCO_3$ burial should closely track saturation if seafloor

dissolution/preservation of $CaCO_3$ was the central oceanic carbon-cycle controlling feedback (Zeebe, 2012). To test the importance of these two mechanisms, we reconstruct $CaCO_3$ burial and saturation across the PETM using nannofossil accumulation rates (NAR) and fragmentation from deep-ocean sediments recovered from Ocean Drilling Program (ODP) sites 1209 (Shatsky Rise, central Pacific) and 1263 (Walvis Ridge, South Atlantic). This approach is combined with new calcium isotope data ($\delta^{44}Ca$) – a proxy for seawater saturation – and a comprehensive reassessment of previously published micropaleontological and geochemical data to constrain interactions between calcareous phytoplankton productivity, ocean chemistry and climate across the PETM.

Unlike all other previous PETM studies that used smear slides, we prepared the samples using standardized settling methods to robustly estimate the absolute abundances of individual particles per gram of rock. We then estimated sedimentation rates with an unprecedented ky-resolution based on helium isotope and $CaCO_3$ contents anchored to astronomical age models (Extended Data Fig. 1; methods) to infer nannofossil accumulation rates (NAR), the mass accumulation rates of the fine ($MAR_{ff}$) and coarse (>63 μm) carbonate fractions ($MAR_{cf}$), and that of abiogenic calcite particles (blades) (Fig. 1; Extended Data Fig. 2). We estimated particle weight of the better-preserved nannofossils at Site 1209 using automated birefringence-based methods, combined with classical scanning electron and optical microscopy (see methods and Supplementary Information) and hence calculated nannofossil mass accumulation rates ($MAR_n$). Our estimates indicate that the fine fraction $CaCO_3$ in the studied samples at Site 1209 contains an average proportion of >88 wt.% nannofossil calcite (Supplementary Information), whereas its accumulation rate ($MAR_{ff}$) is highly correlated with NAR ($R^2$=0.99; $p<0.05$) and $MAR_n$ ($R^2$=0.98; $p<0.05$; Extended Data Table 1). Maximum Paleocene $MAR_{ff}$ values are > 5 times higher at Walvis Ridge (3.5 g/cm$^2$/ky) than at Shatsky Rise (0.6 g/cm$^2$/ky), in remarkable consistency (in relative and absolute values) with modern export fluxes measured at equivalent sites (Milliman, 1993). Because of these very different background values, we thus only refer to the highest resolution changes in $MAR_{ff}$ relative to pre-PETM maximum values ($\Delta MAR_{ff}$) to evaluate changes in nannofossil calcite accumulation (Supplementary Information). Despite these differences in absolute $MAR_{ff}$, the two sites reveal strikingly similar trends in $CaCO_3$ accumulation. We find $MAR_{ff}$ at both sites fell dramatically by >80% across the CIE onset, stayed extremely low (<-50%) for ~80 ky, and rapidly returned to pre-excursion values only by +90-100 ky (Fig. 1). These patterns are largely insensitive to uncertainties of the age models (Extended data Fig. 2).

This >80ky-long phase of low nannofossil ooze burial can be directly compared to our new nannofossil fragmentation data. Nannofossil fragmentation varies inversely relative to $CaCO_3$ saturation (Beaufort et al., 2007) and directly tracks the dissolution of the dominant $CaCO_3$ component, unlike the fragmentation of foraminifera, which dissolve at shallower depths and constitute a subordinate fraction of studied sediments. These new data, together with our $\delta^{44}Ca$ data, calculated $MAR_{cf}$ data and available foraminiferal fragmentation (Petrizzo et al. 2008), provide a coherent history of $CaCO_3$ saturation state at the two studied sites (Fig. 1). At both sites, $CaCO_3$ saturation dropped markedly across the CIE onset and therefore at least partly explains the unusually low $MAR_{ff}$ over the earliest ~30 ky of the event, as shown by coeval peaks in foraminifera and nannofossil fragmentation and lowest $MAR_{cf}$ (Phase I in Fig. 1). Similarly, the marked increase in nannofossil and foraminiferal fragmentation coeval with the decline in $MAR_{cf}$ and $MAR_{ff}$ starting –15 ky prior the CIE onset at Site 1209 likely indicates more intense postdepositional chemical erosion ('burndown') of latest Paleocene sediments exacerbated by low background accumulation rates in the Pacific gyre (Bralower et al., 2014). The coccolith lysocline recovered to pre-excursion values ~40 ky later in the Atlantic than in the Pacific (by +75 and +35 ky and at sites 1263 and 1209, respectively; Fig. 1), consistent with the hypotheses of a second, >50 ky episode of carbon injection (phase II; Fig. 1) directly into the deep Atlantic (Zeebe et al., 2009). Such features could also indicate a southward spread of corrosive N Altantic waters. The coeval episode of maximal surface water saturation at Site 1209 between + 50 and 90 ky is also supported by our new $\delta^{44}Ca$ measurements of the mixed-layer planktic foraminifera *Morozovella velascoensis* (Fig. 1). Previous studies have shown that calcite $\delta^{44}Ca$ values mainly reflect global changes in seawater $\delta^{44}Ca$ values, driven by the balance between weathering input or carbonate output, and changes in fractionation between seawater and calcite (Griffith et al., 2020). Because of the high Paleogene ocean [Ca] content, the marked positive peak toward higher $\delta^{44}Ca$ values between +45 and +90 ky is too large and rapid to be explained by global changes in $\delta^{44}Ca$ of seawater (Komar and Zeebe, 2011), thus pointing to diminished seawater-calcite $\delta^{44}Ca$ fractionation. Although our understanding of environmental factors controlling foraminiferal calcite $\delta^{44}Ca$ fractionation is still in a state of flux (Griffith et al., 2020), culture experiments on inorganic (Lemarchand et al., 2004) and foraminiferal (Roberts et al., 2020) calcite indicate diminished fractionation with increasing $CaCO_3$ saturation and $[CO_3^{2-}]$. Accordingly, and regardless of long-term changes in seawater $\delta^{44}Ca$ values and uncertainties in absolute omega values (Supplementary information), our *M. velascoensis* $\delta^{44}Ca$ record imply a marked

rise in surface water saturation between +45 and +90 ky, in excellent agreement with seafloor $CaCO_3$ saturation proxies (Fig. 1).

A remarkable aspect of our results is the low $\Delta MAR_{ff}$ values (< - 60%) recorded at Site 1209 in the interval of maximum surface and seafloor $CaCO_3$ saturation between +45 and +90 ky (Fig. 1). Although shorter-lived due to more prolonged seafloor dissolution, a similar mismatch is recorded at Site 1263. There, $\Delta MAR_{ff}$ values are still <60% lower than pre-PETM values by +80 ky, when nannofossil fragmentation recovers to pre-PETM values (Fig. 1). This clear decoupling between $CaCO_3$ burial and saturation at the end of the PETM core in both the Pacific and Atlantic oceans is at odds with classical compensation models assuming a constant scaling between these two variables.

It could be argued that the low $CaCO_3$ burial recorded during episodes of high saturation was produced locally by the physical removal of $CaCO_3$ sediments. Winnowing the nannofossil fraction by ocean bottom currents has been for instance proposed as the cause of the anomalous rise of the foraminiferal coarse fraction at Site 1209 (Bralower et al., 2014). The relatively invariant trend of our $MAR_{cf}$ estimates confirms that the rise in the foraminiferal fraction during the PETM at Site 1209 resulted from lower nannofossil dilution (Fig. 1). Nevertheless, our new data reveals no trend toward higher nannofossil weight across the PETM (Extended Data Fig. 3), and therefore does not support this hypothesis. As nannofossil ooze has the same density and size distribution as extraterrestrial $^3$He-bearing interplanetary dust particles (Farley et al., 1997), another testable but previously overlooked consequence of the winnowing hypothesis is that bottom currents should have equally decreased the $^3He_{ET}$ contents in the PETM interval. The large increase in $^3He_{ET}$ contents recorded across the PETM and our age models clearly excludes this possibility (Supplementary Information).

Given the similarity of the deep-sea $\Delta MAR_{ff}$ records from different oceans and hemispheres characterized by distinct bottom-water hydrodynamics, we therefore interpret the drastic decrease in nannofossil accumulation rates recorded at sites 1209 and 1263 as strong evidence for a sustained, > 80 ky drop of net phytoplankton $CaCO_3$ export in tropical gyres during the PETM. In this regard, our new nannofossil weight estimates at Site 1209 reveal no noticeable changes across the PETM at Site 1209, indicating that nannofossil export fluxes rather than calcification drove the major drop in $MAR_{ff}$ (Extended Data Fig. 3). This response contrasts strongly with the overwhelming influence of $pCO_2$ levels and $[CO_3^{2-}]$ on the weight of the dominant living family Noelarhabdaceae over the last 40 ky (Beaufort et al., 2011), likely translating fundamental differences in taxonomic composition between modern and

169 Paleogene coccolithophores as well as long-term evolutionary and ecological trends
170 (Henderiks and Rickaby, 2007).

171 Importantly, several lines of evidence suggest that this decline in net export productivity
172 was not confined to calcareous phytoplankton. The $\Delta MAR_{ff}$ values at Site 1209 remarkably
173 parallel changes in $\delta^{13}C$ gradients between planktonic and benthic foraminifera (Extended
174 Data Fig. 4). Minimal $\delta^{13}C$ gradients during the PETM indicate diminished removal of $^{13}C$-
175 depleted carbon by photosynthesis in superficial waters and are consistent with reduced
176 organic carbon export and diminished productivity (Zachos et al., 2003; Tripati and
177 Elderfield, 2005). We rule out a decline in calcareous phytoplankton productivity as the main
178 cause of this reduced $\delta^{13}C$ gradient, because this group rarely exceeds 20% of phytoplankton
179 carbon uptake in nutrient-depleted gyres (Poulton et al., 2007). Earth system modeling
180 indicates that the similar 1-2 ‰ decrease in the vertical $\delta^{13}C$ gradient recorded at the
181 Cretaceous-Paleogene transition at Site 1209 requires a 50% reduction in total organic
182 primary productivity (Henehan et al., 2019). At Site 1263, Ba isotopes and Ba/Al ratios
183 (Bridgestock et al., 2019) also suggest parallel trends in primary organic and $CaCO_3$
184 productivity in the S Atlantic (Extended Data Fig. 4). These comparisons indicate that total
185 organic productivity and calcareous phytoplankton productivity declined concomitantly and
186 by the same order of magnitude in the tropical Pacific and S Atlantic gyres during the PETM.

187 Interestingly, our $MAR_{ff}$ estimates at Site 1209 do correlate negatively with sea surface
188 temperatures (SST) inferred from *M. velascoensis* $\delta^{18}O$ ($R^2$= 0.53; $p<0.05$) and Mg/Ca ($R^2$=
189 0.57; $p<0.05$) data, suggesting a strong climatic control (Extended Data Table 1). High
190 (extra)tropical PETM SSTs (>35°C), which likely exceeded the upper physiological limits of
191 most marine eukaryotes (Frieling et al., 2017), could explain the crash in both total and
192 $CaCO_3$ productivity recorded at sites 1209 and 1263. Extreme warmth, however, appears less
193 likely to explain the marked (>50%) and prolonged (>50 ky) drop in $MAR_{ff}$ recorded in the
194 high latitude site 690 (Extended Data Fig. 2), where SST likely never exceeded 20-25°C
195 (Dunkley-Jones et al., 2013). More indirectly, modeling of the PETM warming produces,
196 through higher SST and reduced latitudinal gradients (Frieling et al., 2017) enhanced surface
197 ocean stratification, lower deep vertical mixing and upwelling of nutrients into surface waters,
198 where photosynthesis occurs. Enhanced stratification is consistent with nannofossil
199 assemblage at both sites 1209 and 1263, where shallow-dwellers typical of upwelled waters in
200 the Late Paleocene are replaced by deep-water taxa that thrived in times of oligotrophy in
201 surface waters during the PETM (Supplementary Information). Calcareous nannofossil

assemblages, also support thermally-induced stratification and overall oligotrophy in various oceanic sites (Bralower, 2002; Gibbs et al., 2010). Besides, *Thoracosphaera,* a calcareous dinoflagellate cyst generally used as an index of enhanced oligotrophy under stratified water conditions (Vink et al., 2002), is the only calcareous nannofossil investigated in this study showing an increase in absolute abundance and accumulation rate during the PETM at Site 1209 (Fig. 1). We note that such evidence is not incompatible with meso-eutrophic nannofossil assemblages recorded in a few extra-tropical proximal sites, where increased continental runoff and higher nutrients availability may have locally fostered productivity (Gibbs et al., 2006b; Self-Trail et al., 2012). However, trophic conditions during the PETM are less obvious in other proximal sites from tropical paleolatitudes, with some sites recording a primary productivity crash in the core of the PETM as shown by dinoflagellates abundances (Frieling et al., 2017).

All together, these considerations strongly support thermally induced sluggish ocean circulation and stratification as the most likely trigger for the >60% decline in net $CaCO_3$ productivity recorded at sites 1209 and 1263 in the core of PETM. Model simulations show that a 50% drop in $CaCO_3$ export and burial would have led to a considerable build-up of [$HCO_3^-$] and hence increased alkalinity in both surface and deep waters in the recovery interval (50-100 ky after the onset of the PETM) (Luo et al., 2016). Such a build-up of alkalinity and a reversal in saturation at +50 ky at Site 1209 is not only supported by our saturation reconstruction but also by the recent re-evaluation of Mg/Ca-$\delta^{18}O$ records of *M. velascoensis* from Site 1209 using modern foraminiferal Mg/Ca sensitivity to dissolved inorganic carbon (DIC) (Holland et al., 2020). Accordingly, DIC, and by inference [$HCO_3^-$], would have increased markedly between 50-100 ky (Holland et al., 2020). Given the existing pH and SST constraints from at Site 1209 (methods and supplementary information), these various records can be used to reconstruct the history of ocean carbon chemistry and hence constrain the role of phytoplankton productivity carbon cycle feedbacks across the PETM. These reconstructions imply a drastic rise in DIC and [$HCO_3^-$] that is in excellent agreement with the Atlantic simulation of a 50% drop in net $CaCO_3$ export by Luo et al, 2016 but far exceeds their estimates for the Pacific Ocean, where $CaCO_3$ export was held identical to Paleocene values for most of the PETM. Our data thus not only strongly support the fundamental role of biological export in modulating the PETM carbon cycle suggested by their simulation, but further suggest that their conclusion should be extended to a much broader proportion of the ocean.

A complementary and crucial aspect of our reconstructions is that DIC and $CaCO_3$ saturation declined rapidly after 85 ky, implying a rapid and widespread episode of carbon burial. Enhanced carbon drawdown is consistent with the dramatic increase in $\Delta MAR_{ff}$ at both sites and the large (>1000 ppm) drop $pCO_2$ inferred from available records at Site 1209. As high alkalinity enhances atmospheric $CO_2$ absorption into the ocean (Feely et al., 2002), alkalinity buildup due to diminished $CaCO_3$ export represents a simple negative feedback process that could appropriately explain the rapid termination of the PETM. As more atmospheric $CO_2$ was absorbed, SST and stratification decreased, thus restoring nutrient availability and both net organic matter and $CaCO_3$ export, and eventually $CaCO_3$ burial in the vast, already oversaturated and deep-sea areas. In addition, it has been demonstrated that phytoplanktonic calcite act as ballast in fecal pellets and increases organic carbon fluxes to the ocean interior (Poulton et al., 2006), whereas higher $CaCO_3$ planktonic input increases sedimentation rates and accelerates organic carbon burial in the sediment column (Tyson, 1995). The cooling-induced recovery of $CaCO_3$ export thus represents a simple and realistic mechanism to enhance the burial of $^{13}C$-depleted carbon required to explain the puzzling and rapid rise in $\delta^{13}C$ values evident in both continental and oceanic records (Bowen, 2013; Ma et al., 2014; van der Meulen et al., 2020).

The multiple lines of evidence presented here provide a strong case for ocean desertification in the tropical Pacific and Atlantic during the PETM, which elucidate some of the key biogeochemical mechanisms that likely facilitated its rapid termination. Further drilling of supra-lysoclinal oceanic sites is necessary to clarify the history of $CaCO_3$ export fluxes across the PETM onset, which is obscured by extensive dissolution in all available oceanic sites. Beyond the PETM, our findings bring empirical evidence that biocalcifying algae are not simple background players in a warming world but play a pivotal role by regulating or amplifying carbon cycle perturbations (Luo et al., 2016; Boudreau et al., 2018), as suggested for other extreme events of the Phanerozoic, such as the Toarcian Oceanic Anoxic Event (Mattioli et al., 2008) or the most dramatic K-Pg event (Henehan et al., 2019). Identifying such biological thresholds might also reveal crucial for the mitigation of anthropogenic $CO_2$ emissions.

## Methods

### Samples and site selection

The ODP sites 1209 and 1263 were selected for this study due to their central position within the extensive N Pacific and S Atlantic gyres. Due to their relatively shallow position

during PETM (respective paleo-water depths of 1900 m and 1500 m; Takeda and Kaiho, 2007; Zachos et al., 2005), these two sites were minimally affected by dissolution compared to deeper nearby sites and benefit from some of the highest-resolution geochemical records available for deep-sea PETM sites (Colosimo et al., 2006; Zachos et al., 2005; Zachos et al., 2003; Tripati and Elderfield, 2005; Westerhold et al., 2011). We collected samples with a 1 to 5 cm spacing over 0.50 m recording the PETM in Hole 1209B and with 5-10 cm spacing over 2 m in Hole 1263C/D (Supplementary Information).

**Absolute abundances of nannofossil and abiogenic particles.** All calcareous nannofossil slides were prepared following the settling method (Beaufort et al., 2014). A cover slide was weighted before and after the settling of a homogeneous suspension of dry bulk sediment and water supersaturated with respect to $CaCO_3$ for 4 hours in a Petri-dish. Water was carefully aspired with a water pump connected to a micro-pipette to avoid any turbulence. After residual water drying, the cover slide was fixed on a microscope slide using Rhodopass B resin (Polyvinyl acetate). Nannofossil and abiogenic particles abundance were counted in a total of 30 Fields of View (FOV) for each sample with a Leica DM 750 P microscope with 1000X magnification. The studied area is 0.00942 $cm^2$. Five replicates per sample were studied at Site 1209. Absolute nannofossil abundance per gram of sediment were calculated using the formula:

$$x = \frac{n*(l*h)}{m*A} \quad (1)$$

where is $x$ is the absolute abundance value, $n$ is the number of counted specimens in a slide, $l$ is the length of the cover slide, $h$ is the height of the cover slide, $m$ is the mass of the weighted sample and $A$ is the studied surface of the sample.

**Nannofossil fragmentation.** We consider a nannofossils as a fragment when it is less than half. Nannofossil fragmentation was calculated using the sum of whole nannofossil specimens and fragments counted in each sample as follows:

$$Nannofossil\ fragmentation = \frac{\sum fragments}{\sum fragments + \sum whole\ specimens} \quad (2)$$

**Nannofossil and abiogenic particle weight**. Nannofossil weight was estimated at Site 1209 following the method described by Beaufort et al., 2014. For each sample, >1000 images of

individual nannofossils were obtained using a fully automated polarizing microscope Leica DM6000B with an objective HCX PL APO 100/1.47, equipped with a SPOT Flex camera (Diagnostic Instrument) and a pair of circular polarizers, acquired using the Calciprobe macro with two LabView runtimes and treated with the automatic coccolith recognition system SYRACO (Beaufort and Dollfus, 2004) to separate nannofossils and abiogenic calcite particles. All images were inspected and some residual classification errors were corrected manually. The nannofossil images were then classified in 14 separate classes, on the basis of their shape, size and birefringence (Supplementary Information). This part of the process was done manually, since no automatic recognition is available yet for the studied time interval. For each sample, the surface and thickness of each nannofossil was measured in pixel (i.e., brightness) on the obtained gray level images (100 images for each group) with ImageJ, with values ranging from 0 (black) to 255 (white). Nannofossil volume (*Vp*) was calculated (voxel) by multiplying the measured area (*Ap*) and the thickness (*tp*), as below, where "p" stands for pixel:

$$Vp = Ap * tp \quad (3)$$

These values were multiplied by 1.62 µm (the maximum measureable thickness in this configuration) and divided by 255 (the maximum measureable pixel value with a 8 bit camera, see ref Beaufort et al., 2014 for further details).

$$C = Vp * 1.62/255 \quad (4)$$

The obtained C value (voxel*µm) was multiplied by the area of one pixel ($S$=0.0036 µm$^2$ in our case) and by the density of calcite $d$=2.71 g/cm$^3$ to calculate the weight M (pg):

$$M = C * S * d \quad (5)$$

For specimens belonging to *Fasciculithus* and *Discoaster* genera, this method allowed a robust assessment of the surface but systematically underestimated the lith thickness. A number of adjustments were thus necessary to obtain reliable results (Supplementary Information).

The weight of abiogenic calcite blades in each sample at Site 1209 was estimated using their thickness, length and width measured in SEM at 1550x magnification for all the studied samples (Supplementary Information).

**Age models.** Age models for ODP Site 1209 and Leg 208 sites at Walvis Ridge (including Site 1263) were developed assuming that sedimentation rates in these carbonate-rich sequence were predominantly controlled by changes in carbonate accumulation, either as changing net production or preservation (Supplementary Information). Sedimentation rates (SR) were calculated assuming the non-carbonate (i.e., terrigenous) fraction (NCF) flux and the $^3He_{ET}$ flux remained constant during the study interval (Supplementary Information) using the following equation:

$$SR = F_X / ([X] * \rho) \quad (6)$$

where SR is the sedimentation rate in m $ky^{-1}$, $\rho$ the dry bulk density (DBD) in g $cm^{-3}$, $F_x$ is the flux of the considered component X in unit $cm^{-2}$ $ky^{-1}$, and [X] its concentration per gram of sediment. DBD values were estimated at each site using the relationship between shipboard gamma-ray attenuation measurements and discrete DBD measurements (Marcantonio et al., 2009). For each site, $F_X$ was iteratively adjusted to obtain a duration of 94 ± 1 ky between carbon isotope inflexion points A (PETM onset) and F (Zachos et al., 2005). This duration was selected to facilitate comparisons with the widely used age model of Röhl et al. (2007) and is within error in line with the 101 ± 9 ky duration constrained by most recent astronomical age models of expanded continental records of the Bighorn Basin (5 precession cycles; van der Meulen et al., 2020). The resulting $F_X$ for each sedimentary component for each sites is given in Extended Data Fig. 1. The obtained relative changes in SR and age models assuming constant $^3He$ and NCF fluxes show a high degree of self-consistency and appear much more realistic in terms of sedimentology than published astronomical age models for these sites (Supplementary Information).

**Accumulation rates**. We calculated nannofossil accumulation rates using the formula:

$$NAR = X * AR * d \quad (7)$$

where NAR is the nannofossil accumulation rate ($n/m^2/yr$), X is the absolute abundance of nannofossils (n/g), AR is the accumulation rate (cm/ky), d is the dry bulk density of the sediment (see Supplementary Information). Nannofossil mass accumulation rate was calculated using the formula as follows:

$$MARn = \sum MARx \quad (8)$$

where ($MAR_n$ ; $g/cm^2/ky$) $MAR_x$ is the MAR of every nannofossil class that we counted).

The $MAR_x$ of each class was calculated as follows:

$$MARx = NARx * weight(x) * AR * d \quad (9)$$

where $NAR_x$ is the NAR of each class. The MAR of the fine fraction ($MAR_{ff}$ ($g/cm^2/ky$), was calculated using the formula:

$$MARff = CaCO3ff * AR * d \quad (10),$$

where $CaCO_3$ff (wt %) is the weight percent calcium carbonate content of the fine fraction, AR is the accumulation rate (cm/ky) and d is the dry density of the sediment after Bralower et al., 2002 (ship data).

Similarly, we calculated the $MAR_{cf}$, which is the MAR of the coarse fraction.

$$MARcf = CaCO3cf * AR * d \quad (11)$$

**Calcareous particle contribution.** The mass of carbonate produced by nannofossils and calcite blades was calculated as follows:

$$Mass\ CaCO3(i) = X(i) * m(i) \quad (12)$$

Where:

- Mass $CaCO_3$(i)= Mass of $CaCO_3$ produced by every class (i) in gr per gr. of rock;
- X(i)=absolute abundance of (i) in number of nannofossils per gr. of rock;
- m(i)=mean of the weight of (i) in gr.

$$\%CaCO3(i) = (Mass\ CaCO3(i)/CaCO3\%) * 100 \quad (13)$$

Where:

- %$CaCO_3$(i)=percentage of $CaCO_3$ produced by a class of nannofossils
- Mass $CaCO_3$(i)=Mass of $CaCO_3$ produced by every class (i) in gr;
- $CaCO_3$%= % of $CaCO_3$ of each sample.

$$\%CaCO3\ (nanno) = \sum[\%CaCO3\ (i)] \quad (14)$$

Where:

- %$CaCO_3$ (nanno)= percentage of $CaCO_3$ produced by nannofossils;
- %$CaCO_3$(i)=percentage of $CaCO_3$ produced by a class (i).

**Stable calcium isotope measurements.** Washed sediment residuals from the study of Petrizzo, 2007 were dry-sieved and specimens of the photosymbiotic, surface-dwelling planktonic foraminiferal species *Morozovella velascoensis* were hand-picked from the size-fraction 250-355 μm. About 6 specimens per sample were necessary to supply sufficient calcium carbonate and to limit the effect of individual variation on the calcium isotope values. The specimens analyzed were free of sediment infilling or visible dissolution features. Careful observation of the shell ultrastructure of randomly selected specimens at high magnification (2000x) using a Phenom SEM G2 PRO confirmed the excellent preservation of the foraminifera. The specimens of *M. velascoensis* were further ultrasonically cleaned in distilled water, weighted and dissolved in subboiled distilled 1N HCl acid and processed through AG50X-W12 cation exchange resin in 1N HCl medium to dispose of sample matrix (i.e., phosphates, sulfates, alkali elements, and Mg). Ca and Sr fractions were collected in 6N HCl medium, and Ca fractions were separated from Sr by loading samples onto columns filled with Sr-specific resin (Eichrom Sr-Spec) in subboiled distilled 3N $HNO_3$ medium. Blanks for the whole procedure did not exceed 100 ng Ca (Tacail et al., 2017), i.e., about 200 times smaller than the smallest processed Ca samples (about 20 μg). A standard-sample bracketing measurement method was used with the ICP Ca Lyon standard Tacail et al., 2014 as bracketing standard. Measurements of all samples and standards were performed during two sessions in 2018 using a Neptune MC-ICP-MS at the Laboratoire de Géologie de Lyon. The $\delta^{43/42}$Ca-$\delta^{44/42}$Ca values of all measured samples did not deviate statistically from the 0.507 slope predicted by the linear approximation of exponential mass-dependent fractionation. If the calcium isotopic composition of standards is taken into account, the slope of the line is 0.5199. The measurements were systematically checked for long-term precision and accuracy using SRM1486 bone meal NIST secondary standard previously described and analyzed for Ca isotope compositions (Tacail et al., 2016, Heuser et al., 2011, Martin et al., 2015, Tacail et al., 2014, Heuser et al., 2016). SRM1486 yielded constant values across the six different analysis sessions, with an average $\delta^{44/42}$Ca value of −0.98 ± 0.18‰ (2 SE, n = 30), in agreement with previously published values (as listed in Table S3), notably −1.03 ± 0.01‰ (2 SE, n = 120) (Tacail et al., 2014). We also analyzed the commonly used SRM915b clinical-grade carbonate standards, and ICP1 Ca solution used as standard in former studies (Morgan et al., 2011, Channon et al., 2015). All measured $\delta^{44/42}$Ca values of standards and

previously published compositions are given for comparison in Table S3. Long-term external precision was estimated using the SRM1486 standard and yields a 2 SD value of 0.12‰ for $\delta^{44/42}$Ca for 112 analyses, over the two sessions. Values of the $\delta^{44/42}$Ca Ca were converted into $\delta^{44/40}$Ca multiplying by mass fractionation ratio (1/m40-1/m44)/(1/m42-1/m44) = 2.099454809 (where mx is the exact atomic mass of each calcium isotopes). All Ca isotope compositions are expressed in per mil units, using the "delta" notation for the $^{44}Ca/^{40}Ca$ isotope ratios defined as follows:

$$\delta^{44/40}Ca=\left(\frac{(^{44}Ca/^{40}Ca)_{sample}}{(^{44}Ca/^{40}Ca)_{ICP\ Ca\ Lyon}}-1\right)*1000 \quad (15)$$

where $(^{44}Ca/^{40}Ca)_{sample}$ and $(^{44}Ca/^{40}Ca)_{ICP\ Ca\ Lyon}$ are Ca isotope abundance ratios measured in sample and ICP Ca Lyon bracketing standard, respectively.

Calcium isotope values were expressed relative to SRM 915b and modern sea water to compare with literature data. We converted $\delta^{44/42}$ values relatively to ICP Ca Lyon standard in $\delta^{44/42}$ relatively to 915b by adding 0.06. By multiplying by 2.1 (as expressed in the equation above) we can convert it $\delta^{44/40}$. We added 0.72 to all values to express them relatively to 915a and to express values relatively to modern sea water we subtracted 1.88 from values expressed relatively to 915a (Griffith et al., 2008, 2015).

**Ocean carbonate chemistry reconstruction**

The carbonate system can be described by six fundamental parameters ($[CO_3^{2-}]$, $[HCO_3^-]$, DIC, TA, $pCO_2$, and pH), but the knowledge of only two parameters along with T, S, and P, allows the calculation of the four others using published dissociation constants (Zeebe, 2012). For each considered level, we have thus estimated T using average *M. velascoensis* $\delta^{18}O$ values (Zachos et al., 2003), a constant S of 37 salinity unit and P of 7 bar (assuming *M. velascoensis* lived at depth of 70 m), in line with Penmann et al (2014). Carbonate chemistry parameters were then calculated with the CO2syst calculator (https://www.nodc.noaa.gov/ocads/oceans/CO2SYS/co2rprt.html) using dissociation constants from Meherbach et al., 1973 refitted by Dickson and Millero, 1987 and Uppstrom 1974 and applying three complementary approaches: 1) $[CO_3^{2-}]$ were computed from *M. velascoensis* $\delta^{44}Ca$ values assuming an initial concentration of 80 µmol/kg (Zeebe, 2012) and the highest end-member $\delta^{11}B$-derived pH of Penmann et al (2014) to infer all other parameters (DIC, TA, $pCO_2$ and $[HCO_3^-]$); 2) DIC was computed from *M. velascoensis*

Mg/Ca- $\delta^{18}O$ pairs assuming an initial concentration of 2200 µmol/kg (Luo et al., 2016) and the highest end-member $\delta^{11}B$-derived pH of Penmann et al (2014) to infer [$CO_3^{2-}$], TA, $pCO_2$ and [$HCO_3^-$]; 3) pH and DIC were adjusted manually within proxy uncertainties to reproduce trends in saturation recorded at Site 1209 and calculate [$CO_3^{2-}$], TA, $pCO_2$ and [$HCO_3^-$].

**Extended data**

**Extended Data Fig. 1. Sedimentation rates across the PETM in key deep-sea sites**. **a**, Parameters used to derive the age models assuming a constant extraterrestrial helium ($^3He_{ET}$) flux or constant non-carbonate fraction (CNCF) flux and that the interval between carbon isotope inflexion points A and F was deposited within 94 ± 1 ky (Rohl et al., 2007), consistent with the 101 ± 9 ky duration produced for the same time interval by latest astronomical age models of expanded continental records (van der Meulen et al., 2020). The primary NCF, $CaCO_3$ and $^3He_{ET}$ data used to derive these parameters are from Bralower et al. (2014); Farley and Eltgroth (2003); Griffith et al. (2015); Kelly et al. (2010); Murphy et al. (2010); Zachos et al. (2005). Note that the mean PETM $^3He_{ET}$ flux calculated at Site 1209 is within error identical to the $^3He_{ET}$ flux of 5.9± $0.9\times10^{-13}$ $cm^3STPcm^{-2}ka^{-1}$ calculated by Marcantonio et al. (2009) for a 800 ky-long upper Paleocene (-58 Ma) interval from the same site. **b-e**, Stratigraphic changes in sedimentation rates (SR) assuming constant fluxes of NCF (closed dots) and $^3He_{ET}$ (open squares) for the N Pacific ODP Site 1209 (**b**), SE Atlantic ODP sites 1263 (**c**) and 1266 (**d**), and S Ocean ODP Site 690 (**e**). The $^3He_{ET}$-derived SR values were smoothed using 3-point (Site 1209) or 5-point (Site 1266 and 690) running means to reduce the statistical effects of individual, outsized $^3He_{ET}$-bearing particles (Murphy et al., 2010). The green shaded band in **b-e** illustrates the PETM core interval as defined in **a**. PEB = Paleocene-Eocene boundary; ODP = Ocean Drilling Program.

**Extended Data Fig. 2. Carbonate sediment depositional dynamics across the PETM in selected deep oceanic sites**. **a-d**, reconstructions based on $^3He_{ET}$-inferred sedimentation rates; age models; **e-h**, reconstructions based on CNCF-inferred sedimentation rates; **a**, **e**, Bulk carbonate carbon isotope records (Kelly et al., 2005; Murphy et al., 2010; Penman et al., 2014; Takeda and Kaiho, 2007; Zachos et al., 2005). **b**, **f**, Changes in mass accumulation rates of fine fraction (ΔMAR fine fraction) relative to pre-PETM maximum values. **c**, **g**, Mass accumulation rates of the coarse (foraminiferal) fraction. **d**, **h**, Nannofossil fragmentation. The primary coarse fraction data used to derive mass accumulation rates in **b-g** are from ( Kelly et al., 2010; Kelly et al., 2005; Westerhold et al., 2018)

**Extended Data Fig. 3. Stable calcification rates of dominant nannofossil assemblages across the PETM at Site 1209**. Coccolith (**b-c**) and nannolith (**d-e**) weight for the most abundant genera at Site 1209B. Error bars reflect 2 standard error (2 SE).

**Extended Data Fig. 4. Organic and inorganic productivity across the PETM in deep-sea sites**.

**Extended Data Fig. 5.** $\delta^{43/42}$Ca on y-axis (per mil) as a function of $\delta^{44/42}$Ca on x-axis (per mil) relative to ICP Ca Lyon. Ca isotope composition falls on a line with a y axis intercept of 0.0054 in the first graph and 0.0035 in the second one indistinguishable from theoretical 0‰ intercept, and a slope of 0.5769 in the first graph and 0.05199 in the second one, indistinguishable from 0.507 predicted slope according to exponential law linear approximation of mass-dependent fractionation. Error bars correspond to average 2 SD precision on $\delta^{44/42}$Ca (per mil) and $\delta^{43/42}$Ca (per mil). Black dots are samples measured in this study; red dots are standards. The blue lines delimit the prediction interval, and the red lines corresponds to the 95% confidence interval on the regression line.

**Acknowledgements** (optional). This study was supported by the projects LabEx LIO to AM, IUF and IODP France to EM and ANR Oxymore (ANR-18-CE31-0020) to GS. The authors wish to thank Mrs. Ghislaine Broillet for help in sampling preparation. The samples used in this study for nannofossil and geochemical analyses are cured in the Collections de Géologie de l'Université de Lyon (FSL number 707714).

**Author contributions**. AM and GS equally contributed to this paper in conceiving, writing and supervising the work. LB contributed in the data acquisition and interpretation of nannofossil mass. NP acquired nannofossils data at Site 1263 under the supervision of Alessandro Menini. JM and AH equally contributed in the acquisition of calcium isotopes data. FQ helped in the taxonomy of planktonic foraminifera and in the paleoecological interpretation. MRP provided the planktonic foraminifera samples for calcium isotopes analyses. KF provided previously unpublished CaCO3 and 3He data that were fundamental to develop the age model. EM contributed to the paleoceanographic interpretations of the PETM and to the coordination of this research.

**Materials & Correspondence**. Correspondence and requests for materials should be addressed to Alessandro Menini.

**Additional Information**: Supplementary Information is available for this paper. Correspondence and requests for materials should be addressed to Alessandro Menini.

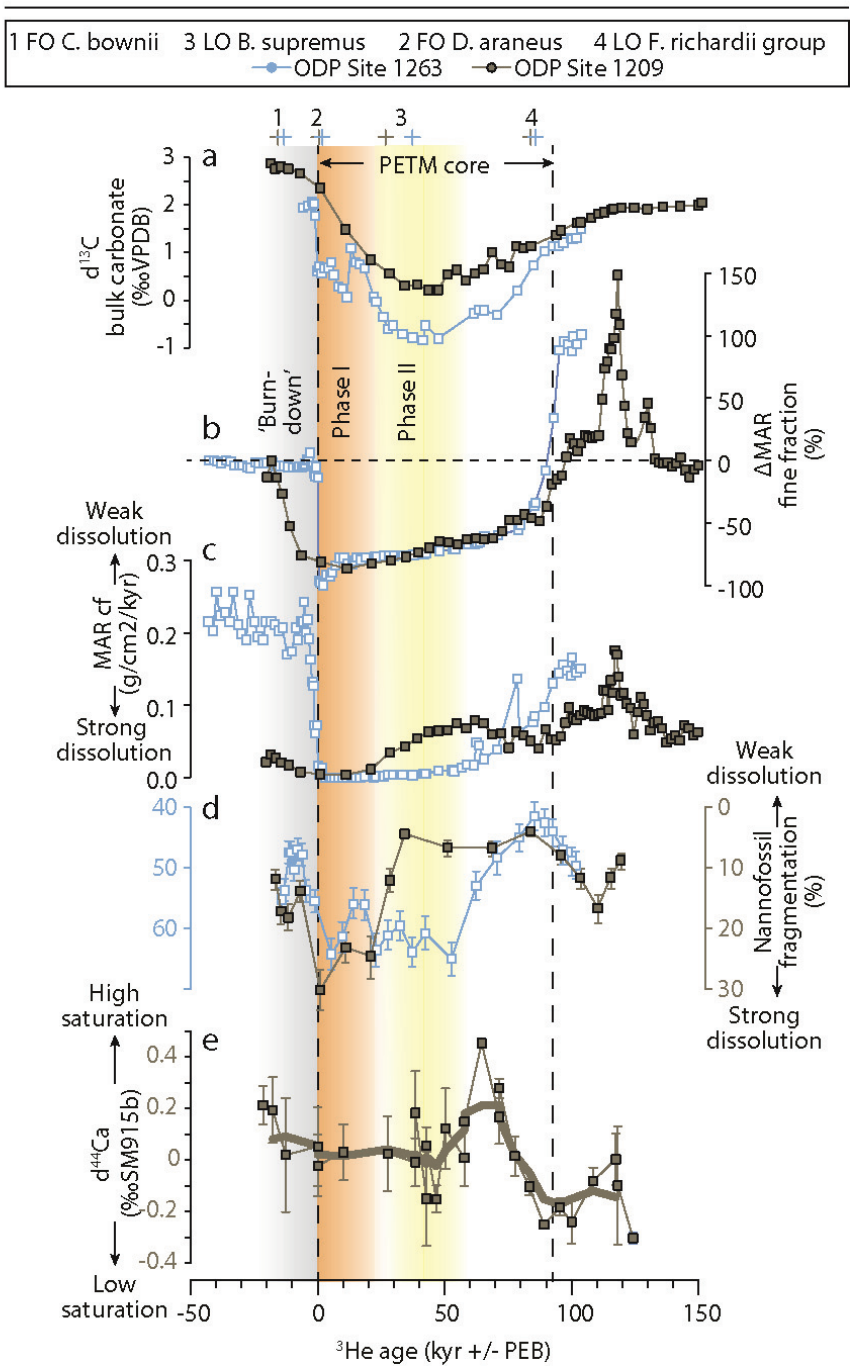


Figure 1. Synthesis of the main parameters discussed in the text for Site 1209 (Tropical Pacific) and 1263 (Tropical Atlantic). Age is expressed relatively to the PETM and reconstructions are based on 3HeET-inferred sedimentation rates. See main text for further details. a., Bulk carbonate carbon isotope records (Kelly et al., 2005; Murphy et al., 2010; Penman et al., 2014; Takeda and Kaiho, 2007; Zachos et al., 2005). b, Changes in mass accumulation rates of fine fraction (ΔMAR fine fraction) relative to pre-PETM maximum values. c, Mass accumulation rates of the coarse (foraminiferal) fraction. d, Nannofossil fragmentation. e., Calcium isotopes. Error bars correspond to 2SD. The thick line corresponds to a 3-points average.
The primary coarse fraction data used to derive mass accumulation rates in b-g are from (Kelly et al., 2010; Kelly et al., 2005; Westerhold et al., 2018)

**a**

| Site/age model | Component X | Methodology | $F_x$ | $F_x$ units | PETM onset | Inflection point F |
|---|---|---|---|---|---|---|
| ODP Site 1209B/CNCF | NCF | Acid leaching | 8.2 | g cm$^{-2}$ myr$^{-1}$ | 196.46 mbsf | 196.23 mbsf |
| ODP Site 1209B/3He | $^3He_{ET}$ | Noble gas mass spectrometry | 5.2 | $10^{-13}$ cm$^3$STPcm$^{-2}$kyr$^{-1}$ | 196.46 mbsf | 196.23 mbsf |
| ODP Site 1263CD/CNCF | NCF | Coulometry | 770.0 | g cm$^{-2}$ myr$^{-1}$ | 335.29 rmcd | 334.11 rmcd |
| ODP Site 1263/3He | $^3He_{ET}$ | Noble gas mass spectrometry | N/A* | N/A* | 335.29 rmcd | 334.11 rmcd |
| ODP Site 1266BC/CNCF | NCF | Acid leaching | 450.0 | g cm$^{-2}$ myr$^{-1}$ | 306.77 rmcd | 306.02 rmcd |
| ODP Site 1266BC/3He* | $^3He_{ET}$ | Noble gas mass spectrometry | 6.7 | $10^{-13}$ cm$^3$STPcm$^{-2}$kyr$^{-1}$ | 306.77 rmcd | 306.02 rmcd |
| ODP Site 690B/CNCF | NCF | Acid leaching | 494.0 | g cm$^{-2}$ myr$^{-1}$ | 170.64 mbsf | 169.1 mbsf |
| ODP Site 690B/3He | $^3He_{ET}$ | Noble gas mass spectrometry | 6.86 | $10^{-13}$ cm$^3$STPcm$^{-2}$kyr$^{-1}$ | 170.64 mbsf | 169.1 mbsf |
| ODP Site 1262A/CNCF | NCF | Coulometry | 320.0 | g cm$^{-2}$ myr$^{-1}$ | 140.11 mbsf | 139.71 mbsf |
| ODP Site 1212B/CNCF | NCF | Coulometry | 20.7 | g cm$^{-2}$ myr$^{-2}$ | 79.92 mbsf | 79.68 mbsf |

*$^3$He contents not published for ODP Site 1263. $^3$He-derived sedimentation rates of Ma et al. (2014) were multiplied by 1.55 to produce a duration of 94 kyr between the PETM onset and F.

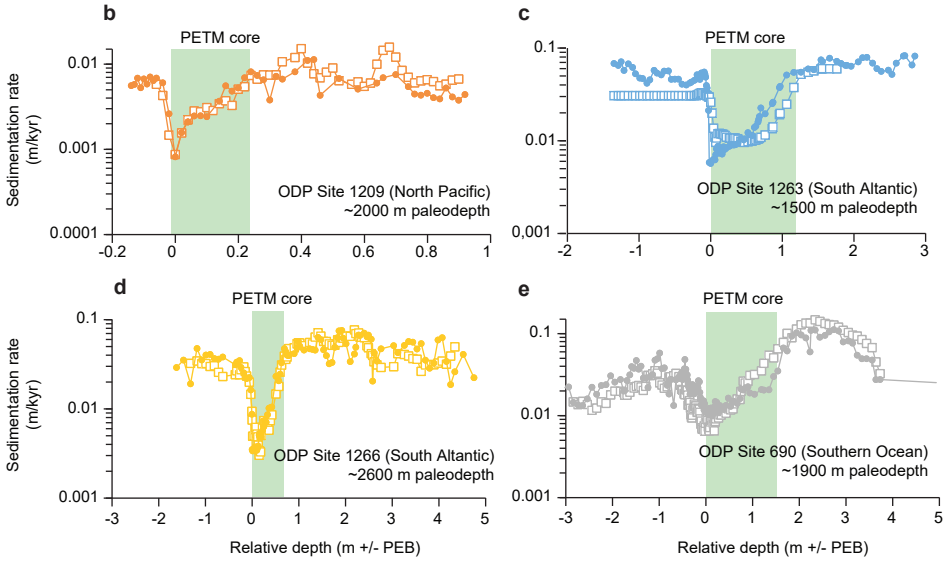


Extended Data Fig.1. Sedimentation rates across the PETM in key deep-sea sites. a, Parameters used to derive the age models assuming a constant extraterrestrial helium (3HeET) flux or constant non-carbonate fraction (CNCF) flux and that the interval between carbon isotope inflexion points A and F was deposited within 94 ± 1 ky (Rohl et al., 2007), consistent with the 101 ± 9 ky duration produced for the same time interval by latest astronomical age models of expanded continental records (van der Meulen et al., 2020). The primary NCF, CaCO3 and 3HeET data used to derive these parameters are from Bralower et al. (2014); Farley and Eltgroth (2003); Griffith et al. (2015); Kelly et al. (2010); Murphy et al. (2010); Zachos et al. (2005). Note that the mean PETM 3HeET flux calculated at Site 1209 is within error identical to the 3HeET flux of 5.9± 0.9×10−13 cm3STPcm−2ka−1 calculated by Marcantonio et al. (2009) for a 800 ky-long upper Paleocene (-58 Ma) interval from the same site. b-e, Stratigraphic changes in sedimentation rates (SR) assuming constant fluxes of NCF (closed dots) and 3HeET (open squares) for the N Pacific ODP Site 1209 (b), SE Atlantic ODP sites 1263 (c) and 1266 (d), and S Ocean ODP Site 690 (e). The 3HeET-derived SR values were smoothed using 3-point (Site 1209) or 5-point (Site 1266 and 690) running means to reduce the statistical effects of individual, outsized 3HeET-bearing particles (Murphy et al., 2010). The green shaded band in b-e illustrates the PETM core interval as defined in a. PEB = Paleocene-Eocene boundary; ODP = Ocean Drilling Program.

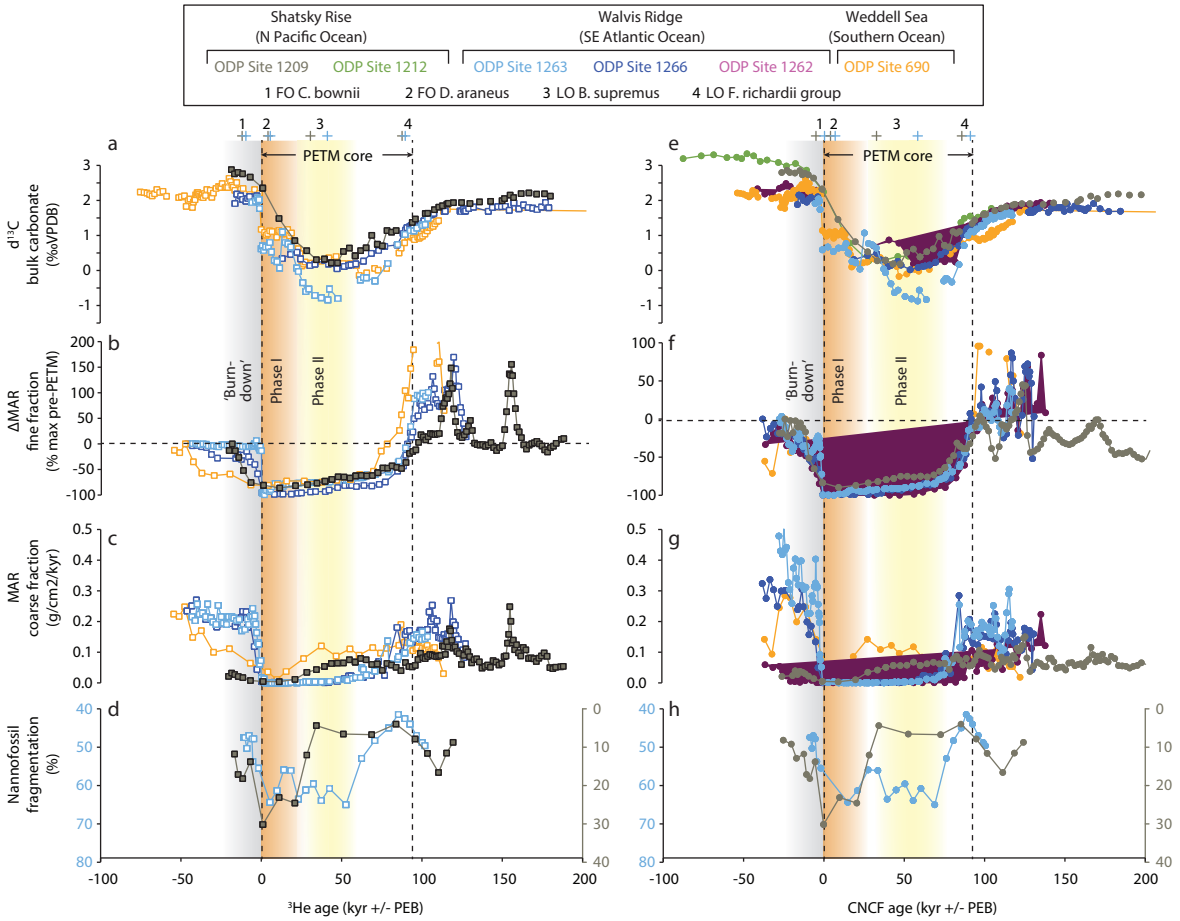


Extended Data Fig. 2. Carbonate sediment depositional dynamics across the PETM in selected deep oceanic sites. a-d, reconstructions based on 3HeET-inferred sedimentation rates; age models; e-h, reconstructions based on CNCF-inferred sedimentation rates; a, e, Bulk carbonate carbon isotope records (Kelly et al., 2005; Murphy et al., 2010; Penman et al., 2014; Takeda and Kaiho, 2007; Zachos et al., 2005). b, f, Changes in mass accumulation rates of fine fraction (ΔMAR fine fraction) relative to pre-PETM maximum values. c, g, Mass accumulation rates of the coarse (foraminiferal) fraction. d, h, Nannofossil fragmentation. The primary coarse fraction data used to derive mass accumulation rates in b-g are from ( Kelly et al., 2010; Kelly et al., 2005; Westerhold et al., 2018)

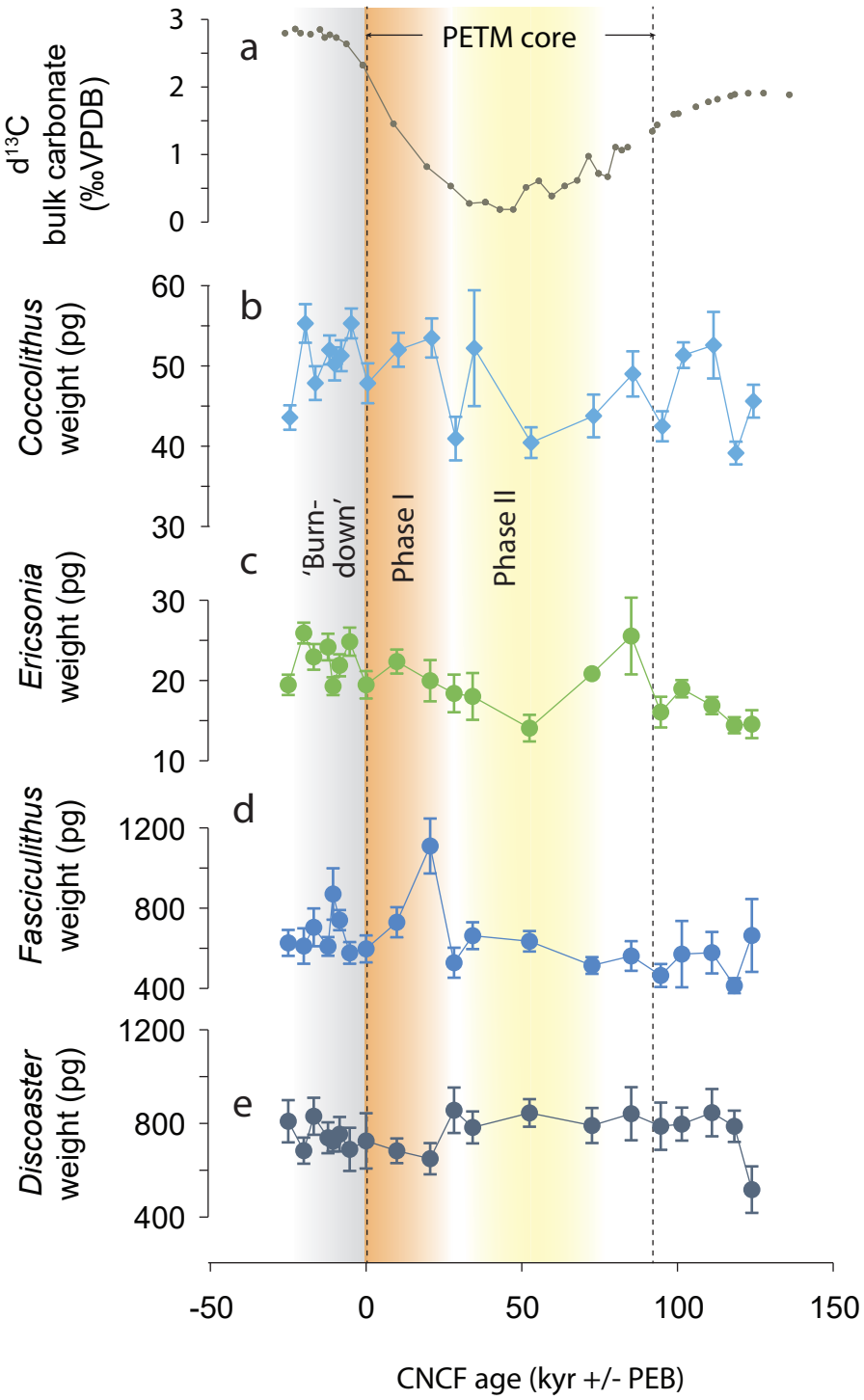


Extended Data Fig. 3. Stable calcification rates of dominant nannofossil assemblages across the PETM at Site 1209. Coccolith (b-c) and nannolith (d-e) weight for the most abundant genera at Site 1209B. Error bars reflect 2 standard error (2 SE).

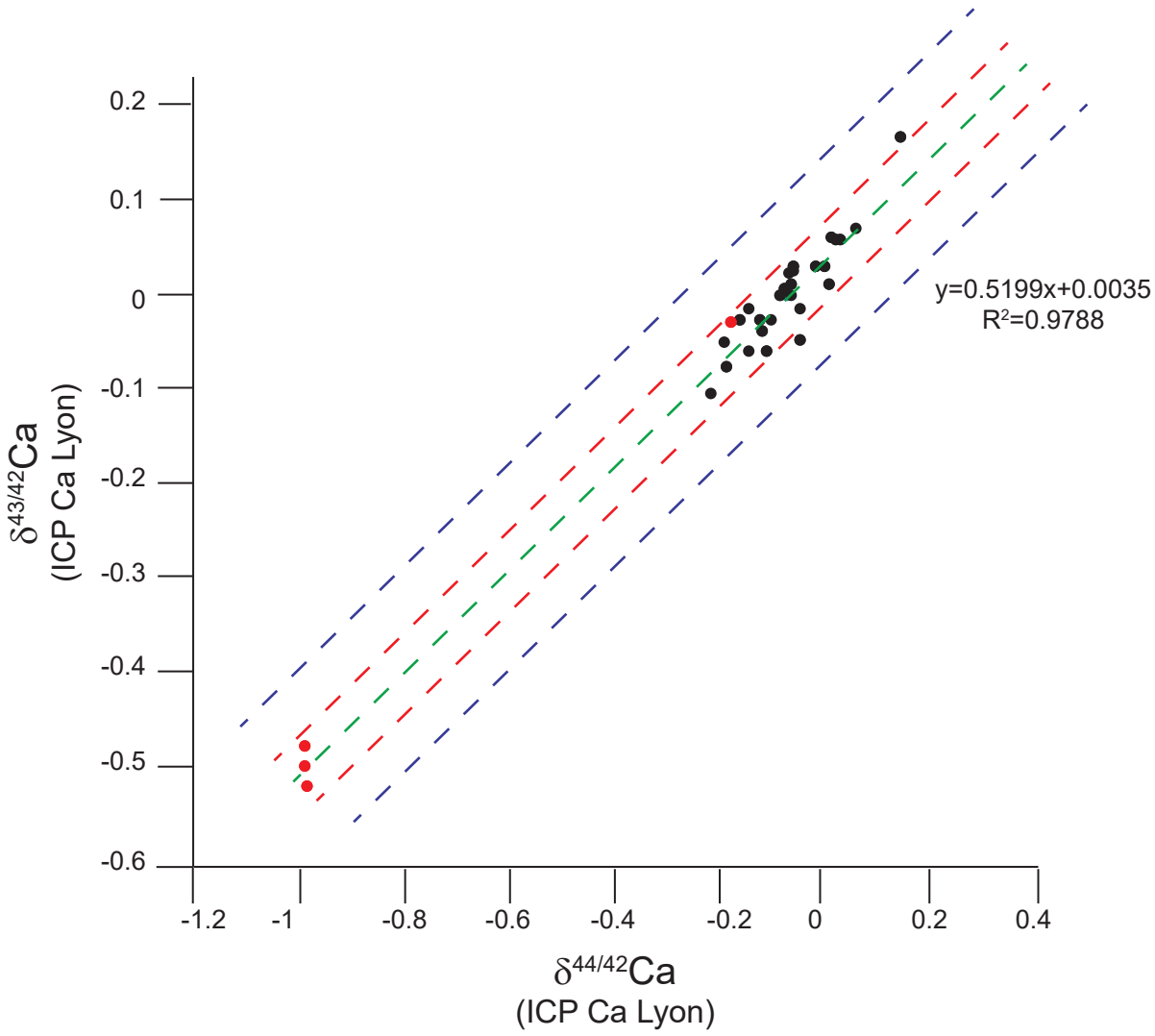


Extended Data Fig. 5. δ43/42Ca on y-axis (per mil) as a function of δ44/42Ca on x-axis (per mil) relative to ICP Ca Lyon. Ca isotope composition falls on a line with a y axis intercept of 0.0054 in the first graph and 0.0035 in the second one indistinguishable from theoretical 0‰ intercept, and a slope of 0.5769 in the first graph and 0.05199 in the second one, indistinguishable from 0.507 predicted slope according to exponential law linear approximation of mass-dependent fractionation. Error bars correspond to average 2 SD precision on δ44/42Ca (per mil) and δ43/42Ca (per mil). Black dots are samples measured in this study; red dots are standards. The blue lines delimit the prediction interval, and the red lines corresponds to the 95% confidence interval on the regression line.

**a**

| | Abs. Ab. | NAR | *Umbilicosphaera* weight | *Coccolithus* weight | *Fasciculithus* weight |
|---|---|---|---|---|---|
| **F** | 2.685 | 20.76 | 4.143 | 2.359 | 3.106 |
| **p (same)** | 8.881E-04 | 2.295E-23 | 5.392E-09 | 7.520E-04 | 9.179E-06 |
| | ***Discoaster* weight** | **Calcite blades lenght** | **Calcite blades width** | **$\delta^{44}$Ca (April 2018)** | **$\delta^{44}$Ca (May 2018)** |
| **F** | 0.9389 | 6.793 | 3.439 | 4.117 | 5.41 |
| **p (same)** | 5.339E-01 | 3.073E-16 | 1.450E-06 | 1.567E-04 | 1.721E-03 |

**b**

| | NAR-MARff | NAR-MARn | MARn-MARff | MARff-Mg/Ca | MARff-Mg/Ca-(M.vel) | MARff-Mg/Ca(A.sol) | MARff-B/Ca (M.vel) | MARff-B/Ca (A.sol) | MARff-pH | *Thoracosphaera* abs.ab-pH | *Thoracospahera* abs.ab-Mg/Ca |
|---|---|---|---|---|---|---|---|---|---|---|---|
| R | 0.81 | 0.65 | 0.84 | -0.85 | -0.76 | -0.76 | 0.51 | 0.82 | 0.70 | -0.66 | 0.66 |
| R^2 | 0.65 | 0.43 | 0.71 | 0.72 | 0.57 | 0.57 | 0.26 | 0.68 | 0.49 | 0.43 | 0.43 |
| p value | 1.22E-06 | 1.52E-04 | 1.61E-04 | 2.98E-12 | 2.62E-09 | 1.35E-07 | 9.68E-06 | 4.71E-05 | 2.72E-03 | 5.45E-03 | 1.51E-02 |

**Extended Data Table 1. a.,** F and p(same) values after one way ANOVA test (See Methods) for Absolute Abundances, NAR, weight of *Umbilicosphaera*, *Coccolithus*, *Fasciculithus*, *Discoaster*, Calcite blades length and width and $\delta^{44}$Ca for the two sessions. **b.,** Pearson's R coefficient, $R^2$ and p(value) resulting from linear modeling to test correlation between all the parameters discussed in the main text. Data are for Site ODP 1209 (Shatsky Rise, Pacific Ocean).

# Supplementary information by Menini et al.

## 1. Samples

### 1.1. Site 1209

Sediment samples were obtained from across the PETM interval at Ocean Drilling Program (ODP) Site 1209 (Shatsky Rise, Central Pacific; 32° 39.1′ N, 158° 30.4′ E; 2387 m water depth; 1900 m paleodepth, Takeda and Kaiho, 2007). The position of the site relative to the PETM paleogeography has been reported in Bralower et al., 2002. Contrarily to the large majority of previous studies of the core 1209B-22H-1 from Site 1209 that used sediments from the working half, the samples we have analyzed for their nannofossil content have been collected from the archive half. Measured $\delta^{13}C$ and $\delta^{18}O$ values of these samples indicate that the working half has been offset downward by 25 mm relative to the archive half (Menini et al., submitted), consistent with the downward offset of 25 mm relative to the archive half during sampling mentioned in (Colosimo et al., 2006). The depths of the samples investigated in this study have therefore been shifted downward by a constant offset of 25 mm to facilitate comparisons with previously published datasets, and all sampling depths have been expressed relative to the main lithological change (i.e., 135 cm below the top of core 1209B-22H-1) to facilitate comparisons between records.

### 1.2. Site 1263

Sediment samples from Ocean Drilling Program (ODP) Site 1263 (Walvis Ridge, Southern-East Atlantic; 28°32′S; 02°47′E; 2717 m water depth; 1500 m paleodepth, Zachos et al., 2004) were also studied for comparison with ODP Site 1209. The position of the site relative to the PETM paleogeography has been reported in Zachos et al., 2004. In line with previous studies (Zachos et al., 2005; Kelly et al., 2010), we analyzed the Hole 1263C between 333.61 and 335.20 rmcd, and Hole 1263D between 335.20 and 335.65 rmcd. The PETM onset is marked by a sharp contact between grayish brown ash-bearing clay above and light gray nannofossil ooze below. Note that our record undersample the PETM onset and associated clay layer located between 335.20 and 335.30 rmcd, with the lowermost studied sample in the core 14H-2 at Hole 1263C being located 7 cm above the base of the clay layer and uppermost sample in the core D4H-1 at Hole 1263D being located 5 cm below the base of the clay layer.

## 2. Age models

### 2.1. Rationale

The Paleocene sediments of the considered sites at Shatsky Rise, Walvis Ridge and Maud Rise are overwhelmingly dominated (>85 wt%) by calcareous planktonic ooze, with subordinate amounts of terrigenous sediments, partly (Site 1263) to almost entirely (Site 1209) supplied as windblown dust (Nicolo and Dickens, 2006; Woodard et al., 2011). The sediments at all sites contain no or negligible amounts (<<0.1%) of biogenic silica and organic carbon (Bralower et al., 2002)(Zachos et al., 2004). In sites where both NCF and extraterrestrial $^3$He ($^3He_{ET}$) contents are available (sites 690, 1266, 1263 and 1209), their striking parallelism suggests a common controlling factor (Farley and Eltgroth, 2003; Murphy et al., 2010). Given the very different (extraterrestrial versus continental) sources and size distribution of these two components (Farley et al., 1997), the most parsimonious explanation is that both the NCF and $^3He_{ET}$ fluxes remained fairly invariable across the PETM interval at each of these locations, and that their remarkable covariation reflects variable dilution by changing $CaCO_3$ accumulation, either through preservation or input. This conclusion is line with studies of Quaternary deep-sea sediments where SR largely depends on CaCO3 fluxes in deep sea sediments. Assuming a constant flux for NCF and $^3He_{ET}$ and knowing their concentrations, the sedimentation rate (SR) can be calculated using the equation:

$$SR = F_X / ([X] * \rho)$$

where SR is the sedimentation rate in m ky$^{-1}$, $\rho$ the dry bulk density (DBD) in g cm$^{-3}$, $F_x$ is the flux of the considered component X in unit cm$^{-2}$ ky$^{-1}$, and [X] its concentration per gram of sediment. DBD values were estimated at each site using the relationship between shipboard gamma-ray attenuation measurements and discrete DBD measurements (Marcantonio et al., 2009). Most previous attempts to infer SR using this method calculated $^3He_{ET}$ fluxes using a calibration interval for which astronomical age models were also available (Farley and Eltgroth, 2003; Murphy et al., 2010). Nevertheless, this approach is limited by the uncertainties associated with duration estimates of the calibration interval (Sluijs et al., 2007), a condition that certainly explains why the PETM duration obtained using this method vary significantly between the considered sites (Murphy et al., 2010).

We have thus considered an alternative approach, in which the interval between carbon isotope inflexion points A (marking the PETM onset) and F, a readily identifiable and widely used segment of the PETM (van der Meulen et al., 2020; Zachos et al., 2005; Zeebe and

Lourens, 2019) is considered of equal duration in all sites, and have then calculated $F_x$ iteratively at each site. This methodology does not provide an independent estimate of the PETM duration, but has the advantage of capturing changes in SR relative to a self-consistent temporal scale for all sites. A similar approach assuming a constant NCF sedimentation rate over a defined interval was used by Stap et al. (2009) to derive an age model for the ETM2-H2 interval at Walvis Ridge. The most notable difference is that their model relies on NCF sedimentation rates (i.e., thickness/time) rather than fluxes (mass/area/time), and hence neglects the influence of changes in DBD. Because DBD values may vary by a factor of 2 between some levels of the Paleocene-Eocene interval at Walvis Ridge, this caveat might explain why the manual adjustment of NCF rates through space and time was required to obtain a self-consistent temporal scale for the different sites.

To facilitate comparisons with the widely used age model of Röhl et al. (2007), we have calibrated our age models assuming that the A-F interval (Zachos et al., 2005) was deposited within 94 ± 1 ky. This estimate is indeed statistically indistinguishable from the 101 ± 9 ky duration constrained by the most recent astronomical age model (5 precession cycles) of expanded continental records of the Bighorn Basin (van der Meulen et al., 2020), where the A-F segment is well defined and cycle counting is facilitated by the absence of dissolution-induced condensation.

Recent astronomical tuning of Walvis Ridge records suggests that the A-F interval might comprise two short eccentricity cycles and lasted 170 ± 30 ky (Zeebe and Lourens, 2019), i.e., almost twice the duration used in our models. This revised duration would imply that the ~7.5 m sedimentary cycles well expressed in the Bighorn Basin correspond to obliquity cycles rather than precession; precession would correspond to the ~3.5 m cycles currently attributed to half-precession (van der Meulen et al., 2020; Westerhold et al., 2018b). If confirmed by independent evidence, the upper estimate would roughly double the relative ages of all samples in our reconstructions, but would leave the relative changes in SR values unaffected. Because SR in the major term in the determination of $MAR_{ff}$ and $MAR_n$, we are therefore confident that the major and long-lived drop in nannofossil accumulation evident from our reconstructions will be resilient to possible future adjustments of the PETM duration.

## 2.2. Shatsky Rise

The approach described above was used to develop a new detailed age model for sites 1209 and 1212. This was done using a comprehensive reexamination of published sedimentological and geochemical records including bulk sediment, benthic and planktonic

foraminifera $\delta^{18}O$ and $\delta^{13}C$ data (Griffith et al., 2015; Penman et al., 2014; Tripati and Elderfield, 2005; Westerhold et al., 2011; Zachos et al., 2003), carbonate contents (Colosimo et al., 2006; Griffith et al., 2015; Zachos et al., 2003), XRF data (Westerhold et al., 2018a), helium isotopes and the non-carbonate fraction (Bralower et al., 2014). No detailed astrochronology exists for the PETM interval at Shatsky Rise, as obliquity and precession-related cycles are not obvious due to low sedimentation rate (SR) and bioturbational smoothing (Westerhold et al., 2018a; Westerhold et al., 2008). Changes in NCF in the carbonate-rich ($CaCO_3$ >90 wt%) sediment from Site 1209B match very well smoothed extraterrestrial $^3He$ ($^3He_{ET}$) contents across the Paleocene-Eocene transition. As argued above, the repeated and parallel increases in NCF and $^3He_{ET}$ most likely reflect episodes of decreased sedimentation rates, either resulting from decreased carbonate input or increased carbonate dissolution, as previously suggested for Fe counts at Site 1209 (Westerhold et al., 2018a). Variable $CaCO_3$ dilution as the main controlling factor of sedimentation rates at Shatsky Rise across the PETM is also supported by parallel increases in ichthyolith (i.e., fish remains) (Tomczik et al., 2015) and Fe counts in core 1209C-11H (Westerhold et al., 2018a).

Because the stratigraphic position of inflection F at Site 1209 was insufficiently constrained by the relatively low resolution bulk carbonate $\delta^{13}C$ records, its position was further refined using the core 9H-5 in Hole B of ODP Site 1212. There, the higher resolution bulk carbonate $\delta^{13}C$ record (Griffith et al., 2015) unambiguously shows it occurs at 79.68 mbsf. The correlation between these two sites and the position of point F at Site 1209 (at 196.23 mbsf, i.e, 22 cm above the main lithological change) was then determined using $\delta^{18}O$ and $\delta^{13}C$ records from both sites, which show a remarkable match in our NCF-derived age models. A notable implication of our age of these age models is that they imply a more than twofold increase in NCF fluxes from Site 1209 to Site 1212 (Extended Data Fig. 1). We are not aware of any independent data that would support such a dramatic increase in terrigeneous fluxes with depth at Shatsky Rise. We note, however, that the NCF values obtained at Site 1209 using coulometry (Colosimo et al., 2006; Zachos et al., 2003) are much more scattered and are offset by about 4% to higher values relative to those obtained using acid digestion (Bralower et al., 2014). As NCF values are derived from coulometric methods at Site 1212 and acid leaching at Site 1212, we therefore attribute these large differences in reconstructed NCF values to methodological biases rather than to much higher terrigenous fluxes in the deeper site.

The developed age models assuming constant NCF and $^3He_{ET}$ fluxes reveal very similar changes in SR throughout the study interval (Extended Data Fig. 1). These trends in SR are

also broadly similar to those estimated for Site 1209 using biohorizon- and stable isotope-based correlations with astronomically-tuned records of southeast Atlantic ODP Site 1262 (Bralower et al., 2014; Kaiho et al., 2006; Penman et al., 2014; Westerhold et al., 2011; Westerhold et al., 2018a; Westerhold et al., 2008) (Penman et al., 2014; Westerhold et al., 2018a), which all point to extreme condensation in the PETM interval. Due to the relatively low number of available tie points, however, these SR were inherently of low resolution (hence showing step-like patterns) compared to our new age models, which allow a more realistic reconstruction of mass accumulation rates at this site.

2.2. Walvis Ridge

As with ODP sites 1266, 1209 and 690, NCF- and $^{3}He_{ET}$-derived SR at Site 1263 show a striking similarity across the PETM (Extended Data Fig. 1). We note that these SR and the resulting MAR derived from our age models provide an internal consistency among the Walvis Ridge sites across the PETM much higher than that implied by precession cycle counts at this location (Röhl et al., 2007; Westerhold et al., 2018b). Crucially, maxima in these precession-based SR and MARff occur at a variable position during the PETM recovery, while they are synchronous in both NCF- and $^{3}He_{ET}$-derived age models. Similarly, the recovery of MARff occurs abruptly and near-synchronously at the PETM core termination in our NCF- and $^{3}He_{ET}$-derived reconstructions, whereas its position appears far more variable in precession-based records. We thus suggest that a robust cycle count across the PETM at Walvis Ridge has been compromised by severe dissolution (and condensation), and we hence discarded the implied SR for our flux reconstructions.

Our age models imply a two-fold decrease in NCF fluxes from the shallowest Site 1263 to the deepest Site 1262 (Extended Data Fig. 1). Unlike data from Shatsky Rise, the $CaCO_3$ data from these two sites were obtained using the same method and device (Zachos et al., 2004, 2005) so that the spatial difference in NCF fluxes reconstructed here cannot be attributed to methodological biases. Such a preferential accumulation of terrigenous material in shallower sites, however, fully agrees with the long-term Paleogene NCF fluxes recorded at Shatsky Rise (Zachos et al., 2004) and with the terrigenous accumulation rates estimated by Stap et al., (2009) for the ETM2 interval.

## 3. Nature, weight and accumulation rates of carbonate components at Site 1209

*Calcareous nannofossils*

The studied nannofossil assemblages at ODP Site 1209 are diverse and generally well preserved, in agreement with previous studies (Gibbs et al., 2006a, b). Nannofossil assemblages are typical of Late Paleocene-Early Eocene (Plate 1) and these are mainly constituted of *Coccolithus* spp., *Toweius* spp., *Fasciculithus* spp., *Discoaster* spp., and *Zygrhablithus bijugatus*.

The preservation of the studied nannofossil assemblages across the PETM at 1209 was further investigated using a Phenom SEM G2 PRO microscope (Menini et al. under review). SEM pictures reveal a slight decline in nannofossil preservation between 1 cm below and above the PETM (-3 kyrs and 16.58 kyrs) from the onset of the event, as previously suggested by Bralower et al., 2014. Coccoliths in those samples are mostly affected by dissolution, consistently with the coeval maximum of nannofossil fragmentation.

Some previous studies of PETM calcareous nannofossil presented abundances using nannofossils/mm$^2$ of the slide, but these invariably used standard smear slides that are far less homogenous in terms of concentration of nannofossils per field of view. The settling method used in our study allows the sediment to settle homogeneously on the cover-slide without any turbulence, so that the number of nannofossils is comparable in different fields of view allowing a more rigorous calculation of nannofossils per gram of rock.

*Nannofossil weight*

We estimated nannofossil weight at ODP Site 1209 following the method described by Beaufort et al., 2014. This method allows the estimate of the thickness of calcite (t) using its birefringence (Dn) and its color in grey-level (GL) in cross-polarized light. This is possible since a linear relationship exists between the thickness of a crystal (t in nm) and the retardation (Γ), which represents the difference between the fast ray and the slow ray produced along the light path within a crystal. Calcareous nannofossil test is made of calcite, and its birefringence is Dn=-0.172. For further details, we refer to Beaufort et al., 2014, where all the optical theory is exhaustively explained.

The nannofossil images obtained using the automated microscope and automatic recognition system SYRACO were classified into 14 separate classes based on the shape, size and birefringence of the nannofossils. The acronyms of the 14 created classes along with the description of the nannofossils featured in each class are listed in Table S1.

| Class | Corresponding nannofossils |
|---|---|
| BAR | *Fasciculithus* Top-Bottom View, *Z. bijugatus* base, *Sphenolithus* spp. |
| CHI | Specimens with a "chi" or a "cross" structure in the central area: *Chiasmolithus* spp., *Cruciplacolithus* spp. |
| CLA | High birefringence specimens, elliptical in shape: *Neocrepidolithus*, *Z. sigmoides* |
| COC | *Coccolithus* spp., *Prinsius* spp., *Toweius* spp. |
| DIS | *Discoaster* spp., *Biantolithus* spp. |
| GEP | Low birefringence specimens, elliptical in shape: *Calcidiscus* spp., *Craticullithus* spp., *Campylosphaera* spp. |
| LAN | *Fasciculithus* spp. |
| PON | *Ellipsolithus* spp., *Pontosphaera* spp. |
| RIE | Particles other than nannofossil |
| SPS | Broken specimens |
| THO | *Thoracosphaera* spp., a calcareous dinocyst |
| UMB | Low birefringence specimens, circular in shape: *Ericsonia* spp., *Umbilicosphaera* spp. |
| ZYG | *Zygrhablithus bijugatus* |
| BRA | *Braarudosphaera* spp. |

Table S1: The different classes created on the basis of shape, birefringence and size of nannofossils.

The estimated weights of the different classes were compared to that of previous studies. The length range of the coccoliths of *Coccolithus* at Site 1209 (6-14µm), one of the main carbonate producers in the studied interval, is slightly wider but in the range of that documented (10-12 µm) for this genus in modern and Holocene sediments (Young and Ziveri, 2000; Beaufort and Heussner, 2001; Cubillos et al., 2012). The estimated weight of *Coccolithus* coccoliths in our PETM samples (~50 pg), however, is 3 to 6 times lower than that estimated for modern *C. pelagicus* (> ~150 pg) studied by Beaufort and Heussner, 2001 and Holocene *C. pelagicus* (~300 pg) studied by Cubillos et al., 2012. This difference is largely attributable to the lower thickness of *Coccolithus* in our material (0.41 µm, as checked under SEM) compared to that reported by Cubilllos et al., 2012 for Holocene samples (1.18 µm). In fact, PETM *Coccolithus* are constituted by *C. pelagicus* and *C. bownii*, the latter being associated with the PETM and dominating the assemblages across the event (Jiang and Wise, 2007). *C. bownii* was described by Jiang and Wise, 2007 as a medium to large broadly elliptical to subcircular *Coccolithus* with a broad, open central area and with a simplified tube structure making the coccolith thinner. Our SEM analyses indicate that several of the investigated *Coccolithus* species generally have a very open central area and a very reduced proximal shield, both characters reducing the coccolith mass, and we refer to these as

belonging to *Coccolithus bownii*. In summary, these considerations indicate that the PETM *Coccolithus* coccoliths were consistently far thinner and lighter than that of living and Holocene representatives, in line with the conclusions of previous studies (Cubillos et al., 2012).

The birefringence method might not provide reliable estimates of the thickness of specimens belonging to *Discoaster* spp. and *Fasciculithus* spp., which are very thick. We have thus measured the thickness of at least 30 specimens for each of these genera in SEM to reevaluate their thickness and eventually correct the automatically acquired values. The birefringence method cannot be correctly applied to *Discoaster* spp. because these are non-birefringent in plan-view (Fig. 4, Young, 1992). The surface of *Discoaster* nannofossils was thus measured in pixel for every automatically taken picture in optical microscope and multiplied by the thickness of 2 µm calculated by repeated SEM measurements to better estimate their volume and weight.

The very thick *Fasciculithus* spp. (3-5 µm) produces high-birefringence colors that hamper the use of grey level images for estimating their thickness (Fig. 5; Beaufort e al., 2014). As for *Discoaster* spp., the surface of *Fasciculithus* was estimated using their basal views in automatically taken pictures and multiplied by the thickness 4.5 µm determined by repeated measurements under SEM.

The obtained nannofossil masses do not show substantial change across the PETM. This record is intriguing in comparison to living coccolithophores. Variations in mass of Noelharbdaceae, which dominate living coccolithophore assemblages from 50 Ma onwards, has been previously correlated to increased $pCO_2$ levels and reduced $CO_3^{2-}$ concentrations in surface waters (Beaufort et al., 2011). Late Paleocene-Early Eocene oceans were dominated by Coccolithaceae and nannoliths (*Fasciculithus* spp., *Discoaster* spp.), which likely thrived under $pCO_2$ levels higher than today. In all oceans at different latitudes, the most abundant taxon during the PETM is *Coccolithus* (e.g, Bralower et al., 2002; Gibbs et al., 2006 a; Agnini et al., 2007; Raffi et al., 2009). *C. pelagicus* is still present in modern oceans but it is restricted to high latitudes, where dissolved $CO_2$ is higher relatively to low-latitudes settings. Thus, it seems like PETM nannofossil masses were relatively "insensitive" to enhanced $pCO_2$ levels, likely because the main species originated during, and were better adapted to, high carbon dioxide levels (Henderiks and Rickaby, 2007).

*Abiogenic calcite ('calcite blades')*

Calcite blades (CB) constitute an intriguing but substantial part of pelagic carbonates preserved at ODP Site 1209 (Colosimo et al., 2006; Stoll et al., 2007c; Bralower et al., 2014). CB are prismatic calcite crystals of micrometric size, the same order of magnitude as nannofossils. Bralower et al. (2014; citing Gibbs et al., 2006a but not found in their paper or dataset) and Stoll et al (2007c) provided semi-qualitative estimate of their abundance at Site 1209. Their data show a distinct peak within the PETM interval, but their record show some noticeable differences, hampering detailed comparison with our data.

We have quantified the shape and absolute abundance of calcite blades at Site 1209 both in optical microscope (1000x magnification) and SEM using the same samples investigated for nannofossils. Their absolute abundance (n/g) and CBAR (calcite blades accumulation rate) ($n/m^2/yr$) were determined using the methodology described above for nannofossils. Their length and width were systematically measured in SEM using 30 specimens/sample at 1550x magnification for all the studied samples. We calculated the volume of all the calcite blades as follows:

$$CBv = l * w * t$$

where $l$ is the length (µm), $w$ is the width (µm) and $t$ is the thickness (µm). We measured calcite blades thickness on the basis of SEM pictures, where we can observe their geometry in 3D. CB weight was thus estimated by multiplying their volume by the calcite density (2.71 g/cm^3).

CBAR, absolute abundances and flux are an order of magnitude lower than those of coccoliths (E^8). However, a five-fold increase in both abundances and CBAR is documented 5 cm above the onset of the PETM, i.e., 50 kyrs after the onset of the event in our preferred age model. We performed ANOVA to compare the mean values of the CB absolute abundance across the event. This test provides us a statistical tool to infer that the average values are statistically different in the core of the event and its aftermath with respect to the intervals below and above, since the null hypothesis is not verified. We do not observe any statistically significant change in the size of calcite blades.

Previous studies interpreted CB as diagenetic minerals that precipitated within the sediment, possibly as a consequence of high Ca and carbonate ion contents resulting from dissolution (Bralower et al., 2014). Their precipitation would have taken place once carbonate saturation recovered (Bralower et al., 2014). Their Sr/Ca ratios are almost an order of magnitude lower

than coeval nannofossils (Stoll et al 2007) and foraminifera (Zachos et al., 2003) and support an abiotic origin. However, precipitation in the sediment would rather result in xenomorphic crystals (cement) showing continuity with grains. Precipitation within pore space seems at the odds with their prismatic shape and their occurrence as isolated crystals without apparent contact with a specific type of particle.

Kozdon et al. (2013) showed SEM image with 10–15 μm sized blade-shaped diagenetic crystallites protruding from pustular muricae of planktic foraminiferal (*M. velascoensis*) for site 865. These are coalesced atop the chamber tips. Pustular biogenic mounds on the surface of morozovellid and acarininid shells might serve as nucleation sites for cementation. Colosimo et al. (2006) also show blade-shaped crystallites that seem detached from the 'mounds' of planktic foraminifers. However, the shape of CB measured in this paper poorly resemble to the cemented blades on planktonic foraminifera pustulae, because they are perfect elongated rhombohedra, with sharply truncated surfaces on both sites of the blade, whilst the cemented crystals on foraminifer pustules have rather an acicular shape.

We alternatively suggest that these CB precipitated near the sediment/water interface in seawater or porewaters, once saturation levels recovered (Stoll et al., 2007c; Dedert et al., 2012). We note that CB absolute abundances and % in mass of carbonate are the highest in the interval where minimum foraminiferal and nannofossil fragmentation occurred and $MAR_{ff}$ is low, there they reach their largest sizes. Hence, these comparisons support the idea that their precipitation was induced by higher $CaCO_3$ saturation state in times where primary and carbonate productivity was still low because of enhanced surface seawater stratification.

*Estimates of the contribution of different components to pelagic carbonate production*

Nannofossils are reported as the main component of the bulk sediment of the studied samples at ODP Site 1209 (70-80% in weight) while planktonic foraminifera only account for 10-20% in weight (Bralower et al., 2014). In order to more precisely quantify the pelagic carbonate accumulation, we calculated the mass of carbonate produced by every component, namely nannofossils, planktonic foraminifera and calcite blades.

The mass of nannofossil and authigenic (CB) calcite and can be calculated as follows:

$$mCaCO3(i) = X(i) * m(i)$$

where *m $CaCO_3$(i)* is the mass of $CaCO_3$ produced by every class *(i)* in gr per gr. of rock, *X(i)* is the absolute abundance of *(i)* in number of particles per gr of rock, *m(i)* is the mean of the weight of *(i)* in gr.

We can calculate the percentage of $CaCO_3$ produced by a class of nannofossils (See section 3) using the following formula:

$$\%CaCO3(i) = (mCaCO3(i)/CaCO3\%) * 100$$

where *m$CaCO_3$(i)* is the mass of $CaCO_3$ produced by every class *(i)* in gr and *$CaCO_3$%* is the percentage of $CaCO_3$ of each sample.

The percentage of $CaCO_3$ produced by nannofossils is calculated as follows:

$$\%CaCO3\ (nanno) = \sum [\%CaCO3\ (i)]$$

where *%$CaCO_3$(i)* is the percentage of $CaCO_3$ produced by a class *(i)*.

This calculation shows that nannofossil calcite compose the bulk of the sediments at Site 1209 and are the main contributors to the fine-fraction (4-10 μm), in agreement with previous studies (Extended Data Fig. 2, Bralower et al., 2014). Planktonic foraminifera, which basically constitute the coarse-fraction (> 63 μm), account up to 10-15 % of the mass of carbonate. Calcite blades account up to ~12 % of bulk $CaCO_3$ during the PETM.

## 4. Nature and accumulation rates of carbonate components at Site 1263

Calcareous nannofossils assemblages at Site 1263 were previously studied by Raffi et al., 2009. However, they only report nannofossils/mm$^2$ of the slide while we studied absolute abundances (n/g) using the settling technique, then we calculated nannofossil accumulation rate (NAR) as detailed in the method section.

Late Paleocene and Early Eocene samples are constituted by nannofossil ooze and chalky nannofossil ooze. Nannofossils compose the bulk of the $CaCO_3$ fraction of the studied samples (90-95 wt. %) while the coarse fraction (>63 μm), which is almost entirely constituted by planktonic foraminifera, is overall lower than 10% in weight (Kelly et al., 2010). Planktonic foraminifera fragmentation is nearly 100% during the core of the PETM and in its aftermath.

| Site | Hole | Core | Section | Top interval | Bottom interval | Depth | Height above LC | Age | Nanno Abs. Ab. | SD | SR 3He 1209 smoothed 3pt update PETM onset | Age 3He 3pt ave | SR CNCF interpolated 1209 | Age CNCF 1209 | nanno frag. 1209 | NAR 3He min 1209 | NAR 3He mean 1209 | NAR 3He max 1209 | NAR CNCF | Dry Bulk Density | MAR ff CNCF 1209 |
|---|---|---|---|---|---|---|---|---|---|---|---|---|---|---|---|---|---|---|---|---|---|
| | | | | (cm) | (cm) | (mbsf) | (m) | (ky) | (n/g) | (n/g) | m/ky | ky +/- PEB | m/ky | ky +/- PEB | % | | n/cm2/ky | | n/cm2/ky | g/cm3 | g/cm2/kyr |
| 1209 | B | 22 | 1 | 90 | 91 | 196.03 | 0.42 | 149.72 | 2.83E+09 | 4.81E+08 | 1.00E-02 | 1.19E+02 | 1.09E-02 | 123.88 | 8.73E+00 | 2.77E+07 | 3.34E+07 | 3.90E+07 | 3.62E+07 | 1.18E+00 | 1.14E+00 |
| 1209 | B | 22 | 1 | 95 | 96 | 196.08 | 0.37 | 140.47 | 3.17E+09 | 1.09E+09 | 1.13E-02 | 1.15E+02 | 7.57E-03 | 118.26 | 1.15E+01 | 2.78E+07 | 4.23E+07 | 5.68E+07 | 2.83E+07 | 1.18E+00 | 7.92E-01 |
| 1209 | B | 22 | 1 | 100 | 101 | 196.13 | 0.32 | 128.93 | 2.90E+09 | 1.06E+09 | 7.28E-03 | 1.09E+02 | 7.08E-03 | 111.06 | 1.66E+01 | 1.57E+07 | 2.47E+07 | 3.37E+07 | 2.40E+07 | 1.17E+00 | 7.32E-01 |
| 1209 | B | 22 | 1 | 105 | 105 | 196.18 | 0.27 | 118.54 | 2.65E+09 | 9.94E+08 | 6.87E-03 | 1.03E+02 | 6.81E-03 | 101.39 | 1.16E+01 | 1.34E+07 | 2.15E+07 | 2.96E+07 | 2.13E+07 | 1.18E+00 | 7.07E-01 |
| 1209 | B | 22 | 1 | 110 | 111 | 196.23 | 0.22 | 108.34 | 3.02E+09 | 9.25E+08 | 5.28E-03 | 9.49E+01 | 6.80E-03 | 94.62 | 7.85E+00 | 1.30E+07 | 1.87E+07 | 2.44E+07 | 2.41E+07 | 1.17E+00 | 7.12E-01 |
| 1209 | B | 22 | 1 | 115 | 116 | 196.28 | 0.17 | 93.60 | 2.87E+09 | 9.49E+08 | 3.40E-03 | 8.30E+01 | 5.08E-03 | 85.14 | 3.98E+00 | 7.66E+06 | 1.14E+07 | 1.52E+07 | 1.71E+07 | 1.17E+00 | 5.07E-01 |
| 1209 | B | 22 | 1 | 120 | 121 | 196.33 | 0.12 | 77.33 | 2.77E+09 | 7.51E+08 | 2.78E-03 | 6.78E+01 | 2.90E-03 | 72.54 | 6.73E+00 | 6.23E+06 | 8.55E+06 | 1.09E+07 | 8.91E+06 | 1.11E+00 | 2.48E-01 |
| 1209 | B | 22 | 1 | 125 | 126 | 196.38 | 0.07 | 57.65 | 1.82E+09 | 8.29E+08 | 2.71E-03 | 5.01E+01 | 2.43E-03 | 52.47 | 6.57E+00 | 2.93E+06 | 5.39E+06 | 7.86E+06 | 4.84E+06 | 1.10E+00 | 1.97E-01 |
| 1209 | B | 22 | 1 | 129 | 130 | 196.42 | 0.03 | 37.62 | 2.55E+09 | 4.64E+08 | 1.84E-03 | 3.33E+01 | 1.80E-03 | 34.22 | 4.37E+00 | 4.16E+06 | 5.08E+06 | 6.00E+06 | 4.97E+06 | 1.08E+00 | 1.43E-01 |
| 1209 | B | 22 | 1 | 130 | 131 | 196.43 | 0.02 | 29.52 | 2.42E+09 | 1.06E+09 | 1.52E-03 | 2.74E+01 | 1.54E-03 | 28.24 | 1.20E+01 | 2.31E+06 | 4.11E+06 | 5.90E+06 | 4.18E+06 | 1.12E+00 | 1.28E-01 |
| 1209 | B | 22 | 1 | 131 | 132 | 196.44 | 0.01 | 16.59 | 2.89E+09 | 1.22E+09 | 1.18E-03 | 2.00E+01 | 1.06E-03 | 20.57 | 2.46E+01 | 2.26E+06 | 3.91E+06 | 5.56E+06 | 3.52E+06 | 1.15E+00 | 1.03E-01 |
| 1209 | B | 22 | 1 | 132 | 133 | 196.45 | 0.00 | 0.00 | 3.73E+09 | 7.36E+08 | 8.46E-04 | 1.01E+01 | 8.04E-04 | 9.86 | 2.31E+01 | 2.96E+06 | 3.68E+06 | 4.41E+06 | 3.50E+06 | 1.17E+00 | 8.19E-02 |
| 1209 | B | 22 | 1 | 133 | 134 | 196.46 | -0.01 | -3.48 | 3.81E+09 | 7.55E+08 | 1.14E-03 | 0.00E+00 | 1.23E-03 | 0.00 | 3.01E+01 | 4.04E+06 | 5.04E+06 | 6.04E+06 | 5.44E+06 | 1.17E+00 | 1.29E-01 |
| 1209 | B | 22 | 1 | 134 | 135 | 196.47 | -0.02 | -5.90 | 3.92E+09 | 5.88E+08 | 1.43E-03 | -7.81E+00 | 2.57E-03 | -5.27 | 1.38E+01 | 5.51E+06 | 6.48E+06 | 7.45E+06 | 1.17E+07 | 1.16E+00 | 2.76E-01 |
| 1209 | B | 22 | 1 | 135 | 136 | 196.48 | -0.03 | -8.09 | 3.09E+09 | 9.58E+08 | 2.80E-03 | -1.25E+01 | 3.60E-03 | -8.51 | 1.82E+01 | 6.92E+06 | 1.00E+07 | 1.31E+07 | 1.29E+07 | 1.16E+00 | 3.86E-01 |
| 1209 | B | 22 | 1 | 136 | 137 | 196.49 | -0.04 | -9.89 | 3.40E+09 | 1.14E+09 | 4.17E-03 | -1.54E+01 | 5.94E-03 | -10.61 | 1.71E+01 | 1.10E+07 | 1.66E+07 | 2.22E+07 | 2.36E+07 | 1.17E+00 | 6.56E-01 |
| 1209 | B | 22 | 1 | 137 | 138 | 196.50 | -0.05 | -11.48 | 3.21E+09 | 7.60E+08 | 4.90E-03 | -1.76E+01 | 6.32E-03 | -12.24 | 1.18E+01 | 1.41E+07 | 1.85E+07 | 2.29E+07 | 2.38E+07 | 1.18E+00 | 6.97E-01 |
| 1209 | B | 22 | 1 | 140 | 141 | 196.53 | -0.08 | -17.10 | 3.99E+09 | 2.02E+08 | | | 6.94E-03 | -16.82 | 1.29E+01 | | | | 3.28E+07 | 1.18E+00 | 7.71E-01 |
| 1209 | B | 22 | 1 | 142 | 143 | 196.55 | -0.10 | -21.20 | 3.77E+09 | 5.93E+08 | | | 6.59E-03 | -20.02 | 9.19E+00 | | | | 2.95E+07 | 1.18E+00 | 7.73E-01 |
| 1209 | B | 2 | 1 | 145 | 146 | 196.58 | -0.13 | -27.70 | 4.60E+09 | 8.43E+08 | | | 5.68E-03 | -25.00 | 8.17E+00 | | | | 3.10E+07 | 1.18E+00 | 6.43E-01 |

Table S2: Compilation of all the data presented in this paper for both Site 1209 and 1263

| 3He MAR nanno mean | SD 3He MAR nanno mean | MARn 3He min 1209 | MARn 3He max 1209 | Thoracosphaera Abs. Ab. spp. | CB Abs. Ab. | CB L | SD | CB w | SD | Nannofossil fragmentation | CaCO3 nanno | SR 3He 1209 3pt ave | Dry Bulk Density | Age 3He 3pt ave | MARff 3He 3ptave 1209 | ΔMARff 3He 3ptave 1209 | MARcf 3He 3ptave 1209 | SR CNCF interpolated 1209 | Age CNCF 1209 | Age composite 1209 | SD composite age | MAR cf CNCF 1209 |
|---|---|---|---|---|---|---|---|---|---|---|---|---|---|---|---|---|---|---|---|---|---|---|
| g/cm2/kyr | g/cm2/kyr | g/cm2/ky | g/cm2/ky | (n/g) | (n/g) | (µm) | (µm) | (µm) | (µm) | (%) | % | m/ky | g/cm3 | ky +/- PEB | g/cm2/ky | | g/cm2/ky | m/kyr | kyr +/- PEB | kyr +/- PEB | kyr | g/cm2/kyr |
| 8.35E-01 | 1.42E-01 | 6.93E-01 | 9.77E-01 | 2.44E+07 | 1.13E+08 | 6.40 | 2.79 | 2.66 | 0.98 | 8.73 | 70.80 | 0.01 | 1.18 | 118.56 | 1.05 | 68.43 | 0.12 | 0.01 | 123.88 | 121.22 | 3.76 | 0.13 |
| 9.61E-01 | 3.30E-01 | 6.32E-01 | 1.29E+00 | 1.98E+07 | 1.79E+08 | 7.26 | 3.30 | 3.17 | 1.88 | 11.53 | 72.06 | 0.01 | 1.18 | 114.54 | 1.18 | 88.96 | 0.14 | 0.01 | 118.26 | 116.40 | 2.63 | 0.09 |
| 7.55E-01 | 2.75E-01 | 4.80E-01 | 1.03E+00 | 1.28E+08 | 4.04E+08 | 7.81 | 2.79 | 3.67 | 1.92 | 16.59 | 88.65 | 0.01 | 1.17 | 109.49 | 0.75 | 20.22 | 0.09 | 0.01 | 111.06 | 110.27 | 1.11 | 0.09 |
| 7.11E-01 | 2.67E-01 | 4.45E-01 | 9.78E-01 | 4.76E+07 | 1.24E+08 | 6.46 | 2.11 | 2.93 | 0.96 | 11.61 | 87.67 | 0.01 | 1.18 | 102.56 | 0.71 | 13.99 | 0.09 | 0.01 | 101.39 | 101.97 | 0.83 | 0.09 |
| 4.73E-01 | 1.45E-01 | 3.29E-01 | 6.18E-01 | 7.77E+07 | 1.14E+08 | 8.48 | 2.92 | 3.21 | 1.08 | 7.85 | 76.61 | 0.00 | 1.17 | 94.89 | 0.55 | -11.74 | 0.06 | 0.01 | 94.62 | 94.76 | 0.20 | 0.08 |
| 3.18E-01 | 1.05E-01 | 2.13E-01 | 4.23E-01 | 7.21E+07 | 9.51E+08 | 12.38 | 3.69 | 4.68 | 1.72 | 3.98 | 79.89 | 0.00 | 1.17 | 82.96 | 0.34 | -45.76 | 0.05 | 0.01 | 85.14 | 84.05 | 1.54 | 0.08 |
| 1.89E-01 | 5.12E-02 | 1.38E-01 | 2.40E-01 | 6.14E+07 | 1.46E+09 | 11.83 | 4.81 | 4.36 | 1.75 | 6.73 | 61.18 | 0.00 | 1.11 | 67.81 | 0.24 | -61.97 | 0.06 | 0.00 | 72.54 | 70.18 | 3.35 | 0.07 |
| 1.88E-01 | 8.57E-02 | 1.02E-01 | 2.73E-01 | 1.06E+08 | 1.10E+09 | 11.91 | 5.21 | 4.16 | 2.14 | 6.57 | 63.23 | 0.00 | 1.10 | 50.15 | 0.22 | -64.81 | 0.07 | 0.00 | 52.47 | 51.31 | 1.64 | 0.06 |
| 1.42E-01 | 2.58E-02 | 1.16E-01 | 1.67E-01 | 1.17E+08 | 1.69E+09 | 11.64 | 5.25 | 4.14 | 2.20 | 4.37 | 71.17 | 0.00 | 1.08 | 33.32 | 0.15 | -76.71 | 0.04 | 0.00 | 34.22 | 33.77 | 0.64 | 0.04 |
| 1.25E-01 | 5.45E-02 | 7.03E-02 | 1.79E-01 | 8.54E+07 | 1.10E+09 | 10.88 | 3.03 | 4.07 | 1.50 | 12.05 | 73.39 | 0.00 | 1.12 | 27.36 | 0.13 | -79.85 | 0.04 | 0.00 | 28.24 | 27.80 | 0.62 | 0.04 |
| 1.15E-01 | 4.86E-02 | 6.64E-02 | 1.64E-01 | 3.62E+07 | 8.02E+08 | 9.16 | 1.97 | 3.36 | 1.17 | 24.57 | 85.00 | 0.00 | 1.15 | 19.95 | 0.11 | -81.74 | 0.01 | 0.00 | 20.57 | 20.26 | 0.44 | 0.01 |
| 9.48E-02 | 1.87E-02 | 7.61E-02 | 1.13E-01 | 1.39E+07 | 4.75E+08 | 8.58 | 3.63 | 3.79 | 1.70 | 23.13 | 96.01 | 0.00 | 1.17 | 10.09 | 0.09 | -86.24 | 0.00 | 0.00 | 9.86 | 9.97 | 0.17 | 0.00 |
| 1.22E-01 | 2.41E-02 | 9.77E-02 | 1.46E-01 | 1.45E+08 | 7.65E+08 | 9.05 | 4.72 | 3.12 | 1.41 | 30.15 | 92.04 | 0.00 | 1.17 | 0.00 | 0.12 | -80.85 | 0.00 | 0.00 | 0.00 | 0.00 | 0.00 | 0.01 |
| 1.59E-01 | 2.38E-02 | 1.35E-01 | 1.83E-01 | 0.00E+00 | 4.09E+08 | 5.83 | 1.81 | 2.98 | 1.10 | 13.80 | 95.98 | 0.00 | 1.16 | -7.81 | 0.15 | -75.57 | 0.01 | 0.00 | -5.27 | -6.54 | 1.80 | 0.01 |
| 3.04E-01 | 9.40E-02 | 2.10E-01 | 3.97E-01 | 5.22E+07 | 5.17E+08 | 9.52 | 5.02 | 3.42 | 1.35 | 18.21 | 93.59 | 0.00 | 1.16 | -12.55 | 0.30 | -52.05 | 0.02 | 0.00 | -8.51 | -10.53 | 2.85 | 0.02 |
| 4.36E-01 | 1.47E-01 | 2.89E-01 | 5.83E-01 | 2.19E+07 | 1.16E+09 | 9.08 | 3.70 | 3.61 | 1.51 | 17.11 | 89.49 | 0.00 | 1.17 | -15.42 | 0.46 | -26.47 | 0.02 | 0.01 | -10.61 | -13.01 | 3.40 | 0.03 |
| 4.70E-01 | 1.11E-01 | 3.59E-01 | 5.81E-01 | 7.43E+07 | 6.70E+08 | 9.12 | 3.46 | 2.58 | 1.21 | 11.78 | 81.61 | 0.00 | 1.18 | -17.62 | 0.54 | -13.49 | 0.03 | 0.01 | -12.24 | -14.93 | 3.81 | 0.04 |
| | | | | 0.00E+00 | 7.11E+08 | 10.30 | 3.76 | 3.85 | 2.13 | 12.88 | 85.03 | | 1.18 | | | | | 0.01 | -16.82 | -20.19 | 4.77 | 0.04 |
| | | | | 5.12E+07 | 7.12E+08 | 8.94 | 2.49 | 3.03 | 0.80 | 9.19 | 93.33 | | 1.18 | | | | | 0.01 | -20.02 | -23.86 | 5.43 | |
| | | | | 0.00E+00 | 5.86E+08 | 8.26 | 2.43 | 3.29 | 1.55 | 8.17 | 91.13 | | 1.18 | | | | | 0.01 | -25.00 | -29.45 | 6.29 | 0.02 |

| MAR ff CNCF 1209 | MAR ff composite 1209 | Coccolithus | Coc 1SE | Ericsonia | Eri 1SE | Fasciculithus | Fasc 1SE | Discoaster | Dis 1SD |
|---|---|---|---|---|---|---|---|---|---|
| g/cm2/kyr | g/cm2/kyr | (pg) | (pg) | (pg) | (pg) | (pg) | (pg) | (pg) | (pg) |
| 1.14 | 1.10 | 45.61 | 2.05 | 14.56 | 1.74 | 663.98 | 181.55 | 517.18 | 99.37 |
| 0.79 | 0.99 | 39.15 | 1.42 | 14.43 | 1.00 | 413.81 | 37.39 | 787.75 | 66.82 |
| 0.73 | 0.74 | 52.58 | 4.15 | 16.87 | 1.07 | 578.17 | 103.3 | 845.98 | 100.98 |
| 0.71 | 0.71 | 51.35 | 1.59 | 18.97 | 1.07 | 570.94 | 165.32 | 797.09 | 70.47 |
| 0.71 | 0.63 | 42.48 | 1.87 | 16.06 | 1.91 | 464.44 | 57.22 | 788.15 | 100.9 |
| 0.51 | 0.42 | 49.01 | 2.82 | 25.54 | 4.78 | 561.69 | 73.89 | 841.51 | 113.39 |
| 0.25 | 0.24 | 43.77 | 2.66 | 20.85 | 0.00 | 514.40 | 41.63 | 791.07 | 74.85 |
| 0.20 | 0.21 | 40.45 | 1.91 | 14.06 | 1.66 | 635.03 | 50.95 | 844.82 | 58.86 |
| 0.14 | 0.14 | 52.21 | 7.22 | 18.02 | 2.91 | 662.85 | 66.89 | 782.92 | 68.24 |
| 0.13 | 0.13 | 40.95 | 2.71 | 18.39 | 2.34 | 528.06 | 74.72 | 856.2 | 97.1 |
| 0.10 | 0.11 | 53.49 | 2.44 | 19.98 | 2.57 | 1109.80 | 136.91 | 649.27 | 66.67 |
| 0.08 | 0.08 | 52.01 | 2.11 | 22.36 | 1.50 | 729.90 | 74.78 | 683.09 | 52.69 |
| 0.13 | 0.12 | 47.84 | 2.48 | 19.47 | 1.71 | 597.11 | 67.2 | 725.45 | 118.09 |
| 0.28 | 0.21 | 55.29 | 1.86 | 24.84 | 1.75 | 577.06 | 54.05 | 689.25 | 92.2 |
| 0.39 | 0.34 | 51.27 | 1.93 | 21.90 | 1.37 | 740.39 | 50.22 | 753.93 | 73.7 |
| 0.66 | 0.56 | 50.26 | 2.06 | 19.29 | 1.11 | 870.60 | 128.13 | 723.87 | 42.61 |
| 0.70 | 0.62 | 51.99 | 1.81 | 24.17 | 1.66 | 609.35 | 46.58 | 738.67 | 65.98 |
| 0.77 | 0.77 | 47.86 | 2.10 | 22.94 | 1.60 | 704.45 | 94.19 | 830.61 | 79.05 |
| 0.77 |  | 55.29 | 2.40 | 25.91 | 1.30 | 611.27 | 88.24 | 683.7 | 55.7 |
| 0.64 |  | 43.57 | 1.52 | 19.46 | 1.27 | 626.87 | 64.64 | 809.24 | 90.17 |

| Depth | Height above lithological change | Age 3He 3pt ave | Age CNCF 1209 | Age composite 1209 | d42Ca ICP Lyon | 1SD | Date | d44/42Ca915b | SD | d44/40Ca915b | SD | d44/40Ca915a | SD | reconstructed SW/915b | SD | reconstructed SW/sw |
|---|---|---|---|---|---|---|---|---|---|---|---|---|---|---|---|---|
| 196.04 | 0.41 | 117.67 | 122.92 | 120.30 | -0.11 | 0.11 | april 2018 | -0.05 | 0.17 | -0.10 | 0.36 | 0.62 | 1.08 | 1.92 | -0.80 | 0.04 |
| 196.05 | 0.40 | 116.93 | 121.88 | 119.41 | -0.06 | 0.05 | april 2018 | 0.00 | 0.11 | 0.00 | 0.23 | 0.72 | 0.95 | 2.02 | -0.93 | 0.14 |
| 196.23 | 0.22 | 94.89 | 94.62 | 94.76 | -0.15 | 0.02 | april 2018 | -0.09 | 0.08 | -0.18 | 0.16 | 0.54 | 0.88 | 1.84 | -1.00 | -0.04 |
| 196.28 | 0.17 | 82.96 | 85.14 | 84.05 | -0.11 | 0.01 | april 2018 | -0.05 | 0.07 | -0.10 | 0.16 | 0.62 | 0.88 | 1.92 | -1.00 | 0.04 |
| 196.32 | 0.13 | 71.24 | 75.76 | 73.50 | 0.07 | 0.02 | april 2018 | 0.13 | 0.08 | 0.28 | 0.16 | 1.00 | 0.88 | 2.30 | -1.00 | 0.42 |
| 196.34 | 0.11 | 64.29 | 68.91 | 66.60 | 0.16 | 0.00 | april 2018 | 0.22 | 0.06 | 0.45 | 0.13 | 1.17 | 0.85 | 2.47 | -1.03 | 0.59 |
| 196.36 | 0.09 | 57.48 | 60.72 | 59.10 | 0.01 | 0.00 | april 2018 | 0.00 | 0.11 | 0.01 | 0.23 | 0.73 | 0.95 | 2.03 | -0.93 | 0.15 |
| 196.38 | 0.07 | 50.15 | 52.47 | 51.31 | 0.00 | 0.07 | april 2018 | 0.06 | 0.13 | 0.12 | 0.28 | 0.84 | 1.00 | 2.14 | -0.88 | 0.26 |
| 196.40 | 0.05 | 42.63 | 44.05 | 43.34 | -0.03 | 0.03 | april 2018 | 0.03 | 0.09 | 0.06 | 0.20 | 0.78 | 0.92 | 2.08 | -0.96 | 0.20 |
| 196.41 | 0.04 | 38.30 | 39.39 | 38.85 | 0.03 | 0.08 | april 2018 | 0.09 | 0.14 | 0.18 | 0.29 | 0.90 | 1.01 | 2.20 | -0.87 | 0.32 |
| 196.43 | 0.02 | 27.36 | 28.24 | 27.80 | -0.05 | 0.07 | april 2018 | 0.01 | 0.13 | 0.03 | 0.27 | 0.75 | 0.99 | 2.05 | -0.89 | 0.17 |
| 196.45 | 0.00 | 10.09 | 9.86 | 9.97 | -0.05 | 0.05 | april 2018 | 0.01 | 0.11 | 0.03 | 0.23 | 0.75 | 0.95 | 2.05 | -0.93 | 0.17 |
| 196.46 | -0.01 | 0.00 | 0.00 | 0.00 | -0.07 | 0.06 | april 2018 | -0.01 | 0.12 | -0.02 | 0.25 | 0.70 | 0.97 | 2.00 | -0.91 | 0.12 |
| 196.48 | -0.03 | -12.55 | -8.51 | -10.53 | -0.05 | 0.11 | april 2018 | 0.01 | 0.17 | 0.02 | 0.35 | 0.74 | 1.07 | 2.04 | -0.81 | 0.16 |
| 196.50 | -0.05 | -17.62 | -12.24 | -14.93 | 0.03 | 0.06 | april 2032 | 0.09 | 0.12 | 0.19 | 0.25 | 0.91 | 0.97 | 2.21 | -0.91 | 0.33 |
| 196.52 | -0.07 | -21.46 | -15.31 | -18.38 | 0.04 | 0.04 | april 2018 | 0.10 | 0.10 | 0.21 | 0.20 | 0.93 | 0.92 | 2.23 | -0.96 | 0.35 |
| | | | | | | | | | | | | | | | | |
| 195.99 | 0.46 | 123.68 | 128.79 | 126.23 | -0.20 | 0.01 | may 2018 | -0.14 | 0.07 | -0.30 | 0.15 | 0.42 | 0.87 | 1.72 | -1.01 | -0.16 |
| 196.14 | 0.31 | 108.11 | 109.38 | 108.75 | -0.10 | 0.02 | may 2018 | -0.04 | 0.08 | -0.08 | 0.18 | 0.64 | 0.90 | 1.94 | -0.98 | 0.06 |
| 196.20 | 0.25 | 99.56 | 98.62 | 99.09 | -0.17 | 0.04 | may 2018 | -0.11 | 0.10 | -0.24 | 0.21 | 0.48 | 0.93 | 1.78 | -0.95 | -0.10 |
| 196.26 | 0.19 | 88.76 | 89.24 | 89.00 | -0.18 | 0.00 | may 2018 | -0.12 | 0.06 | -0.25 | 0.13 | 0.47 | 0.85 | 1.77 | -1.03 | -0.11 |
| 196.30 | 0.15 | 77.29 | 81.21 | 79.25 | -0.05 | 0.04 | may 2018 | 0.01 | 0.10 | 0.02 | 0.20 | 0.74 | 0.92 | 2.04 | -0.96 | 0.16 |
| 196.32 | 0.13 | 71.24 | 75.79 | 73.52 | 0.02 | 0.05 | may 2018 | 0.08 | 0.11 | 0.17 | 0.23 | 0.89 | 0.95 | 2.19 | -0.93 | 0.31 |
| 196.39 | 0.06 | 46.48 | 48.35 | 47.42 | -0.13 | 0.02 | may 2018 | -0.07 | 0.08 | -0.15 | 0.18 | 0.57 | 0.90 | 1.87 | -0.98 | -0.01 |
| 196.40 | 0.05 | 42.63 | 44.02 | 43.33 | -0.13 | 0.09 | may 2018 | -0.07 | 0.15 | -0.15 | 0.31 | 0.57 | 1.03 | 1.87 | -0.85 | -0.01 |
| 196.41 | 0.04 | 38.30 | 39.39 | 38.85 | -0.06 | 0.04 | may 2018 | 0.00 | 0.11 | -0.01 | 0.23 | 0.71 | 0.95 | 2.01 | -0.93 | 0.13 |
| 196.46 | -0.01 | 0.00 | 0.00 | 0.00 | -0.04 | 0.07 | may 2018 | 0.02 | 0.13 | 0.05 | 0.28 | 0.77 | 1.00 | 2.07 | -0.88 | 0.19 |
| 196.58 | -0.13 | -33.89 | -25.00 | -29.45 | -0.09 | 0.00 | may 2018 | -0.03 | 0.06 | -0.07 | 0.13 | 0.65 | 0.85 | 1.95 | -1.03 | 0.07 |

| Site | Hole | Core | Section | Top interval | Bottom interval | Rmcd | Depth to LC | CNCF Age | 3He age | CNCF SR |
|---|---|---|---|---|---|---|---|---|---|---|
| 1263 | C | 14 | 1A | 129 | 130 | 333.61 | 1.66 | 100.51 | 101.81 | 0.08 |
| 1263 | C | 14 | 1A | 139 | 140 | 333.71 | 1.56 | 99.17 | 100.14 | 0.07 |
| 1263 | C | 14 | 1A | 149 | 150 | 333.81 | 1.46 | 97.39 | 98.09 | 0.06 |
| 1263 | C | 14 | 2A | 09 | 10 | 333.90 | 1.37 | 96.03 | 96.66 | 0.06 |
| 1263 | C | 14 | 2A | 29 | 30 | 334.10 | 1.17 | 92.46 | 92.55 | 0.05 |
| 1263 | C | 14 | 2A | 39 | 40 | 334.20 | 1.07 | 90.57 | 89.34 | 0.05 |
| 1263 | C | 14 | 2A | 49 | 50 | 334.30 | 0.97 | 88.57 | 85.29 | 0.04 |
| 1263 | C | 14 | 2A | 59 | 60 | 334.40 | 0.87 | 85.47 | 79.36 | 0.03 |
| 1263 | C | 14 | 2A | 69 | 70 | 334.50 | 0.77 | 80.61 | 70.65 | 0.02 |
| 1263 | C | 14 | 2A | 79 | 80 | 334.60 | 0.67 | 76.22 | 62.50 | 0.02 |
| 1263 | C | 14 | 2A | 89 | 90 | 334.70 | 0.57 | 68.97 | 52.68 | 0.01 |
| 1263 | C | 14 | 2A | 99 | 100 | 334.80 | 0.47 | 60.35 | 42.45 | 0.01 |
| 1263 | C | 14 | 2A | 104 | 105 | 334.85 | 0.42 | 55.52 | 37.32 | 0.01 |
| 1263 | C | 14 | 2A | 109 | 110 | 334.90 | 0.37 | 50.41 | 32.42 | 0.01 |
| 1263 | C | 14 | 2A | 114 | 115 | 334.95 | 0.32 | 44.91 | 27.73 | 0.01 |
| 1263 | C | 14 | 2A | 119 | 120 | 335.00 | 0.27 | 39.36 | 23.05 | 0.01 |
| 1263 | C | 14 | 2A | 124 | 125 | 335.05 | 0.22 | 33.55 | 18.42 | 0.01 |
| 1263 | C | 14 | 2A | 129 | 130 | 335.10 | 0.17 | 27.51 | 14.03 | 0.01 |
| 1263 | C | 14 | 2A | 134 | 135 | 335.15 | 0.12 | 20.83 | 9.81 | 0.01 |
| 1263 | C | 14 | 2A | 139 | 140 | 335.20 | 0.07 | 14.78 | 5.39 | 0.01 |
| 1263 | D | 4 | 1A | 72 | 73 | 335.32 | -0.05 | -1.42 | -1.00 | 0.04 |
| 1263 | D | 4 | 1A | 82 | 84 | 335.42 | -0.15 | -3.46 | -4.12 | 0.05 |
| 1263 | D | 4 | 1A | 87 | 88 | 335.47 | -0.20 | -4.47 | -5.71 | 0.05 |
| 1263 | D | 4 | 1A | 92 | 93 | 335.52 | -0.25 | -6.04 | -7.99 | 0.04 |
| 1263 | D | 4 | 1A | 97 | 98.00 | 335.57 | -0.30 | -6.51 | -8.64 | 0.04 |
| 1263 | D | 4 | 2A | 02 | 03 | 335.62 | -0.35 | -7.73 | -10.27 | 0.04 |
| 1263 | D | 4 | 2A | 07 | 08 | 335.67 | -0.40 | -9.22 | -12.22 | 0.04 |
| 1263 | D | 4 | 2A | 12 | 13 | 335.72 | -0.45 | -10.37 | -13.85 | 0.05 |

| 3He sed rate (cm/ky) | density (g/cm3) | Abs. Abundance | NAR CNCF (g/cm2/ky) | NAR 3He (g/cm2/ky) |
|---|---|---|---|---|
| 0.06 | 1.27 | 4.73E+09 | 4.68E+08 | 3.61E+08 |
| 0.06 | 1.32 | 4.25E+09 | 4.00E+08 | 3.36E+08 |
| 0.06 | 1.37 | | | |
| 0.05 | 1.43 | 3.66E+09 | 3.11E+08 | 2.86E+08 |
| 0.04 | 1.45 | 3.37E+09 | 2.67E+08 | 1.83E+08 |
| 0.02 | 1.52 | 4.66E+09 | 3.62E+08 | 1.75E+08 |
| 0.02 | 1.44 | 3.85E+09 | 2.15E+08 | 1.09E+08 |
| 0.01 | 1.59 | 2.52E+09 | 1.04E+08 | 5.65E+07 |
| 0.01 | 1.68 | 3.05E+09 | 1.00E+08 | 5.93E+07 |
| 0.01 | 1.66 | 4.05E+09 | 1.14E+08 | 7.09E+07 |
| 0.01 | 1.75 | 2.24E+09 | 4.49E+07 | 3.90E+07 |
| 0.01 | 1.72 | 2.10E+09 | 3.79E+07 | 3.47E+07 |
| 0.01 | 1.66 | 2.57E+09 | 4.47E+07 | 4.23E+07 |
| 0.01 | 1.70 | 2.10E+09 | 3.29E+07 | 3.76E+07 |
| 0.01 | 1.70 | 2.66E+09 | 4.06E+07 | 4.82E+07 |
| 0.01 | 1.68 | 2.46E+09 | 3.65E+07 | 4.43E+07 |
| 0.01 | 1.69 | 2.32E+09 | 3.30E+07 | 4.30E+07 |
| 0.01 | 1.63 | 2.06E+09 | 2.63E+07 | 3.93E+07 |
| 0.01 | 1.65 | 2.56E+09 | 3.44E+07 | 5.07E+07 |
| 0.01 | 1.53 | 1.96E+09 | 2.11E+07 | 2.87E+07 |
| 0.03 | 1.34 | 2.66E+09 | 1.32E+08 | 1.09E+08 |
| 0.03 | 1.35 | 3.11E+09 | 1.93E+08 | 1.36E+08 |
| 0.03 | 1.35 | 3.42E+09 | 2.14E+08 | 1.42E+08 |
| 0.03 | 1.33 | 3.41E+09 | 2.02E+08 | 1.39E+08 |
| 0.03 | 1.29 | 3.66E+09 | 1.99E+08 | 1.45E+08 |
| 0.03 | 1.29 | 3.92E+09 | 2.02E+08 | 1.55E+08 |
| 0.03 | 1.29 | 4.70E+09 | 2.47E+08 | 1.86E+08 |
| 0.03 | 0.84 | 3.89E+09 | 1.50E+08 | 9.99E+07 |

| MARn CNCF (g/cm2/kyrs) | Rn 3He (g/cm2/kyrs) |
|---|---|
| 9.14 | 7.03 |
| 9.44 | 7.94 |
| 0.00 | 0.00 |
| 7.53 | 6.92 |
| 5.97 | 4.10 |
| 8.00 | 3.87 |
| 4.39 | 2.24 |
| 2.84 | 1.54 |
| 2.08 | 1.23 |
| 2.31 | 1.43 |
| 1.22 | 1.06 |
| 0.99 | 0.91 |
| 0.87 | 0.83 |
| 0.83 | 0.95 |
| 0.92 | 1.09 |
| 0.82 | 1.00 |
| 0.47 | 0.61 |
| 0.38 | 0.57 |
| 0.45 | 0.66 |
| 0.38 | 0.52 |
| 2.38 | 1.96 |
| 4.94 | 3.48 |
| 4.93 | 3.27 |
| 3.82 | 2.62 |
| 4.30 | 3.14 |
| 3.14 | 2.41 |
| 4.26 | 3.20 |
| 3.03 | 2.01 |

The studied nannofossil assemblages are fairly diverse in the studied interval at Site 1263. The preservation of calcareous nannofossils is reported to be moderate to good, but the 6-cm interval from 335.27 to 335.21 rmcd (base of the CIE) shows evidence for dissolution (Raffi et al. 2009). Although most of the coccoliths and nannoliths we observed in the new slides as well in SEM (Phenom SEM G2 PRO microscope) are moderately to well preserved, strongly etched specimens coexist in the same sample. This record is indicative of a fluctuating accumulation rate. In times of reduced sediment accumulation, nannofossils were longer exposed to corrosive conditions at the water-sediment interface. Such conditions likely alternated with higher sedimentation rate inducing a more rapid nannofossil burial and better preservation. Nannofossil fragmentation is consistently higher at Site 1263 that at Site 1209, varying between 35% and 65% (in the core of the PETM).

## 5. Calcium isotopes at Site 1209

### 5.1. Sampling and methodology

The calcium isotope composition of carbonate sediments and fossils has been proposed as a tool for reconstructing the variations in Ca cycling in the geological past (e.g., De La Rocha and DePaolo, 2000; Farkaš et al., 2007a; Griffith et al., 2008a; Blättler et al., 2011, 2012; Fantle and Tipper, 2014). As species-specific $\delta^{44/40}$Ca fractionation effects have been reported in planktonic foraminifera, (Griffith et al., 2008; Kisakureh et al., 2011), we have restricted our analyses to the species *Morozovella velascoensis*, a photosymbiotic, surface dwelling species that occupied oligotrophic settings at low and middle latitudes during the Late Paleocene and the earliest Eocene (Norris et al., 1996, Kelly et al. 1996, Quillévéré et al., 2001). This species is very abundant at Site 1209 (Petrizzo, 2007-2008) and dominates planktonic foraminifera assemblages across the PETM. Foraminifera were carefully selected: cement-filled specimens were carefully avoided.

The samples were carefully ultrasonicated to further eliminate any trace of diagenetic cements. After several tests, we found that six specimens per sample are needed for Ca isotope analyses. This corresponds to ~0.1 mg of calcite. The chemical processing of samples follows the technique described in Tacail et al., 2014 and consists of a chemical-chromatography. Every sample was dissolved in subboiled distilled 1N HCl acid and processed through AG50X-W12 cation exchange resin in 1N HCl medium to dispose of sample matrix (i.e., phosphates, sulfates, alkali elements, and Mg). Ca and Sr fractions were collected in 6N HCl medium. Ca fractions were then separated from Sr by loading samples onto columns filled with Sr-specific resin (Eichrom Sr-Spec) in subboiled distilled 3N $HNO_3$

medium. Blanks for the whole procedure did not exceed 100 ng Ca (Tacail et al., 2014). This is 200 times smaller than the smallest processed Ca samples (about 20 µg) and should not affect the measured isotopic compositions beyond the measurement precision.

A standard-sample bracketing measurement method was used with the ICP Ca Lyon standard (Tacail et al., 2014) as bracketing standard. Measurements of all samples and standards were performed during two sessions in 2018. The $\delta^{43/42}$Ca-$\delta^{44/42}$Ca values of all measured materials show an excellent positive correlation, with a slope close to the 0.507 slope predicted by the linear approximation of exponential mass-dependent fractionation. If the calcium isotopic composition of standards is taken into account, the slope of the line is 0.5199.

The measurements were systematically checked for long-term precision and accuracy using SRM1486 bone meal NIST secondary standard previously described and analyzed for Ca isotope compositions (Tacail et al., 2016; Martin et al., 2015, Tacail et al., 2014). SRM1486 yielded constant values across the six different analysis sessions, with an average $\delta^{44/42}$Ca value of −0.98 ± 0.18 ‰ (2 SE, n = 30), in agreement with previously published values (as listed in Table S4), notably −1.03 ± 0.01 ‰ (2 SE, n = 120) (Tacail et al., 2016). We also analyzed the commonly used SRM915b clinical-grade carbonate standards, and ICP1 Ca solution used as standard in former studies (Morgan et al., 2012; Channon et al., 2015,). All measured $\delta^{44/42}$Ca values of standards and previously published compositions are given for comparison in Table S3. Long-term external precision was estimated using the SRM1486 standard and yields a 2 SD value of 0.12‰ for $\delta^{44/42}$Ca for 112 analyses, over the two sessions. Values of the $\delta^{44/42}$Ca can be converted into $\delta^{44/40}$Ca multiplying by mass fractionation ratio (1/m40-1/m44)/(1/m42-1/m44) = 2.099454809 (where mx is the exact atomic mass of each calcium isotopes). All Ca isotope compositions are expressed in per mil units, using the "delta" notation for the $^{44}Ca/^{40}Ca$ isotope ratios defined as follows:

$$\delta^{44/40}\mathrm{Ca}=\left(\frac{(^{44}\mathrm{Ca}/^{40}\mathrm{Ca})_{\mathrm{sample}}}{(^{44}\mathrm{Ca}/^{40}\mathrm{Ca})_{\mathrm{ICP\ Ca\ Lyon}}}-1\right)*1000$$

where $(^{44}Ca/^{40}Ca)_{sample}$ and $(^{44}Ca/^{40}Ca)_{\text{ICP Ca Lyon}}$ are Ca isotope abundance ratios measured in sample and ICP Ca Lyon bracketing standard, respectively. The accuracy and long-term precision of analyses was checked periodically through the analyses of SRM1486 bone meal NIST standard.

| Standard | Source | n | δ44/42Ca Ca‰; ± 2SD relative to ICP Ca Lyon |
|---|---|---|---|
| SRM1486 (cow bone meal) | This study (April 2018) | 2 | -0.97 ±0.00 |
| | This study (April 2018) | 10 | -0.97±0.16 |
| | This study (May2018) | 10 | -0.96±0.18 |
| | Tacail et al., 2017 | 147 | -1.03 ±0.12 |
| | Tacail et al., 2014 | 17 | -0.96 ±0.14 |
| | Tacail et al., 2016 | 120 | -1.03 ±0.13 |
| | Martin et al., 2015 | 37 | -1.04 ±0.11 |
| SRM915b (Ca carbonate) | This study (May 2018) | 3 | -0.16±0.03 |
| | Tacail et al., 2017 | 4 | -0.16 ±0.04 |
| | Tacail et al., 2014 | 11 | -0.12 ±0.07 |
| | Tacail et al., 2016 | 4 | -0.14 ±0.06 |
| | Martin et al., 2015 | 13 | -0.15 ±0.11 |

Table S3. δ44/42Ca values of standards as measured in this study (in per mil relative to ICP Ca Lyon standard) compared with previously published values.

We performed ANOVA to compare the means of $\delta^{44/42}$Ca isotopic data (Extended Data Table 1). This test provides us with a statistical tool to confidentially assess that the means are statistically different each-others, since the null hypothesis is not verified.

5.2. Likely causes of changes in calcium isotope values

5.2.1. Diagenesis

A previous study of the PETM in Pacific Ocean sites attributed much of variability in the bulk carbonate $\delta^{44}$Ca record to secondary calcite precipitation (Griffith et al., 2015). Evidence for pervasive, secondary overgrowth in planktonic foraminifera across the PETM does exist in the Pacific Ocean at ODP Site 865 in the form of μm-sized calcite blades precipitated along the foraminiferal muricae and specimens partially or entirely cemented with 100-500 μm calcite crystallites (Edgar et al., 2015; Kozdon et al., 2013). Although no comparable crystallites have been documented at Site 1209, the frosty texture of foraminifera points to a certain degree of secondary overgrowth (Colosimo et al., 2006), which could have increased $\delta^{44}$Ca values substantially (Griffith et al., 2015). Because Sr contents of abiogenic calcite are

around an order of magnitude lower than that of biogenic material, even slightly higher secondary overgrowth should be reflected by substantially lower Sr/Ca ratio (Kozdon et al., 2013; Stoll et al., 2007c). The invariant Sr/Ca record of *Morozovella velascoensis* at Site 1209 (Zachos et al., 2003) suggests that secondary calcite overgrowth, if any, has been relatively uniform over the studied time interval. As argued for the boron isotope composition of this species from the same site (Babila et al., 2018), this strongly suggests that relative changes in *Morozovella velascoensis* $\delta^{44}Ca$ composition were preserved.

5.2.2. Secular changes in seawater $\delta^{44}Ca$ values

Assuming it is mostly primary, our $\delta^{44}Ca$ record should reflect changes in $\delta^{44}Ca$ of seawater and isotope fractionation of the calcifying organism (Griffith et al., 2008a; Fantle, 2010; Blättler et al., 2011, 2012; Fantle and Tipper, 2014). One notable feature likely resulting from the first option is the long-term, 0.2 permil decrease of $\delta^{44}Ca$ values recorded between 0 and 100 kyr at Site 1209. This change is consistent both in magnitude and duration with a warming-induced increase in continental weathering and riverine, $^{44}Ca$-depleted Ca input to the ocean. Modeling indicates this process should have increased oceanic Ca contents and decreased $\delta^{44}Ca$ values, with global seawater lowest values predicted around 100 kyr after the PETM onset (Komar and Zeebe, 2011, 2016), in excellent agreement with the lowest $\delta^{44}Ca$ values recorded by our data at Site 1209. This increase in weathering at the PETM onset is corroborated by a coeval shift to more radiogenic Os values in several sites (Dickson et al., 2015). The PETM $\delta^{44}Ca$ and Os records bear strong similarities with those of the Toarcian Oceanic Anoxic Event (Brazier et al., 2015), for which is osmium and calcium isotopes also point to increased continental weathering (Ravizza, 2001, Dickson, 2015). More quantitatively, however, the magnitude of the PETM decrease in $\delta^{44}Ca$ values recorded between 0 and 100 kyr at Site 1209 exceeds previous model-predictions (Komar and Zeebe, 2011). Simulations involving relatively small increase in weathering due to the input of 4500 Pg of carbon indicate that such $\delta^{44}Ca$ changes should be less than 0.05‰, i.e., below standard measurement uncertainty (Komar and Zeebe, 2011). Nevertheless, carbon emissions have been revised upward since then using boron isotope constraints to more than 10,000 Pg (Gutjahr et al., 2017; Penman and Zachos, 2018). Modeling of >10,000 PgC input over 100 kyr for end-Permian conditions produces a larger, 0.1‰ shift in $\delta^{44}Ca$ values, which is still lower than that suggested by our data. Seawater $\delta^{44}Ca$ values could have been further lowered by a slowing down of the biological carbon pump (Komar and Zeebe, 2016), as suggested by our data from Site 1209. Although changes in calcium isotope fractionation might have been involved as well (see below), our new data invalidate previous simulations suggesting that the

476 PETM perturbation was insufficient to impact the calcium isotope budget and supports
477 higher-end estimates of carbon input during the PETM.
478
479 5.2.3. Changes in calcium isotope fractionation
480 Because of the long residence time of Ca (~1 Ma; Berner and Berner, 1996) relative to the
481 ocean mixing time in the global ocean, more rapid (<100 kyr) and larger changes in global
482 seawater $\delta^{44}Ca$ are very unlikely. This is particularly true for the Paleocene-Eocene interval
483 during which Ca content was almost twice higher than today. The 0.5 permil positive
484 excursion recorded between 50 and 100 kyr at Site 1209 can thus hardly be explained by a
485 global change in seawater $\delta^{44}Ca$ unless invoking the combination of unrealistically large
486 swings of calcium input or burial and unidentified and highly fractionated sources. This
487 positive peak recorded between + 50 and + 100 kyrs thus requires changes in foraminiferal
488 calcium isotope fractionation, as suggested by the absence of such a large shift in the bulk
489 carbonate record of the nearby ODP Site 1212 Griffith et al., 2015). The bulk sediment $\delta^{44}Ca$
490 values should indeed mainly reflect that of nannofossils, which according to our calculations
491 overwhelmingly dominate the bulk carbonate at Shatsky Rise. Modern experiments suggest
492 that coccolithophore and foraminifera possess very different calcium incorporation pathways
493 and hence their calcium isotope fractionations are likely controlled by different mechanisms.
494 We note however that such differences between and within these two groups cannot be taken
495 into account when dealing only with $\delta^{44}Ca$ values of the bulk sediment, which is necessarily a
496 complex mixture of different nannofossil and foraminiferal species as well as secondary
497 calcite particles such as the blades present in Site 1209.
498 Several parameters might influence calcium isotope fractionation of planktonic
499 foraminifera shells (Fantle and Tipper, 2014), including calcification rate, growth rate,
500 temperature (Gussone et al., 2003; Sime et al., 2005), salinity and seawater carbonate
501 chemistry (Kisakureh et al., 2011). The measured $\delta^{44/40}Ca$ values show no correlation with
502 previously published size estimates (Petrizzo et al., 2008) and Sr/Ca contents (Zachos et al.,
503 2003) for this genus and, paleotemperature proxies such as $\delta^{18}O$ and Mg/Ca (Zachos et al.,
504 2003; Tripati and Elderfield, 2005). Changes in seawater carbonate chemistry thus appears the
505 most likely cause of this large positive peak recorded between + 50 and + 100 kyrs. The
506 interval recording this positive $\delta^{44/40}Ca$ excursion records higher seafloor carbonate
507 oversaturation, as suggested by lowest foraminiferal and nannofossil fragmentation and
508 highest CB abundance. According to theoretical calculations of Nielsen et al. (2012),

509 however, such a phase of diminished calcium isotope fractionation should reflect higher
510 seawater [Ca]/[$CO_3^{2-}$] ratio. Because large and abrupt changes in [Ca] would require
511 unrealistic large swings in input and burial fluxes (see above), highest $\delta^{44/40}$Ca values would
512 point to minimal [$CO_3^{2-}$] at +80 kyrs. This is at odds with most model simulations indicating
513 that [$CO_3^{2-}$] decreased markedly due to massive CO2 input at the onset of the PETM and
514 increased afterwards due to higher riverine input (Komar and Zeebe, 2011). This mismatch
515 suggests that $d^{44/40}$Ca fractionation was somehow largely decoupled from [$CO_3^{2-}$] values
516 during the PETM. Alternatively, $d^{44/40}$Ca fractionation could have increased with [$HCO_3^-$]
517 rather than with [$CO_3^{2-}$]. In both field and experimental studies, the influence of this major
518 parameter on foraminiferal calcium isotope fractionation has been seldom tested, because it is
519 classically inversely proportional to [$CO_3^{2-}$] in modern oceans (refs). On geological
520 timescales, however, the two parameters might be somehow decoupled. Different models
521 simulate relatively invariant [$HCO_3^-$] at the PETM onset followed by a steady distinct rise to
522 maximum values some 80 kyrs afterwards resulting from higher riverine input and lower
523 calcite burial (Komar and Zeebe, 2011; Luo et al., 2016). Importantly, bicarbonate ion levels
524 decrease slowly in the model of Komar and Zeebe (2011) where carbonate export is held
525 constant. In the model of Luo et al., 2016, a long-lived 50% decrease Accordingly, the
526 decrease to lower $\delta^{44/40}$Ca values between + 80 kyr and 100 kyrs would imply a rapid
527 superficial [$HCO_3^-$] decrease, in line with coeval rapid rise of calcite export flux suggested by
528 our $MAR_{ff}$ data.
529
530 **Statistical treatment of data.** We performed statistical treatment of data using the software
531 PAST 3.25. We performed One-way ANOVA (ANalysis Of VAriance) on NAR, nannofossil
532 weight, calcite blades length and width and $\delta^{44}$Ca separately, in order to test that the observed
533 stratigraphic trends are statistically significant. One-way ANOVA is a statistical method for
534 testing the null hypothesis that several univariate samples are taken from populations with the
535 same mean. The samples are assumed to be close to normally distributed and have similar
536 variances.
537 The test statistic F is computed as
538
539 $$F = MSbg / MSwg$$

540 Where $MS_{bg}$ is is the mean square between groups and $MS_{wg}$ is the mean square within
541 groups. The p value is based on F with degrees of freedom between groups ($df_{bg}$) and and

degrees of freedom within groups ($df_{wg}$; Hammer et al., 2001). This test allows us to confidentially assess that the mean values are statistically different each-others, since the null hypothesis is not verified. For NAR, calcite blades length and width and $\delta^{44}Ca$, "F value" is always much higher than 1 and p-value is always <0.05. We also analyzed for the same parameters the table of "post-hoc" pairwise comparisons, based on the Tukey-Kramer test. This test shows us that the "P-equal" values of pre-PETM and post-PETM respect to PETM values are very small. This means that the mean values of pre-PETM and post-PETM samples respectively to PETM ones are statistically different. For nannofossil weight, "F value" is around 1 and p-value is systematically <0.05. However, Tukey-Kramer test indicates that "P-equal" values of pre-PETM and post-PETM relative to PETM values are large thus we cannot reject the null-hypothesis. This means that no statistically significant weight differences do exist between samples. (See Extended Data Table 1)

We also tested a linear model to NAR, $MAR_{ff}$, $MAR_n$ to test correlation with temperature and *p*H, as recorded by Mg/Ca ratio and $\delta^{11}B$ isotope values, respectively and excluding samples belonging to the dissolution interval. Inclusion of the samples corresponding to the dissolution interval has negligible effect on the correlation between the different parameters. NAR and $MAR_n$ show a good and significant correlation ($R^2$=0.65, p<0.05 at Site 1209; $R^2$=0.57, p<0.05 at 1263), as well as $MAR_n$ and $MAR_{ff}$ (e.g., site 1209; $R^2$=0.70, p<=0.05). $MAR_{ff}$ at Site 1209 correlates positively with *p*H ($R^2$=0.59, p<<0.05) but is better correlated with Mg/Ca ($R^2$=0.72, p<0.05). At Site 1209, $MAR_{ff}$ correlates very poorly with B/Ca ($R^2$=0.02, p>0.05).

Thus, we calculated the correlation between $MAR_{ff}$, Mg/Ca and B/Ca for *M. velascoensis* and for *A. soldadoensis*. For both species, both Mg/Ca and B/Ca are well correlated to $MAR_{ff}$ (*A. soldadoensis* B/Ca $R^2$=0.77, p<0.05; Mg/Ca $R^2$= 0.57, p<0.05 - *M. velascoensis* B/Ca $R^2$=0.51, p<0.05; Mg/Ca $R^2$= 0.57, p<0.05). This is not only in agreement with the temperature dependence of the measured Mg/Ca values but also with evidences of strong species-specific B/Ca dependence on calcification temperature.
*Thoracosphaera* absolute abundance does positively correlate to Mg/Ca and to *p*H as measured from boron isotopes at Site 1209 ($R^2$=0.43, p<0.05). However, *Thoracosphaera* percentage shows highest correlation with Mg/Ca ($R^2$=0.63, p<0.05) than to *p*H ($r^2$=0.50, p>0.05). (See Extended Data Table 1)

## References


- Agnini, C., Fornaciari, E., Rio, D., Tateo, F., Backman, J., Giusberti, L., 2007. Responses of calcareous nannofossil assemblages, mineralogy and geochemistry to the environmental perturbations across the Paleocene/Eocene boundary in the Venetian Pre-Alps. Marine Micropaleontology 63(1–2), 19–38.
- Agnini, C., Spofforth, D. J., Dickens et al., 2016. Stable isotope and calcareous nannofossil assemblage record of the late Paleocene and early Eocene (Cicogna section). Climate of the Past (4), 883–909.
- Babila, T.L., Penman, D.E., Hönisch, B., Kelly, D.C., Bralower, T.J., Rosenthal, Y., Zachos, J.C., 2018. Capturing the global signature of surface ocean acidification during the Palaeocene–Eocene Thermal Maximum. Philosophical Transactions A 376.
- Beaufort L., Barbarin, N., Gally Y., 2014. Optical measurements to determine the thickness of calcite crystals and the mass of thin carbonate particles such as coccoliths. Nature protocols 9(3), 633–642.
- Beaufort, L., Dollfus, D., 2004. Automatic recognition of coccoliths by dynamical neural networks. Marine Micropaleontology 51(1–2), 57–73.
- Beaufort, L., Heussner, S. 2001. Seasonal dynamics of calcareous nannoplankton on a West European continental margin: the Bay of Biscay. Marine Micropaleontology, 43(1-2), 27–55.
- Beaufort, L., Probert, I., Buchet, N., 2007. Effects of acidification and primary production on coccolith weight: Implications for carbonate transfer from the surface to the deep ocean. Geochemistry, Geophysics, Geosystems, 8(8).
- Beaufort, L., Probert, I., de Garidel-Thoron et al., 2011. Sensitivity of coccolithophores to carbonate chemistry and ocean acidification. Nature, 476(7358), 80–83.
- Berner, E.K., Berner, R.A., 1996. Global Environment: Water, Air, and Geochemical Cycles. Prentice Hall, New Jersey. 376 pp.
- Blättler, C. L., Henderson, G. M., & Jenkyns, H. C. (2012). Explaining the Phanerozoic Ca isotope history of seawater. Geology 40(9), 843–846.
- Blättler, C. L., Jenkyns, H. C., Reynard, L. M., & Henderson, G. M. 2011. Significant increases in global weathering during Oceanic Anoxic Events 1a and 2 indicated by calcium isotopes. Earth and Planetary Science Letters 309(1-2), 77–88.
- Boudreau, B. P., Middelburg, J. J., & Luo, Y. (2018). The role of calcification in carbonate

compensation. Nature Geoscience, 11(12), 894–900.

- Bowen, G. J., 2013. Up in smoke: A role for organic carbon feedbacks in Paleogene hyperthermals. Global and Planetary Change 109, 18–29
- Bralower, T., Premoli Silva, I., Malone, M., 2002. Leg 198, Proceedings of the Ocean Drilling Program: Initial reports, 148.
- Bralower, T.J., 2002. Evidence of surface water oligotrophy during the Paleocene–Eocene Thermal Maximum: nannofossil assemblage data from Ocean Drilling Program Site 690 Maud Rise, Weddell Sea. Paleoceanography 17, 1–13.
- Bralower, T.J., Kelly, D.C., Gibbs, S., Farley, K., Eccles, L., Lindemann, T.L., Smith, G.J., 2014. Impact of dissolution on the sedimentary record of the Paleocene–Eocene thermal maximum. Earth and Planetary Science Letters 401, 70–82.
- Bralower, T.J., Kelly, D.C., Gibbs, S., Farley, K., Eccles, L., Lindemann, T.L., Smith, G.J., 2014. Impact of dissolution on the sedimentary record of the Paleocene–Eocene thermal maximum. Earth and Planetary Science Letters 401, 70–82.
- Bralower, T.J., Premoli Silva, I., Malone, M.J., et al., 2002. Proc. ODP, Initial Reports., 198: College Station, TX (Ocean Drilling Program).
- Brazier, J. M., Suan, G., Tacail, T., Simon, L., Martin, J. E., Mattioli, E., Balter, V., 2015. Calcium isotope evidence for dramatic increase of continental weathering during the Toarcian oceanic anoxic event (Early Jurassic). Earth and Planetary Science Letters 411, 164–176.
- Bridgestock, L., Hsieh, Y. T., Porcelli, D., & Henderson, G. M. (2019). Increased export production during recovery from the Paleocene–Eocene thermal maximum constrained by sedimentary Ba isotopes. Earth and Planetary Science Letters, 510, 53-63.
- Channon, M. B., Gordon, G. W., Morgan, J. L., Skulan, J. L., Smith, S. M., Anbar, A. D., 2015. Using natural, stable calcium isotopes of human blood to detect and monitor changes in bone mineral balance. Bone, 77, 69-74.
- Colosimo, A.B., Bralower, T.J., Zachos, J.C., 2006. Evidence for lysocline shoaling at the Paleocene/Eocene thermal maximum on Shatsky rise, northwest Pacific. Proceeding of the Ocean Drilling Program. Scientific Results 198, 1–36.
- Colosimo, A.B., Bralower, T.J., Zachos, J.C., 2006. Evidence for lysocline shoaling at the Paleocene/Eocene thermal maximum on Shatsky Rise, northwest Pacific, Proceedings of the Ocean Drilling Program: Scientific Results. Texas A & M University.
- Cubillos, J. C., Henderiks, J., Beaufort, L., Howard, W. R., Hallegraeff, G. M., 2012. Reconstructing calcification in ancient coccolithophores: Individual coccolith weight and

morphology of *Coccolithus pelagicus* (sensu lato). Marine Micropaleontology 92 29–39.

- De La Rocha, C.L., De Paolo, D.J., 2000. Isotopic Evidence for Variations in the Marine Calcium Cycle Over the Cenozoic. Science 289, 1176–1178
- Dickens, G.R., Castillo, M.M., Walker, J.G.C., 1997. A blast of gas in the latest Paleocene: Simulating first-order effects of massive dissociation of oceanic methane hydrate, Geology 25, 259–262.
- Dickens, G.R., O'Neil, J.R., Rea, D.K., Owen, R.M., 1995. Dissociation of oceanic methane hydrate as a cause of the carbon isotope excursion at the end of the Paleocene. Paleoceanography 10, 965–971
- Dickson, Journal of Chemical Thermodynamics 22, 113–127, 1990.
- Dickson, A. J., Cohen, A. S., Coe, A. L., Davies, M., Shcherbinina, E. A., & Gavrilov, Y. O., 2015. Evidence for weathering and volcanism during the PETM from Arctic Ocean and Peri-Tethys osmium isotope records. Palaeogeography, Palaeoclimatology, Palaeoecology 438, 300–307.
- Edgar, K. M., Anagnostou, E., Pearson, P. N., & Foster, G. L., 2015. Assessing the impact of diagenesis on $\delta^{11}B$, $\delta^{13}C$, $\delta^{18}O$, Sr/Ca and B/Ca values in fossil planktic foraminiferal calcite. Geochimica et Cosmochimica Acta 166, 189–209.
- Fantle, M. S., Tipper, E. T., 2014. Calcium isotopes in the global biogeochemical Ca cycle: implications for development of a Ca isotope proxy. Earth-Science Reviews,129, 148–177.
- Farkaš, J., Böhm, F., Wallmann, K., Blenkinsop, J., Eisenhauer, A., van Geldern, R., Munnecke, A., Voigt, S., Veizer, J., 2007a. Calcium isotope record of Phanerozoic oceans: implications for chemical evolution of seawater and its causative mechanisms. Geochim. Cosmochim. Acta 71, 5117–5134.
- Farley, K. A., Love, S. G., Patterson, D. B., 1997. Atmospheric entry heating and helium retentivity of interplanetary dust particles. Geochimica et Cosmochimica Acta, 61(11), 2309–2316.
- Farley, K.A., Eltgroth, S.F., 2003. An alternative age model for the Paleocene–Eocene thermal maximum using extraterrestrial 3He. Earth and Planetary Science Letters 208, 135–148.
- Farley, K.A., Love, S.G., Patterson, D.B., 1997. Atmospheric entry heating and helium retentivity of interplanetary dust particles. Geochimica et Cosmochimica Acta 61, 2309–2316.
- Frieling, J., Gebhardt, H., Huber et al., 2017. Extreme warmth and heat-stressed plankton in the tropics during the Paleocene-Eocene Thermal Maximum. Science advances 3(3),

e1600891.

- Gibbs, S. J., Stoll, H. M., Bown, P. R., Bralower, T. J., 2010. Ocean acidification and surface water carbonate production across the Paleocene–Eocene thermal maximum. Earth and Planetary Science Letters 295(3–4), 583–592.
- Gibbs, S.J., Bralower, T.J., Bown, P.R., Zachos, J.C., Bybell, L.M., 2006. Shelf and open-ocean calcareous phytoplankton assemblages across the Paleocene–Eocene thermal maximum: implication for global productivity gradients. Geology 34 (4), 233–236.
- Griffith, E. M., Fantle, M. S., Eisenhauer, A., Paytan, A., Bullen, T. D., 2015. Effects of ocean acidification on the marine calcium isotope record at the Paleocene–Eocene Thermal Maximum. Earth and Planetary Science Letters 419, 81–92.
- Griffith, E. M., Paytan, A., Caldeira, K., Bullen, T. D., Thomas, E., 2008. A dynamic marine calcium cycle during the past 28 million years. Science 322(5908), 1671–1674.
- Griffith, E. M., Schauble, E. A., Bullen, T. D., & Paytan, A., 2008. Characterization of calcium isotopes in natural and synthetic barite. Geochimica et Cosmochimica Acta, 72(23) 5641–5658.
- Griffith, E. M., Schmitt, A. D., Andrews, M. G., & Fantle, M. S. (2020). Elucidating modern geochemical cycles at local, regional, and global scales using calcium isotopes. Chemical Geology, 534, 119445.
- Griffith, E.M., Fantle, M.S., Eisenhauer, A., Paytan, A., Bullen, T.D., 2015. Effects of ocean acidification on the marine calcium isotope record at the Paleocene–Eocene Thermal Maximum. Earth and Planetary Science Letters 419, 81–92.
- Griffith, E.M., Fantle, M.S., Eisenhauer, A., Paytan, A., Bullen, T.D., 2015. Effects of ocean acidification on the marine calcium isotope record at the Paleocene–Eocene Thermal Maximum. Earth and Planetary Science Letters 419, 81–92.
- Griffith, E.M., Paytan, A., Kozdon, R., Eisenhauer, A., Ravelo, A.C., 2008. Influences on the fractionation of calcium isotopes in planktonic foraminifera. Earth and Planetary Sciences Letters 268, 124–136.
- Gussone, N., Eisenhauer, A., Heuser, A., et al., 2003. Model for kinetic effects on calcium isotope fractionation ($\delta^{44}Ca$) in inorganic aragonite and cultured planktonic foraminifera. Geochimica et Cosmochimica Acta, 67(7), 1375–1382.
- Gutjahr, M., Ridgwell, A., Sexton, P. F., Anagnostou, E., Pearson, P. N., Pälike, H., ... & Foster, G. L., 2017. Very large release of mostly volcanic carbon during the Palaeocene–Eocene Thermal Maximum. Nature 548(7669), 573–577.
- Henderiks, J., Rickaby, R. E., 2007. A coccolithophore concept for constraining the

Cenozoic carbon cycle. Biogeosciences 4, 323–329.

- Henehan, M. J., Ridgwell, A., Thomas, E., Zhang et al., 2019. Rapid ocean acidification and protracted Earth system recovery followed the end-Cretaceous Chicxulub impact. Proceedings of the National Academy of Sciences 116(45), 22500–22504.
- Heuser, A., Eisenhauer, A., Scholz-Ahrens, K. E., & Schrezenmeir, J, 2016. Biological fractionation of stable Ca isotopes in Göttingen minipigs as a physiological model for Ca homeostasis in humans. Isotopes in environmental and health studies 52(6) 633-648.
- Holland, K., Branson, O., Haynes, L. L. et al., 2020. Constraining multiple controls on planktic foraminifera Mg/Ca. Geochimica et Cosmochimica Acta 273 116–136.
- Jiang, S., Wise Jr, S. W., 2007. Taxonomic note: A new *Coccolithus* species that thrived during the Paleocene/Eocene Thermal Maximum. Journal of Nannoplankton Research 29, 88–91.
- Jones, T. D., Lunt, D. J., Schmidt, D. N., Ridgwell, A., Sluijs, A., Valdes, P. J., & Maslin, M., 2013. Climate model and proxy data constraints on ocean warming across the Paleocene–Eocene Thermal Maximum. Earth-Science Reviews 125 123–145.
- Kaiho, K., Takeda, K., Petrizzo, M.R., Zachos, J.C., 2006. Anomalous shifts in tropical Pacific planktonic and benthic foraminiferal test size during the Paleocene–Eocene thermal maximum. Palaeogeography, Palaeoclimatology, Palaeoecology 237, 456–464.
- Kelly, C. D., Bralower, T. J., Zachos, J. C., Silva, I. P., Thomas, E., 1996. Rapid diversification of planktonic foraminifera in the tropical Pacific (ODP Site 865) during the late Paleocene thermal maximum. Geology 24(5), 423–426.
- Kelly, D. C., Zachos, J. C., Bralower, T. J., Schellenberg, S. A., 2005. Enhanced terrestrial weathering/runoff and surface ocean carbonate production during the recovery stages of the Paleocene-Eocene thermal maximum. Paleoceanography 20(4).
- Kelly, D.C., Nielsen, T.M.J., McCarren, H.K., Zachos, J.C., Röhl, U., 2010. Spatiotemporal patterns of carbonate sedimentation in the South Atlantic: Implications for carbon cycling during the Paleocene–Eocene thermal maximum. Palaeogeography, Palaeoclimatology, Palaeoecology 293, 30–40.
- Kelly, D.C., Zachos, J.C., Bralower, T.J., Schellenberg, S.A., 2005. Enhanced terrestrial weathering/runoff and surface ocean carbonate production during the recovery stages of the Paleocene-Eocene thermal maximum. Paleoceanography 20.
- Kennett, J.P., Stott, L.D., 1991. Abrupt deep-sea warming, palaeoceanographic changes and benthic extinctions at the end of the Palaeocene. Nature 353, 225–229.
- Kısakürek, B., Eisenhauer, A., Böhm, F., Hathorne, E. C., Erez, J., 2011. Controls on

calcium isotope fractionation in cultured planktic foraminifera, Globigerinoides ruber and Globigerinella siphonifera. Geochimica et Cosmochimica Acta 75(2), 427–443.

- Komar, N., Zeebe, R. E., 2011. Oceanic calcium changes from enhanced weathering during the Paleocene-Eocene thermal maximum: No effect on calcium-based proxies. Paleoceanography, 26(3).
- Komar, N., Zeebe, R. E., 2016. Calcium and calcium isotope changes during carbon cycle perturbations at the end-Permian. Paleoceanography 31(1), 115–130.
- Kozdon, R., Kelly, D. C., Kitajima, K., Strickland, A., Fournelle, J. H., & Valley, J. W., 2013. In situ $\delta^{18}O$ and Mg/Ca analyses of diagenetic and planktic foraminiferal calcite preserved in a deep-sea record of the Paleocene-Eocene thermal maximum. Paleoceanography,28(3), 517–528.
- Lemarchand, D., Wasserburg, G. J., Papanastassiou, D. A., 2004. Rate-controlled calcium isotope fractionation in synthetic calcite. Geochimica et cosmochimica acta, 68(22), 4665–4678.
- Luo, Y., Boudreau, B. P., Dickens, G. R., Sluijs, A., & Middelburg, J. J. (2016). An alternative model for CaCO3 over-shooting during the PETM: biological carbonate compensation. Earth and Planetary Science Letters, 453, 223–233.
- Ma, Z., Gray, E., Thomas, E., Murphy, B., Zachos, J., & Paytan, A. (2014). Carbon sequestration during the Palaeocene–Eocene Thermal Maximum by an efficient biological pump. Nature Geoscience 7(5), 382–388.
- Marcantonio, F., Thomas, D.J., Woodard, S., McGee, D., Winckler, G., 2009. Extraterrestrial 3He in Paleocene sediments from Shatsky Rise: Constraints on sedimentation rate variability. Earth and Planetary Science Letters 287, 24–30.
- Marcantonio, F., Thomas, D.J., Woodard, S., McGee, D., Winckler, G., 2009. Extraterrestrial 3He in Paleocene sediments from Shatsky Rise: Constraints on sedimentation rate variability. Earth and Planetary Science Letters 287, 24–30.
- Martin, J.E., Tacail, T., Adnet. S., Girard, C., Balter, V., 2015. Calcium isotopes reveal the trophic position of extant and fossil elasmobranchs. Chemical Geology 415, 118–125.
- Mattioli, E., Pittet, B., Suan, G., Mailliot, S. 2008. Calcareous nannoplankton changes across the early Toarcian oceanic anoxic event in the western Tethys. Paleoceanography 23(3).
- Mehrbach, C., Culberson, C. H., Hawley, J. E., & Pytkowicx, R. M. (1973). Measurement of the apparent dissociation constants of carbonic acid in seawater at atmospheric pressure 1. Limnology and oceanography 18(6), 897–907.
- Milliman, J. D., 1993. Production and accumulation of calcium carbonate in the ocean:

budget of a nonsteady state. Global geochemical cycles 7(4), 927–957.

- Morgan, J. L., Skulan, J. L., Gordon, G. W., Romaniello, S. J., Smith, S. M., & Anbar, A. D., 2012. Rapidly assessing changes in bone mineral balance using natural stable calcium isotopes. Proceedings of the National Academy of Sciences 109(25), 9989-9994.47.
- Murphy, B.H., Farley, K.A., Zachos, J.C., 2010. An extraterrestrial 3He-based timescale for the Paleocene–Eocene thermal maximum (PETM) from Walvis Ridge, IODP Site 1266. Geochimica et Cosmochimica Acta 74, 5098–5108.
- Murphy, B.H., Farley, K.A., Zachos, J.C., 2010. An extraterrestrial 3He-based timescale for the Paleocene–Eocene thermal maximum (PETM) from Walvis Ridge, IODP Site 1266. Geochimica et Cosmochimica Acta 74, 5098–5108.
- Nicolo, M.J., Dickens, G.R., 2006. Data Report: Terrigenous Grain-Size Distributions at Sites 1263 and 1267: Testing the Applicability of Leg 208 Sediments for Eolian Analysis, in: Kroon, D., Zachos, J.C., Richter, C. (Eds.), Proceedings of the Ocean Drilling Program, Scientific Results Volume 208, College Station, TX 1–13.
- Nielsen, L. C., Druhan, J. L., Yang, W., Brown, S. T., DePaolo, D. J., 2012. Calcium isotopes as tracers of biogeochemical processes. In Handbook of environmental isotope geochemistry, 105–124. Springer, Berlin, Heidelberg.
- Norris, R. D., 1996. Symbiosis as an evolutionary innovation in the radiation of Paleocene planktic foraminifera. Paleobiology, 461–480.
- Penman, D. E., Zachos, J. C., 2018. New constraints on massive carbon release and recovery processes during the Paleocene-Eocene Thermal Maximum. Environmental Research Letters 13(10), 105008.
- Penman, D.E., Hönisch, B., Zeebe, R.E., Thomas, E., Zachos, J.C., 2014. Rapid and sustained surface ocean acidification during the Paleocene-Eocene Thermal Maximum. Paleoceanography 29, 2014 PA002621.
- Penman, D.E., Turner, S.K., Sexton, P.F., Norris, R.D., Dickson, A.J., Boulila, S., Ridgwell, A., Zeebe, R.E., Zachos, J.C., Cameron, A., Westerhold, T., Röhl, U., 2016. An abyssal carbonate compensation depth overshoot in the aftermath of the Palaeocene-Eocene Thermal Maximum. Nature Geosciece 9, 575–580.
- Petrizzo, M. R., 2007. The onset of the Paleocene–Eocene Thermal Maximum (PETM) at Sites 1209 and 1210 (Shatsky Rise, Pacific Ocean) as recorded by planktonic foraminifera. Marine Micropaleontology 63(3–4), 187–200.
- Petrizzo, M. R., Leoni, G., Speijer, R. P., De Bernardi, B., & Felletti, F. (2008). Dissolution susceptibility of some Paleogene planktonic foraminifera from ODP site 1209 (Shatsky Rise,

Pacific Ocean). The Journal of Foraminiferal Research, 38(4), 357–371.

- Poulton, A. J., Sanders, R., Holligan, P. M., Stinchcombe, M. C., Adey, T. R., Brown, L., Chamberlain, K., 2006 Phytoplankton mineralization in the tropical and subtropical Atlantic Ocean. Global Biogeochemical Cycles 20(4).
- Quillévéré, F., Norris, R. D., Moussa, I., Berggren, W. A., 2001. Role of photosymbiosis and biogeography in the diversification of early Paleogene acarininids (planktonic foraminifera). Paleobiology 27(2), 311–326.
- Ravizza, G., Norris, R. N., Blusztajn, J., Aubry, M. P., 2001. An osmium isotope excursion associated with the late Paleocene thermal maximum: Evidence of intensified chemical weathering. Paleoceanography16(2), 155–163.
- Ridgwell, A. (2007). Interpreting transient carbonate compensation depth changes by marine sediment core modeling. Paleoceanography, 22(4).
- Ridgwell, A., Zeebe, R. E., 2005. The role of the global carbonate cycle in the regulation and evolution of the Earth system. Earth and Planetary Science Letters, 234(3–4), 299–315.
- Roberts, J., Kaczmarek, K., Skinner, L.C., Bijma J., Bradbury, H., Turchyn A.V., Misra, S., Lithium Isotopes in Benthic Foraminifera, GCA 2020.
- Röhl, U., Westerhold, T., Bralower, T.J., Zachos, J.C., 2007. On the duration of the Paleocene–Eocene thermal maximum (PETM). Geochemistry, Geophysics, Geosystems 8.
- Self-Trail, J. M., Powars, D. S., Watkins, D. K., Wandless, G., 2012. Calcareous nannofossil assemblage changes across the Paleocene-Eocene thermal maximum: Evidence from a shelf setting, Marine Micropaleontology 92–93, 61–80.
- Sime, N. G., Christina, L., Galy, A., 2005. Negligible temperature dependence of calcium isotope fractionation in 12 species of planktonic foraminifera. Earth and Planetary Science Letters 232(1–2), 51–66.
- Sluijs, A., Bowen, G., Brinkhuis, H., Lourens, L., Thomas, E., 2007. The Palaeocene-Eocene Thermal Maximum super greenhouse: biotic and geochemical signatures, age models and mechanisms of global change. Deep Time Perspectives on Climate Change: Marrying the Signal From Computer Models and Biological Proxies, 323–347.
- Stap, L., Sluijs, A., Thomas, E., Lourens, L., 2009. Patterns and magnitude of deep sea carbonate dissolution during Eocene Thermal Maximum 2 and H2, Walvis Ridge, southeastern Atlantic Ocean. Paleoceanography 24.
- Stoll, H. M., Bains, S., 2003. Coccolith Sr/Ca records of productivity during the Paleocene-Eocene thermal maximum from the Weddell Sea. Paleoceanography 18(2), 1–11.
- Stoll, H., Shimizu, N., Arevalos, A., Matell, N., Banasiak, A., Zeren, S. ,2007. Insights on

coccolith chemistry from a new ion probe method for analysis of individually picked coccoliths. Geochemistry, Geophysics, Geosystems, 8(6).

- Tacail T, Albalat E, Télouk P, Balter V., 2014. A simplified protocol for measurement of Ca isotopes in biological samples. J. Anal. At.Spectrom. 29,5 29–535.
- Tacail, T., Télouk, P., Balter, V., 2016. Precise analysis of calcium stable isotope variations in biological apatites using laser ablation MC-ICPMS. Journal of Analytical Atomic Spectrometry 31(1), 152–162.
- Tacail, T., Thivichon-Prince, B., Martin, J. E., Charles, C., Viriot, L., Balter, V., 2017. Assessing human weaning practices with calcium isotopes in tooth enamel. Proceedings of the National Academy of Sciences 114(24), 6268–6273.
- Takeda, K., Kaiho, K., 2007. Faunal turnovers in central Pacific benthic foraminifera during the Paleocene-Eocene thermal maximum. Palaeogeography, Palaeoclimatology, Palaeoecology 251, 175–197.
- Takeda, K., Kaiho, K., 2007. Faunal turnovers in central Pacific benthic foraminifera during the Paleocene–Eocene thermal maximum. Palaeogeography, Palaeoclimatology, Palaeoecology 251, 175–197.
- Tripati, A., Elderfield, H., 2005. Deep-sea temperature and circulation changes at the Paleocene-Eocene thermal maximum. Science, 308(5730), 1894–1898.
- Tripati, A., Elderfield, H., 2005. Deep-Sea Temperature and Circulation Changes at the Paleocene-Eocene Thermal Maximum. Science 308, 1894–1898.
- Tyson, R. V., 1995. Abundance of organic matter in sediments: TOC, hydrodynamic equivalence, dilution and flux effects. In Sedimentary organic matter. 81–118. Springer, Dordrecht.
- Uppstrom, L. R. (1974). The boron/chlorinity ratio of deep-sea water from the Pacific Ocean. Deep Sea Research 21, 161–162.
- van der Meulen, B., Gingerich, P. D., Lourens, L. J., Meijer, N., van Broekhuizen, S., van Ginneken, S., Abels, H. A., 2020. Carbon isotope and mammal recovery from extreme greenhouse warming at the Paleocene–Eocene boundary in astronomically-calibrated fluvial strata, Bighorn Basin, Wyoming, USA. Earth and Planetary Science Letters 534, 116044.
- van der Meulen, B., Gingerich, P.D., Lourens, L.J., Meijer, N., van Broekhuizen, S., van Ginneken, S., Abels, H.A., 2020. Carbon isotope and mammal recovery from extreme greenhouse warming at the Paleocene–Eocene boundary in astronomically-calibrated fluvial strata, Bighorn Basin, Wyoming, USA. Earth and Planetary Science Letters 534, 116044.
- Vink, A., Brune, A., Höll, C., Zonneveld, K. A., Willems, H., 2002. On the response of

calcareous dinoflagellates to oligotrophy and stratification of the upper water column in the equatorial Atlantic Ocean. Palaeogeography, Palaeoclimatology, Palaeoecology 178(1–2), 53–66.

- Westerhold, T., Röhl, U., Donner, B., McCarren, H. K., Zachos, J. C., 2011. A complete high-resolution Paleocene benthic stable isotope record for the central Pacific (ODP Site 1209). Paleoceanography 26(2).
- Westerhold, T., Röhl, U., Donner, B., McCarren, H.K., Zachos, J.C., 2011. A complete high-resolution Paleocene benthic stable isotope record for the central Pacific (ODP Site 1209). Paleoceanography 26.
- Westerhold, T., Röhl, U., Donner, B., Zachos, J. C., 2018. Global extent of early Eocene hyperthermal events: A new Pacific benthic foraminiferal isotope record from Shatsky Rise (ODP Site 1209). Paleoceanography and Paleoclimatology 33(6), 626–642.
- Westerhold, T., Röhl, U., Donner, B., Zachos, J.C., 2018. Global Extent of Early Eocene Hyperthermal Events: A New Pacific Benthic Foraminiferal Isotope Record From Shatsky Rise (ODP Site 1209). Paleoceanography and Paleoclimatology 33, 626–642.
- Westerhold, T., Röhl, U., Donner, B., Zachos, J.C., 2018a. Global Extent of Early Eocene Hyperthermal Events: A New Pacific Benthic Foraminiferal Isotope Record From Shatsky Rise (ODP Site 1209). Paleoceanography and Paleoclimatology 33, 626–642.
- Westerhold, T., Röhl, U., Raffi, I., Fornaciari, E., Monechi, S., Reale, V., Bowles, J., Evans, H.F., 2008. Astronomical calibration of the Paleocene time. Palaeogeography, Palaeoclimatology, Palaeoecology 257 377–403.
- Westerhold, T., Röhl, U., Wilkens, R.H., Gingerich, P.D., Clyde, W.C., Wing, S.L., Bowen, G.J., Kraus, M.J., 2018b. Synchronizing early Eocene deep-sea and continental records – cyclostratigraphic age models for the Bighorn Basin Coring Project drill cores. Clim. Past 14, 303–319.
- Woodard, S.C., Thomas, D.J., Hovan, S., Röhl, U., Westerhold, T., 2011. Evidence for orbital forcing of dust accumulation during the early Paleogene greenhouse. Geochemistry, Geophysics, Geosystems 12.
- Young, J. R. (1992). The description and analysis of coccolith structure. Nannoplankton Research. Hamrsmid B, Young JR (eds) ZPZ, Knihovnicha, 35–71.
- Young, J. R., Ziveri, P. ,2000. Calculation of coccolith volume and it use in calibration of carbonate flux estimates. Deep sea research Part II: Topical studies in oceanography, 47(9-11), 1679–1700.
- Zachos, J. C., Dickens, G. R., Zeebe, R. E., 2008. An early Cenozoic perspective on

greenhouse warming and carbon-cycle dynamics. Nature, 451(7176), 279–283.

- Zachos, J.C., Kroon, D., Blum, P., Bowles, J., Gaillot, P., Hasegawa, T., Hathorne, E.C., Hodell, D. A., Kelly, D. C., Jung, J. H., Keller, S. M., Lee, Y. S., Leuschner, D. C., Lohmann, K. C., Lourens, L., Monechi, S., Nicolo, M., Raffi, I., Riesselman, C., Röhl, U., Schellenber, S. A., Schmidt, D., Slujis A., Thomas, D., Thomas, E., Vallius, H. , 2004. Early Cenozoic extreme climates: the Walvis Ridge transect. Proceedings of the Ocean Drilling Program. Initial Reports 208.
- Zachos, J.C., Rohl, U., Schellenberg, S.A., Sluijs, A., Hodell, D.A., Kelly, D.C., Thomas, E., Nicolo, M., Raffi, I., Lourens, L.J., McCarren, H., Kroon, D., 2005. Rapid acidification of the ocean during the Paleocene-Eocene thermal maximum. Science 308, 1611–1615.
- Zeebe, R. E. (2012). History of seawater carbonate chemistry, atmospheric CO 2, and ocean acidification. Annual Review of Earth and Planetary Sciences, 40(141), 2012.
- Zeebe, R. E., Zachos, J. C., Dickens, G. R., 2009. Carbon dioxide forcing alone insufficient to explain Palaeocene–Eocene Thermal Maximum warming. Nature Geoscience, 2(8), 576–580.

# Chapitre 5: Conclusions et synthèse

## Conclusion et synthèse

Dans les précédents chapitres du manuscrit j'ai discuté des deux intervalles de temps individuellement. L'objectif de ce dernier chapitre est de comparer les deux intervalles de temps par rapport à la réponse des nannofossiles calcaires.

1. Biostratigraphie

Les deux chapitres de biostratigraphie m'ont permis de mettre en évidence que 1) : les biozonations standards (Bown, 1987 ; Bown 1998 ; Mattioli et Erba, 1999 ; Martini 197 ; Okada et Bukry,1980) ne fournissent pas une résolution suffisante pour étudier des évènements de quelque centaines de milliers d'année de durée ; 2) : il est nécessaire d'avoir une biostratigraphie à très haute résolution pour étudier des évènements tels que le PETM et les deux évènements (Pl/To et T-OAE) au Pliensbachien-Toarcien. Les données biostratigraphiques ont été représentés par rapport à la courbe des isotopes stables du carbone ($\delta^{13}C$). Pour le Pliensbachien-Toarcien, j'ai pu mettre en évidence qu'il y a un épisode majeur d'apparitions autour de la limite Pliensbachien-Toarcien, contrairement au T-OAE qui ne représente ni un épisode de diversification ni d'extinction pour les nanofossiles. Ceci est en partie lié à l'augmentation des placolithes, qui domineront les assemblages pour le reste Mésozoïque et Cénozoïque et en partie liés à des condensations dans plusieurs bassins de la Tethys autour de la limite. Pour le PETM, j'ai pu mettre en évidence que le record sédimentaire a une influence majeure sur l'ordre des évènements. Similairement au Pliensbachien-Toarcien, la présence de discontinuités à la limite explique certaines différences d'une localité à l'autre. Cependant, il existe un certain dégrée de diachronisme, affectant également les marques biostratigraphiques utilisées dans les zonations standards. La limite Paléocène-Eocène est caractérisée par plusieurs origines et extinctions, à différence de la limite Pliensbachien Toarcien. De même, l'on enregistre des changements au sein des communautés des nanofossiles calcaires. Certains de ces événements, jamais ne pris en compte dans les biozonations antérieures, se sont avérés cohérents, avec un degré de diachronisme moindre que les marqueurs biostratigraphiques utilisés précédemment. Finalement j'obtiens un nouveau schéma de biozonation à haute résolution avec une résolution moyenne de 50-100 kyrs par zone. De plus, je corrèle les événements

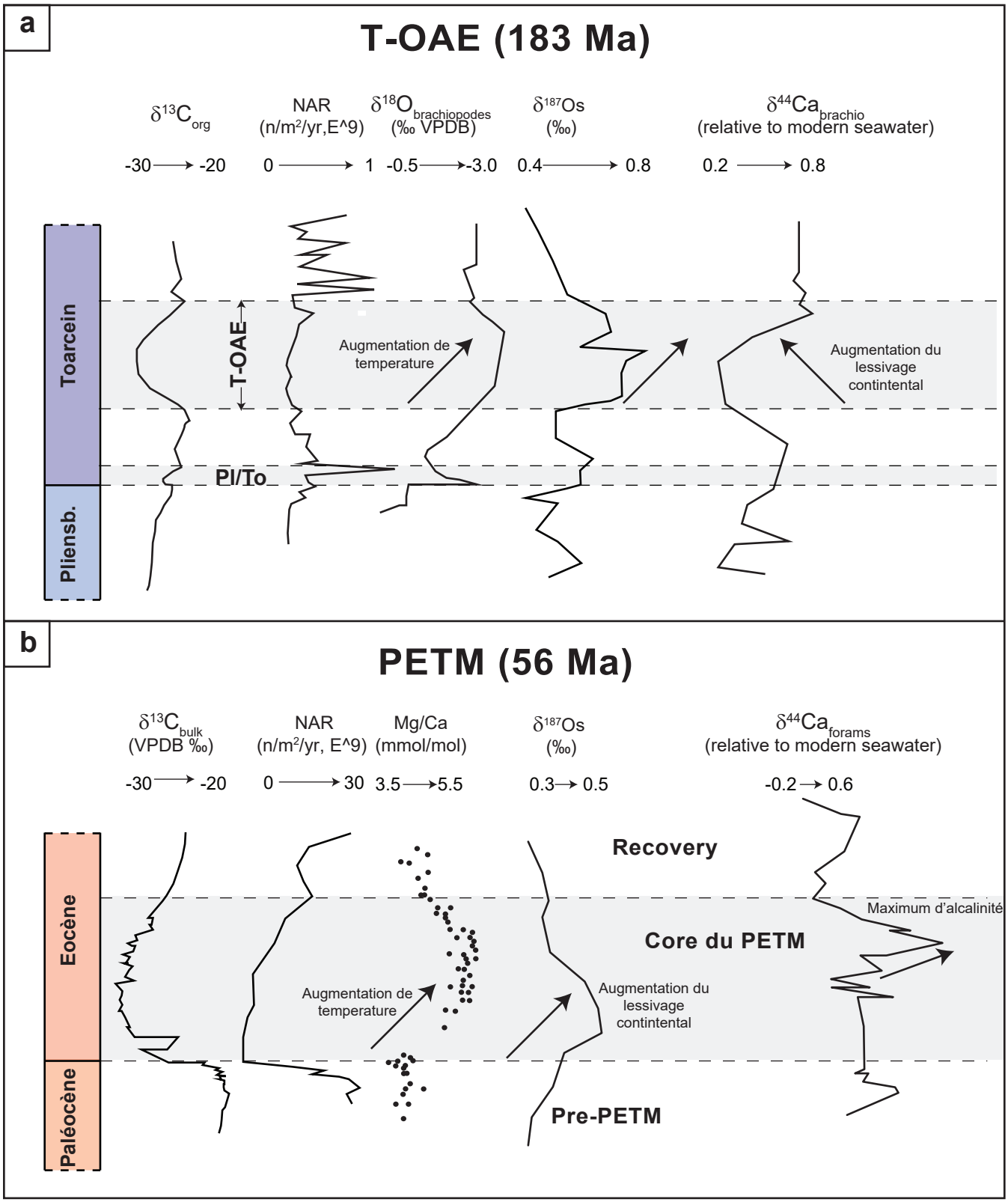


**Fig. 1.** Figure de synthèse de comparaison entre les deux cas d'études discutés dans ce manuscrit: l'événement anoxique du Toarcien (a; T-OAE) et le Maximum thermique à la limite Paléocène-Eocène (b; PETM). Pour les deux événements la courbe des isotopes stables du carbone mesurés sur la matière organique totale pour le T-OAE ($\delta^{13}C_{bulk}$) et sur roche totale pour le PETM ($\delta^{13}C_{org}$) et le NAR provenant des forages Mochras pour le T-OAE e du site 1209 (Pacifique Equatoriel) pour le PETM. Le $\delta^{18}O_{brachiopodes}$ mesurés sur des coquilles de brachiopodes d'après Suan et al. 2008 à Peniche (Bassin Lusitanien, Portugal). Le rapport Mg/Ca mesuré sur des coquilles de l'espèce *Morozovella velascoensis* d'après Penman et al., 2014 au site 1209. Le $\delta^{187}Os$ mesurés sur roche totale d'après Percival et al., 2016 pour le T-OAE à Mochras et d'après Ravizza et al., 2001 pour le PETM. Le $\delta^{44}Ca_{forams}$ mesuré sur des coquilles de l'espèce *Morozovella velascoensis* au site 1209 provient de ce travail (PETM) Le $\delta^{44}Ca_{brachiopodes}$ mesuré sur des coquilles de brachiopodes à Peniche d'après Suan et al., 2008.

biostratigraphiques et les nouvelles zones aux différentes phases caractérisant l'excursion négative des isotopes du carbone définissant la limite Paléocène-Éocène.

2. Est-ce le PETM un évènement océanique anoxique ? Indices provenant des assemblages à nanofossiles calcaires

Malgré plusieurs auteurs se soient intéressés à ces deux épisodes de profonds changements environnementaux et ont mis en évidences des aspects similaires entre le T-OAE et le PETM (Cohen et al., 2007), la comparaison entre les changements biotiques au sein des communautés planctoniques ça n'a jamais été faite auparavant. Il est nécessaire de préciser que les assemblages du Jurassique Inferieur sont totalement différentes de celles du Paléogène (Bown, 1998). Cependant, malgré le fait que la différence au sein des assemblages est due au chemin évolutif des nanofossiles, la réponse et leur sensibilité aux changements paleonvironnementaux restent analogues au cours des temps géologiques. Cela nous permet donc de comparer ces deux évènements, séparés par 130 Ma d'histoire de la Terre, en s'appuyant sur le fait qu'ils présentent déjà de nombreuses similitudes. Pour cela, ils sont les candidats parfaits pour cette étude (Fig.1a,b).

Comme pour le T-OAE, le PETM a été caractérisée par changements au sein des communautés marines, y compris les nanofossiles, et une excursion négative majeure des isotopes du carbone dans les réservoirs de carbone marins et continentaux (par exemple, Koch et al., 1992 ; Schouten et al., 2007). Des travaux récents ont souligné des similitudes, notamment le réchauffement climatique et un lessivage continentale plus efficace (Cohen et al., 2007 ; Hesselbo et al., 2007). Bien que ce ne soit pas aussi clair que pour le T-OAE, des conditions d'hypoxie généralisée (Remmelzwaal et al., 2019) atteignant parfois des conditions d'anoxie au moins en proximité des plateformes continentales (Nicolo et al., 2010), pourraient avoir également marqué le PETM (Sluijs et al., 2006, 2008, 2014). Pour cela, certains auteurs parlent d'un « événement océanique anoxique naissant » (e.g., Cohen et al., 2007). Les deux événements peuvent être liés de manière causale, les deux étant associé à un apport massif de carbone appauvri en $^{13}C$ (Dickens et al. 1995, 1997 ; Hesselbo et al. 2000 ; Svensen et al., 2007). Sur la base des résultats collecté pendant ce travail de thèse,

on peut conclure que les enregistrements qui nous fournissent les nanofossiles au T-OAE et au PETM présentent des similitudes et des différences.

Sur la base d'assemblages de nanofossiles, ainsi que de données provenant des foraminifères planctoniques et benthiques et les dinoflagellés, des travaux récents suggèrent que les conditions trophiques étaient profondément différentes dans les zones proximales et dans les zones distales pendant le PETM (Bralower, 2002 ; Tremolada et Bralower, 2004 ; Gibbs et al., 2006b). Similairement au T-OAE, des pics en abondance relative et absolue de taxons indiquant des eaux froides et une fécondité élevée (*Prinsius*, *Hornibrookina*, *Biscutum, Chiasmolithus*) sont observées dans les sédiments pélagiques (Site 1209, 1263) et proximaux (e.g., Kharouba, Tunisie) déposés avant le PETM. Ces taxons sont remplacés par des taxons d'eaux chaudes, ce qui indique également des conditions plus oligotrophes dans les eaux de surface. Inversement, l'on enregistre un pic des taxons adaptés à des eaux de surface moins salines durant le T-OAE (Calyculaceae). Dans les deux cas, les assemblages de nanofossiles indiquent un une stratification des masses d'eau. Pendant le PETM, la stratification était plus marquée dans les zones océaniques, comme indiquée par les assemblages et par l'analyse en composante principales (ACP). En particulier, le score factoriel qui est contrôlé par *Thoracosphaera*, est particulièrement stable pendant le PETM dans les gyres océaniques (Site, 1209) alors que dans les zone proximales les conditions étaient beacoup plus fluctuantes. Dans ces zones, les assemblages à nanofossiles montrent une alternance entre des conditions plutôt mésotrophes et des conditions oligotrophes. Cependant, l'ACP montre aussi que l'intervalle du PETM est caractérisé par *Discoaster* malformées, *Rhomboaster* et *Coccolithus bownii* (taxons d'excursion) ce qui est un trait commun du PETM indépendamment de l'environnement de dépôt, en plein accord avec les données de littérature (e.g., Bralower et Self-Trail., 2016). Au PETM, on observe un effondrement spectaculaire (>60 %) et durable (>80 000 ans) de la production nette de $CaCO_3$ dans l'océan Atlantique et Pacifique en milieux tropical en raison de la stratification des océans induite par le réchauffement et de la diminution de la disponibilité des nutriments. Nos enregistrements montrent que l'excès d'alcalinité qui en résulte, suggéré par les données de fragmentation des nanofossiles ainsi que par les isotopes du calcium, a été rapidement consommé lorsque la production et l'enfouissement du $CaCO_3$ ont repris, déclenchant un stockage rapide et massif du carbone inorganique et organique. En revanche, dans les zones

proximales l'on enregistre une disponibilité accrue des nutriments. La différence de productivité entre les zones proximales et distales pendant le PETM ressemble quelque peu les variations observées entre le marge nord et sud de la Téthys à travers le T-OAE. Cependant, ces variations, dans le contexte de la paléogéographie toarcienne, se peuvent probablement traduire en un contraste entre un climat humide le long de la marge nord et conditions plus arides aux paléolatitudes tropicales, plutôt qu'en terme de distance par rapport aux continents et, ainsi, aux sources de nutriments. Un apport important et rapide de $CO_2$ dans l'océan devrait produire une chute du *p*H de l'eau de mer et entrainer ainsi une remontée de la profondeur de compensation des carbonates (CCD). C'est certainement le cas pour le PETM, car comme en témoigne la dissolution généralisée des carbonates des fonds marins (e.g., Zachos et al., 2005 ; Zeebe, 2012 ; Penman et al., 2014. Penman et al., 2016). Une baisse du *p*H de l'eau de mer pendant la T-OAE a été évoquée par Tremolada et al., 2005 pour expliquer les enregistrements de sédiments dans le Bassin de Cantabrie (nord de l'Espagne). Ici, l'intervalle correspondant à l'événement (T-OAE) est stérile en nanofossiles calcaires. Toutefois, il faut noter que ce bassin et d'autres bassins épicontinentaux de la Téthys occidentale étaient très peu profondes (moins de 200 m selon Bjerrum et al. (2001), et un telle montée de la CCD semble peu probable. Alternativement, on propose que les milieux du nord-ouest de Téthys, plus proche de la Laurasian Seaway, enregistrent des conditions environnementales peu favorables au nanofossiles calcaires. En effet, similairement aux observations de Tremolada et al., 2005, les nanofossiles sont absents dans des sédiments déposés pendant le T-OAE dans le forage de Brown Moor (nord de l'Angleterre ; Bucefalo Palliani et al., 2002). Les données provenant du forage Mochras (Pays de Galle) montrent des résultats très similaires pendant, car l'abondance absolue et le flux de nanofossiles diminuent brutalement pendant le T-OAE.

En particulier, le $\delta^{13}C$ au PETM suggère un gradient vers des valeurs plus négatives en passant du Site 1209 à Kharouba : ceci pourrait indiquer une productivité globalement faible au niveau de la gyre océanique (Site 1209) et progressivement plus forte dans le proximal (Kharoube ; Fig. 4, chapitre 3.1). C'est intéressant également pour ce qui concerne les NAR : plus forts dans les trois sites avant l'événement, puis faibles dans le *core* et forts à nouveau dans la phase de recovery. Comme pour le

d13C, les flux les plus faibles (productivité globalement faible) au 1209 et 4 ordres de grandeurs plus forte à Kharouba. On observe exactement la même chose au Toarcien

Finalement, l'étude des taux d'accumulation des nanofossiles (NAR) montre que aussi bien pour le PETM que pour le T-OAE il existe une différence de 4 ordre de grandeurs entre les sites le plus oligotophes (e.g., ODP 1209 pour le PETM, Grèce au T-OAE : Kafousia et al., 2011 et les sites les plus proximaux, caractérisés par des conditions plus mesotrophes (e.g., Kharouba au PETM et Brown Moore Borehole, Angleterre).

Comme le PETM, le T-OAE est un évènement hyperthermique (réchauffement climatique global) et plusieurs indices suggèrent une meilleure efficacité du lessivage continentale. Lors de chaque événement, la distribution de la production carbonatée par les nanofossiles varie considérablement entre les sites étudiés, probablement en raison de l'hydrographie et la proximité des continents. La dissolution généralisée des carbonates pélagiques observés pour le PETM ne sont pas connus pour le T-OAE, peut-être en raison de la rareté des coupes du Jurassique Inferieur déposées en eau profonde. Des recherches futures devraient se focaliser sur les coupe du Toarcian qui présentent des sédiments d'eaux profondes, comme celles de sud-ouest du Japon (Hori, 1997).

3. Causes probables des modifications des valeurs isotopiques du calcium

La composition isotopique du calcium des sédiments carbonatés et des fossiles a été proposée comme outil pour reconstituer les variations du cycle du calcium dans le passé géologique (e.g., De La Rocha et DePaolo, 2000 ; Farkaš et al., 2007a ; Griffith et al., 2008a ; Blättler et al., 2011, 2012 ; Fantle et Tipper, 2014). Comme des effets de fractionnement spécifiques à l'espèce $\delta^{44/4}$0Ca existent chez les foraminifères planctoniques, (Griffith et al., 2008 ; Kisakureh et al, 2011), nous avons limité nos analyses à l'espèce *Morozovella velascoensis*, une espèce photosymbiotique vivant en surface et qui occupait des milieux oligotrophes aux basses et moyennes latitudes pendant le Paléocène superieur et l'Éocène inferieur (Norris et al., 1996, Kelly et al. 1996, Quillévéré et al., 2001). Cette espèce est très abondante au site 1209 (Petrizzo, 2007-2008) et domine les assemblages de foraminifères planctoniques au PETM

### 3.1. Diagenèse

Une étude précédente sur le PETM sur des sites de l'océan Pacifique attribuait une grande partie de la variabilité de l'enregistrement du $\delta^{44}Ca$ mesurés sur roche totale à la précipitation de calcite secondaire (Griffith et al., 2015). Des preuves de précipitation de calcite secondaire sur les coquilles des foraminifères planctoniques pendant le PETM existent dans l'océan Pacifique au site ODP 865 sous la forme de bâtonnets de calcite de taille micrométriques précipités le long des *muricae* des foraminifères et de spécimens partiellement ou entièrement cimentés avec des cristallites de calcite de 100-500 µm de longeur (Edgar et al., 2015 ; Kozdon et al., 2013). Bien que la présence de cristallites comparables n'ait pas été documentée au site 1209, la texture givrée (*frosty*) des foraminifères indique un certain degré de précipitation secondaire (Colosimo et al., 2006), qui pourrait avoir augmenté considérablement les valeurs de $\delta^{44}Ca$ (Griffith et al., 2015). Comme la teneur en Sr de la calcite abiogène est inférieure d'environ un ordre de grandeur à celle de la calcite biogène, une surcroissance secondaire (même légèrement plus importante) devrait se traduire par un rapport Sr/Ca nettement plus faible (Kozdon et al., 2013 ; Stoll et al., 2007c). Le rapport Sr/Ca invariant de *Morozovella velascoensis* au site 1209 (Zachos et al., 2003) suggère que la croissance secondaire de calcite, si elle existe, a été relativement uniforme sur l'intervalle de temps étudié. Comme le suggère la composition isotopique du Bore de cette espèce au même site (Babila et al., 2018), il est raisonnable que les changements relatifs de la composition de *Morozovella velascoensis* $\delta^{44}Ca$ ont été préservés.

### 3.2. Changements séculaires dans l'eau de mer $\delta^{44}Ca$

En supposant qu'il soit principalement primaire, notre enregistrement du $\delta^{44}Ca$ devrait refléter les changements dans $\delta^{44}Ca$ de l'eau de mer et le fractionnement isotopique des organismes calcifiant (Griffith et al., 2008a ; Fantle, 2010 ; Blättler et al., 2011, 2012 ; Fantle et Tipper, 2014). Une caractéristique notable résultant probablement de la première option est la diminution à long terme, de 0,2 ‰, des valeurs de $\delta^{44}Ca$ enregistrées entre 0 et 100 kyr au site 1209. Ce changement est cohérent à la fois en termes d'ampleur et de durée avec une augmentation du lessivage continental induite par le réchauffement, en favorisant l'apport de calcium isotopiquement appauvri dans l'océan.

Les modèles indiquent que ce processus devrait avoir augmenté la teneur en Ca de l'océan et diminué les valeurs de $\delta^{44}Ca$, les valeurs les plus faible de l'eau de mer étant prévues autour de 100 kyr après le début du PETM (Komar et Zeebe, 2011, 2016), en excellent accord avec les valeurs les plus faibles de $\delta^{44}Ca$ enregistrées par nos données au 1209. Cette augmentation de l'altération au début du PETM est corroborée par un changement contemporain vers des valeurs de l'osmium plus radiogènes et cela dans plusieurs sites (Dickson et al., 2015). Les données du $\delta^{44}Ca$ du PETM et les valeurs de l'osmium présentent de fortes similitudes avec celles de l'événement océanique anoxique de Toarcian (Brazier et al., 2015), pour lequel les isotopes de l'osmium et du calcium indiquent également une augmentation de l'altération continentale (Ravizza, 2001, Dickson, 2015). Plus quantitativement, cependant, l'ampleur de la diminution du PETM dans les valeurs de $\delta^{44}Ca$ enregistrés entre 0 et 100 kyr au site 1209 est supérieure aux prédictions proposées par les modèles précédents (Komar et Zeebe, 2011). Les simulations impliquant une augmentation relativement faible de l'altération continentale due à l'apport de 4500 Pg de carbone, indiquent que ces changements de $\delta^{44}Ca$ devraient être inférieurs à 0,05‰, c'est-à-dire inférieurs à l'incertitude de mesure standard (Komar et Zeebe, 2011). Néanmoins, les émissions de carbone ont été révisées à la hausse en utilisant les isotopes du bore (plus de 10 000 Pg ; Gutjahr et al., 2017 ; Penman et Zachos, 2018). La modélisation d'un apport de plus de 10 000 PgC sur 100 kyr pour les conditions à la limite Permo-Trias produit un décalage plus important, de 0,1‰, des valeurs de $\delta^{44}Ca$, qui reste inférieur à celui suggéré par nos données. Les valeurs de $\delta^{44}Ca$ pour l'eau de mer auraient pu être encore plus faibles par un ralentissement de la pompe biologique du carbone (Komar et Zeebe, 2016), comme le suggèrent nos données du site 1209. Bien que des changements dans le fractionnement des isotopes de calcium aient pu également être impliqués (voir ci-dessous), nos nouvelles données invalident les simulations précédentes suggérant que la perturbation du PETM était insuffisante pour avoir un impact sur le budget des isotopes de calcium et soutiennent des estimations plus élevées de l'apport de carbone pendant le PETM.

### 3.3. Changements dans le fractionnement des isotopes de calcium

En raison de la longue durée de résidence du Ca (~1 Ma ; Berner et Berner, 1996) par rapport au temps de mélange dans l'océan global, des changements plus rapides (<100 kyr) et plus importants dans l'eau de mer mondiale $\delta^{44}Ca$ sont très peu

probables. Cela est particulièrement vrai pour l'intervalle Paléocène-Eocène pendant lequel la teneur en Ca était presque deux fois plus élevée qu'aujourd'hui. L'excursion positive de 0,5 ‰ enregistrée entre 50 et 100 kyr au site 1209 peut donc être difficilement expliquée par un changement global de l'eau de mer en $\delta^{44}Ca$, à moins d'invoquer la combinaison de fluctuations irréalistes de l'apport ou de l'enfouissement de calcium et de sources non identifiées et fortement fractionnées. Ce pic positif enregistré entre + 50 et + 100 kyrs nécessite donc des changements dans le fractionnement des isotopes de calcium chez les foraminifères, comme le suggère l'absence d'un tel changement dans l'enregistrement de roche totale au voisin site ODP 1212 (Griffith et al., 2015). Les valeurs de $\delta^{44}Ca$ mesurées sur roche totale devraient en effet refléter principalement celles des nanofossiles, qui, selon nos calculs, dominent largement le pourcentage de carbonate à Shatsky Rise. Les expériences modernes suggèrent que les coccolithophores et les foraminifères possèdent des voies d'incorporation du calcium très différentes et donc que leurs fractionnements en isotopes de calcium sont probablement contrôlés par des mécanismes différents. Nous notons cependant que de telles différences entre et au sein de ces deux groupes ne peuvent être prises en compte lorsqu'on traite uniquement des valeurs $\delta^{44}Ca$ mesurés sur roche totale, qui est nécessairement un mélange complexe de différentes espèces nanofossiles et foraminifères ainsi que de particules de calcite secondaires telles que les lamelles (*calcite blades*) présentes au site 1209.

Plusieurs paramètres pourraient influencer le fractionnement des isotopes de calcium des coquilles de foraminifères planctoniques (Fantle et Tipper, 2014), notamment le taux de calcification, le taux de croissance, la température (Gussone et al., 2003 ; Sime et al., 2005), la salinité et la chimie des carbonates d'eau de mer (Kisakureh et al., 2011). Les valeurs mesurées de $\delta^{44/40}Ca$ ne montrent aucune corrélation avec les estimations de taille publiées précédemment (Petrizzo et al., 2008) et les teneurs en Sr/Ca (Zachos et al., 2003) pour ce genre et, les indicateurs de paléotempérature tels que le $\delta^{18}O$ et le Mg/Ca (Zachos et al., 2003 ; Tripati et Elderfield, 2005). Les changements de la chimie des carbonates de l'eau de mer semblent donc être la cause la plus probable du pic positif enregistré entre + 50 et + 100 kyrs. L'intervalle enregistrant cette excursion positive de $\delta^{44/40}Ca$ enregistre une sursaturation plus importante des carbonates du fond marin, comme le suggèrent la plus faible

fragmentation des foraminifères et des nanofossiles et la plus forte abondance de *calcite blades*. Cependant, selon les calculs théoriques de Nielsen et al. (2012), une telle phase de fractionnement réduit des isotopes de calcium devrait refléter un rapport [Ca]/[$CO_3^{2-}$] plus élevé de l'eau de mer. Étant donné que des changements importants et brusques du [Ca] nécessiteraient des variations importantes et irréalistes des flux d'entrée et d'enfouissement (voir ci-dessus), les valeurs les plus élevées de $\delta^{44/40}$Ca indiqueraient un taux minimal de [$CO_3^{2-}$] à +80 kyrs. Ceci est en contradiction avec la plupart des simulations de modèles qui indiquent que le [$CO_3^{2-}$] a diminué de manière significative en raison d'un apport massif de $CO_2$ au début du PETM et a augmenté par la suite en raison d'un apport fluvial plus important (Komar et Zeebe, 2011). Ce décalage suggère que le fractionnement $\delta^{44/40}$Ca était en quelque sorte largement découplé des valeurs [$CO_3^{2-}$] pendant le PETM. Par ailleurs, le fractionnement $\delta^{44/40}$Ca aurait pu augmenter avec le [$HCO_3^-$] plutôt qu'avec le [$CO_3^{2-}$]. Dans les études de terrain et expérimentales, l'influence de ce paramètre majeur sur le fractionnement des isotopes de calcium foraminifères a rarement été testée, car il est classiquement inversement proportionnel au [$CO_3^{2-}$] dans les océans modernes. Cependant, à l'échelle des temps géologiques, les deux paramètres pourraient être d'une manière ou d'une autre découplés. Différents modèles simulent un [$HCO_3^{2-}$] relativement invariant au début du PETM, suivi d'une augmentation constante et distincte jusqu'à des valeurs maximales d'environ 80 kyrs par la suite, résultant d'un apport fluvial plus important et d'un enfouissement de calcite plus faible (Komar et Zeebe, 2011 ; Luo et al., 2016). Il est important de noter que les niveaux d'ions bicarbonate diminuent lentement dans le modèle de Komar et Zeebe (2011) où l'exportation de carbonate est maintenue constante. Dans le modèle de Luo et al, 2016, on observe une diminution de 50% à long terme. En conséquence, la diminution vers des valeurs inférieures de $\delta^{44/40}$Ca entre + 80 kyr et 100 kyrs impliquerait une diminution superficielle rapide [$HCO_3^-$], en accord avec l'augmentation rapide du flux d'exportation de calcite suggérée par nos données $MAR_{ff}$.

## 4. Perspectives

Dans ce travail de thèse je me suis concentré sur l'étude de deux événements marqués par des profondes perturbations du cycle d carbone, une hausse de températures de au moins 5-6°C en moyenne (Zachos et al., 2004 ; Suan et al., 2008a) et un changement dans la chimie des océans, au moins au PETM associé à une réduction du *p*H de 0.3 unités (Penman et al., 2014 ; Babila et al., 2018).

Pour valider le modèle de compensation biologique proposé et étendre ces conclusions, il est nécessaire d'appliquer la même approche sur d'autres événements comparables au PETM et au T-OAE. Un intervalle qui mériterait d'être investigué est l'Eocène Inferieur, entre 57 Ma et 54 Ma, car de nombreux événements d'acidification de plus faible amplitude que le PETM sont enregistrés dans les sédiments océaniques. Du Pacifique et de l'Atlantique. L'étude combinée des taux de fragmentation et d'accumulation des restes de phytoplancton calcaire (NAR), des taux d'accumulation en masse de la fraction fine (< 63 µm ; $MAR_{ff}$) et des isotopes du calcium pourrait permettre de répondre à deux questions scientifiques fondamentales:

1) comment l'export de carbonate a-t-il varié lors d'épisodes moins intenses de réchauffement et d'acidification de l'océan ;

2) ces épisodes sont-ils systématiquement associés à des changements de saturation de la calcite des eaux superficielles et profondes, ou existe-t-il des effets de seuil ? Cette étude permettrait de reconstruire très finement l'export carbonaté et la saturation en calcite sur un intervalle de plusieurs millions d'années afin de mieux contraindre le couplage entre la biologie et la chimie des océans.

Les résultats présentés dans cette thèse montrent qu'il y a un lien étroit mais variable temporellement entre biologie et chimie des océans : il est nécessaire de valider ces hypothèses sur d'autres événements moins extrêmes et potentiellement moins affectés par des problèmes de dissolution et de préservation.

Finalement, ces résultats permettront de déterminer l'importance respective des modèles existant et de mieux comprendre le rôle de la compensation chimique et biologique pendant l'Anthropocène.

## Bibliographie


- Adelseck, C.G., Geehan, G.W., Roth, P.H., 1973. Experimental evidence for the selective dissolution and overgrowth of calcareous nannofossils during diagenesis. Geological Society of America Bulletin 84, 2755–2762.
- Agnini, C., Fornaciari, E., Raffi, I., Catanzariti, R., Pälike, H., Backman, J., Rio, D., 2014. Biozonation and biochronology of Paleogene calcareous nannofossils from low and middle latitudes. Newsletters on Stratigraphy 47, 131–181
- Agnini, C., Fornaciari, E., Rio, D., Tateo, F., Backman, J., Giusberti, L., 2007. Responses of calcareous nannofossil assemblages, mineralogy and geochemistry to the environmental perturbations across the Paleocene/Eocene boundary in the Venetian Pre-Alps. Marine Micropaleontology 63(1–2), 19–38.
- Agnini, C., Muttoni, G., Kent, D. V., Rio, D., 2006. Eocene biostratigraphy and magnetic stratigraphy from Possagno, Italy: The calcareous nannofossil response to climate variability. Earth and Planetary Science Letters 241, 815–830.
- Agnini, C., Spofforth, D. J., Dickens et al., 2016. Stable isotope and calcareous nannofossil assemblage record of the late Paleocene and early Eocene (Cicogna section). Climate of the Past (4), 883–909.
- Alegret, L., Ortiz, S., and Molina, E., 2009. Extinction and recovery of benthic foraminifera across the Paleocene–Eocene Thermal Maximum at the Alamedilla section (Southern Spain). Palaeogeography, Palaeoclimatology, Palaeoecology, 279(3–4), 186–200.
- Ali, J. R., Kent, D. V., Hailwood, E. A., 2000. Magnetostratigraphic reinvestigation of the Palaeocene/Eocene boundary interval in Hole 690B, Maud Rise, Antarctica. Geophysical Journal International 141(3), 639–646.
- Al-Suwaidi, A.H., Hesselbo, S.P., Damborenea, S.E., Manceñido, M.O., Jenkyns, H.C., Riccardi, A.C., Angelozzi, G.N., Baudin, F., 2016. The Toarcian Oceanic Anoxic Event (Early Jurassic) in the Neuquén Basin, Argentina: A Reassessment of Age and Carbon Isotope Stratigraphy. The Journal of Geology.
- Angori, E., Monechi, S., 1995. High-resolution calcareous nannofossils biostratigraphy across the Paleocene/Eocene boundary at Caravaca (southern Spain). Israel Journal of Earth Sciences 44, 197– 206.

- Arias, C.F., 1991. Las asociaciones de ostrácodos del Domeriense superior y Toarciense inferior de la Cordillera Ibérica. Coloquios de Paleontología 43, 79–99.
- Arias, C.F., 1995. Los ostrácodos del Toarciense inferior en la Cordillera Ibérica. Ph. D. Thesis. Fac. C. Geológicas. Univ. Complutense Madrid, Spain.
- Aubry, M.-P., 1995. Towards an upper Paleocene–lower Eocene high resolution stratigraphy based on calcareous nannofossils stratigraphy. Israel Journal of Earth Sciences 44, 239– 253.
- Aubry, M.-P., 1998. Early Paleogene calcareous nannoplankton evolution: a tale of climatic amelioration. In: Aubry, M.-P., Lucas, S., Berggren, W.A. (Eds.), Late Paleocene and Early Eocene Climatic and Biotic Evolution. Columbia University Press, New York, 158–203
- Aubry, M.-P., 1999. Late Paleocene–early Eocene sedimentary history in western Cuba: implications for the LPTM and for regional tectonic history. Micropaleontology 45, 5 –18.
- Aubry, M.-P., 2001. Provincialism in the photic zone during the LPTM. In: Ash, A., Wing, Abstract Volume, Powell, S. (Eds.), Climate and Biota of the Early Paleogene. International Meeting, p. 6
- Aubry, M.P., Cramer, B.S., Miller, K.G., Wright, J.D., Kent, D. V., Olsson, R.K., 2000. Late Paleocene event chronology: Unconformities, not diachrony. Bulletin de la Societé. Geologique de France 171 (3), 367–378
- Aze, T., Pearson, P.N., Dickson, A.J., Badger, M.P.S.S., Bown, P.R., Pancost, R.D., Gibbs, S.J., Huber, B.T., Leng, M.J., Coe, A.L., Cohen, A.S., Foster, G.L., 2014. Extreme warming of tropical waters during the Paleocene-Eocene thermal maximum. Geology 42 (9),739–742
- Babila, T.L., Penman, D.E., Hönisch, B., Kelly, D.C., Bralower, T.J., Rosenthal, Y., Zachos, J.C., 2018. Capturing the global signature of surface ocean acidification during the Palaeocene–Eocene Thermal Maximum. Philosophical Transactions A 376.
- Bailey, T. R., Y. Rosenthal, McArthur, J.M., van de Schootbrugge, B., Thirlwall M. F., 2003. Paleoceanographic changes of the late Pliensbachian- early Toarcian interval: A possible link to the genesis of an oceanic anoxic event, Earth and Planetary Sciences Letters 212, 307–320.

- Bains, S., Norris, R. D., Cordfield, R. M., Faul, K. L., 2000. Termination of global warmth at the Palaeocene/Eocene boundary through productivity feedback. Nature 407, 171–174.
- Bains, S., R. Corfield, M., Norris, R. D., 1999. Mechanisms of climate warming at the end of the Paleocene, Science 285, 724–727.
- Bassoullet, J.P., Elmi, S., Poisson, A., Cecca, F., Bellion, Y., Guiraud, R., Baudin, F., 1993. Mid Toarcian. In: Dercourt, J., Ricou, L.E., Vrielynck, B. (Eds.), Atlas Tethys Paleoenvironmental Maps, BEICIP-FRANLAB, Rueil-Malmaison. 63–80.
- Beaufort, L., Barbarin, N., Gally, Y., 2014. Optical measurements to determine the thickness of calcite crystals and the mass of thin carbonate particles such as coccoliths. Nature Protocols 9 (3), 633–642
- Beaufort, L., Heussner, S., 2001. Seasonal dynamics of calcareous nannoplankton on a West European continental margin: The Bay of Biscay. Marine Micropaleontology 43(1–2), 27–55.
- Beaufort, L., Probert, I., Buchet, N., 2007. Effects of acidification and primary production on coccolith weight: Implications for carbonate transfer from the surface to the deep ocean. Geochemistry, Geophysics, Geosystems, 8(8).
- Beaufort, L., Probert, I., de Garidel-Thoron et al., 2011. Sensitivity of coccolithophores to carbonate chemistry and ocean acidification. Nature, 476(7358), 80–83.
- Bécaud, M., 2002. Le Toarcien de la bordure sud et sud-est du Massif armoricain (Deux-Sèvres et Vendée). Le naturaliste vendéen 2, 3-33.
- Bécaud, M., 2005. Ammonites peu connues du Toarcien inférieur du sud-ouest de la Vendée. Le naturaliste vendéen 5, 45-48.
- Bécaud, M., 2006. Les Hildoceratidae (Ammonitina) du Toarcien de la bordure sud et sud est du Massif armoricain (France). Docum. Lab. Géologie Lyon 162, 1-148.
- Berner, E.K., Berner, R.A., 1996. Global Environment: Water, Air, and Geochemical Cycles. Prentice Hall, New Jersey. 376 pp.
- Billard, C., Inouye, I., 2004. What is new in coccolithophore biology?. In Coccolithophores (pp. 1-29). Springer, Berlin, Heidelberg.

- Blair, S., Watkins, D. K., 2009. High-resolution calcareous nannofossil biostratigraphy for the Coniacian/Santonian Stage boundary, Western Interior Basin. Cretaceous Research 30, 367–384.
- Blättler, C. L., Henderson, G. M., Jenkyns, H. C., 2012. Explaining the Phanerozoic Ca isotope history of seawater. Geology 40(9), 843–846.
- Blättler, C. L., Jenkyns, H. C., Reynard, L. M., & Henderson, G. M., 2011. Significant increases in global weathering during Oceanic Anoxic Events 1a and 2 indicated by calcium isotopes. Earth and Planetary Science Letters 309(1-2), 77–88.
- Blomeier, D.P.G., Reijmer, J.J.G., 1999. Drowning of a lower Jurassic carbonate platform: Jbel Bou Dahar, High Atlas, Morocco. Facies 41, 81–110.
- Bodin, S., Krencker, F. N., Kothe, T., Hoffmann, R., Mattioli, E., Heimhofer, U., Kabiri, L., 2016. Perturbation of the carbon cycle during the late Pliensbachian - early Toarcian: New insight from high-resolution carbon isotope records in Morocco. Journal of African Earth Sciences, 116, 89–104. https://doi.org/10.1016/j.jafrearsci.2015.12.018
- Bodin, S., Mattioli, E., Fröhlich, S., Marshall, J. D., Boutib, L., Lahsini, S., and Redfern, J., 2010, Documentation of Early Toarcian (Jurassic) carbon isotope negative shifts and nutrient changes along the Northern Gondwana margin (High Atlas, Morocco): palaeoenvironmental implications: Palaeogeo., Palaeoclim., Palaeoecol. 297, 377–390.
- Boomer, I., Lord, A.R., Page, K.N.., Bown, P.R., Lowry, F.M.D., Riding, J.B., 2009. The biostratigraphy of the Upper Pliensbachian–Toarcian (Lower Jurassic) sequence at Ilminster, Somerset. Journal of Micropalaeontology 28, 67–85.
- Boudreau, B. P., Middelburg, J. J., & Luo, Y. (2018). The role of calcification in carbonate compensation. Nature Geoscience, 11(12), 894–900.
- Bour, I., Mattioli, E., Pittet, B.,2007. Nannofacies analysis as a tool to reconstruct paleoenvironmental changes during the Early Toarcian anoxic event. Palaeogeography, Palaeoclimatology, Palaeoecology 249(1–2), 58–79.
- Bowen, G. J., 2013. Up in smoke: A role for organic carbon feedbacks in Paleogene hyperthermals. Global and Planetary Change 109, 18–29

- Bown, P. R., 2005a. Palaeogene calcareous nannofossils from the Kilwa and Lindi areas of coastal Tanzania (Tanzania Drilling Project 2003-4). J. Nannoplankton Res. 27 (1), 2005, 21–95.
- Bown, P. R., 2010. Calcareous nannofossils from the Paleocene/Eocene Thermal Maximum interval of southern Tanzania (TDP Site 14). Journal of Nannoplankton Research. 31(1), 11–38.
- Bown, P. R., Dunkley Jones, T., 2006. New Paleogene calcareous nannofossil taxa from coastal Tanzania: Tanzania Drilling Project Sites 11 to 14. Journal of Nannoplankton Research 28 (1), 17–34.
- Bown, P. R., Pearson, P., 2009. Calcareous plankton evolution and the Paleocene/Eocene thermal maximum event: New evidence from Tanzania. Marine Micropaleontology 71, 60–70.
- Bown, P.R., 1987. Taxonomy, evolution and biostratigraphy of Late Triassic-early Jurassic calcareous nannofossils. Special Papers in Paleontology 38, 1–118.
- Bown, P.R., 2005b. Cenozoic calcareous nannofossils biostratigraphy, ODP Leg 198 Site 1208 (Shatsky Rise, northwest Pacific Ocean). In Bralower, T.J., Premoli Silva, I., and Malone, M.J. Proceedings of the Ocean Drilling Program. Scientific Results 198, 1– 44.
- Bown, P.R., 2016. Paleocene calcareous nannofossils from Tanzania (TDP sites 19, 27 and 38). J. Nannoplankton Res, The calcareous nannofossil genus Ericsonia in the upper Paleocene 149 36 (1), 1–32.
- Bown, P.R., Cooper, M.K.E., 1998. Jurassic. In: Bown, P.R. (Ed), Calcareous Nannofossil Biostratigraphy, British Micropalaeontological Society Series. Chapman and Hall/Kluwer Academic Publishers, London, 86–131.
- Bralower, T., Clay Kelly, D., Gibbs, S., Farley, K., Eccles, L., Lindemann, T.L., Smith, G. S., 2014. Impact of dissolution on the sedimentary record of the Paleocene–Eocene thermal maximum. Earthy and Planetary Sciences Letters 401, 70–82.
- Bralower, T.J., 2002. Evidence of surface water oligotrophy during the Paleocene–Eocene Thermal Maximum: nannofossil assemblage data from Ocean Drilling Program Site 690 Maud Rise, Weddell Sea. Paleoceanography 17, 1–13.
- Bralower, T.J., Kelly, D.C., Gibbs, S., Farley, K., Eccles, L., Lindemann, T.L.,

Smith, G.J., 2014. Impact of dissolution on the sedimentary record of the Paleocene–Eocene thermal maximum. Earth and Planetary Science Letters 401, 70–82.

- Bralower, T.J., Mutterlose, J., 1995. Calcareous nannofossil biostratigraphy of ODP Site 865, Allison Guyot, Central Pacific Ocean: a tropical Paleogene reference section. In: Winterer, E.L., Sager, W.W., Firth, J.V. (Eds.), Proceedings of the Ocean Drilling Program. Scientific Results 143, 31– 72.
- Bralower, T.J., Premoli Silva, I., Malone, M.J., et al., 2002. Proc. ODP, Initial Reports., 198: College Station, TX (Ocean Drilling Program).
- Bralower, T.J., Self-Trail, J.M., 2016. Nannoplankton malformation during the Paleocene-Eocene Thermal Maximum and its paleoecological and paleoceanographic significance. Paleoceanography 31, 1423–1439.
- Bramlette, M. N., Sullivan, F. R., 1961. Coccolithophorids and related nannoplankton of the early Tertiary in California. Micropaleontology, 129-188.
- Brand, W. A., Coplen, T.B., Vogl, J., Rosner, M., Prohaska, T., 2014. Assessment of international reference materials for isotope-ratio analysis. Pure and Applied Chemistry 8866, 425¬–467.
- Brazier, J. M., Suan, G., Tacail, T., Simon, L., Martin, J. E., Mattioli, E., Balter, V., 2015. Calcium isotope evidence for dramatic increase of continental weathering during the Toarcian oceanic anoxic event (Early Jurassic). Earth and Planetary Science Letters 411, 164–176.
- Bridgestock, L., Hsieh, Y. T., Porcelli, D., & Henderson, G. M. (2019). Increased export production during recovery from the Paleocene–Eocene thermal maximum constrained by sedimentary Ba isotopes. Earth and Planetary Science Letters, 510, 53-63.
- Bucefalo Palliani, R. B., Cirilli S., Mattioli E., 1998. Influences of the relative sea level fluctuations on the primary productivity, an example from the early Toarcian Umbria-Marche basin (central Italy), Palaeogeogeography, Palaeoclimatology and Paleoecology 142, 33–50.
- Bukry, D., 1973. Low-latitude coccolith biostratigraphic zonation. In: Edgar, N.T., Saunders, J.B., et al. Initial Reports of the Deep Sea Drilling Project 15. U.S. Government Printing Office, Washington, 685–703.

- Bukry, D., 1975. Coccolith and silicoflagellate stratigraphy, northwestern Pacific Ocean, Deep Sea Drilling Project Leg 32. In: Larson, R.L., Moberly, R., et al. Initial Reports of the Deep Sea Drilling Project 32. U.S. Government Printing Office, Washington, 677– 701.
- Bybell, L.M., Self-Trail, J.M., 1995. Evolutionary, biostratigraphic, and taxonomic study of calcareous nannofossils from a continuous Paleocene-Eocene boundary section in New Jersey. US Geological Survey Professional Paper 1554.
- Bybell, L.M., Self-Trail, J.M., 1997. Late Paleocene and early Eocene calcareous nannofossils from three boreholes in an onshore-offshore transect from New Jersey to the Atlantic Continental Rise. Proceedings of the Ocean Drilling Program. Scientific results 150, 91–110.
- Caldeira, K., Wickett, M. E., 2005 Ocean model predictions of chemistry changes from carbon dioxide emissions to the atmosphere and ocean. Journal of Geophysical Research: Oceans 110(C9).
- Cande, S.C., Kent, D.V., 1995. Revised calibration of the geomagnetic polarity timescale for the Late Cretaceous and Cenozoic. Journal of Geophysical Research 100, 6093– 6095.
- Casellato, C.E., Erba, E., 2015. Calcareous nannofossil biostratigraphy and paleoceanography of the toarcian oceanic anoxic event at colle di sogno (Southern Alps, Northern Italy). Rivista Italiana di Paleontologia e Stratigrafia 121, 297–327.
- Cecca, F., Macchioni, F., 2004. The two Early Toarcian (Early Jurassic ) extinction events in ammonoids. Lethaia 3, 35-56.
- Channon, M. B., Gordon, G. W., Morgan, J. L., Skulan, J. L., Smith, S. M., Anbar, A. D., 2015. Using natural, stable calcium isotopes of human blood to detect and monitor changes in bone mineral balance. Bone, 77, 69-74.
- Clémence, M. E., Gardin, S., Bartolini, A. 2015. New insights in the pattern and timing of the Early Jurassic calcareous nannofossil crisis. Palaeogeography, Palaeoclimatology, Palaeoecology 427, 100–108.
- Cohen, A. S., Coe, A. L., Harding, S. M., Schwark, L., 2004. Osmium isotope evidence for the regulation of atmospheric CO2 by continental weathering. Geology, 32(2), 157–160.

- Cohen, A. S., Coe, A. L., Kemp, D. B., 2007. The Late Palaeocene–Early Eocene and Toarcian (Early Jurassic) carbon isotope excursions: a comparison of their time scales, associated environmental changes, causes and consequences. Journal of the Geological Society 164(6), 1093–1108.
- Colosimo, A.B., Bralower, T.J., Zachos, J.C., 2006. Evidence for lysocline shoaling at the Paleocene/Eocene thermal maximum on Shatsky rise, northwest Pacific. Proceeding of the Ocean Drilling Program. Scientific Results 198, 1–36.
- Comas-Rengifo, M. J., Gómez, J. J., Goy, A., Herrero, C., Osete, M. L., Palencia, A., 2010. A complementary section for he proposed Toarcian (Lower Jurassic) global stratotype: the Almonacid de la Cuba sections (Spain). Stratigraphy and Geological Correlation 18, 133–152.
- Comas-Rengifo, M. J., Gómez, J. J., Goy, A., Herrero, C., Perilli, N., Rodrigo, A., 1999. El Jurásico Inferior en la sección de Almonacid de la Cuba (Sector central de la Cordillera Ibérica), Zaragoza, España. Cuad. Geol. Ibér. 25, 27-57.
- Cope, J.C.W., 1984. The Mesozoic history of Wales. Proc. Geol. Assoc.95, 373–385.
- Copestake, P., Johnson, B., 2014. Lower Jurassic Foraminifera from the Llanbedr (Mochras Farm) Borehole, North Wales, UK. Monograph of the Palaeontographical Society 167.
- Courtinat, B., Pittet, B., Mattioli, E., Rio, M., 2007. Marine microplankton and calcareous nannofossil palaeoecology of the Toarcian stratotype. Geobios 40, 785–800.
- Crouch, E. M., Dickens, G. R., Brinkhuis, H., Aubry, M. P., Hollis, C. J., Rogers, K. M., and Visscher, H., 2003. The Apectodinium acme and terrestrial discharge during the Paleocene–Eocene thermal maximum: new palynological, geochemical and calcareous nannoplankton observations at Tawanui, New Zealand. Palaeogeography, Palaeoclimatology, Palaeoecology 194(4), 387–403.
- Crouch, E., Heilmann-Clausen, C., Brinkhuis H., Morgans H. E.G., Rogers K.M., Egger, H., Schmitz, B., 2001. Global dinoflagellate event associated with the late Paleocene thermal maximum. Geology 29(4), 315–318.
- Cubillos, J. C., Henderiks, J., Beaufort, L., Howard, W. R., Hallegraeff, G. M., 2012. Reconstructing calcification in ancient coccolithophores: Individual coccolith weight and morphology of *Coccolithus pelagicus* (sensu lato). Marine

Micropaleontology 92, 29–39.

- Dallanave, E., Agnini, C., Muttoni, G., Rio, D., 2009. Magneto-biostratigraphy of the Cicogna section (Italy): Implications for the late Paleocene-early Eocene time scale. Earth and Planetary Science Letters 285, 39–51.
- De La Rocha, C.L., De Paolo, D.J., 2000. Isotopic Evidence for Variations in the Marine Calcium Cycle Over the Cenozoic. Science 289, 1176–1178
- Dera, G., Neige, P., Dommergues, J. L., Brayard, A., 2011. Ammonite paleobiogeography during the Pliensbachian–Toarcian crisis (Early Jurassic) reflecting paleoclimate, eustasy, and extinctions. Global and Planetary Change, 78(3-4), 92–105.
- Dera, G., Pellenard, P., Neige, P., Deconinck, J.-F., Pucéat, E., Dommergues, J.-L., 2009. Distribution of clay minerals in Early Jurassic Peritethyan seas: Palaeoclimatic significance inferred from multiproxy comparisons. Palaeogeography, Palaeoclimatology, Palaeoecology 271, 39–51.
- Dera, G., Pucéat, E., Pellenard, P., Neige, P., Delsate, D., Joachimski, M. M., et al., 2009. Water mass exchange and variations in seawater temperature in the NW Tethys during the Early Jurassic: evidence from neodymium and oxygen isotopes of fish teeth and belemnites. Earth and Planetary Science Letters 286(1–2), 198–207.
- Dickens, G.R., Castillo, M.M., Walker, J.G.C., 1997. A blast of gas in the latest Paleocene: Simulating first-order effects of massive dissociation of oceanic methane hydrate, Geology 25, 259–262.
- Dickens, G.R., O'Neil, J.R., Rea, D.K., Owen, R.M., 1995. Dissociation of oceanic methane hydrate as a cause of the carbon isotope excursion at the end of the Paleocene. Paleoceanography 10, 965–971
- Dickson, Journal of Chemical Thermodynamics 22,113–127, 1990.
- Dickson, A. J., Cohen, A. S., Coe, A. L., Davies, M., Shcherbinina, E. A., & Gavrilov, Y. O., 2015. Evidence for weathering and volcanism during the PETM from Arctic Ocean and Peri-Tethys osmium isotope records. Palaeogeography, Palaeoclimatology, Palaeoecology 438, 300–307.
- Dickson, A. G., Millero, F. J., 1987. A comparison of the equilibrium constants for the dissociation of carbonic acid in seawater media. Deep Sea Research Part A. Oceanographic Research Papers 34(10), 1733–1743.

- Dromart, G., Allemand, P., Garcia, J.-P., Robin, C., 1996. Variation cyclique de la production carbonatée au Jurassique le long d'un transect Bourgogne-Ardèche, Est-France. Bull. Soc. Géol. Fr. 167, 423–433.
- Duncan, R. A., Hooper, P. R., Rehacek, J., Marsh, J. S., Ducan, A. R., 1997. The timing and duration of the Karoo igneous sevent, southern Gondwana. Journal of Geophysical Research 102, 127–138.
- Edgar, K. M., Anagnostou, E., Pearson, P. N., & Foster, G. L., 2015. Assessing the impact of diagenesis on $\delta^{11}B$, $\delta^{13}C$, $\delta^{18}O$, Sr/Ca and B/Ca values in fossil planktic foraminiferal calcite. Geochimica et Cosmochimica Acta 166, 189–209.
- Elmi, S., 2007. Pliensbachian/Toarcian boundary: the proposed GSSP of Peniche (Portugal). Ciências da Terra (UNL) 16, 7-16.
- Elmi, S., Rulleau, L., Gabilly, J., Mouterde, R., 1997. Ammonites: Toarcien. In: Cariou, E., Hantzpergue, P. (Eds.), Biostratigraphie du Jurassique ouest-européen et méditerranéen: Zonations parallèles et distribution des invertebrés et microfossiles. Groupe Français d'Etude du Jurassique. Bulletin du Centre de Recherches, Elf Exploration Production, 17, pp. 25-36 + 120-125.
- Erba, E., 2004. Calcareous nannofossils and Mesozoic oceanic anoxic events. Marine Micropaleontology 52 (1–4), 85–106.
- Erbacher, J., Mosher, D.C., Malone, Berti, D., Bice, K. L., Bostock, H., Jürgen Brumsack, H., Danelian, T., Glatz, C., Heidersdorf, F., Henderiks, J., Janecek, T., Junium, C., Le Callonec, L., MacLeod, K., Meyers, P. A., Mutterlose, J., Nishi, H., Norris, R., Ogg, J. G., O'Regan, M., Rea, B., Sexton, P., Sturt, H., Suganuma, Y., Thurow, J.W., Wilson, P. A., Wise, S. W., 2004. Demerara rise: equatorial cretaceous and Paleogene paleoceanographic transect, Western Atlantic (Leg 207, Sites 1257–1261). Proceedings of the Ocean Drilling Program 207, 1–89.
- Fabry, V. J., Seibel, B. A., Feely, R. A., Orr, J. C., 2008 . Impacts of ocean acidification on marine fauna and ecosystem processes. ICES Journal of Marine Science 65(3), 414-432.
- Fantasia, A., Föllmi, K. B., Adatte, T., Spangenberg, J. E., Montero-Serrano, J. C., 2018. The Early Toarcian oceanic anoxic event: Paleoenvironmental and paleoclimatic change across the Alpine Tethys (Switzerland). Global and Planetary Change, 162, 53–68.
- Fantle, M. S., Tipper, E. T., 2014. Calcium isotopes in the global biogeochemical

Ca cycle: implications for development of a Ca isotope proxy. Earth-Science Reviews,129, 148–177.

- Farkaš, J., Böhm, F., Wallmann, K., Blenkinsop, J., Eisenhauer, A., van Geldern, R., Munnecke, A., Voigt, S., Veizer, J., 2007a. Calcium isotope record of Phanerozoic oceans: implications for chemical evolution of seawater and its causative mechanisms. Geochim. Cosmochim. Acta 71, 5117–5134.
- Farley, K. A., Love, S. G., Patterson, D. B., 1997. Atmospheric entry heating and helium retentivity of interplanetary dust particles. Geochimica et Cosmochimica Acta, 61(11), 2309–2316.
- Farley, K.A., Eltgroth, S.F., 2003. An alternative age model for the Paleocene–Eocene thermal maximum using extraterrestrial 3He. Earth and Planetary Science Letters 208, 135–148.
- Farley, K.A., Love, S.G., Patterson, D.B., 1997. Atmospheric entry heating and helium retentivity of interplanetary dust particles. Geochimica et Cosmochimica Acta 61, 2309–2316.
- Farrimond, P., G. Eglington, and S. C. Brassel, 1989. Toarcian anoxic event in Europe: An organic geochemical study, Marine and Petroleum Geology 6, 136–147.
- Fatela, F., Taborda, R., 2002. Confidence limits of species proportions in microfossil assemblages. Marine Micropaleontology 45(2), 169–174.
- Ferreira, J., Mattioli, E., Pittet, B., Cachão, Spangenberg, J.E., 2015. Palaeoecological insights on Toarcian and lower Aalenian calcareous nannofossils from the Lusitanian Basin (Portugal). Paleogeography, Paleoclimatology, Paleoecology 436, 245-262.
- Ferreira, J., Mattioli, E., Suchéras-Marx, B., Giraud, F., Duart, L., V., Pitter, B., Hassler, A., Spangenberg, J., 2019. Western Tethys Early and Middle Jurassic calcareous nannofossils biostratigraphy. Earth-Science Reviews 197, 1–19.
- Ferreira, J., Mattioli, E., van de Schootbrugge, B., 2017. Palaeoenvironmental vs. evolutionary control on size variation of coccoliths across the Lower-Middle Jurassic, Paleogeography, Paleoclimatology, Paleoecology. 465, 177–192.
- Fraguas, Á., Comas-Rengifo, M. J., Gómez, J. J., Goy, A., 2012. The calcareous nannofossil crisis in Northern Spain (Asturias province) linked to the Early

Toarcian warming-driven mass extinction. Marine Micropaleontology 94–95, 58–71.

- Fraguas, Á., Comas-Rengifo, M. J., Gómez, J. J., Goy, A., 2012. The calcareous nannofossil crisis in Northern Spain (Asturias province) linked to the Early Toarcian warming-driven mass extinction. Marine Micropaleontology 94–95, 58–71.
- Fraguas, Á., Erba, E., 2010. Biometric analyses as a tool for the differentiation of two coccolith species of the genus Crepidolithus (Pliensbachian, Lower Jurassic) in the Basque-Cantabrian Basin (Northern Spain). Marine Micropaleontology 77, 125–136.
- Frieling, J., Gebhardt, H., Huber et al., 2017. Extreme warmth and heat-stressed plankton in the tropics during the Paleocene-Eocene Thermal Maximum. Science advances 3(3), e1600891.
- Frieling, J., Peterse, F., Lunt, D. J., Bohaty, S. M., Sinninghe Damsté, J. S., Reichart, G. J., Sluijs, A., 2019. Widespread warming before and elevated barium burial during the Paleocene-Eocene Thermal Maximum: Evidence for methane hydrate release ?. Paleoceanography and paleoclimatology, 34(4), 546–566.
- Fu, X., Wang, J., Feng, X., Wang, D., Chen, W., Song, C., Zeng, S., 2016. Early Jurassic carbon-isotope excursion in the Qiangtang Basin (Tibet), the eastern Tethys: Implications for the Toarcian Oceanic anoxic event. Chemical Geology 442, 62–72.
- Fu, X., Wang, J., Feng, X., Wang, D., Chen, W., Song, C., Zeng, S., 2016. Early Jurassic carbon-isotope excursion in the Qiangtang Basin (Tibet), the eastern Tethys: Implications for the Toarcian Oceanic anoxic event. Chemical Geology 442, 62–72.
- Gabilly J., 1976. Le Toarcien à Thouars et dans le Centre-Ouest de la France. Biostratigraphie. Évolution de la faune (Harpoceratinae - Hildoceratinae); collection: Comité français de Stratigraphie - Les stratotypes français, vol. 3. Paris, éd. du CNRS, 217 p.
- Gabilly, J., 1964. Stratigraphie et limite de l'étage Toarcien Thouars et dans les régions voisines. Coll. Jurassique, Luxembourg (1962). C. R. Mém. Inst. Grand Duc., Sect. Sci. Nat. Phys. Math., pp. 193-201.

- Gabilly, J., 1973. Le Toarcien du Poitou. Biostratigraphie de la région du stratotype. Évolution des Hildocerataceae (Ammonitina) (Doctoral dissertation), Poitiers, 546 p.
- Garzarella, A., Raffi, I., 2018. Taxonomy and evolutionary relationships within the calcareous nannofossil genus Ericsonia in the upper Paleocene. Rivista Italiana di Paleontologia e Stratigrafia 124 (1), 129–150.
- Gautier, F., Mouterde, R., 1964. Stratigraphie - lacunes et irrégularités des dépôts à la limite du Jurassique inferieur et du jurassique moyen de la bordure nord des chaines ibériques (Espagne). Comptes rendus hebdomadaires des séances de l'académie des sciences 258, 3064.
- Geisen, M., Bollmann, J., Herrle, J.O., Mutterlose, J., Young, J.R., 1999. Calibration of the random settling technique for calculation of absolute abundances of calcareous nannoplankton. Micropaleontology 45, 437– 442.
- Gibbs, S. J., Stoll, H. M., Bown, P. R., Bralower, T. J., 2010. Ocean acidification and surface water carbonate production across the Paleocene–Eocene thermal maximum. Earth and Planetary Science Letters 295(3–4), 583–592.
- Gibbs, S., Shackleton, N., Young, J., 2004. Orbitally forced climate signals in mid-Pliocene nannofossil assemblages. Marine Micropaleontology 51(1–2), 39–56.
- Gibbs, S.J., Bralower, T.J., Bown, P.R., Zachos, J.C., Bybell, L.M., 2006a. Shelf and open-ocean calcareous phytoplankton assemblages across the Paleocene–Eocene thermal maximum: implication for global productivity gradients. Geology 34 (4), 233–236.
- Gibbs, S.J., Bralower, T.J., Bown, P.R., Zachos, J.C., Bybell, L.M., 2006b. Shelf and open-ocean calcareous phytoplankton assemblages across the Paleocene–Eocene thermal maximum: implication for global productivity gradients. Geology 34 (4), 233–236.
- Gibbs, S. J., Bown, P. R., Ridgwell et al., 2016. Ocean warming, not acidification, controlled coccolithophore response during past greenhouse climate change. Geology 44(1), 59-62.
- Gómez, J. J., Comas – Rengifo, M. J., Goy, A., 2016. Palaeoclimatic oscillations in the Pliensbachian (Early Jurassic) of the Asturian Basin (Northern Spain). Clim. Past, 12, 1199–1214.

- Gómez, J. J., Goy, A., Canales, M. L., 2008. Seawater temperature and carbon isotope variations in belemnites linked to mass extinction during the Toarcian (Early Jurassic) in Central and Northern Spain. Comparison with other European sections. Palaeogeography Palaeoclimatology Palaeoecology 258, 28–58.
- Goy, A., Martínez, G., 1990. Biozonacion del Toarciense en el área de La Almunia de Doña Godina-Ricla (Sector Central de la Cordillera Ibérica). Cuadernos Geología Ibérica 14, 9–44.
- Gradstein, F. M., Ogg, J. G., Schmitz, M. B., Ogg, G. M., 2012. The geologic time scale.
- Griffith, E. M., Fantle, M. S., Eisenhauer, A., Paytan, A., Bullen, T. D., 2015. Effects of ocean acidification on the marine calcium isotope record at the Paleocene–Eocene Thermal Maximum. Earth and Planetary Science Letters 419, 81–92.
- Griffith, E. M., Paytan, A., Caldeira, K., Bullen, T. D., Thomas, E., 2008a. A dynamic marine calcium cycle during the past 28 million years. Science 322(5908), 1671–1674.
- Griffith, E. M., Schauble, E. A., Bullen, T. D., & Paytan, A., 2008b. Characterization of calcium isotopes in natural and synthetic barite. Geochimica et Cosmochimica Acta, 72(23) 5641–5658.
- Griffith, E. M., Schmitt, A. D., Andrews, M. G., Fantle, M. S., 2020. Elucidating modern geochemical cycles at local, regional, and global scales using calcium isotopes. Chemical Geology, 534, 119445.
- Griffith, E.M., Paytan, A., Kozdon, R., Eisenhauer, A., Ravelo, A.C., 2008. Influences on the fractionation of calcium isotopes in planktonic foraminifera. Earth and Planetary Sciences Letters 268, 124–136.
- Gussone, N., Eisenhauer, A., Heuser, A., et al., 2003. Model for kinetic effects on calcium isotope fractionation ($\delta^{44}Ca$) in inorganic aragonite and cultured planktonic foraminifera. Geochimica et Cosmochimica Acta, 67(7), 1375–1382.
- Gutjahr, M., Ridgwell, A., Sexton, P. F., et al., 2017. Very large release of mostly volcanic carbon during the Palaeocene–Eocene Thermal Maximum. Nature 548(7669), 573–577.

- Hammer, Ø., Harper, D. A., Ryan, P. D., 2001. PAST: Paleontological statistics software package for education and data analysis. Palaeontologia electronica, 4(1), 9.
- Handley, L., Pearson, P., McMillan, I.K., Pancost, R.D., 2008. Large terrestrial and marine carbon and hydrogen isotope excursions in a new Paleocene/Eocene boundary section from Tanzania. Earth and Planetary Science Letters 275, 17–25.
- Haq, B. U., Loqmann G. P., 1976. Early Cenozoic calcareous nannoplankton biogeography of the Atlantic ocean. Marine Micropaleontology 1, 119–194.
- Hay, W.W., 1972. Probabilistic stratigraphy. Eclogae Geologicae Helveticae 65, 255–266.
- Hay, W.W., 1972. Probabilistic stratigraphy. Eclogae Geologicae Helveticae 65, 255–266.
- Henderiks, J., Rickaby, R. E., 2007. A coccolithophore concept for constraining the Cenozoic carbon cycle. Biogeosciences 4, 323–329.
- Henehan, M. J., Ridgwell, A., Thomas, E., Zhang et al., 2019. Rapid ocean acidification and protracted Earth system recovery followed the end-Cretaceous Chicxulub impact. Proceedings of the National Academy of Sciences 116(45), 22500–22504.
- Hermoso, M., Minoletti, F., Rickaby, R.E.M., Hesselbo, S.P., Baudin, F., Jenkyns, H.C., 2012. Dynamics of a stepped carbon-isotope excursion: Ultra high-resolution study of Early Toarcian environmental change. Earth and Planetary Science Letters 319–320, 45–54.
- Herrero, C., 1992. Los foraminífero del Toarciense inferior de la Cordillera Ibérica. Tesis Doctoral, Facultad de Ciencias Geológicas, Universidad Complutense de Madrid, 523 pp.
- Hesselbo, S. P., Bjerrum, C. J., Hinnov, L. A., MacNiocaill, C., Miller, K. G., Riding, J. B., van de Schootbrugge, B., 2013. Mochras borehole revisited: a new global standard for Early Jurassic earth history.
- Hesselbo, S. P., Gröcke, D. R., Jenkyns, H. C., Bjerrum, C. J., Farrimond, P., Bell, H. S. M., Green, O. R., 2000. Massive dissociation of gas hydrate during a Jurassic oceanic anoxic event. Nature 406(6794), 392–395.

- Hesselbo, S. P., Jenkyns, H. C., Duarte, L. V., Oliveira, L. C. 2007. Carbon-isotope record of the Early Jurassic (Toarcian) Oceanic Anoxic Event from fossil wood and marine carbonate (Lusitanian Basin, Portugal). Earth and Planetary Science Letters 253(3–4), 455–470.
- Hesselbo, S.P., 2008. Sequence stratigraphy and inferred relative sea-level change from the onshore British Jurassic. Proceedings of the Geologists' Association 119, 19–34.
- Hesselbo, S.P., 2008. Sequence stratigraphy and inferred relative sea-level change from the onshore British Jurassic. Proceedings of the Geologists' Association, 119, 19–34.
- Hesselbo, S.P., Jenkyns, H.C., Duarte, L.V., Oliveira, L.C.V., 2007. Carbon-isotope record of the Early Jurassic (Toarcian) Oceanic Anoxic Event from fossil wood and marine carbonate (Lusitanian Basin, Portugal). Earth Planet. Sci. Lett. 253, 455–470.
- Heuser, A., Eisenhauer, A., Scholz-Ahrens, K. E., & Schrezenmeir, J, 2016. Biological fractionation of stable Ca isotopes in Göttingen minipigs as a physiological model for Ca homeostasis in humans. Isotopes in environmental and health studies 52(6) 633-648.
- Holland, K., Branson, O., Haynes, L. L. et al., 2020. Constraining multiple controls on planktic foraminifera Mg/Ca. Geochimica et Cosmochimica Acta 273 116–136.
- Hori, R. S., 1997. The Toarcian radiolarian event in bedded cherts from southwestern Japan, Marine Micropaleontology 30, 159 – 169.
- Houghton, J. T., 2001. Climate Change 2001: The Scientific Basis.
- Huang, C.,Hesselbo, S. P., 2014. Pacing of the Toarcian Oceanic Anoxic Event (Early Jurassic) from astronomical correlation of marine sections. Gondwana Research, 25, 1348–1356.
- Iglesias-Rodriguez, M. D., Halloran, P. R., Rickaby et al., 2008. Phytoplankton calcification in a high-CO2 world. Science 320(5874), 336-340.
- Ivimey-Cook, H.C., 1971. Stratigraphical palaeontology of the Lower Jurassic of the Llanbedr (Mochras Farm) Borehole. In: Woodland, A.W. (Ed.), The Llanbedr (Mochras Farm) Borehole. Institute of Geological Sciences, 87–92.
- Izumi, K., Kemp, D. B., Itamiya, S., & Inui, M. (2018). Sedimentary evidence for enhanced hydrological cycling in response to rapid carbon release during the

early Toarcian oceanic anoxic event. Earth and Planetary Science Letters 481, 162–170.

- Jenkyns, H. C. (2010). Geochemistry of oceanic anoxic events. Geochemistry, Geophysics, Geosystems 11(3).
- Jenkyns, H. C., Jones, C. E., GrÖcke, D. R., Hesselbo, S. P., Parkinson, D. N., 2002. Chemostratigraphy of the Jurassic System: applications, limitations and implications for palaeoceanography. Journal of the Geological Society 159(4), 351–378.
- Jenkyns, H.C., 1988. The Early Toarcian (Jurassic) anoxic event: stratigraphic, sedimentary and geochemical evidence. Am. J. Sci. 288, 101–151.
- Jenkyns, H.C., Clayton, C.J., 1997. Lower Jurassic epicontinental carbonates and mudstones from England and Wales: chemostratigraphic signals and the early Toarcian anoxic event. Sedimentology, 44: 687–706.
- Jiang, S., Wise Jr, S. W., 2007. Taxonomic note: A new *Coccolithus* species that thrived during the Paleocene/Eocene Thermal Maximum. Journal of Nannoplankton Research 29, 88–91.
- Jiang, S., Wise, S.W., 2006. Surface-water chemistry and fertility variations in the tropical Atlantic across the Paleocene/Eocene Thermal Maximum as evidenced by calcareous nannoplankton from ODP Leg 207, Hole 1259B. Revue de Micropaléontologie 49, 227–244.
- Jones, T. D., Lunt, D. J., Schmidt, D. N., Ridgwell, A., Sluijs, A., Valdes, P. J., & Maslin, M., 2013. Climate model and proxy data constraints on ocean warming across the Paleocene–Eocene Thermal Maximum. Earth-Science Reviews 125 123–145.
- Kafousia, N., Karakitsios, V., Mattioli, E., Kenjo, S., Jenkyns, H. C., 2014. The toarcian oceanic anoxic event in the ionian zone, Greece. Palaeogeography, Palaeoclimatology, Palaeoecology 393, 135–145.
- Kahn, A., Aubry, M.P., 2004. Provincialism associated with the Paleocene/Eocene thermal maximum: Temporal constraint. Marine Micropaleontology 52, 117–131.
- Kaiho, K., Takeda, K., Petrizzo, M.R., Zachos, J.C., 2006. Anomalous shifts in tropical Pacific planktonic and benthic foraminiferal test size during the Paleocene–Eocene thermal maximum. Palaeogeography, Palaeoclimatology,

Palaeoecology 237, 456–464.

- Karoui-Yaakoub, N., M'barek-Jemaï, M. B., Cherni, R., 2011. Le passage Paléocène/Eocène au nord de la Tunisie (Jebel Kharouba): foraminifères planctoniques, minéralogie et environnement de dépôt. Revue de Paléobiologie 30(1), 105–121.
- Katz, M. E., Wright, J. D., Miller, K. G., Cramer, B. S., Fennel, K., Falkowski, P. G., 2005. Biological overprint of the geological carbon cycle. Marine Geology 217(3-4), 323–338.
- Kelly, C. D., Bralower, T. J., Zachos, J. C., Silva, I. P., Thomas, E., 1996. Rapid diversification of planktonic foraminifera in the tropical Pacific (ODP Site 865) during the late Paleocene thermal maximum. Geology 24(5), 423–426.
- Kelly, D. C., 2002. Response of Antarctic (ODP Site 690) planktonic foraminifera to the Paleocene–Eocene thermal maximum: faunal evidence for ocean/climate change. Paleoceanography 17(4), 23–1.
- Kelly, D. C., Zachos, J. C., Bralower, T. J., Schellenberg, S. A., 2005. Enhanced terrestrial weathering/runoff and surface ocean carbonate production during the recovery stages of the Paleocene-Eocene thermal maximum. Paleoceanography 20(4).
- Kelly, D.C., Bralower, T., J., Zachos, J.C., 1998. Evolutionary consequences of the latest Paleocene thermal maximum for tropical planktonic foraminifera. Palaeogeography, Palaeoclimatology, Palaeoecology 141, 139–161.
- Kelly, D.C., Nielsen, T.M.J., McCarren, H.K., Zachos, J.C., Röhl, U., 2010. Spatiotemporal patterns of carbonate sedimentation in the South Atlantic: Implications for carbon cycling during the Paleocene–Eocene thermal maximum. Palaeogeography, Palaeoclimatology, Palaeoecology 293, 30–40.
- Kelly, D.C., Zachos, J.C., Bralower, T.J., Schellenberg, S.A., 2005. Enhanced terrestrial weathering/runoff and surface ocean carbonate production during the recovery stages of the Paleocene-Eocene thermal maximum. Paleoceanography 20.
- Kemp, D. B., Coe, A. L., Cohen, A. S., Weedon, G. P., 2011. Astronomical forcing and chronology of the early Toarcian (Early Jurassic) oceanic anoxic event in Yorkshire, UK. Paleoceanography 26(4).

- Kemp, D.B., Coe, A.L., Cohen, A.S., Schwark, L., 2005. Astronomical pacing of methane release in the Early Jurassic period. Nature 437, 396–399.
- Kennedy, J., Gale, A.S., Bown, P.R., Caron, M., Davey, R.,Gröcke, D., Wray, D.S. 2000. Integrated stratigraphy of the Aptian-Albian boundary interval in the Marnes Bleues, at the Col de Pré-Guittard, Arnayon (Drôme), and at Tartonne (Alpes-de-Haute-Provence), France, a candidate Global Boundary Stratotype Section and Boundary Point for the base of the Albian stage. Cretaceous Research 21, 591–720.
- Kennett, J.P., Stott, L.D., 1991. Abrupt deep-sea warming, palaeoceanographic changes and benthic extinctions at the end of the Palaeocene. Nature 353, 225–229.
- Kısakürek, B., Eisenhauer, A., Böhm, F., Hathorne, E. C., Erez, J., 2011. Controls on calcium isotope fractionation in cultured planktic foraminifera, Globigerinoides ruber and Globigerinella siphonifera. Geochimica et Cosmochimica Acta 75(2), 427–443.
- Koch, P. L., J. C. Zachos, and P. D. Gingerich (1992), Correlation between isotope records in marine and continental carbon reservoirs near the Palaeocene/Eocene boundary, Nature 358, 319– 322.
- Komar, N., Zeebe, R. E., 2011. Oceanic calcium changes from enhanced weathering during the Paleocene-Eocene thermal maximum: No effect on calcium-based proxies. Paleoceanography, 26(3).
- Komar, N., Zeebe, R. E., 2016. Calcium and calcium isotope changes during carbon cycle perturbations at the end-Permian. Paleoceanography 31(1), 115–130.
- Korte, C. and Hesselbo, S. P, 2011. Shallow-marine carbon- and oxygen isotope and elemental records indicate icehouse-greenhouse cycles during the Early Jurassic, Paleoceanography 26, PA4219.
- Kozdon, R., Kelly, D. C., Kitajima, K., Strickland, A., Fournelle, J. H., & Valley, J. W., 2013. In situ $\delta^{18}O$ and Mg/Ca analyses of diagenetic and planktic foraminiferal calcite preserved in a deep-sea record of the Paleocene-Eocene thermal maximum. Paleoceanography,28(3), 517–528.
- Krebs, C.J., 1998. Ecological methodology (2nd edition). Addison Wesley Longman (Eds., Pearson Education), pp. 620.

- Kroon, D., Norris, R.D., Klaus, A., 1998. Proceeding of the Ocean Drilling Program. Initial Reports 171B.
- Lemarchand, D., Wasserburg, G. J., Papanastassiou, D. A., 2004. Rate-controlled calcium isotope fractionation in synthetic calcite. Geochimica et cosmochimica acta, 68(22), 4665–4678.
- Léonide, P., Floquet, M., Durlet, C., Baudin, F., Pittet, B., Lécuyer, C., 2012. Drowning of a carbonate platform as a precursor stage of the Early Toarcian global anoxic event (Southern Provence sub-Basin, South-east France). Sedimentology 59, 156–184.
- Little, C.T.S., Benton, M.J., 1995. Early Jurassic mass extinction: a global long term event. Geology 23, 495–498.
- Littler, K., Hesselbo, S. P., Jenkyns, H. C., 2010. A carbon-isotope perturbation at the Pliensbachian–Toarcian boundary: evidence from the Lias Group, NE England. Geological Magazine, 147(2), 181-192.
- Lu G., Keller, G., Adattte T., Ortiz, N., Molina, E., 1996. Long-term ($10^5$) or short-term ($10^3$) $\delta^{13}C$ excursion nearthe Palaeocene-Eocene transition: evidence from the Tethys. Terra Nova 8, 347-355.
- Luo, Y., Boudreau, B. P., Dickens, G. R., Sluijs, A., & Middelburg, J. J. (2016). An alternative model for CaCO3 over-shooting during the PETM: biological carbonate compensation. Earth and Planetary Science Letters, 453, 223–233.
- Ma, Z., Gray, E., Thomas, E., Murphy, B., Zachos, J., & Paytan, A. (2014). Carbon sequestration during the Palaeocene–Eocene Thermal Maximum by an efficient biological pump. Nature Geoscience 7(5), 382–388.
- Mailliot, S., Mattioli, E., Guex, J., Pittet, B., 2006. The Early Toarcian anoxia, a synchronous event in the Western Tethys? An approach by quantitative biochronology (Unitary Associations), applied on calcareous nannofossils. Palaeogeography, Palaeoclimatology, Palaeoecology, 240(3–4), 562–586.
- Mallarino, G., Goldstein, R.H., Di Stefano, P., 2002. New approach for quantifying water depth applied to the enigma of drowning of carbonate platforms. Geology 30, 783–786.
- Marcantonio, F., Thomas, D.J., Woodard, S., McGee, D., Winckler, G., 2009. Extraterrestrial 3He in Paleocene sediments from Shatsky Rise: Constraints on sedimentation rate variability. Earth and Planetary Science Letters 287, 24–30.

- Martin, J.E., Tacail, T., Adnet. S., Girard, C., Balter, V., 2015. Calcium isotopes reveal the trophic position of extant and fossil elasmobranchs. Chemical Geology 415, 118–125.
- Martindale, R.C., Aberhan, M., 2017. Response of macrobenthic communities to the Toarcian Oceanic Anoxic Event in northeastern Panthalassa (Ya Ha Tinda, Alberta, Canada). Palaeogeography, Palaeoclimatology, Palaeoecology 478, 103–120.
- Martinez, M., Krencker, F.-N., Mattioli, E., Bodin, S., 2017. Orbital chronology of the Pliensbachian – Toarcian transition from the Central High Atlas Basin (Morocco). Newsletters on Stratigraphy 50(1), 47–69.
- Martini, E., 1971. Standard Tertiary and Quaternary calcareous nannoplankton zonation. In: Farinacci, A., Proceedings of the 2nd International Conference on Planktonic Microfossils 2, 739– 785
- Mattioli, E. 1996. New calcareous nannofossil species from the Early Jurassic of Tethys. Rivista Italiana di Paleontologia e Stratigrafia 102(3).
- Mattioli, E., Erba E., 1999. Synthesis of calcareous nannofossil events in tethyan lower and middle Jurassic successions. Rivista Italiana di Paleontologia e Stratigrafia 105, 343–376.
- Mattioli, E., Pittet, B., 2002. Contribution of calcareous nannoplankton to carbonate deposition: a new approach applied to the Lower Jurassic of central Italy. Marine micropaleontology, 45(2), 175–190.
- Mattioli, E., Pittet, B., Palliani, R., Rohl, H.-J., Schmid-Rohl, A., Morettini, E., 2004b. Phytoplankton evidence for the timing and correlation of palaeoceanographical changes during the early Toarcian oceanic anoxic event (Early Jurassic). Journal of the Geological Society 161(4), 685–693.
- Mattioli, E., Pittet, B., Petitpierre, L., Mailliot, S., 2009. Dramatic decrease of pelagic carbonate production by nannoplankton across the Early Toarcian anoxic event (T-OAE). Global and Planetary Change 65(3–4), 134–145.
- Mattioli, E., Pittet, B., Suan, G., Mailliot, S. 2008. Calcareous nannoplankton changes across the early Toarcian oceanic anoxic event in the western Tethys. Paleoceanography 23(3).
- Mattioli, E., Pittet, B., Young, J.R., Bown, P.R., 2004a. Biometric analysis of Pliensbachian-Toarcian (Lower Jurassic) coccoliths of the family Biscutaceae:

intra- and interspecific variability versus palaeoenvironmental influence. Marine Micropalaeontology 52, 5–27.

- Mattioli, E., Pittet, B., Young, J.R., Bown, P.R., 2004b. Biometric analysis of Pliensbachian-Toarcian (Lower Jurassic) coccoliths of the family Biscutaceae: intra- and interspecific variability versus palaeoenvironmental influence. Marine Micropalaeontology 52, 5-27.
- Mattioli, E., Plancq, J., Boussaha, M., Duarte, L.V., Pittet, B., 2013. Calcareous nannofossil biostratigraphy: new data from the Lower Jurassic of the Lusitanian Basin. Comunicacoes Geologicas T. 100, 100 (Especial I), 69–76.
- McArthur, J. M., D. T. Donovan, M. F. Thirwall, B. W. Fouke, and D. Mattey, 2000. Strontium isotope profile of early Toarcian (Jurassic) oceanic anoxic event, the duration of ammonite biozones, and belmnite palaeotemperature, Earth and Planetary Sciences Letters 179, 269–285.
- McArthur, J.M., Donovan, D.T., Thirwall, M.F., Fouke, B.W., Mattey, D., 2000. Strontium isotope profile of early Toarcian (Jurassic) oceanic anoxic event, the duration of ammonite biozones, and belmnite palaeotemperature. Earth Planet. Sci. Lett. 179, 269–285.
- McCarren, H., Thomas, E., Hasegawa, T., Röhl, U., Zachos, J.C., 2008. Depth dependency of the Paleocene-Eocene carbon isotope excursion: Paired benthic and terrestrial biomarker records (Ocean Drilling Program Leg 208, Walvis Ridge). Geochemistry, Geophysics, Geosystems 9, 1–10.
- McElwain, J.C.,Wade-Murphy, J., Hesselbo, S.P., 2005. Changes in carbon dioxide during an oceanic anoxic event linked to intrusion into Gondwana coals. Nature 435, 479–482.
- Medd, A. W., 1982. Nannofossil zonation of the English Middle and Upper Jurassic. Marine Micropalentology. 7, 73–95.
- Mehrbach, C., Culberson, C. H., Hawley, J. E., & Pytkowicx, R. M. (1973). Measurement of the apparent dissociation constants of carbonic acid in seawater at atmospheric pressure 1. Limnology and oceanography 18(6), 897–907.
- Menini, A., Mattioli, E., Spangenberg, J. E., Pittet, B., and Suan, G., 2019. New calcareous nannofossil and carbon isotope data for the Pliensbachian/Toarcian boundary (Early Jurassic) in the western Tethys and their paleoenvironmental implications. Newsletters on Stratigraphy, 173–196.

- Mensik, H., 1965. Stratigraphie und Palaegeographie des marinen Jura in der nord-westlichen Iberischen Keten (Spanien). Bein. Geol. lb., 55-102.
- Milliman, J. D., 1993. Production and accumulation of calcium carbonate in the ocean: budget of a nonsteady state. Global geochemical cycles 7(4), 927–957.
- Monechi, S., Angori, E., von Salis, K., 2000. Calcareous nannofossil turnover around the Paleocene/Eocene transition at Alamedilla (southern Spain). Bulletin de la Soceté Géologique de France 171 (4), 477–489.
- Morard, A., Guex, J., Bartolini, A., Morettini, E., De Wever, P., 2003. A new scenario for the Domerian - Toarcian transition. Bull. Soc. géol. Fr. 4, 351–356.
- Morgan, J. L., Skulan, J. L., Gordon, G. W., Romaniello, S. J., Smith, S. M., & Anbar, A. D., 2012. Rapidly assessing changes in bone mineral balance using natural stable calcium isotopes. Proceedings of the National Academy of Sciences 109(25), 9989-9994.47.
- Murphy, B.H., Farley, K.A., Zachos, J.C., 2010. An extraterrestrial 3He-based timescale for the Paleocene–Eocene thermal maximum (PETM) from Walvis Ridge, IODP Site 1266. Geochimica et Cosmochimica Acta 74, 5098–5108.
- Mutterlose, J., Linnert, C., Norris, R., 2007. Calcareous nannofossils from the Paleocene-Eocene Thermal Maximum of the equatorial Atlantic (ODP Site 1260B): Evidence for tropical warming. Marine Micropaleontology 65, 13–31.
- Nicolo, M. J., Dickens, G. R., Hollis, C. J., 2010. South Pacific intermediate water oxygen depletion at the onset of the Paleocene-Eocene thermal maximum as depicted in New Zealand margin sections. Paleoceanography 25(4).
- Nicolo, M.J., Dickens, G.R., 2006. Data Report: Terrigenous Grain-Size Distributions at Sites 1263 and 1267: Testing the Applicability of Leg 208 Sediments for Eolian Analysis, in: Kroon, D., Zachos, J.C., Richter, C. (Eds.), Proceedings of the Ocean Drilling Program, Scientific Results Volume 208, College Station, TX 1–13.
- Nielsen, L. C., Druhan, J. L., Yang, W., Brown, S. T., DePaolo, D. J., 2012. Calcium isotopes as tracers of biogeochemical processes. In Handbook of environmental isotope geochemistry, 105–124. Springer, Berlin, Heidelberg.
- Noël, D., 1965. Sur les Coccolithes du Jurassique Européen et d'Afrique du Nord. Éditions du Centre National de la Recherche Scientifique, 110-111, Paris.

- Noël, D., 1972. Nannofossiles calcaires de sediments jurassiques finement laminés. Bull. Mus. Hist. Natur., 3e sér., 75, pp. 95-116, 9 text-figs., 15 pls.
- Norris, R. D., 1996. Symbiosis as an evolutionary innovation in the radiation of Paleocene planktic foraminifera. Paleobiology, 461–480.
- O'Dea, S.A., Gibbs, S.J., Bown, P.R., Young, J.R., Poulton, A.J., Newsam, C., Wilson, P.A., 2014. Coccolithophore calcification response to past ocean acidification and climate change. Nature Communcations 5 (5363).
- Okada, H., and Honjo, S., 1973. The distribution of oceanic coccollithophorids in the Pacific,Deep Sea Res. Oceanogr. Abstr., 20, 355– 374.
- Okada, H., Bukry, K., 1980. Supplementary modification and introduction of code numbers to the low-latitude coccolith biostratigraphic zonation. Marine Micropaleontology 5, 321–325.
- Paasche, E., 1968. Biology and physiology of coccolithophorids, Annual Review of Microbiology 22, 71–86.
- Pagani, M., Zachos, J. C., Freeman, K. H., Tipple, B., Bohaty, S., 2005. Marked decline in atmospheric carbon dioxide concentrations during the Paleogene. Science 309(5734), 600–603.
- Page, K.N., 2003. The Lower Jurassic of Europe: its subdivision and correlation. Geol. Surv. Den. Greenl. Bull.1, 23–59.
- Pak, D. K., Miller, K. G., 1992. Paleocene to Eocene benthic foraminiferal isotopes and assemblages: Implications for deep water circulation, Paleoceanography 7, 405– 422.
- Pak, D., Miller, K., Browning, J., 1997. Global significance of an isotopic record from the New Jersey coastal plain: linkage between the shelf and deep sea in the late Paleocene to early Eocene. In Proceedings of the Ocean Drilling Program. Scientific results 156, 305–315.
- Pálfy, J., Smith, P.L., 2000. Synchrony between Early Jurassic extinction, oceanic anoxic event, and the Karoo-Ferrar flood basalt volcanism. Geology 28, 747-750.
- Palliani, R. B., Mattioli, E., Riding, J. B., 2002. The response of marine phytoplankton and sedimentary organic matter to the early Toarcian (Lower Jurassic) oceanic anoxic event in northern England. Marine micropaleontology 46(3–4), 223–245.

- Pancost, R. D., Crawford, N., Magness, S., Turner, A., Jenkyns, H. C., Maxwell, J. R., 2004. Further evidence for the development of photic-zone euxinic conditions during Mesozoic oceanic anoxic events, Journal of the Geological Society of London, 161, 1–12.
- Penman, D. E., Zachos, J. C., 2018. New constraints on massive carbon release and recovery processes during the Paleocene-Eocene Thermal Maximum. Environmental Research Letters 13(10), 105008.
- Penman, D.E., Hönisch, B., Zeebe, R.E., Thomas, E., Zachos, J.C., 2014. Rapid and sustained surface ocean acidification during the Paleocene-Eocene Thermal Maximum. Paleoceanography 29, 2014 PA002621.
- Penman, D.E., Turner, S.K., Sexton, P.F., Norris, R.D., Dickson, A.J., Boulila, S., Ridgwell, A., Zeebe, R.E., Zachos, J.C., Cameron, A., Westerhold, T., Röhl, U., 2016. An abyssal carbonate compensation depth overshoot in the aftermath of the Palaeocene-Eocene Thermal Maximum. Nature Geosciece 9, 575–580.
- Perch-Nielsen, K., 1985. Cenozoic calcareous nannofossils. In: Bolli, H.M., Saunders, J.B., Perch-Nielsen, K. Plankton Stratigraphy. Cambridge University Press, Cambridge, 427–554.
- Percival, L. M. E., Witt, M. L. I., Mather, T. A., Hermoso, M., et al., 2015. Globally enhanced mercury deposition during the end-Pliensbachian extinction and Toarcian OAE: A link to the Karoo–Ferrar Large Igneous Province. Earth and Planetary Science Letters 428, 267–280.
- Percival, L.M.E., Cohen, A.S., Davies, M.K., Dickson, A.J., Hesselbo, S.P., Jenkyns, H.C., Leng, M.J., Mather, T.A., Storm, M.S., Xu, W., 2016. Osmium isotope evidence for two pulses of increased continental weathering linked to Early Jurassic volcan-ism and climate change. Geology 44, 759–762.
- Peti, L., Thibault, N., Clémence, M.-E., Korte, C., Dommergues, J.-L., Bougeault, C., Pellenard, P., Jelby, M.E., Ullmann, C.V., 2017. Sinemurian–Pliensbachian calcareous nannofossil biostratigraphy and organic carbon isotope stratigraphy in the Paris Basin: Calibration to the ammonite biozonation of NW Europe. Palaeogeography, Palaeoclimatology, Palaeoecology 468, 142–161.
- Petrizzo, M. R., 2007. The onset of the Paleocene–Eocene Thermal Maximum (PETM) at Sites 1209 and 1210 (Shatsky Rise, Pacific Ocean) as recorded by planktonic foraminifera. Marine Micropaleontology 63(3–4), 187–200.

- Petrizzo, M. R., Leoni, G., Speijer, R. P., De Bernardi, B., & Felletti, F., 2008. Dissolution susceptibility of some Paleogene planktonic foraminifera from ODP site 1209 (Shatsky Rise, Pacific Ocean). The Journal of Foraminiferal Research, 38(4), 357–371.
- Philippe, M., Pujialon, S., Suan, G., Mousset, S., Thévenard, F., Mattioli, E., 2017. The palaeolatitudinal distribution of fossil wood genera as a proxy for European Jurassic terrestrial climate. Palaeogeography, Palaeoclimatology, Palaeoecology 466, 373 –381.
- Pittet, B., Suan, G., Lenoir, F., Vitor, L., Mattioli, E., 2014. Carbon isotope evidence for sedimentary discontinuities in the lower Toarcian of the Lusitanian Basin (Portugal): Sea level change at the onset of the Oceanic Anoxic Event. Sedimentary Geology, 303, 1–14.
- Poulton, A. J., Sanders, R., Holligan, P. M., Stinchcombe, M. C., Adey, T. R., Brown, L., Chamberlain, K., 2006 Phytoplankton mineralization in the tropical and subtropical Atlantic Ocean. Global Biogeochemical Cycles 20(4).
- Price, G. D., 1999. The evidence and implications of polar ice during the Mesozoic, Earth-Sciences Reviews 48, 183–210.
- Quillévéré, F., Norris, R. D., Moussa, I., Berggren, W. A., 2001. Role of photosymbiosis and biogeography in the diversification of early Paleogene acarininids (planktonic foraminifera). Paleobiology 27(2), 311–326.
- Raffi, I., Backman, J., Pälike, H., 2005. Changes in calcareous nannofossil assemblages across the Paleocene/Eocene transition from the paleo-equatorial Pacific Ocean. Palaeogeography, Palaeoclimatology, Palaeoecology 226, 93–126.
- Raffi, I., Backman, J., Zachos, J.C., Sluijs, A., 2009. The response of calcareous nannofossil assemblages to the Paleocene Eocene Thermal Maximum at the Walvis Ridge in the South Atlantic. Marine Micropaleontology 70, 201–212.
- Raffi, I., De Bernardi, B., 2008. Response of calcareous nannofossils to the Paleocene– Eocene thermal maximum: observations on composition, preservation and calcification in sediments from ODP Site 1263 (Walvis Ridge - SW Atlantic). Marine Micropaleontology 69, 119–138.
- Ravizza G., Norris R. N., Blusztajn J., Aubry M.P., 2001. An osmium isotope excursion associated with the late Paleocene thermal maximum: Evidence of

intensified chemical weathering. Paleoceanography and Paleoclimatology 16(2), 155–163

- Reggiani, L., Mattioli, E., Pittet, B., Duarte, L.V., Veiga de Oliveira, L.C., Comas-Rengifo, M.J., 2010. Pliensbachian (Early Jurassic) calcareous nannofossils from the Peniche section (Lusitanian Basin, Portugal): A clue for palaeoenvironmental reconstructions. Marine Micropaleontology 75 (1–4), 1–16.
- Reolid, M., Emanuela, M., Nieto, L.M., Rodriguez-Tovar, F.J., 2014. The Early Toarcian Oceanic Anoxic Event in the External Subbetic (Southiberian Palaeomargin, Westernmost Tethys): Geochemistry, nannofossils and ichnology. Palaeogeography, Palaeoclimatology, Palaeoecology 411, 79–94.
- Révész, K., Landwehr, J.M., 2002. $\delta^{13}C$ and $\delta^{18}O$ isotopic composition of $CaCO_3$ measured by continuous flow isotope ratio mass spectrometry: statistical evaluation and verification by application to Devils Hole core DH-11 calcite. Rapid Communications in Mass Spectrometry 16, 2102–2114.
- Ridgwell, A., 2007. Interpreting transient carbonate compensation depth changes by marine sediment core modeling. Paleoceanography, 22(4).
- Ridgwell, A., Zeebe, R. E., 2005. The role of the global carbonate cycle in the regulation and evolution of the Earth system. Earth and Planetary Science Letters, 234(3–4), 299–315.
- Riley, T. R., Millar, I. L., Watkeys, M.K., Curtis, M. L., Leat, P.T., Klausen, M. B., Fanning, C. M., 2004. U–Pb zircon (SHRIMP) ages for the Lebombo rhyolites, South Africa: refining the duration of Karoo volcanism. Journal of the Geological Society 161(4), 547–550.
- Roberts, J., Kaczmarek, K., Skinner, L.C., Bijma J., Bradbury, H., Turchyn A.V., Misra, S., Lithium Isotopes in Benthic Foraminifera, GCA 2020.
- Rocha, R. Mattioli, E., Duarte, L.V., Pittet, B., Elmi, S., Mouterde, R., Cabral, M.C., Comas-Rengifo, M.J., Gómez, J.J., Goy, A., Hesselbo, S.P., Jenkyns, H.C., Littler, K., Mailliot, S., Veiga de Oliveira, L.C., Osete, M.L., Perilli, N., Pinto, S., Ruget, C. and Suan, G., 2016. Base of the Toarcian Stage of the Lower Jurassic defined by the Global Boundary Stratotype Section and Point (GSSP) at the Peniche section (Portugal). Episodes 39, 460-481.
- Röhl, H. J., A. Schmid-Röhl, O. Wolfgang, A. Frimmel, S. Lorenz, 2001. The Posidonia Shale (Lower Toarcian) of SW-Germany: An oxygen-depleted

ecosystem controlled by sea level and palaeoclimate, Palaeogeogeogr. Palaeoclimatol. Palaeoecol., 165, 27 – 52.

- Rohl, H. J., Schmid-Rohl, A., O. Frimmel, Wolfgang, A., Lorenz, S., 2001. The Posidonia Shale (Lower Toarcian) of SW-Germany: An oxygen-depleted ecosystem controlled by sea level and palaeoclimate, Palaeogeogeogry, Palaeoclimatology, Palaeoecology 165, 27–52.
- Röhl, U., L. J. Abrams, 2000, High-resolution, downhole and non-destructive core measurements from Sites 999 and 1001 in the Caribbean Sea: Application to the late Paleocene thermal maximum, Proceedings of the Ocean Drilling Program Sci. Results 165, 191–203.
- Röhl, U., L. J. Abrams, 2000, High-resolution, downhole and non-destructive core measurements from Sites 999 and 1001 in the Caribbean Sea: Application to the late Paleocene thermal maximum, Proceedings of the Ocean Drilling Program Sci. Results 165, 191–203.
- Röhl, U., Westerhold, T., Bralower, T.J., Zachos, J.C., 2007. On the duration of the Paleocene–Eocene thermal maximum (PETM). Geochemistry, Geophysics, Geosystems 8
- Romein, A.J.T., 1979. Lineages in early Paleogene calcareous nannoplankton (Doctoral dissertation, Utrecht University), 76–78.
- Rosales, I., Quesada, S., Robles, S., 2004. Paleotemperature variations of Early Jurassic seawater recorded in geochemical trends of belemnites from the Basque - Cantabrian basin, northern Spain. Palaeogeography, Palaeoclimatology, Palaeoecology 203, 253–275.
- Rosales, I., Quesada, S., Robles, S., 2004. Paleotemperature variations of Early Jurassic seawater recorded in geochemical trends of belemnites from the Basque - Cantabrian basin, northern Spain. Palaeogeography, Palaeoclimatology, Palaeoecology 203, 253–275.
- Rost, B., Riebesell, U., 2004. Coccolithophores and the biological pump: responses to environmental changes. In Coccolithophores (pp. 99-125). Springer, Berlin, Heidelberg.
- Roth, P.H., 1984. Preservation of calcareous nannofossils and fine-grained carbonate particles in mid-Cretaceous sediments from the southern Angola

Basin. In: Hay, W.W. (Ed.), Initial Reports of Deep Sea Drilling Project 75. U.S. Government Printing Office, Washington, 651–655.

- Ruhl, M., Hesselbo, S. P., Hinnov, L., Jenkyns, H. C., Xu, W., et al., 2016. Astronomical constraints on the duration of the Early Jurassic Pliensbachian Stage and global climatic fluctuations. Earth and Planetary Science Letters 455, 149–165.
- Sabatino, N., Neri, R., Bellanca, A., Jenkyns, H. C., Baudin, F., Parisi, G., Masetti, D., 2009. Carbon-isotope records of the Early Jurassic (Toarcian) oceanic anoxic event from the Valdorbia (Umbria–Marche Apennines) and Monte Mangart (Julian Alps) sections: palaeoceanographic and stratigraphic implications. Sedimentology 56, 1307–1328.
- Sandoval, J., Bill, M., Aguado, R., O'Dogherty, L., Rivas, P., Morard, A., Guex, J., 2012. The Toarcian in the Subbetic basin (southern Spain): Bio-events (ammonite and calcareous nannofossils) and carbon-isotope stratigraphy. Palaeogeography, Palaeoclimatology, Palaeoecology, 342–343(May 2012), 40–63. Shannon, C.E., Weaver, W., 1949. The Mathematical Theory of Communication, Univ. of Ill. Press, Urbana, Ill.
- Schmid-Rohl, A., Rohl, H. J., O. Frimmel, W., A., Schwark L., 2002, Palaeoenvironmental recontruction of lower Toarcian epiconrinental black shales (Posidonia Shale, SW Germany): Global versus regional control, Geobios (Jodhpur India) 35, 13–20.
- Schneidermann, N., 1977. Selective dissolution of recent coccoliths in the Atlantic Ocean. In: Ramsay, A.T.S. (Ed.), Oceanic Micropaleontology. Vol. 2, pp. 1009–1053.
- Schouten, S., M. Woltering, W. I. C. Rijpstra, A. Sluijs, H. Brinkhuis, and J. S. Sinninghe Damste, 2007. The Paleocene-Eocene carbon isotope excursion in higher plant organic matter: Differential fractionation of angiosperms and conifers in the Arctic, Earth and Planetary Sciences Letters 258, 581–592.
- Self-Trail, J. M., Powars, D. S., Watkins, D. K., Wandless, G., 2012. Calcareous nannofossil assemblage changes across the Paleocene-Eocene thermal maximum: Evidence from a shelf setting, Marine Micropaleontology 92–93, 61–80.

- Self-Trail, J. M., Powars, D. S., Watkins, D. K., Wandless, G., 2012. Calcareous nannofossil assemblage changes across the Paleocene-Eocene thermal maximum: Evidence from a shelf setting, Marine Micropaleontology 92–93, 61–80,
- Sellwood, B.W., Jenkyns, H.C., 1975. Basins and swells and the evolution of an epeiric sea (Pliensbachian–Bajocian of Great Britain). Journal of the Geological Society of London 131, 373–388.
- Shamrock, J. L., Watkins, D. K., 2012. Eocene calcareous nannofossil biostratigraphy and community structure from Exmouth Plateau, Eastern Indian Ocean (ODP Site 762). Stratigraphy 9 (1), 1–11.
- Sime, N. G., Christina, L., Galy, A., 2005. Negligible temperature dependence of calcium isotope fractionation in 12 species of planktonic foraminifera. Earth and Planetary Science Letters 232(1–2), 51–66.
- Simms, M.J., Chidlaw, N., Morton, N., Page, K.N., 2004. British Lower Jurassic Stratigraphy. Geological Conservation Review Series 30. Joint Nature Conservation Committee, Peterborough.
- Sluijs, A., Bowen, G., Brinkhuis, H., Lourens, L., Thomas, E., 2007. The Palaeocene-Eocene Thermal Maximum super greenhouse: biotic and geochemical signatures, age models and mechanisms of global change. Deep Time Perspectives on Climate Change: Marrying the Signal From Computer Models and Biological Proxies, 323–347.
- Sluijs, A., Brinkhuis, H., Schouten, S., Bohaty, S. M., John, C. M., Zachos, J. C. et al., 2007. Environmental precursors to rapid light carbon injection at the Palaeocene/Eocene boundary. Nature, 450(7173), 1218–1221.
- Sluijs, A., Röhl, U., Schouten, S., Brumsack, H. J., Sangiorgi, F., Damsté, J. S. S., Brinkhuis, H., 2008. Arctic late Paleocene–early Eocene paleoenvironments with special emphasis on the Paleocene-Eocene thermal maximum (Lomonosov Ridge, Integrated Ocean Drilling Program Expedition 302). Paleoceanography 23(1).
- Sluijs, A., Schouten, S., Pagani, M. et al., 2006. Subtropical Arctic Ocean temperatures during the Palaeocene/Eocene thermal maximum. Nature 441, 610–613.

- Sluijs, A., Van Roij, L., Harrington et al., 2014. Warming, euxinia and sea level rise during the Paleocene–Eocene Thermal Maximum on the Gulf Coastal Plain: implications for ocean oxygenation and nutrient cycling. Climate of the Past 10, 1421–1439, 2014.
- Spangenberg, J.E., Herlec, U., 2006. Hydrocarbon biomarkers in the Topla-Mežica zinc-lead deposits, northern Karavanke/Drau Range, Slovenia: Paleoenvironment at the site of ore formation. Economic Geology 101(5), 997-1021.
- Stap, L., Sluijs, A., Thomas, E., Lourens, L., 2009. Patterns and magnitude of deep sea carbonate dissolution during Eocene Thermal Maximum 2 and H2, Walvis Ridge, southeastern Atlantic Ocean. Paleoceanography 24.
- Stoll, H. M., Bains, S., 2003. Coccolith Sr/Ca records of productivity during the Paleocene-Eocene thermal maximum from the Weddell Sea. Paleoceanography 18(2), 1–11.
- Stoll, H. M., Shimizu N., Archer D., Ziveri P., 2007. Coccolithophore productivity response to greenhouse event of the Paleocene–Eocene Thermal Maximum. Earth and Planetary Science Letters 258, 192–206.
- Stoll, H. M., Shimizu N., Arevalos A., Matell N., Banasiak A, Zeren S., 2007. Insights on coccolith chemistry from a new ion probe method for analysis of individually picked coccoliths. Geochemistry, Geophysics, Geosystems 8 (6), 1–8.
- Storm, M. S., Hesselbo, S. P., Jenkyns, H. C., Ruhl, M., Ullmann, C. V., Xu, W. et al., 2020. Orbital pacing and secular evolution of the Early Jurassic carbon cycle. Proceedings of the National Academy of Sciences 117(8), 3974–3982.
- Storme, J.Y., Devleeschouwer, X., Schnyder, J., Cambier, G., Baceta, J.I., Pujalte, V., Di Matteo, A., Iacumin, P., Yans, J., 2012. The Palaeocene/Eocene boundary section at Zumaia (Basque-Cantabric Basin) revisited: New insights from high-resolution magnetic susceptibility and carbon isotope chemostratigraphy on organic matter ($\delta^{13}C_{org}$). Terra Nova 24, 310–317.
- Stradner, H., Papp, A., 1961. Tertiäre Discoasteriden aus Österreich und deren stratigraphische Bedeutung mit Hinweisen auf Mexico, Rumanien und Italien. Jahrbuch der Geologischen Bundesanstalt (Wien) 7, 1–159.

- Suan, G., Mattioli, E., Pittet, B., Lécuyer, C., Suchéras-Marx, B., Duarte et al., 2010. Secular environmental precursors to Early Toarcian (Jurassic) extreme climate changes. Earth and Planetary Science Letters 290 (3–4), 448–458.
- Suan, G., Mattioli, E., Pittet, B., Lécuyer, C., Suchéras-Marx, B., Duarte, L.V., Martineau, F., 2010. Secular environmental precursors to Early Toarcian (Jurassic) extreme climate changes. Earth and Planetary Science Letters 290(3–4), 448–458.
- Suan, G., Mattioli, E., Pittet, B., Mailliot, S., Lécuyer, C., 2008a. Evidence for major environmental perturbation prior to and during the Toarcian (Early Jurassic) oceanic anoxic event from the Lusitanian Basin, Portugal, Paleoceanography 23, PA1202.
- Suan, G., Pittet, B., Bour, I., Mattioli, E., Duarte, L. V., Mailliot, S., 2008b. Duration of the Early Toarcian carbon isotope excursion deduced from spectral analysis: consequence for its possible causes. Earth and Planetary Science Letters 267(3–4), 666–679.
- Suchéras-Marx, B., Mattioli, E., Allemand, P., Giraud, F., Pittet, B., Plancq, J., & Escarguel, G. (2019). The colonization of the oceans by calcifying pelagic algae.
- Svensen, H., Planke, S., Chevallier, L., Malthe-Sorenssen, A., Corfu, F., Jamtveit, B., 2007. Hydrothermal venting of greenhouse gases triggering Early Jurassic global warming. Earth and Planetary Sciences Letters 256, 554–566.
- Tacail T, Albalat E, Télouk P, Balter V., 2014. A simplified protocol for measurement of Ca isotopes in biological samples. J. Anal. At.Spectrom. 29,5 29–535.
- Tacail, T., Télouk, P., Balter, V., 2016. Precise analysis of calcium stable isotope variations in biological apatites using laser ablation MC-ICPMS. Journal of Analytical Atomic Spectrometry 31(1), 152–162.
- Tacail, T., Thivichon-Prince, B., Martin, J. E., Charles, C., Viriot, L., Balter, V., 2017. Assessing human weaning practices with calcium isotopes in tooth enamel. Proceedings of the National Academy of Sciences 114(24), 6268–6273.
- Takeda, K., Kaiho, K., 2007. Faunal turnovers in central Pacific benthic foraminifera during the Paleocene-Eocene thermal maximum. Palaeogeography, Palaeoclimatology, Palaeoecology 251, 175–197.

- Them, T.R., Gill, B. C., Caruthers, A.H., Gröcke, D.R., Tulsky, E.T., Martindale, R.C., … Smith, P.L., 2017. High-resolution carbon isotope records of the Toarcian Oceanic Anoxic Event (Early Jurassic) from North America and implications for the global drivers of the Toarcian carbon cycle. Earth and Planetary Science Letters 459, 118–126.
- Thierry, J. and Barrier, E., 2000. Middle Toarcian. In: J. Dercourt and M.e.a. Gaetani (Eds.), Atlas Peri-Tethys, Palaeogeographical Maps CCGM/CGMW, Paris.
- Thierstein, H.R., Roth, P.H., 1991. Stable isotopic and carbonate cyclicity in Lower Cretaceous deep-sea sediments: Dominance of diagenetic effects. Marine Geology 97, 1– 34.
- Thierstein, H. R., Corte`s, M. Y., Haidar, A. T., 2004. Plankton community behaviour on ecological and evolutionary timescales: When models confront evidence, in Coccolithophores From Molecular Processes to Global Impact, edited by H. R. Thierstein and J. R. Young, 455– 480.
- Thomas, E., Shackleton, N.J., 1996. The latest Paleocene benthic foraminiferal extinction and stable isotope anomalies. In: Knox, R.O., Corfield, R.M., Dunay, R.E. Correlation of the Early Paleogene in Northwest Europe. Geological Society of London Special Publication 101, 40–441.
- Thomas, E., Shackleton, N.J., 1996. The latest Paleocene benthic foraminiferal extinction and stable isotope anomalies. In: Knox, R.O., Corfield, R.M., Dunay, R.E. Correlation of the Early Paleogene in Northwest Europe. Geological Society of London Special Publication 101, 40–441.
- Tjalsma, R. C., Lohmann, G. P., 1983. Paleocene-Eocene bathyal and abyssal benthic foraminifera from the Atlantic Ocean. Micropaleontology Special Publication 4, 1–90.
- Tremolada, F., Bralower, T.J., 2004. Nannofossil assemblage fluctuations during the Paleocene-Eocene Thermal Maximum at Sites 213 (Indian Ocean) and 401 (North Atlantic Ocean): Palaeoceanographic implications. Marine Micropaleontology 52, 107–116.
- Tremolada, F., Van de Schootbrugge, B., Erba, E., 2005. Early Jurassic schizosphaerellid crisis in Cantabria, Spain: implications for calcification rates

and phytoplankton evolution across the Toarcian oceanic anoxic event. Paleoceanography 20(2).

- Tripati, A., Elderfield, H., 2005. Deep-sea temperature and circulation changes at the Paleocene-Eocene thermal maximum. Science, 308(5730), 1894–1898.
- Tyson, R. V., 1995. Abundance of organic matter in sediments: TOC, hydrodynamic equivalence, dilution and flux effects. In Sedimentary organic matter. 81–118. Springer, Dordrecht.
- Uppstrom, L. R. (1974). The boron/chlorinity ratio of deep-sea water from the Pacific Ocean. Deep Sea Research 21, 161–162.
- van de Schootbrugge, B., McArthur, J.M., Bailey, J.M., Rosenthal, Y., Wright, J.M., Miller, K.G., 2005, Toarcian oceanic anoxic event: An assessment of global causes using belemnite C isotope records, Paleoceanography, 20.
- van der Meulen, B., Gingerich, P. D., Lourens, L. J., Meijer, N., van Broekhuizen, S., van Ginneken, S., Abels, H. A., 2020. Carbon isotope and mammal recovery from extreme greenhouse warming at the Paleocene–Eocene boundary in astronomically-calibrated fluvial strata, Bighorn Basin, Wyoming, USA. Earth and Planetary Science Letters 534, 116044.
- Vink, A., Brune, A., Höll, C., Zonneveld, K. A., Willems, H., 2002. On the response of calcareous dinoflagellates to oligotrophy and stratification of the upper water column in the equatorial Atlantic Ocean. Palaeogeography, Palaeoclimatology, Palaeoecology 178(1–2), 53–66.
- von Salis, K., Monechi, S., Bybell, L.M., Young, J., 2000. Remarks on the calcareous nannofossil markers Rhomboaster and Tribrachiatus around the Paleocene/Eocene boundary. Journal of the Geological Society of Sweden 122, 138–140.
- Wei, W., Zhong, S., 1996. Taxonomy and magnetobiochronology of Tribrachiatus and Rhomboaster, two genera of calcareous nannofossils. Journal of Paleontology 70, 7– 22.
- Westerhold, T., Röhl, U., Donner, B., McCarren, H. K., Zachos, J. C., 2011. A complete high-resolution Paleocene benthic stable isotope record for the central Pacific (ODP Site 1209). Paleoceanography 26(2).
- Westerhold, T., Röhl, U., Donner, B., Zachos, J. C., 2018. Global extent of early Eocene hyperthermal events: A new Pacific benthic foraminiferal isotope record

from Shatsky Rise (ODP Site 1209). Paleoceanography and Paleoclimatology 33(6), 626–642.

- Westerhold, T., Röhl, U., Laskar, J., Raffi, I., Bowles, J., Lourens, L.J., Zachos, J.C., 2007. On the duration of magnetochrons C24r and C25n and the timing of early Eocene global warming events: Implications from the Ocean Drilling Program Leg 208 Walvis Ridge depth transect. Paleoceanography 22, 1–19.
- Westerhold, T., Röhl, U., Raffi, I., Fornaciari, E., Monechi, S., Reale, V., Bowles, J., Evans, H.F., 2008. Astronomical calibration of the Paleocene time. Palaeogeography, Palaeoclimatology, Palaeoecology 257 377–403.
- Westerhold, T., Röhl, U., Wilkens, R.H., Gingerich, P.D., Clyde, W.C., Wing, S.L., Bowen, G.J., Kraus, M.J., 2018b. Synchronizing early Eocene deep-sea and continental records – cyclostratigraphic age models for the Bighorn Basin Coring Project drill cores. Clim. Past 14, 303–319.
- Wiggan, N.J., Riding, J.B., Fensome, R.A., Mattioli, E., 2018. The Bajocian (Middle Jurassic): A key interval in the early Mesozoic phytoplankton radiation. Earth-Science Reviews 180, 126-146.
- Wignall, P.B., Hallam, A., Newton, R.J., Sha, J.G., Reeves, E., Mattioli, E., Crowley, S., 2006. An eastern Tethyan (Tibetan) record of the Early Jurassic (Toarcian) mass extinction event. Geobiology 4, 179–190.
- Winter, A., Siesser W.G., 2006. Coccolithophores. Cambridge University Press.
- Wise, S.W., Wind, F.H., 1977. Mesozoic and Cenozoic calcareous nannofossils recovered by DSDP Leg 36 drilling on the Falkland Plateau, south-west Atlantic sector of the Southern Ocean. Initial Reports of the Deep Sea Drilling Project 36, 269–491.
- Woodard, S.C., Thomas, D.J., Hovan, S., Röhl, U., Westerhold, T., 2011. Evidence for orbital forcing of dust accumulation during the early Paleogene greenhouse. Geochemistry, Geophysics, Geosystems 12.
- Woodland, A. W., 1971. The Llanbedr (Mochras Farm) Borehole,Report 71/18, Institute of Geological Sciences.
- Xu, W., Ruhl, M., Jenkyns, H. C., Hesselbo, S. P., Riding, J. B., et al., 2017. Carbon sequestration in an expanded lake system during the Toarcian oceanic anoxic event. Nature Geoscience, 10(2), 129-134.

- Xu, W., Ruhl, M., Jenkyns, H. C., Leng, M. J., Huggett, J. M., et al., 2018. Evolution of the Toarcian (Early Jurassic) carbon-cycle and global climatic controls on local sedimentary processes (Cardigan Bay Basin, UK). Earth and Planetary Science Letters 484, 396–411.
- Young, J. R., 1992. The description and analysis of coccolith structure. Nannoplankton Research. Hamrsmid B, Young JR (eds) ZPZ, Knihovnicha, 35–71.
- Young, J. R., 1994. Functions of coccoliths, in Coccolithophores, edited by A. Winter and W. Siesser, 63–82.
- Young, J. R., Ziveri, P., 2000. Calculation of coccolith volume and it use in calibration of carbonate flux estimates. Deep sea research Part II: Topical studies in oceanography, 47(9-11), 1679–1700.
- Zachos, J. C., Dickens, G. R., Zeebe, R. E., 2008. An early Cenozoic perspective on greenhouse warming and carbon-cycle dynamics. Nature, 451(7176), 279–283.
- Zachos, J.C., Kroon, D., Blum, P., Bowles, J., Gaillot, P., Hasegawa, T., Hathorne, E.C., Hodell, D. A., Kelly, D. C., Jung, J. H., Keller, S. M., Lee, Y. S., Leuschner, D. C., Lohmann, K. C., Lourens, L., Monechi, S., Nicolo, M., Raffi, I., Riesselman, C., Röhl, U., Schellenber, S. A., Schmidt, D., Slujis A., Thomas, D., Thomas, E., Vallius, H. , 2004. Early Cenozoic extreme climates: the Walvis Ridge transect. Proceedings of the Ocean Drilling Program. Initial Reports 208.
- Zachos, J.C., Lohmann, K.C., Walker, J.C.G., Wise, S.W. Jr., 1993. Abrupt climate change and transient climates during the Paleogene: A marine perspective, J. Geol. 101, 191 – 213.
- Zachos, J.C., Pagani, M., Sloan, L.C., Billups, K., Thomas, E., 2001. Trends, rhythms, and aberrations in global climate 65 Ma to present. Science 292, 686–693.
- Zachos, J.C., Rohl, U., Schellenberg, S.A., Sluijs, A., Hodell, D.A., Kelly, D.C., Thomas, E., Nicolo, M., Raffi, I., Lourens, L.J., McCarren, H., Kroon, D., 2005. Rapid acidification of the ocean during the Paleocene-Eocene thermal maximum. Science 308, 1611–1615.
- Zeebe, R. E., 2012. History of seawater carbonate chemistry, atmospheric CO 2, and ocean acidification. Annual Review of Earth and Planetary Sciences,

40(141), 2012.

- Zeebe, R. E., Zachos, J. C., Dickens, G. R., 2009. Carbon dioxide forcing alone insufficient to explain Palaeocene–Eocene Thermal Maximum warming. Nature Geoscience, 2(8), 576–580.
- Zeebe, R.E., Lourens, L.J., 2019. Solar System chaos and the Paleocene–Eocene boundary age constrained by geology and astronomy. Science 365, 926–929.

## Annexe 1 : Liste taxinomique

Dans cette liste sont reportés tous les taxa cités dans cette thèse. La taxinomie et les références bibliographiques suivent Bown, 1987, Bown, 1998, de Kaenel and Bergen, 1993, Mattioli et al., 2004a et Menini et al., 2019 pour l'intervalle Pliensbachien-Toarcien. La taxinomie et les références bibliographiques suivent Perch-Nielsen, 1985 et Bown 2005a pour le Paléocène-Eocène.

### Liste taxinomique pour l'intervalle Pliensbachien-Toarcien

*Axopodorhabdus atavus* (Grün et al., 1974) Bown, 1987

*Axopodorhabdus cylindratus* (Noël, 1965) Wind and Wise in Wise and Wind, 1977

*Biscutum dubium* (Noël, 1965) Grün in Grün et al., 1974

*Biscutum grande* Bown, 1987

*Biscutum intermedium* Bown, 1987

*Bussonius prinsii* (Noël, 1973) Goy, 1979

*Calyculus* spp. Noël, 1973

*Carinolithus poulnabronei* Mattioli, 1996

*Carinolithus superbus* (Deflandre in Deflandre and Fert, 1954) Prins in Grün et al., 1974

*Crepidolithus cavus* Prins ex Rood et al., 1973

*Crepidolithus crassus* (Deflandre in Deflandre and Fert, 1954) Noël, 1965

*Crepidolithus crucifer* Prins 1969

*Crepidolithus granulatus* Bown, 1987

*Crepidolithus impontus* Grün et al., 1974

*Crucirhabdus minutus* Jafar, 1983

*Crucirhabdus primulus* Prins, 1969 ex Rood et al., 1973 emend.

*Diductius constan*s Goy in Goy et al., 1979

*Ethmorhabdus crucifer* Noël, 1965

*Ethmorhabdus gallicus* Noël, 1965

*Lotharingius barozii* Noël, 1973

*Lotharingius crucicentralis* (Medd, 1971) Grün and Zweili, 1980

*Lotharingius frodoi* Mattioli, 1996

*Lotharingius hauffii* Grün and Zweili in Grün et al., 1974

*Lotharingius sigillatus* (Stradner, 1961) Prins in Grün et al., 1974

*Lotharingius umbriensis* Mattioli, 1996

*Lotharingius velatus* Bown and Cooper, 1989

*Mazaganella protensa* Bown, 1987

*Mitrolithus elegans* Deflandre in Deflandre and Fert, 1954

*Mitrolithus jansae* (Wiegand, 1984) Bown and Young in Young et al., 1986

*Mitrolithus lenticularis* Bown, 1987

*Orthogonoides hamiltoniae* Wiegand, 1984

*Parhabdolithus liasicus* Deflandre in Grassé, 1952

*Parhabdolithus liasicus* subsp. *distinctus* Bown, 1987

*Parhabdolithus liasicus* subsp. *liasicus* Deflandre in Grassé, 1952

*Schizosphaerella* Deflandre & Dangeard, 1938

*Silimiscutum cruciulus* subsp*. avitum* Mattioli et al., 2004b

*Similiscutum cruciulus* subsp. *cruciulus* Mattioli et al., 2004b

*Similiscutum finchii* (Crux, 1984 emend. Bown, 1987) de Kænel and Bergren, 1993

*Similiscutum novum* (Goy, 1979) Mattioli et al., 2004

*Similiscutum precarium* de Kænel and Bergen, 1993

*Sollasites arctus* (Noël, 1973) Bown, 1987

*Sollasites* sp. Black, 1967

*Stradnerlithus* Black, 1971

*Tubirhabdus patulus* Prins ex Rood et al., 1973

*Zygrhablithus bijugatus* Deflandre 1959

*Zygrhablithus* Deflandre 1959

**Liste taxinomique pour l'intervalle Paléocène-Eocène**

*Bomolithus aquilus* Bown 2010

*Bomolithus megastypus* (Bramlette and Sullivan 1961) Bown 2010

*Bomolithus* Roth 1973

*Bomolithus supremus* Bown and Dunkley Jones 2006

*Braarudosphaera* Deflandre 1957

*Bussonius leufuensis* Bown and Kielbowicz, 1987 in Bown, 1987

*Calciosolenia aperta* (Hay and Mohler 1967) Bown 2005a

*Campylosphaera dela* (Bramlette and Sullivan 1961) Hay and Mohler 1967

*Campylosphaera differta* Bown 2010

*Campylosphaera eodela* Bukry 1971

*Campylosphaera* Kamptner 1963

*Chiasmolithus bidens* (Bramlette and Sullivan 1961) Hay and Mohler 1967

*Chiasmolithus consuetus* (Bramlette and Sullivan 1961) Hay and Mohler 1967

*Chiasmolithus* Hay et al. 1966

*Coccolithus bownii* Jiang and Wise 2007

*Coccolithus pelagicus* Schiller 1930

*Coccolithus* Schwarz 1894

*Cruciplacolithus* Hay and Mohler 1967

*Discoaster anartios* Bybell and Self-Trail 1995

*Discoaster araneus* Bukry 1971

*Discoaster delicatus* Bramlette and Sullivan 1961

*Discoaster diastypus* Bramlette and Sullivan 1961

*Discoaster lenticularis* Bramlette and Sullivan 1961

*Discoaster mohleri* Bukry and Percival 1971

*Discoaster multiradiatus* Bramlette and Riedel 1954

*Discoaster nobilis* Martini 1961

*Discoaster salisburgensis* Stradner 1961

*Discoaster* Tan 1927

*Discorhabdus ignotus* (Górka, 1957) Perch-Nielsen, 1968

*Discorhabdus striatus* Moshkovitz & Ehrlich, 1976

*Ericsonia aliquanta* Bown 2016

*Ericsonia* Black 1964

*Ericsonia orbis* Bown 2016

*Ericsonia robusta* (Bramlette and Sullivan 1961) Edwards and Perch-Nielsen 1975

*Ericsonia subpertusa* Hay and Mohler 1967

*Fasciculithus alanii* Perch-Nielsen 1971

*Fasciculithus* Bramlette and Sullivan 1961

*Fasciculithus hayi* Haq 1971

*Fasciculithus involutus* Bramlette and Sullivan 1961

*Fasciculithus mitreus* Gartner 1971

*Fasciculithus richardii* group *sensu* Agnini et al. 2014

*Fasciculithus richardii* Perch-Nielsen 1971

*Fasciculithus schaubii* Hay and Mohler 1967

*Fasciculithus thomasii* Perch-Nielsen 1971

*Fasciculithus tonii* Perch-Nielsen 1971

*Fasciculithus tympaniformis* Hay and Mohler 1967

*Fasciculithus tympaniformis* Hay and Mohler *in* Hay et al. 1967

*Gladiolithus* Jordan and Chamberlain 1992

*Gladiolithus flabellatus* (Halldal and Markali 1955) Jordan and Chamberlain 1993

*Hornibrookina* Edwards, 1973

*Holodiscolithus* Roth 1970

*Jakubowskia leoniae* Varol 1989

*Markalius apertus* Perch Nielsen 1979

*Prinsius* Hay and Mohler 1967

*Rhombiaster calcitrapa* group *sensu* Raffi et al. 2005

*Rhomboaster* (Bramlette and Sullivan 1961)

*Semiholodithus* Perch-Nielsen 1971

*Semiholodithus biskayae* Perch-Nielsen 1971

*Semiholodithus dimidus* Bown 2005

*Semiholodithus kanungoi* Bown 2005

*Semiholodithus tentorium* Bown 2005

*Sphenolithus anarrhopus* Bukry and Bramlette 1969

*Sphenolithus* Deflandre *in* Grassé, 1952

*Sphenolithus moriformis* group *sensu* Agnini et al. 2014

*Thoracosphaera* Kamptner 1927

*Toweius callosus* Perch-Nielsen 1971

*Toweius eminens* (Bramlette and Sullivan, 1961) Perch-Nielsen, 1971

*Toweius* Hay and Mohler 1967

*Toweius serotinus* Bybell and Self Trail 1995

*Tribrachiatus bramlettei* (Bronnimann and Stradner 1960) Proto-Decima et al. 1975

*Tribrachiatus* Shamrai 1963